Sodium Lanthanide Fluoride Nanocrystals: Colloidal Synthesis, Applications as Nano-Bioprobes, and Fundamental Investigations on Epitaxial Growth

by

Noah John Joe Johnson
M.Sc., Martin-Luther-Universität, 2006
B.Tech., University of Madras, 2002

A Dissertation Submitted in Partial Fulfillment
of the Requirements for the Degree of

DOCTOR OF PHILOSOPHY

in the Department of Chemistry

© Noah John Joe Johnson, 2012
University of Victoria

All rights reserved. This dissertation may not be reproduced in whole or in part, by photocopy or other means, without the permission of the author.

Supervisory Committee

Sodium Lanthanide Fluoride Nanocrystals: Colloidal Synthesis, Applications as Nano-Bioprobes, and Fundamental Investigations on Epitaxial Growth

by

Noah John Joe Johnson
M.Sc., Martin-Luther-Universität, 2006
B.Tech., University of Madras, 2002

Supervisory Committee

Dr. Ir. Franciscus C. J. M. van Veggel (Department of Chemistry)
Supervisor

Dr. Alexandre G. Brolo (Department of Chemistry)
Departmental Member

Dr. Natia L. Frank (Department of Chemistry)
Departmental Member

Dr. Chris Papadopoulos (Department of Electrical & Computer Engineering)
Outside Member

Abstract

Supervisory Committee

Dr. Ir. Franciscus C. J. M. van Veggel (Department of Chemistry)

Supervisor

Dr. Alexandre G. Brolo (Department of Chemistry)

Departmental Member

Dr. Natia L. Frank (Department of Chemistry)

Departmental Member

Dr. Chris Papadopoulos (Department of Electrical & Computer Engineering)

Outside Member

The ability to grow materials in the nanometric size regime with controlled shape and size provide a fundamental synthetic challenge, while allowing for evaluation of such unique nanostructures in multiple applications. In this dissertation, colloidal sodium lanthanide fluoride ($NaLnF_4$) nanocrystals are described with an overall emphasis on i) size control, ii) surface chemistry related towards their applications as nano-bioprobes, and iii) the synthesis and fundamental aspects of epitaxial layer growth generally referred as core-shell nanocrystals.

Chapter 1 provides a brief overview on the basic aspects of colloidal nanocrystals. In Chapter 2, synthesis and surface modification of colloidal sodium lanthanide fluoride nanocrystals, epitaxial growth, and their applications in optical and magnetic resonance imaging is reviewed. Chapter 3 describes a phase transfer protocol utilizing polyvinylpyrrolidone and subsequent silica coating of initially hydrophobic upconverting nanocrystals. This protocol is extended in Chapter 4 using end-group functionalized polyvinylpyrrolidone and demonstrates tunability of surface charge and functional groups on upconverting nanocrystals for targeted labeling of human prostate cancer cells. The

synthesis of size-tunable $NaGdF_4$ nanocrystals below 10 nm is described in Chapter 5. These nanocrystals are evaluated for their efficacy in magnetic resonance imaging (MRI), and a fundamental insight into the effect of surface gadolinium ions in T_1 MRI contrast enhancement is presented. Chapter 6 demonstrates the synthesis of tunable, epitaxial layers on upconverting (core) nanocrystals. A novel synthetic strategy is demonstrated, by deliberate defocusing and self-focusing of differently sized nanocrystals driven by the common physical phenomenon of Ostwald ripening. Utilizing the contraction of lanthanide ions along the series, a fundamental investigation on the effect of compressive/tensile strain epitaxial layer growth is presented in Chapter 7. The fundamental rule of minimal lattice mismatch for epitaxial growth takes into account only the magnitude of mismatch and not the sign of mismatch caused by a compressive/tensile strained layer. A strong asymmetric effect between the compressive/tensile layer growth given the same magnitude of lattice mismatch is observed, demonstrating the necessity of including the sign of mismatch to generate isotropic (conformal)/ pseudomorphic (coherent) epitaxial growth. Finally, in Chapter 8 conclusions and possible future work are discussed.

Table of Contents

List of Tables

List of Figures

List of Abbreviations

AIBN	2,2'-azobisisobutyronitrile
CA(s)	contrast agent(s)
CTA	chain transfer agent
DAPI	4',6-diamidino-2-phenylindole
DCM	dichloromethane
DLS	dynamic light scattering
DMF	dimethylformamide
DMSA	dimercaptosuccinic acid
DMSO	dimethyl sulfoxide
EDC	*N*-(3-dimethylaminopropyl)-*N'*-ethylcarbodiimide hydrochloride
EDS	energy-dispersive X-ray spectroscopy
EELS	electron energy-loss spectroscopy
EMU	energy migration-mediated upconversion
EPR	enhanced permeability and retention
FT-IR	fourier transform-infrared
Gd-DOTA	gadolinium-tetraazacyclododecanetetraacetic acid
Gd-DTPA	gadolinium-diethylenetriaminepentacetate
HAADF	high-angle annular dark-field imaging
HR	high-resolution
ICP-MS	inductively coupled plasma mass spectroscopy
IS	inner sphere
JCPDS	Joint Committee on Powder Diffraction Standards
LNCaP	lymph node carcinoma of the prostate
LRET	luminescence resonance energy transfer
ML(s)	monolayer(s)
MRI	Magnetic Resonance Imaging
MWCO	molecular weight cut-off
NC(s)	nanocrystal(s)

NHS	*N*-hydroxysulfosuccinimide sodium salt
NIR	near-infrared
NMR	nuclear magnetic resonance
NP(s)	nanoparticle(s)
OS	outer sphere
PAA	poly(acrylic acid)
PC3	prostate cancer cell line
PDI	polydispersity index
PEG	poly(ethylene glycol)
PMAO	poly(maleic anhydride-*alt*-1-octadecene)
PMT	photo-multiplier tube
PSMA	prostate specific membrane antigen
PVP	polyvinylpyrrolidone
PVP-COOH	carboxylic acid functionalized polyvinylpyrrolidone
PVP-Mal	maleimide functionalized polyvinylpyrrolidone
PVP-NH_2	amine functionalized polyvinylpyrrolidone
RE	rare-earth
RF	radio frequency
SA	surface area
SNC(s)	sacrificial nanocrystal(s)
SPIO	superparamagnetic iron oxide
SS	secondary sphere
TEM	transmission electron microscopy
TEOS	tetraethyl orthosilicate
TGA	thermogravimetric analysis
UCNC(s)	upconverting nanocrystal(s)
UV	ultraviolet
VP	1-vinylpyrrolidone
XRD	X-ray diffraction
0D	zero-dimensional
2D	two-dimensional

Acknowledgments

I extend my deepest gratitude to everyone who helped, encouraged, mentored and stood by me along this whole sojourn as a graduate student, while I only cared about the next reaction to be successful and 'nothing else'. First and foremost, I would like to thank my mentor Prof. Frank van Veggel, without whom none of this would have been possible. His constant encouragement, and scientific discussions pushed me to investigate and understand some of the most challenging and basic aspects of colloidal chemistry. I am fortunate to have worked under his tutelage, as he mentored and supported my pursuits (giving me complete freedom to explore), but kept me on track all these years.

I would like to thank all the van Veggel group members with whom I have shared most of these years. Specially, I thank Dr. N. M. Sangeetha for teaching me and making me to appreciate and understand chemistry in a broader perspective.

I thank Dr. X. Duan, and Rob Sahota at the Deeley Research Centre (DRC, BC cancer center, Victoria) for helping me to learn and trouble-shoot with the cell cultures, and guiding me through the entire project. I am grateful to Prof. Robert Burke for helping me with the cell imaging studies. I thank Prof. Scott Prosser and Wendy Oakden at University of Toronto for the relaxivity measurements. I also thank Dr. Andreas Korinek at McMaster University for helping me with the analysis of core-shell samples.

I thank my PhD committee members for their advice and input on my research. I have also had the privilege to learn from their teaching in my early graduate school days. I am also grateful to Prof. Robert Scott, University of Saskatchewan for agreeing to be the external examiner.

I would like to thank Dr. Jody Spence, and Dr. Ori Granot at UVic for helping me with the ICP-MS, and MALDI-MS measurements, respectively. I am also grateful for the assistance from the other support staff throughout these years.

To my loving parents and loving sister (also to the cute new addition, my nephew), I am thankful for your constant support all these years, and the unfailing love you gave me. You are my strength and all I want to say is, I LOVE YOU.

Finally, I thank my Saviour for his Enduring Mercy and Everlasting Love.

Chapter 1. General Introduction

Nanomaterials are defined as materials where at least one dimension is in the size range of 1 - 100 nm.[1] The ability to shrink materials to such small dimensions results in increased surface to volume ratio and an unprecedented access to size-dependent properties that might not be possible with their larger counterparts.[2,3] Manipulation of matter in such nanodimensions has been explored in the past few decades as a potential tool to influence a wide spectrum of basic and applied investigations ranging from health sciences to energy storage, and quantum computing.[2,4,5] The advent of nanotechnology as a field of intense scientific exploration is further fuelled and supported by the advancement in characterization techniques of materials in nanodimensions. Colloidal bottom-up synthesis of nanocrystals, though challenging, is one of the major routes explored as it offers high degree of flexibility and ease of implementation without the need for costly set-up as that needed for top-down techniques.[6] In case of colloidal bottom-up approach utilizing molecular precursors as building blocks for constructing materials in nanodimensions warrants a complete control of manifold parameters. In short, the utility of nanomaterials starts with the ability to control precisely and understand the underlying growth parameters to manipulate matter synthetically in nanometer size regime for their potential use in various applications.

The overall synthetic parameters governing the growth of colloidal nanocrystals and the fundamental understanding of their growth is still a major field of intense research. The generality of nanocrystal growth in solution involves three major steps, i) active monomer formation and supersaturation, ii) nucleation, and iii) growth of the existing

nuclei into nanocrystals.[7,8] While these steps are general the parameters influencing each step are not universal and optimal reaction conditions need to be determined for the synthesis of different nanocrystals.

The interaction of nanomaterials with their surroundings or environment is largely influenced by the surface properties given their large surface to volume ratio. The organic ligands used in colloidal synthesis of nanomaterials stabilize them from aggregation and imparts dispersibility in suitable solvents, polymers, etc. However, from an applications standpoint the ligands used in the synthesis often need to be replaced or modified based on their potential application. For example, colloidal nanocrystals with long chain fatty acids as surface ligands (*e.g.* oleates) make them incompatible with aqueous systems or biological applications. Poor choice of surface ligands with respect to the application will lead to irreversible aggregation of the nanocrystals resulting in deterioration of their properties. In this regard, the ability to modify and manipulate the surface properties of the colloidal nanocrystals is of fundamental research interest along with the ability to synthesize colloidal nanocrystals. While the control on synthesis affords high quality nanocrystals, the control on the surface chemistry allows for integrating them with their specific end-use applications. These two aspects form the fundamental basis of exploration in developing colloidal nanocrystals for potential applications.

Colloidal nanocrystals given their larger surface to volume ratio interact with their environment more strongly which can be either advantageous or deleterious depending on their end-use applications. For example, in case of luminescent nanocrystals the interaction with solvent environment is highly deleterious for some potential applications and such nanocrystals have to be separated spatially from their local environment. This

requirement is satisfied by growing a shell (an epitaxial layer) of a closely lattice matched material on the core nanocrystals.[9] This approach enhances the properties of the spatially isolated core nanocrystals and also allows for integrating multiple functions into a single nanocrystal by selective choice of the epitaxial shell material.

The development of any colloidal nanocrystal needs to address one or more of these three basic design considerations:

1) Synthesis control with narrow size-distribution ($\sigma < 5\%$);
2) Flexible and tunable surface modification strategies depending of the application;
3) Ability to control and deposit epitaxial material to isolate spatially the core from the local environment.

The control over these parameters allows for developing high quality nanocrystals and their integration with the application without compromising their unique properties.

In this dissertation colloidal synthesis of sodium lanthanide fluoride ($NaLnF_4$) is explored for their potential applications as nano-bioprobes in optical and magnetic resonance imaging (MRI). The lanthanide series starting from lanthanum (Z = 57) to lutetium (Z = 71) form a unique series of 15 elements with almost similar chemical properties. This arises from the fact that the 4f valence electrons of lanthanide ions are shielded by fully filled 5s and 5p orbitals. This chemical similarity was considered boring in a general chemistry perspective in the 1970s by Pimentel and Sprately, "Lanthanum has only one important oxidation state in aqueous solution, the +3 state. With few exceptions, this tells the whole boring story about the other 14 lanthanides."[10] However the uniqueness of the lanthanides lies in their electronic properties and has been utilized in wide range of applications, such as solid state lighting, lasers, displays, optical

amplifiers in telecommunication, and in health sciences as magnetic resonance imaging (MRI) contrast agents.[11-16] They are still being explored for multiple potential applications and this scope is further widened with the advent of nanotechnology.

In Chapter 2, a brief overview of the properties of lanthanides in general, followed by their applications in optical imaging and magnetic resonance imaging is discussed. The general approach of synthesizing lanthanide-based colloidal nanocrystals is reviewed with a primary focus on sodium lanthanide fluoride ($NaLnF_4$) nanocrystals. A summary of known surface modification techniques on lanthanide-based nanocrystals and requirements for their utilization as nano-bioprobes is then discussed. Finally, epitaxial growth techniques and the challenges in obtaining control over the epitaxial shell growth parameters to synthesize core-shell nanocrystals are explained.

Chapter 3 demonstrates a general protocol for phase transfer of upconverting $NaYF_4$ nanocrystals to water. Utilizing a commercially available amphiphilic polymer polyvinylpyrrolidone (PVP) the surface oleates in the as-synthesized $NaYF_4$ are replaced to obtain water dispersible upconverting nanocrystals. The success of the approach is further validated by coating a thin shell of silica on the phase-transferred nanocrystals utilizing the affinity of PVP to silica. Further comparison with reverse micro-emulsion based silica coating methods and this protocol is provided demonstrating the advantage of the developed protocol.

In Chapter 4, a further advancement of the PVP coating to generate surface functional groups for further specific surface reactions is demonstrated. End-group functionalized PVP with either a terminal carboxylic acid or amino group were obtained by free-radical polymerization of vinylpyrrolidone. By replacing the unfunctionalized commercial PVP

with the end-group functionalized PVP it's demonstrated that one can easily manipulate the surface charge of the phase-transferred nanocrystals while simultaneously providing functional groups for tagging biomolecules. The success of this approach is demonstrated using human prostate cancer cells as a target for specific labeling. LNCaP cells are human prostate adenocarcinoma cells which over-express prostate specific membrane antigen (PSMA). By tagging the end-group functionalized PVP-coated nanocrystals with antibody (anti-PSMA) it's demonstrated that these nanocrystals can potentially be used for target specific uptake.

Chapter 5 demonstrates the synthesis of $NaGdF_4$ nanocrystals with size tunability below 10 nm. The developed synthetic protocol is the first evidence of size tunable lanthanide-based nanocrystals below 10 nm. This allowed for evaluating their size dependent properties as magnetic resonance imaging (MRI) contrast agents. For the first time an unequivocal evidence is shown for the surface gadolinium ions being the major contributor for T_1 relaxivity enhancement. Further analysis shows that the surface gadolinium ions on a larger nanocrystal affect the relaxivity more strongly than that on a smaller nanocrystal due to difference in their rotational correlation time.

The requirement of epitaxial shell thickness tunability and a novel approach to achieve precisely tunable epitaxial shell growth on upconverting nanocrystals is presented in Chapter 6. The results demonstrate that the conventional explanation of the core nanocrystals acting as nuclei/seeds for further epitaxial shell growth is not true and a ripening-mediated growth mode is responsible for the epitaxial shell growth. Based on these results a unique synthetic protocol utilizing the size-dependent dissolution and growth of nanocrystals based on a fundamental colloidal phenomenon of ripening is

described. Furthermore, precisely tunable shell growth and integration of one or more functionality within a single nanocrystal is demonstrated.

While the lanthanide ions along the series are chemically almost identical, their physical properties are not the same along the series. The size of lanthanide ions gradually decreases along the series generally known as the lanthanide contraction. In epitaxial shell growth the shell/epitaxial material adapts to the substrate (core) lattice parameter resulting in interfacial strain. To grow an epitaxial shell, the general rule of thumb is to have minimal mismatch and thus minimum interfacial strain between the core and the shell material. However, this general rule only considers the magnitude of mismatch and not the sign of mismatch caused by a compressive or tensile strained epitaxial layer. Utilizing the lanthanide contraction along the series multiple compressive and tensile strained hetero-epitaxial shell growth on $NaYF_4$ core nanocrystals is investigated in Chapter 7. This rule breaks down when the sign of mismatch is taken into account and a strong asymmetric effect is observed between the compressive and tensile strained thick epitaxial growth. While the former is not conformal even with minimal mismatch, the latter is conformal and pseudomorphic with relatively larger lattice mismatch. Further discussion with well-known examples in literature is also provided substantiating the observed asymmetric effect between the tensile and compressive epitaxial layer growth.

Finally, conclusions and possible future work is described in Chapter 8. The body of this dissertation combines the synthetic aspects, surface modification techniques, and epitaxial layer growth to achieve better control towards the use of $NaLnF_4$ as nano-bioprobes.

Chapter 2. Synthesis, Surface Functionalization, and Applications of Colloidal Sodium Lanthanide Fluoride Nanocrystals

2.1. Introduction

The majority of colloidal nanocrystals investigated in the past few decades is primarily based on metallic nanocrystals (for example gold colloids) and semiconductor-based nanocrystals, referred to as quantum dots. The unique size- and shape-dependent optical properties of these colloidal nanocrystals are of fundamental interest in a variety of research fields.[2,3] Over the years, scientists have developed multiple synthetic routes to obtain metallic and semiconductor nanocrystals with both size and shape control, generating simple 0D structures (referred as nanoparticles) to higher order structures such as nanorods, nanowires, tripods, and tetrapods.[8,17-21] The development of synthetic protocols for generating such plethora of shape and dimensions arises from the access to unique optical properties which can potentially be used for various applications such a bio-imaging tools, energy storage, and quantum computing.[2,4,5] Colloidal synthesis and investigations of lanthanide-based nanocrystals for various applications is relatively new compared to the advancement in metallic and semiconductor nanocrystals. However, this class of nanocrystals has attracted great interest in the past decade as their optical transitions (absorption and emission) are not highly sensitive to their shape and size but arise from the lanthanide dopant ions in the nanocrystal. This gives an added degree of freedom as one can selectively vary the dopant ion in the nanocrystal to vary the optical property without the need for changing the size and shape.

The optical properties of the lanthanides arise from the forbidden electronic transitions within the 4f orbitals. The parity forbidden intra-4f transitions occur due to inter-mixing of transitions, like the allowed 4f-5d transition. The forbidden nature of the intra-4f transitions results in very low extinction coefficients (< 10 $M^{-1}cm^{-1}$) for the lanthanide ions along the series and long lifetimes (up to tens of milliseconds).[22] The energy levels of the lanthanide series are shown in Figure 2.1. Moreover, the shielding of the 4f orbital from the local environment by the filled 5s and 5p orbitals, results in their optical transitions to be less affected from local crystal field effects and thus do not change a lot in different host (nanocrystal) matrices. This leads to unique emission and excitation in lanthanide-based nanocrystals which is characteristic of the dopant lanthanide ion in the nanocrystal matrix. Generally, the well-known nanocrystal matrices for doping lanthanide ions are either that of oxide, fluoride, phosphate matrices (for example Y_2O_3, Gd_2O_3, La_2O_3, LaF_3, $NaYF_4$, and $LaPO_4$).[23-27] Mainly with respect to their optical properties, fluoride-based matrices are highly suitable because of their very low phonon energy (lattice vibrational energy).

The unique optical properties of lanthanide-based nanocrystals are mainly investigated in nanotechnology towards their use as optical imaging agents. This arises from multiple advantages compared to the previously explored metal and semiconductor nanocrystals. For example, lanthanide-based nanocrystals have a very high photo-stability and do not photo-bleach or undergo photo-oxidation, the optical transitions are not sensitive to the size and shape of the nanocrystal, and are less toxic compared to some of the semiconductor quantum dots.[28] The unique optical transitions allow for selective doping

of lanthanide ion of interest in a host nanocrystal and emissions spanning ultra-violet (UV) to near-infrared (NIR) can easily be obtained.

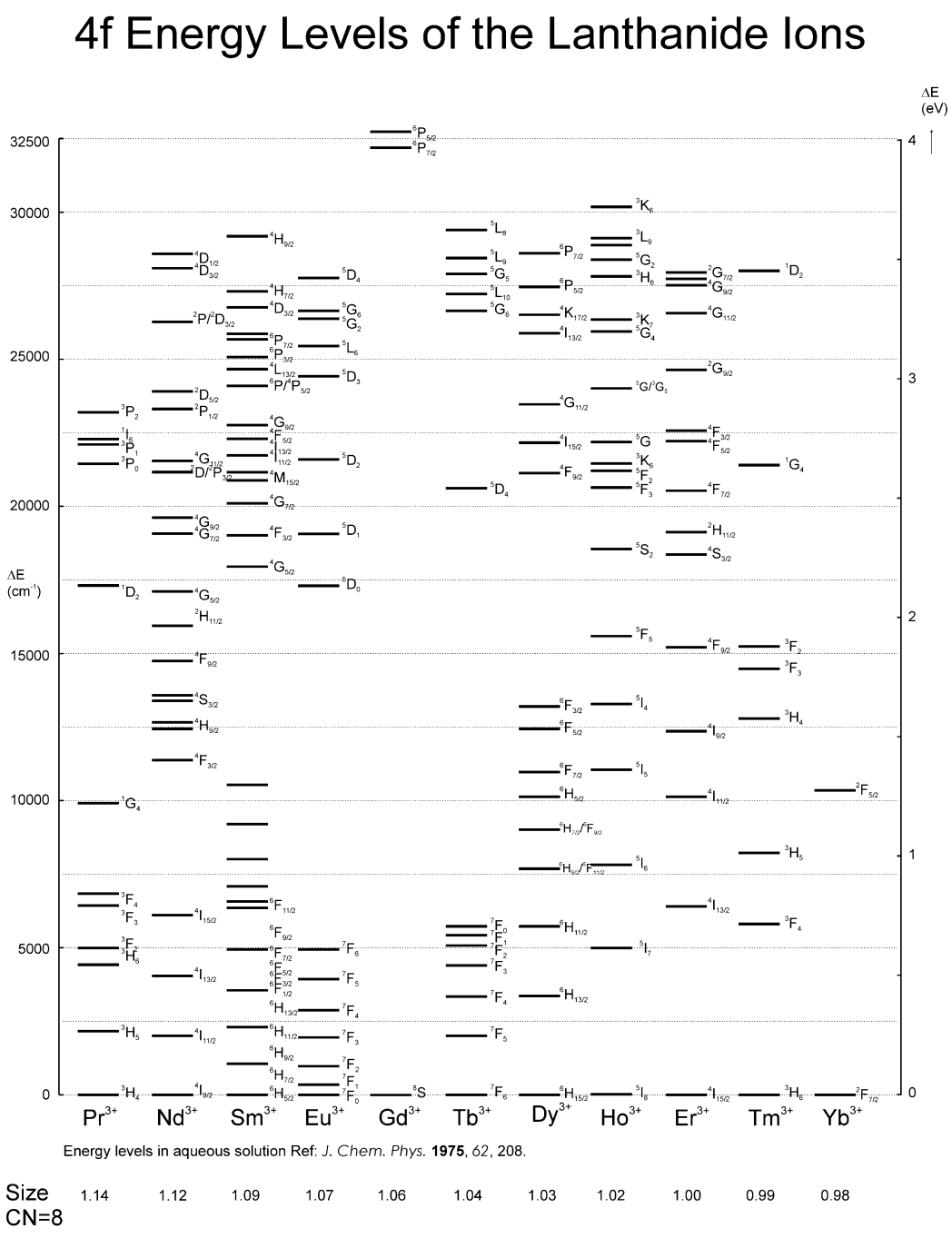

Figure 2.1. Energy levels of selected lanthanide ions in aqueous solution.

The development of colloidal, lanthanide-based nanocrystals as bio-imaging tools is primarily focussed on their use in optical imaging and magnetic resonance imaging (MRI).[22,28-31] In case of optical imaging a unique process of upconversion by selective doping of lanthanide ions in this class of nanomaterials is of significant research interest. Upconversion is a process that converts two or more lower-energy photons to one higher-energy photon.[32] The most studied lanthanide ion combinations for upconversion is the Yb^{3+}/Er^{3+} co-doped and Yb^{3+}/Tm^{3+} co-doped nanocrystals. Yb^{3+} has a higher extinction coefficient compared to other lanthanide ions and acts a sensitizer in this process. Exciting the Yb^{3+} to its long lived excited state, Yb^{3+} transfers its energy to a nearby Er^{3+} or Tm^{3+} ion. The excited Er^{3+} or Tm^{3+} absorbs one more photon from an excited Yb^{3+} ion to populate a higher energy level. The energy transfer and the subsequent emission ranging from visible to NIR wavelengths from these two combinations (Yb^{3+}/Er^{3+} co-doped and Yb^{3+}/Tm^{3+} co-doped) are shown in Figure 2.2. The technological significance of this process in bio-imaging is that the excitation/emission in NIR wavelengths has a deeper penetration and less scattering in biological tissues compared to visible excitation/emission. Moreover, the biological tissues do not autofluoresce under NIR excitation and thus allows for background free imaging.

A variety of nanocrystal host matrices for upconversion have been reported as mentioned earlier, however the thermodynamically stable (β) $NaYF_4$ is the most efficient upconverting host matrix known to date.[33] In the next section the synthesis of colloidal nanocrystals and developments in $NaYF_4$ nanocrystal synthesis and surface modification techniques are described. The use of lanthanide-based nanocrystals in magnetic resonance imaging is discussed separately in section 2.5.

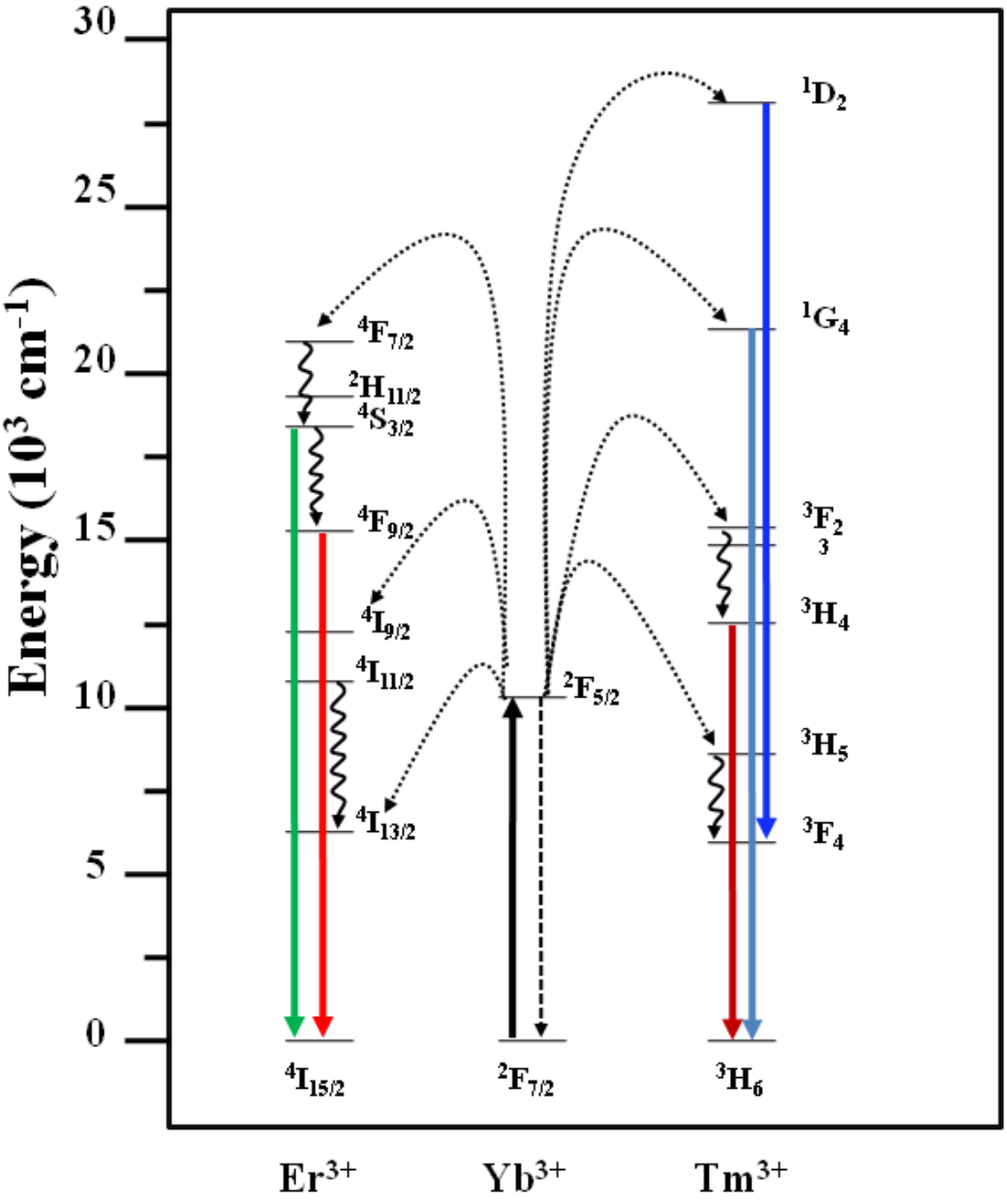

Figure 2.2. Schematic energy level diagram of the upconversion process of Er^{3+} and Tm^{3+} co-doped with sensitizer Yb^{3+} upon 980 nm excitation. The solid, dotted, and curly lines represent excitation/emission, energy transfer, and multiphonon relaxation processes, respectively.

2.2. Colloidal Synthesis of Nanocrystals

The most important requirement in the synthesis of colloidal nanocrystals is the control over their size and shape with a narrow distribution (generally less than 5% standard deviation). To understand and exploit the properties of nanocrystals it is essential to synthesize nanocrystals with uniform size and shape. In 1993, Murray *et al.* reported the first synthesis of highly uniform CdSe nanocrystals with size distribution less than 10%.[34] This report demonstrated for the first time that by careful design and controlling the reaction conditions colloidal route can potentially be used to produce relatively uniform sized nanocrystals. The reported method is generally called the "hot injection" method and the growth of uniform nanocrystals can be understood by the LaMer model shown in Figure 2.3. Injection of highly reactive precursors into a hot coordinating solvent makes it instantaneously supersaturated with active monomers derived from the decomposition of the reactive precursors. In this supersaturated condition, burst of nucleation happens forming crystal nuclei while the coordinating solvent retards the growth and allows for slow growth conditions for the nuclei. The subsequent growth of the nuclei under these controlled conditions allows for size focusing and thus uniform nanocrystals. Ever since this seminal paper, a wide range of colloidal nanocrystals have been synthesized with size distribution less than 5% using the hot injection method.[35] However, the extension of this method remains challenging due to inherent limitations. In this method the precursors should be highly reactive to induce high supersaturation immediately upon injection and such a highly reactive precursor for various materials is often limited. Moreover, the rapid injection is limited to small scale synthesis and changes in injection rate dramatically influence the size distribution of the nanocrystals.[35] In this regard, Hyeon and coworkers demonstrated the use of "heat-up" method for iron oxide nanocrystals in

2001 and further extended it to other metal oxide nanocrystals.[36,37] In this heat-up method the precursors are mixed with the coordinating solvents at room temperature and then heated to reflux and aged to obtain uniform nanocrystals. They also demonstrated the benefit of this method by performing multi-gram scale synthesis of monodisperse colloidal nanocrystals. In general, the "hot injection" method results in smaller nanocrystals as they are performed in supersaturated condition resulting in a burst of nucleation, and a large excess of nuclei, while the “heat-up” method often results in less nuclei and thus larger nanocrystals. These two major synthetic protocols formed the basis of initial exploration in the synthesis of uniformly sized colloidal sodium lanthanide fluoride nanocrystals ($NaLnF_4$).

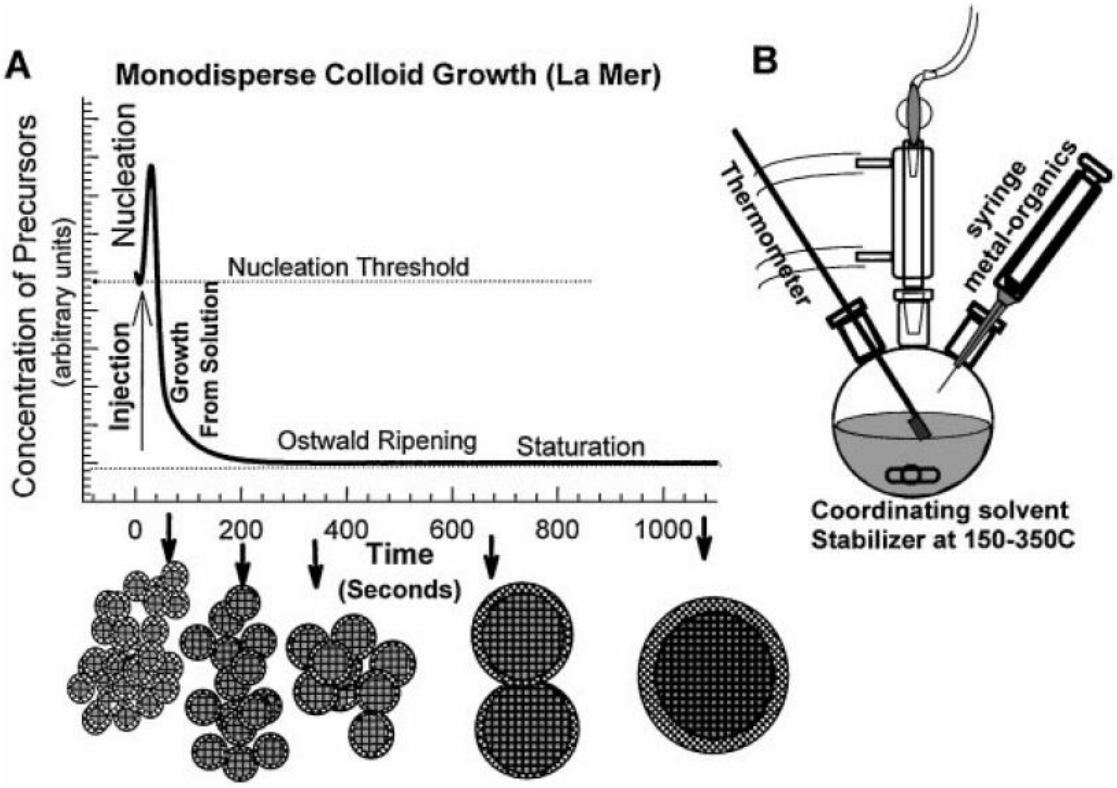

Figure 2.3. (A) Cartoon depicting the stages of nucleation and growth of monodisperse NCs in the framework of the LaMer model. **(B)** Representation of the synthetic set-up employed in the hot-injection method. Reprinted with permission from Ref.[8] Copyright 2000 Annual Reviews.

2.2.1. Synthesis of sodium lanthanide fluoride nanocrystals

Sodium lanthanide fluoride ($NaLnF_4$) exists in two polymorphs, the isotropic kinetically stable cubic (α) crystal structure, and the anisotropic thermodynamically stable hexagonal (β) crystal structure as shown in Figure 2.4. The first report on monodisperse colloidal synthesis of the $NaLnF_4$ nanocrystals were demonstrated by Capobianco (in 2007), Yan (in 2006) and their coworkers for the cubic and the thermodynamic polymorphs, respectively.[38,39] Capobianco and coworkers used a thermal decomposition reaction of trifluoroacetate precursors of the lanthanide salts by the hot-injection method into a mixture of oleic acid and octadecene (at 300 °C) to grow cubic $NaYF_4$ nanocrystals with a narrow size distribution ($\sigma < 5\%$). Yan and coworkers used a two-step approach based on the heat-up method to grow hexagonal $NaLnF_4$ nanocrystals. In the first step they used the trifluoroacetate precursors of both the sodium and lanthanide salts in oleic acid/oleylamine/1-octadecene to synthesize the cubic $NaLnF_4$. These cubic nanocrystals were then purified and in the second step, by carefully changing the amount of sodium trifluoroacetate relative to the cubic nanocrystals in oleic acid/1-octadecene followed by controlling the reaction temperature, the hexagonal $NaLnF_4$ were synthesized. The upconversion emission in the hexagonal phase of $NaYF_4$ is about an order of magnitude higher than the cubic phase of $NaYF_4$. This prompted investigations into the synthesis of hexagonal phase $NaYF_4$ compared to that of the cubic phase synthesis demonstrated by Capobianco and coworkers. The major limitation in the synthesis of hexagonal phase developed earlier is the necessity of a two-step approach. Chow and coworkers modified the protocol by having only oleylamine as the coordinating solvent and demonstrated the synthesis of hexagonal phase $NaYF_4$ in a single step with size distribution less than 10%.[40]

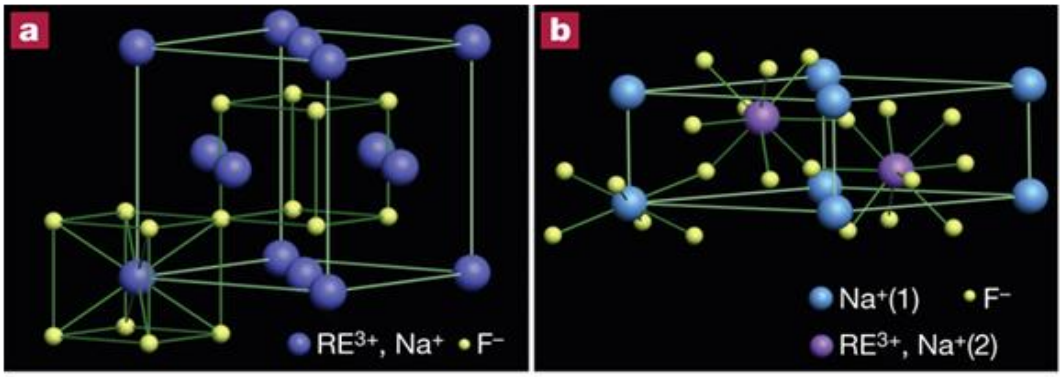

Figure 2.4. (a,b) Schematic presentation of cubic and hexagonal phase $NaREF_4$ structures, respectively. In the cubic phase, equal numbers of F^- cubes contain cations and vacancies. In the hexagonal phase, an ordered array of F^- ions offers two types of cation sites: one occupied by Na^+ and the other occupied randomly by RE^{3+} and Na^+. Reprinted with permission from Ref.[41] Copyright 2010 Nature Publishing Group.

In 2008, Zhang and coworkers developed a highly reproducible synthesis replacing the trifluoroacetate precursors with lanthanide chloride salts.[42,43] The process involves the mixing of lanthanide chloride salts with oleic acid (coordinating) and octadecene (non-coordinating) at room temperature and heating under vacuum at 140 °C to form the lanthanide oleate precursor. To this mixture, sodium and fluoride (NaOH, NH_4F) sources were added at room temperature followed by heating at 300 °C and aging to generate hexagonal phase $NaYF_4$. This synthesis protocol reproducibly generates hexagonal phase $NaYF_4$ with size distribution less than 5% and is the most widely used procedure to date. Moreover, they also demonstrated that, by varying the oleic acid concentration, the shape of the nanocrystal can be manipulated into nanospheres, nanoellipses, and hexagonal nanoplates. Recently, Murray and coworkers demonstrated a single step rapid synthesis using trifluoroacetate precursors by heating the reaction flask in molten salt bath.[44] The use of molten salt bath as the heat source ensures rapid heating of the solution uniformly

(up to 100 °C/minute) and thus overcomes the disparity in decomposition temperature among various trifluoroacetate salts. In this protocol they demonstrated multiple morphologies as shown in Figure 2.5 by adjusting the reaction time and/or the ratio of sodium to lanthanide trifluoroacetates.

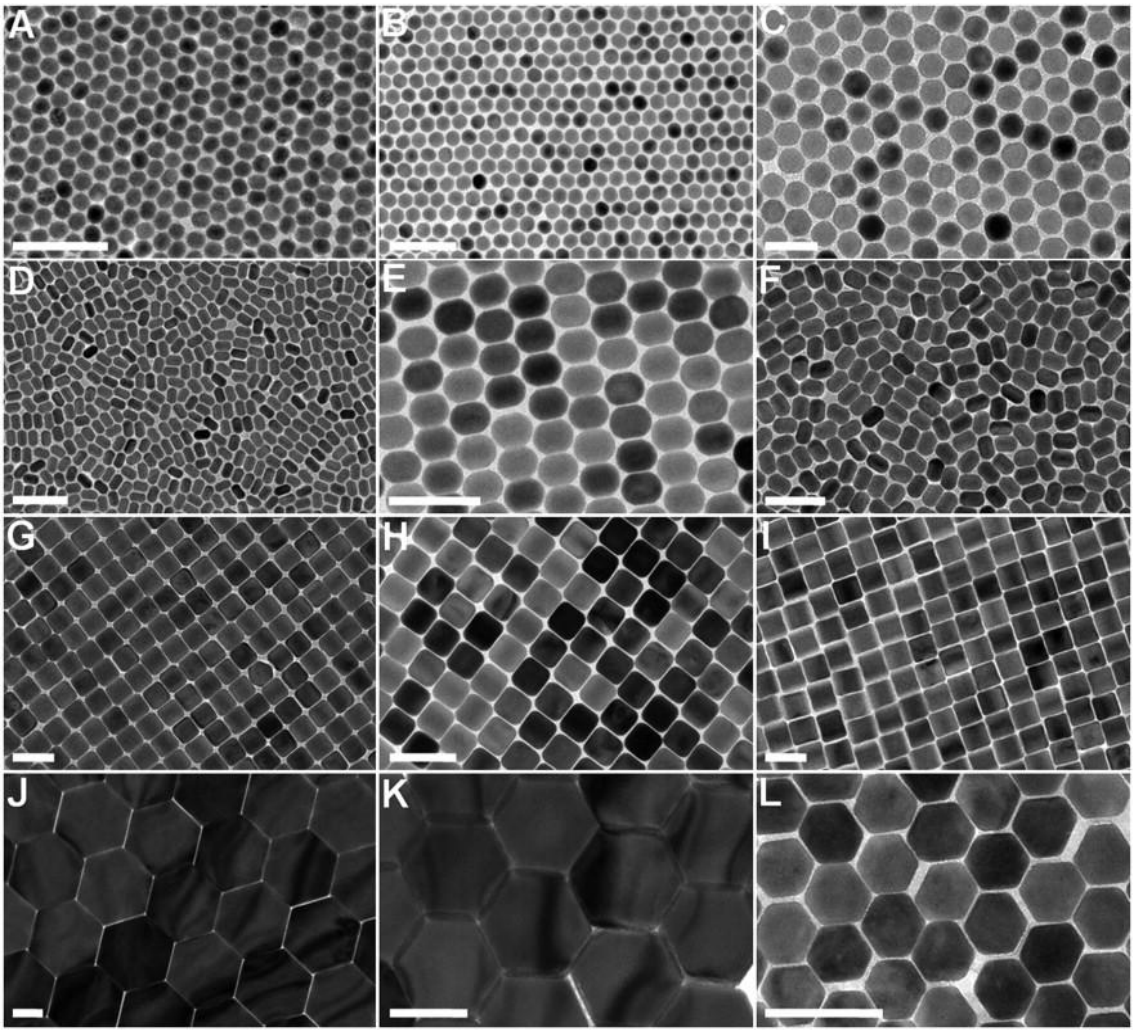

Figure 2.5. TEM images of the β-$NaYF_4$-based UCNCs. **(A, D, G, J)** $NaYF_4$: Yb/Er (20/2 mol%) UCNCs. **(B, E, H, K)** $NaYF_4$: Yb/Tm (22/0.2 mol%) UCNCs. **(F, I)** $NaYF_4$: Yb/Ho (20/2 mol%) UCNCs. **(C, L)** $NaYF_4$: Yb/Ce/Ho (20/11/2 mol%) UCNCs. All scale bars represent 100 nm. Reprinted with permission from Ref.[44] Copyright 2010 National Academy of Sciences.

The solution growth of β-$NaYF_4$ nanocrystals is known to grow in a monomer-depleted regime, where the kinetic product (α-$NaYF_4$) formed at lower temperature dissolves at higher temperature to nucleate into the thermodynamic phase (β), followed by inter-particle ripening to yield uniform β-$NaYF_4$ nanocrystals.[39,40,45] Experimental confirmation for this growth process is shown in Chapter 6. These developed protocols especially address the synthesis of β-$NaYF_4$ nanocrystals, and the parameters are not the same when extending to other lanthanides. This deviation and modification of reaction conditions to generate uniform nanocrystals is demonstrated for β-$NaGdF_4$ in Chapter 5.

2.2.2. Synthesis of core-shell nanocrystals

The optical properties of the $NaYF_4$ nanocrystals are heavily quenched by the high-energy vibrations of the solvent molecules and this can be overcome by growing an epitaxial shell on the core nanocrystals. The epitaxial shell is defined as a crystalline overlayer on the crystalline core nanocrystals, where the shell is commensurate to the core. The epitaxial shell confines the emissive dopant ions to the core and spatially screens them from the surrounding environment resulting in enhancement of the optical properties. Zhang and coworkers developed the widely used shell growth technique for upconverting β-$NaYF_4$ nanocrystals.[46] In this protocol, the core upconverting β-$NaYF_4$ nanocrystals are first grown as explained earlier in a separate reaction flask. Subsequently, the core nanocrystals are mixed with the respective shell lanthanide precursors at room temperature in a second step along with the solvents and then heated up following the same growth conditions of core nanocrystals. This protocol is termed as a seed-mediated growth, where the core nanocrystals act as seeds for subsequent epitaxial growth by directing the crystallization of the shell materials on the core nanocrystals.

However, as described in Chapter 6 this general assumption is not always true. The growth process is driven by ripening of nanocrystals rather than the core nanocrystals acting as seeds. This mechanism and the demonstration of a self-focusing growth process to generate tunable epitaxial shells are discussed in detail in Chapter 6.

The growth of epitaxial shell on the core nanocrystals such as an undoped shell of $NaYF_4$ on upconverting doped $NaYF_4$ core nanocrystals is hard to confirm by general characterization techniques given the identical nature of the core and shell matrix. In this regard our group investigated the core/shell composition with high-angle annular dark-field transmission electron microscopy (HAADF-TEM), electron energy-loss spectroscopy (EELS), and energy-dispersive X-ray spectroscopy (EDS).[47] For this study $NaYF_4$/$NaGdF_4$ core/shell nanocrystals were employed. Given the similar lattice parameters of lanthanide ions along the series such composite structures are generally expected to grow with minimal lattice strain as their lattice mismatch is relatively low. Figure 2.6 shows the HAADF-TEM image of $NaYF_4$/$NaGdF_4$ core/shell nanocrystals, the contrast between the core (dark) and shell (bright) is due to the difference in atomic number (Z-contrast) of yttrium and gadolinium. However, the images clearly show that the shell is not isotropic on the core and in some cases the core is exposed. This is quite contrary to the general expectation based on the minimal mismatch rule for generating core-shell structures. Moreover, the understanding of the factors resulting in such anisotropic deposition of shell materials is fundamental for designing ideal core-shell nanocrystals (*i.e.* centro-symmetric growth of shell around the core with uniform shell thickness in all dimensions). These fundamentals on generating ideal core-shell nanocrystals and the minimal lattice mismatch rule are discussed in detail in Chapter 7.

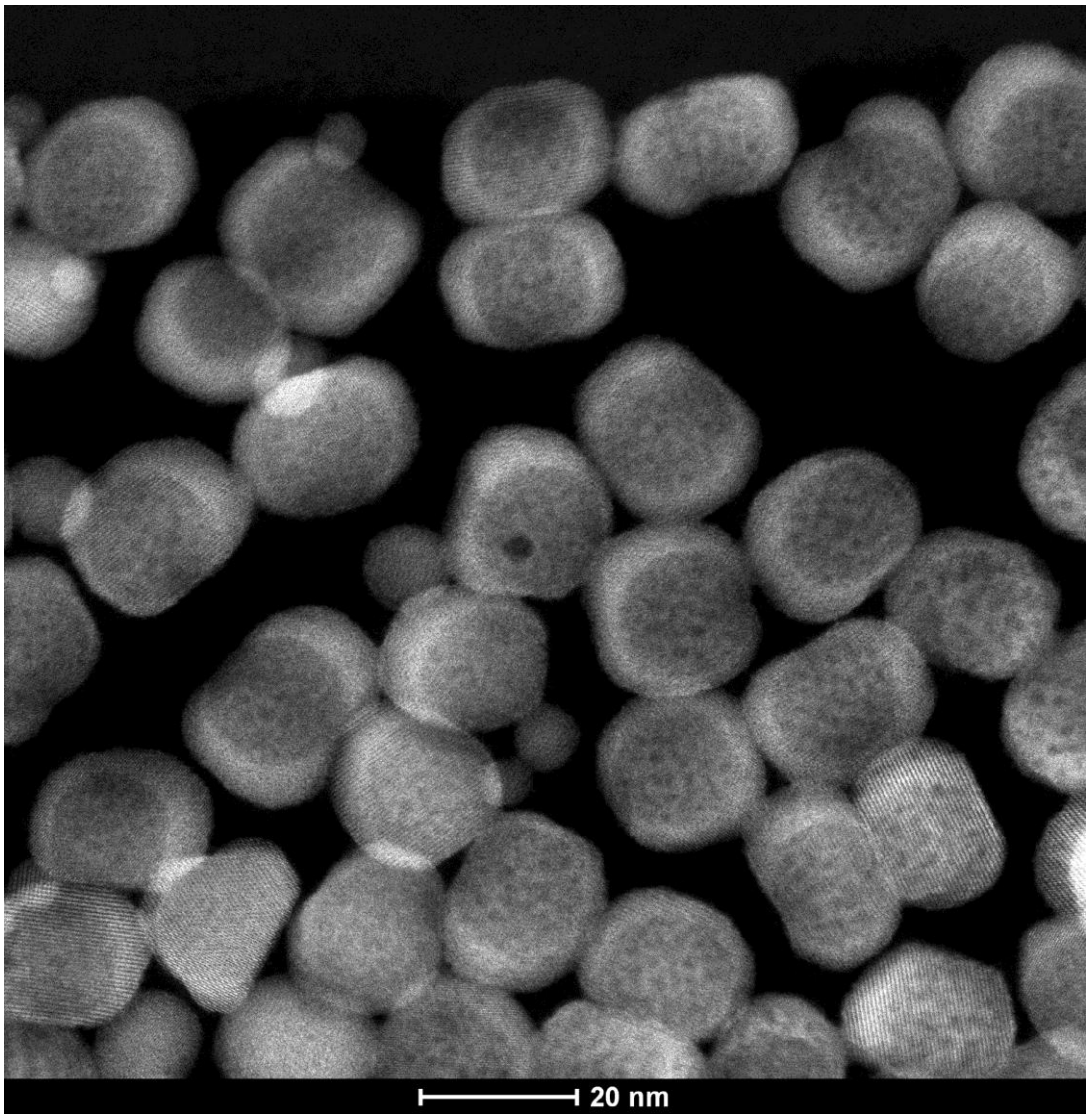

Figure 2.6. Low-magnification HR-HAADF image of $NaYF_4/NaGdF_4$ core/shell NCs. Both core (dark) and shell (bright) materials are visible in the image. Reprinted with permission from Ref.[47] Copyright 2011 American Chemical Society.

2.3. Surface Modification of Colloidal Sodium Lanthanide Fluoride Nanocrystals

The synthesis of the core and core-shell nanocrystals described earlier involves the use of high-temperature reactions and uses organic long-chain fatty acids (oleic acid) as coordinating ligands. The oleic acid molecules are coordinated to the nanocrystal surface as their oleates and allows for dispersing the nanocrystals in organic solvents. For using these nanocrystals as nano-bioprobes it is inevitable that their surface ligands need to be modified to make them hydrophilic. Generally the surface modification strategies used to date are ligand exchange, ligand oxidation reaction, interdigitation/micellization using amphiphilic ligands based on hydrophobic-hydrophobic interaction, and silanization or silica coating.

2.3.1. Ligand exchange

The surface oleate ligands on the nanocrystal surface are not covalently bonded but are only weakly coordinated by ionic interactions to the surface lanthanide ions.[48] This allows for easy replacement of the oleate ligands on the nanocrystal surface with suitable hydrophilic ligands. The choice of replacing ligand is based on their final application and often the choice is to use multi-chelating ligands or excess ligands to replace the weakly coordinated surface oleates. The general protocol is to mix the oleate-stabilized nanocrystals with the replacing ligand in a common solvent and the ligand exchange is performed either at room temperature by just stirring for extended duration for complete exchange or slightly heated depending on the solvent to shorten the exchange reaction time. To date, various ligand exchange protocols have been developed for $NaLnF_4$ nanocrystals. Few examples of ligands used for replacing the surface oleates are polyacrylic acid (PAA),[49-51] poly(ethyleneglycol)-phosphate (PEG-phosphate),[52] 3-

mercaptopropionic acid,[53,54] dimercaptosuccinic acid (DMSA),[55] and citrate.[56,57] It is often preferred to use long chain polymers instead of a short organic molecule, as the former provide more stable dispersions.

2.3.2. Interdigitation/micellization based on hydrophobic-hydrophobic interactions

Interdigitation/micellization of the surface oleate ligands on the nanocrystal surface with an amphiphilic polymer having both hydrophobic chains and hydrophilic chains/groups is a simple strategy to phase transfer hydrophobic nanocrystals. The hydrophobic part of the amphiphilic polymer driven by hydrophobic-hydrophobic interactions with the surface oleates self-assembles on the nanocrystal surface while the hydrophilic part forms the external layer making the nanocrystals dispersible in water. Examples of this strategy in phase transfer of oleate-stabilized $NaYF_4$ nanocrystals include, PEG-phospholipids,[58] poly(acrylic acid) (PAA) modified with octylamine and PEG,[59] poly(maleic anhydride-*alt*-1-octadecene) (PMAO) modified with PEG.[60] The original oleate ligands are not replaced in this strategy and the added layer forms a secondary coating on the nanocrystals. In general, the phase-transferred nanocrystals by interdigitation have a longer colloidal stability than that of ligand exchanged nanocrystals. However, the hydrodynamic size of the nanocrystals after interdigitation is often larger than the ligand exchange approach and thus limiting their use towards *in vivo* studies where the overall hydrodynamic size has to be kept minimal.

2.3.3. Ligand oxidation reaction

The surface oleate ligands on the nanocrystal surface are modified in this protocol by specific chemical reaction of the surface ligands to generate functional groups and simultaneous phase transfer to water. For example, using the Lemieux-von Rudloff

reagent the oleate ligands can directly be oxidized into azelaic acids, providing free carboxylic acid groups on the surface and water dispersibility.[61] Yan *et al.* demonstrated that using ozone, the oleates could be reacted to form azelaic acid or azelaic aldehyde depending on the presence of either CH_3SCH_3 or a mixture of CH_3COOH and H_2O_2.[62] However, this protocol is very limited to these few examples and is not highly flexible like the other surface modification procedures.

2.3.4. Silica coating

In silica coating a continuous network of cross-linked siloxane bonds (-Si-O-Si-) are formed on the nanocrystal surface from the hydrolysis and condensation reaction of tetraethyl orthosilicate in the presence of ammonium hydroxide as catalyst. The choice of silica coating is mainly due to the high biocompatibility of silica and the surface silanol groups (-Si-OH) can easily be functionalized with wide variety of functional silanes for further bio-conjugation. In case of hydrophobic $NaLnF_4$ nanocrystals the silica coating is performed using a reverse microemulsion approach.[63] Using surfactants, a water in oil reverse emulsion is produced and the nanocrystals are coated individually with uniform silica shells as shown in Figure 2.7. However, the excess surfactants used in the protocol are hard to remove and often lead to irreversible aggregation and precipitation once the silica-coated nanocrystals are removed from the emulsion. This is discussed in detail in Chapter 3.

Recently, there is increased interest in mesoporous silica shells on $NaLnF_4$.[64,65] Mesoporous silica shells are generated by using specific organic molecules as templates during the growth of silica, which are later removed by either calcination or pH

treatment. The mesopores offer sites for incorporating drugs, functional molecules and are generally investigated for drug delivery.

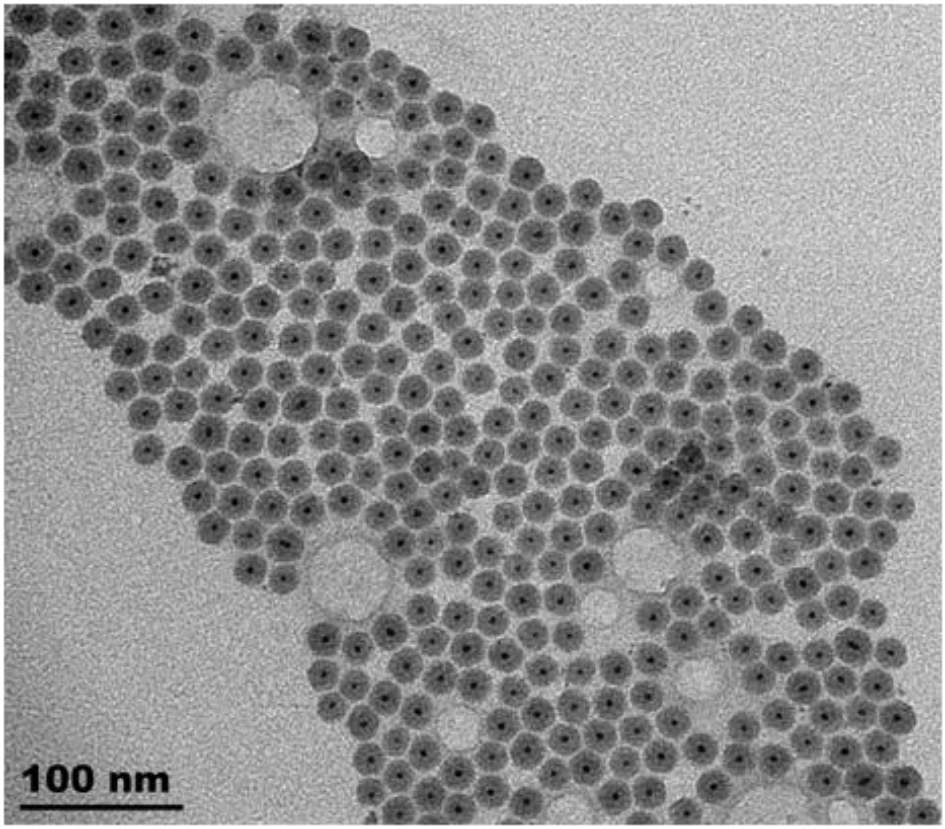

Figure 2.7. TEM image of silica-coated $NaGdF_4$ nanocrystals by reverse-microemulsion approach. The dark spots are the $NaGdF_4$ nanocrystals, and the amorphous inorganic silica shell surrounding them has a lower contrast.

The above sections summarize the general routes explored to date in surface modification of hydrophobic sodium lanthanide fluoride nanocrystals to make them hydrophilic and suitable in biolabeling applications. However, integrating these hydrophilic phase-transferred nanocrystals needs to address further design considerations to make them suitable for diagnostic applications *in vivo/in vitro*. The utility of these nanocrystals in cancer diagnosis and the surface modification requirements are discussed in the following section.

2.4. Design Considerations for the Application of Colloidal Nanocrystals in Cancer Diagnosis

Colloidal nanocrystals conjugated with targeting ligands (for example antibodies, aptamers), can be used to target the active sites (receptors) of tumor cells, and the tumor microenvironment (such as tumor vasculatures) with high specificity and affinity. This potentially leads to the active localization of the nanocrystals in the tumor cells and allows for diagnosis and treatment.[66-69] However, the localization can also occur by passive uptake of the nanocrystals by nonspecific cellular uptake through an enhanced permeability and retention effect (EPR).[66,67] Tumors have leaky vasculature which leads to the preferential accumulation of nanocrystals through the EPR effect. The localization of nanocrystals through the active and passive mechanism is shown in Figure 2.8.

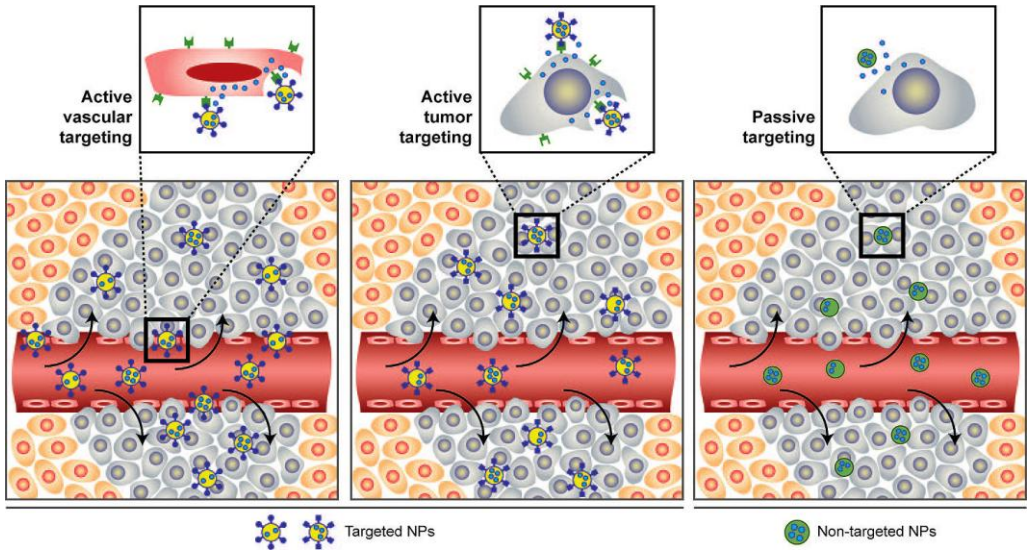

Figure 2.8. NCs engineered for vascular targeting by incorporating ligands that bind to endothelial cell-surface receptors and vascular tissue synergistically for targeting both the vascular tissue and target cells (left), NCs accumulation and cell uptake through receptor-mediated endocytosis by "active targeting" (middle), and accumulation of NCs passively in tumors and inflamed tissue through the EPR effect by "passive targeting" (right). Reprinted with permission from Ref.[67] Copyright 2009 American Chemical Society.

The surface ligands can trigger non-specific adsorption of proteins onto the nanocrystal surface, referred as surface opsonization or biofouling. The biofouling can induce immune response, thus reducing the nanocrystal biocompatibility and duration of circulation *in vivo*.[68,69] To specifically target/localize nanocrystals to the tumor cells surface biofouling needs to be avoided.

The surface ligands used to stabilize nanocrystals in hydrophilic environments should ideally address these challenges if one needs to actively target cancer cells. Most of the surface modification strategies explored in case of sodium lanthanide fluoride nanocrystals discussed in Section 2.3 do not address these challenges. Most of the surface ligands used to date in this class of nanocrystals have never been tested for biofouling/opsonization. In some cases, such as the silica coating, though they are well known for their biocompatibility (low toxicity), studies have shown that they are prone to high degree of surface biofouling.[70,71]

Polymers such as polyethylene glycol (PEG) and polyvinylpyrrolidone (PVP) are well known examples to avoid opsonization, and are known to have longer blood circulation time.[71-73] While there are multiple studies with PEG-based ligands, in this dissertation the utility of PVP as a specific targeting ligand is studied.

2.5. Gadolinium-based Nanocrystals for MRI Applications

Magnetic Resonance Imaging (MRI) is a powerful medical diagnostic tool, where the relaxation of water protons exposed to an external magnetic field is used to obtain morphological and anatomical information. It is a non-invasive imaging technique with unlimited tissue penetration and high spatial resolution. The principle of MRI is the same as that of nuclear magnetic resonance (NMR), and deals with water protons present in the

tissues and other organs. The water content in a human on an average is about 80% and thus MRI can potentially be used for probing any part of the human body. The spins of the hydrogen nuclei are randomly aligned, which align either parallel or antiparallel to the applied magnetic field. The aligned spins precess under a specified frequency, known as the Larmor frequency. This alignment is then perturbed by a 'resonance' frequency in the radio-frequency (RF) range, resulting in protons to absorb energy to excite them to the antiparallel state. After the RF pulse is turned off the excited nuclei return to the lower-energy state. The time it takes for the nuclei to return to the lower-energy state is governed by the exponential time constant called the relaxation time, and the relaxing nuclei induces an electric current detected by an RF-receiver. There are two different relaxation pathways, one is the longitudinal or T_1 relaxation (spin-lattice relaxation) and other is the transverse or T_2 relaxation (spin-spin relaxation). The relaxation of water protons is heavily dependent on their surroundings, thus protons relax at different relaxation times and this gives the contrast in magnetic resonance images. Both the relaxation pathways give different imaging contrasts, the T_2 relaxation is a signal-decreasing effect and gives dark contrast, while the T_1 relaxation is signal-increasing effect and gives bright contrast. In general, the T_2 contrast renders images of lower contrast than T_1 contrasted bright images because of their dark signal.[74] The potential use of gadolinium to enhance the T_1 contrast is discussed below, followed by the use of gadolinium-based nanocrystals in T_1 contrast enhancement.

2.5.1. T_1 MRI contrast agents

Contrast agents in MRI enhance the signal and provide enhanced contrast by interacting with the relaxation of water protons. The gadolinium (Gd^{3+}) ion has 7

unpaired 4f electrons, which is the largest of any metal ion. The unpaired electrons in gadolinium ion interact with the nuclear magnetization of water molecules and shorten the relaxation time of water protons. The magnetic field of these unpaired electrons does not extend very far, and so the water protons only at close proximity and that are directly bound to the contrast agent are affected. Thus, tissues with the contrast agent appear brighter than that of their surroundings or other tissues, leading to enhanced contrast of the region of interest.

Gadolinium-based contrast agents are clinically used to enhance T_1 contrast.[75] Gd^{3+} ions are toxic, and this is overcome by using gadolinium complexes, for example Gd-DTPA (diethylenetriaminepentacetate). Chelation with DTPA ensures the elimination of gadolinium from the body and also makes it metabolically inert. Given the toxicity of the contrast agents, the performance of contrast agents is measured against their concentration ($mM^{-1}s^{-1}$) and the general expectation is to have large relaxivity (which is the reciprocal of the relaxation time of water protons) with lower gadolinium ion concentration. This requirement led to intense exploration towards the understanding of the contrast mechanism with gadolinium complexes.

The total relaxivity (r) enhancement provided by a gadolinium complex is sum of the individual contributions of inner-sphere (IS), secondary-sphere (SS), and outer-sphere (OS) water protons.[76] The IS contribution is from the water molecules directly bound to the gadolinium ion, while the SS contribution arises from the water molecules hydrogen bonded to the chelate, and the OS contribution is from the water molecules in close proximity (*i.e.* the diffusion sphere around the complex). The major contribution for the relaxivity enhancement arises from the IS effect and the other two contributions (SS and

OS) are minimal in case of gadolinium complexes.[16,76] The inner sphere contribution is given by the following equation:

(1)

where [CA] is the concentration of contrast agents, q is the hydration number of gadolinium bound water, T_{1M} is the time fluctuation of the Gd^{3+}-proton interaction, and τ_M is the mean residence lifetime of the Gd^{3+} bound water. These contributions add up to the inner-sphere effect. Especially the T_{1M} is affected by three other factors, the rotation of the gadolinium complex, the exchange rate of the bound water, and the electron paramagnetic relaxation. These multiple complex factors collectively affect the relaxivity of the inner sphere water protons. However, in clinically relevant field strengths (0.5 - 1.5 Tesla) the major contribution towards relaxivity enhancement in case of gadolinium complexes is their rotation correlation time.[77-79] Increasing the rotational time of the complex leads to increase in relaxivity, thus the first exploration of enhancing the relaxivity of gadolinium complexes were based on tethering them to large molecules such as polymers, dendrimers, and proteins.[80,81] This approach was further extended by covalently anchoring the gadolinium chelates to different nanostructure frameworks such as silica, gold, or bundling them into liposomes, and viral capsids.[81] These structures have multiple gadolinium ions in a single structure and thus allowed for increased local contrast and high relaxivity as they tumble slowly compared to individual complexes. The main challenge in these above approaches is that the number of ions that can be localized is limited by the number of anchoring sites available, and more often, the functionalization is tedious (multistep reactions) and expensive.[29] Large number of gadolinium ions can easily be bundled in colloidal nanocrystals and offers distinct

advantages over the previous class of gadolinium contrast agents. This is discussed in detail in Chapter 5. The general approach and advancement in synthesis of gadolinium-based nanocrystals is discussed below.

2.5.2. Synthesis of gadolinium-based nanocrystals

The first reports on gadolinium-based nanocrystals were demonstrated using GdF_3 by our group,[82] followed by Tillement and coworkers report on Gd_2O_3.[83] The exploration was further extended to $GdPO_4$ by Suzuki and coworkers.[84,85] These colloidal nanocrystals demonstrated that multiple gadolinium ions could easily be incorporated into a single structure without the need for tedious (multistep reactions) surface functionalization and anchoring of gadolinium complexes as described earlier. The relaxivity enhancement per contrast agent in these nanocrystals was a few thousand times higher than the commercial gadolinium complexes. Especially, Tillement and coworkers synthesized three different sizes of Gd_2O_3 nanocrystals between 2 - 5 nm and studied the size dependent contrast (Figure 2.9) at different gadolinium ion concentrations. They also performed *in vivo* studies in mouse and demonstrated the contrast enhancement and biodistribution for the first time. The nanocrystals reported in these earlier works were synthesized in water or polyol (*e.g.* ethylene glycol) solutions, and thus were directly dispersible in water for relaxivity studies. However, the nanocrystals synthesized did not have a good size control, and limited their suitability for clinical explorations.[29,74] Synthesis of colloidal nanocrystals in high-boiling organic solvents allows for controlled nucleation and growth at elevated temperatures, resulting in good size and size dispersion control. However, there are no known reported synthesis protocols for these nanocrystals (GdF_3, Gd_2O_3, and $GdPO_4$) with size control in high-boiling organic solvents.

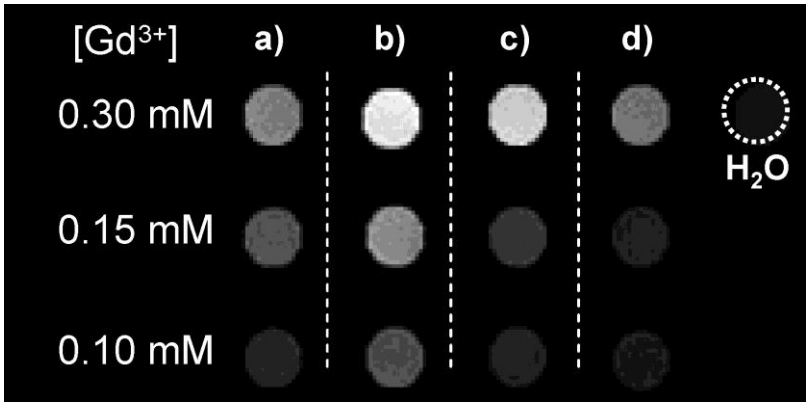

Figure 2.9. T_1-weighted images for various gadolinium element concentrations of **(a)** Gd−DOTA, hybrid nanoparticles with **(b)** 2.2 nm, **(c)** 3.8 nm, and **(d)** 4.6 nm sized Gd_2O_3 core (T = 25°C). Reprinted with permission from Ref.[83] Copyright 2007 American Chemical Society.

The advancement in the synthesis of $NaYF_4$ nanocrystals described earlier led to the interest in exploration of this class of colloidal nanocrystals, by either doping gadolinium ions in the matrix or by completely replacing the yttrium with gadolinium. The synthesis protocol was mainly tuned to accommodate upconverting lanthanide ions in $NaGdF_4$ nanocrystal matrix allowing for simultaneous optical and MR imaging capabilities.[50,86-88] The synthesized nanocrystals were highly uniform and generally of sizes above 15 nm. This however limited their use in relaxivity enhancement and the relaxivity values per gadolinium ion were lower (~1 $mM^{-1}s^{-1}$) than the clinical complexes (~6 $mM^{-1}s^{-1}$). Most of the gadolinium ions are not on the surface given their large size and thus reducing their interaction with surrounding water protons.

The synthesis of nanocrystals in water/polyol-based systems results in polydisperse small nanocrystals with high relaxivity values, while the synthesis of nanocrystals in organic solvents results in monodisperse large nanocrystals with poor relaxivity values. This shortcoming resulted in no systematic evaluation of the contrasting mechanism in colloidal inorganic gadolinium-based contrast agents. A synthesis protocol is described

for size and size-distribution controlled synthesis of small $NaGdF_4$ and the contrasting mechanism is discussed in Chapter 5.

2.6. Summary

In this chapter, colloidal synthesis of nanocrystals in general and the requirement of size and size-dispersion control are introduced. The unique advantages of the lanthanide-based nanocrystals in optical and magnetic resonance imaging are highlighted. The colloidal synthesis of sodium lanthanide fluoride nanocrystals is now widely available with good size and size dispersion control. However, most of the current studies in this class of nanocrystals are directed towards the modulation of emission colors by changing the luminescent ions in the matrix, or changing the host matrix. Especially, efforts to explore and integrate these nanocrystals with their end-use applications are limited. Moreover, the basic growth mechanism of core-shell nanocrystals is not well understood, and often overlooked with a general opinion that there is no lattice strain effect on the epitaxial growth because of the similarity of the lanthanide ion size along the series.

In this dissertation, sodium lanthanide fluoride nanocrystals are investigated for their applications as optical and magnetic resonance imaging nano-bioprobes. Previously known limitations are addressed by demonstrating new protocols of surface functionalization for targeted labeling, and size-tunable colloidal synthesis for MRI applications. The growth mechanism of core-shell nanocrystals is explored and a highly flexible protocol for tuning the shell thickness is presented. Finally, the hitherto unknown effects of lattice strain in lanthanide nanocrystals are investigated, and fundamental conditions needed to generate conformal/isotropic shell growth pertaining to colloidal nanocrystals of any lattice mismatched materials are demonstrated.

Chapter 3. Facile Ligand-Exchange with Polyvinylpyrrolidone and subsequent Silica Coating of Hydrophobic Upconverting Nanocrystals

(This chapter is reproduced with permission from Ref.[89] Copyright 2010 The Royal Society of Chemistry.)

3.1. Introduction

Inorganic nanocrystals (NCs) have widely been studied for their use towards biological applications. NCs based on quantum dots and metals such as gold and silver show unique size dependent optical properties and their use as bioprobes has been studied extensively.[90-92] Recently, there is an increased interest towards the use of lanthanide-based NCs. This can be attributed to the use of heavy metals and toxicity related to some of the quantum dots[93,94] and sensitive size/shape dependent optical properties of gold and silver NCs which overlap with the biological tissue fluorescence in the visible region. Trivalent lanthanide ions have unique luminescent properties due to shielding of the valence 4f electrons by the filled 5s and 5p orbitals. The f-f transitions of the trivalent lanthanide ions result in sharp, narrow spectral bands and are highly specific to the ion. Different lanthanide-doped luminescent materials have been reported in literature,[25,83,95-99] among which, lanthanide-doped β-$NaYF_4$ (hexagonal) upconverting nanocrystals (UCNCs) are being studied extensively for biological applications because of their highly efficient upconversion luminescence.[100] When co-doped with Yb^{3+} ions, lanthanide-doped $NaYF_4$ yields upconversion emission ranging from visible to NIR wavelengths for excitation with a low energy NIR light of 980 nm. This selectivity of the emission

wavelength using a single excitation source, higher penetration depth, and low auto-fluorescence from the biological tissues at NIR wavelengths has resulted in an increased interest in this class of NCs.

Synthesis of near-monodisperse β-$NaYF_4$ usually involves the use of high-boiling, non-aqueous solvents and oleate as the coordinating ligand. The resulting NCs are hydrophobic and form stable colloidal dispersions in non-polar organic solvents. In order to use these UCNCs for biological applications they have to be rendered water-dispersible *via* phase-transfer. Different strategies have been reported for the phase transfer of β-$NaYF_4$ hydrophobic NCs from organic to aqueous phase, *viz*. silica coating in reverse microemulsion,[43] coating with an amphiphilic polymer shell,[101] and ligand exchange.[53] Silica coating within a reverse microemulsion leads to silica-coated particles and allows for the facile phase transfer of the NCs to aqueous solvents. Coating with amphiphilic polymer shells involves the use of polymers with both hydrophobic and hydrophilic segments in their backbone. On mixing the NCs protected with a hydrophobic ligand with the amphiphilic polymer, the hydrophobic ligand interdigitates with the hydrophobic segment of the polymer and the hydrophilic part of the polymer sticks out into water, rendering the NCs dispersible in water. In case of ligand exchange, the hydrophobic ligands on the surface of the NCs are replaced with hydrophilic small molecules or polymer chains, resulting in water-dispersible NCs. This strategy has largely been studied with different silanes[102] and water-soluble polymers. Polymers with functional groups or heteroatoms which can coordinate to the surface of the NCs are being explored widely over simple molecules, as they yield highly stable dispersions of NCs in water after ligand exchange, because of their bulky framework. The ligand

exchange with polymers has largely been focused on poly(acrylic acid) (PAA)[103] and phosphine oxide-PEG based polymers[104,105] and not much attention has been paid to other water-soluble polymers such as polyvinylpyrrolidone (PVP) that can coordinate to the NC surface.

PVP is a biocompatible, non-toxic, water-soluble polymer used in different pharmaceutical applications.[106,107] The ability of the polymer chains to stabilize the surface of NCs during growth is termed as the protective value of the polymer and PVP stands out with a high protective value.[108] PVP chains coordinate to different NC surfaces through their carbonyl groups and have been used in the synthesis of metal[17,109] and magnetic nanoparticles.[110] When PVP is used as a coordinating ligand to synthesize $NaYF_4$, the obtained NCs are of the α-phase and polyhedral in shape with particle sizes greater than 30 nm.[111] Wang *et al.* reported on β-phase $NaYF_4$ stabilized by PVP using a hydrothermal method.[112] The synthesized NCs were on an average 40 nm in size and polydisperse, other hydrothermal methods reported in literature also have reported on particle sizes greater than 50 nm and mostly polydisperse.[113-116] On the other hand, β-phase $NaYF_4$ obtained in high-boiling solvents with oleates as stabilizing ligand are monodisperse and particle sizes less than 20 nm can easily be obtained. As smaller size and monodispersity play a vital role in determining their suitability for biological applications, this chapter describes the preparation of PVP-stabilized upconverting β-$NaYF_4$ *via* ligand exchange by replacing the hydrophobic oleate ligands. The NCs thus obtained are highly monodisperse and spherical in shape with particle sizes around 20 nm. The use of these NCs for biological applications (*in vivo*) would be particularly advantageous as PVP is reported to have good anti-fouling properties,[71] longer blood

circulation time than the widely used poly(ethylene glycol) (PEG), minimum tissue distribution, and low accumulation in vital organs.[117] To show that the exchange was successful, utilizing the affinity of PVP to silica[118] the PVP-stabilized UCNCs were coated with a thin silica shell. By growing a silica shell, these PVP-stabilized UCNCs can be used as targeted probes as the silica shell can easily be functionalized by co-hydrolysis of functional silanes.

Silica coating on oleate-stabilized β-$NaYF_4$ NCs reported in literature have largely been done by the reverse microemulsion route, wherein the silica coating is done in water-in-oil emulsions and the particles stabilized by surfactants during growth. This one-step strategy could be tuned to obtain silica shells of varying thickness.[119] Although this synthetic route is simple, there is a tendency for the silica-coated particles to aggregate which leads to necking between the silica beads when they are removed from the emulsions.[120] Graf *et al.* showed thin silica coatings on citrate-stabilized gold nanoparticles using PVP to stabilize the nanoparticles from aggregation in ethanol.[118] This methodology has not been investigated for oleate-stabilized hydrophobic NCs for growing thin silica shells. In this chapter it is demonstrated that this method of silica coating can be extended to oleate-stabilized β-$NaYF_4$ NCs after ligand-exchange with PVP. Dispersions of PVP-stabilized NCs obtained in this way have very good colloidal stability in a wide range of solvents and can readily be coated with a thin silica shell. Moreover, upconversion luminescence studies on the PVP-stabilized and silica-coated UCNCs were done and compared with the oleate-stabilized $NaYF_4$ UCNCs. The protocol demonstrated in this chapter can be extended to other oleate-stabilized NCs having affinity to PVP chains.

3.2. Results and Discussion

The lanthanide chlorides, sodium hydroxide and ammonium fluoride were heated to 300 °C in a mixture of octadecene and oleic acid and subsequently aged for 90 min at that temperature to obtain β-$NaYF_4$. The initially formed kinetic product, α-$NaYF_4$ is transformed to the more stable product, β-$NaYF_4$ upon aging at a high temperature.[40,113] The β-$NaYF_4$ NCs co-doped with Yb^{3+}(20%) and Er^{3+}(2%) thus obtained were characterized using TEM and powder X-ray diffraction. The TEM image (Figure 3.1A) of the synthesized oleate-stabilized $NaYF_4$ NCs shows that the particles are spherical with a narrow size distribution (21 ± 0.5 nm). The particles on the TEM grids show a long range ordering into hexagonal, closed-packed structure because of their narrow size distribution and are regularly spaced (~3.3 nm) by the surface stabilizing oleate ligand. The XRD pattern (Figure 3.2A) shows that pure β-$NaYF_4$ NCs were obtained and the peaks match well with the standard spectral lines of β-$NaYF_4$ (JCPDS #16-0334). The average crystallite size determined from X-ray diffraction data (20 nm), is in good agreement with the size determined from TEM analysis. The surface oleate ligands allow for the formation of stable, optically transparent dispersions of these NCs in non-polar organic solvents such as toluene, hexane, and chloroform.

3.2.1. Ligand exchange of the hydrophobic UCNCs with PVP

The ligand exchange step allows for almost complete exchange of the oleate ligands with a hydrophilic ligand and opens the pathway to disperse them in aqueous media and their use in different biological applications. Amphiphilic PVP was selected as it has been shown to coordinate well with $NaYF_4$ NCs.[111] A toluene dispersion of oleate-stabilized NCs was mixed with PVP dissolved in a mixture of DCM and DMF to form a clear

dispersion. This mixture was then refluxed at 100 °C to exchange the oleates with PVP. The exchange reaction is believed to be driven by mass action as the excess PVP in the medium slowly replaces the surface oleate ligand and the high temperature helps in the dynamic solvation of the ligands during exchange.[121] PVP-stabilized UCNCs after exchange were dried and dispersed in different solvents to yield stable, optically clear dispersions (Figure 3.3).

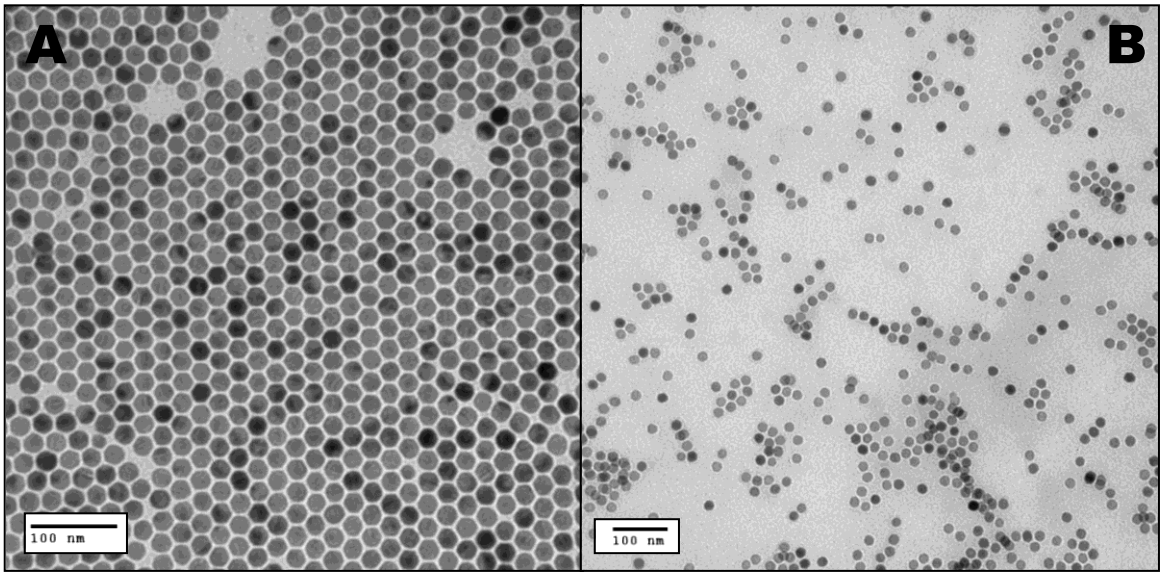

Figure 3.1. TEM images of $NaYF_4$:Yb^{3+}/Er^{3+} NCs **(A)** oleate-stabilized, and **(B)** ligand-exchanged with PVP.

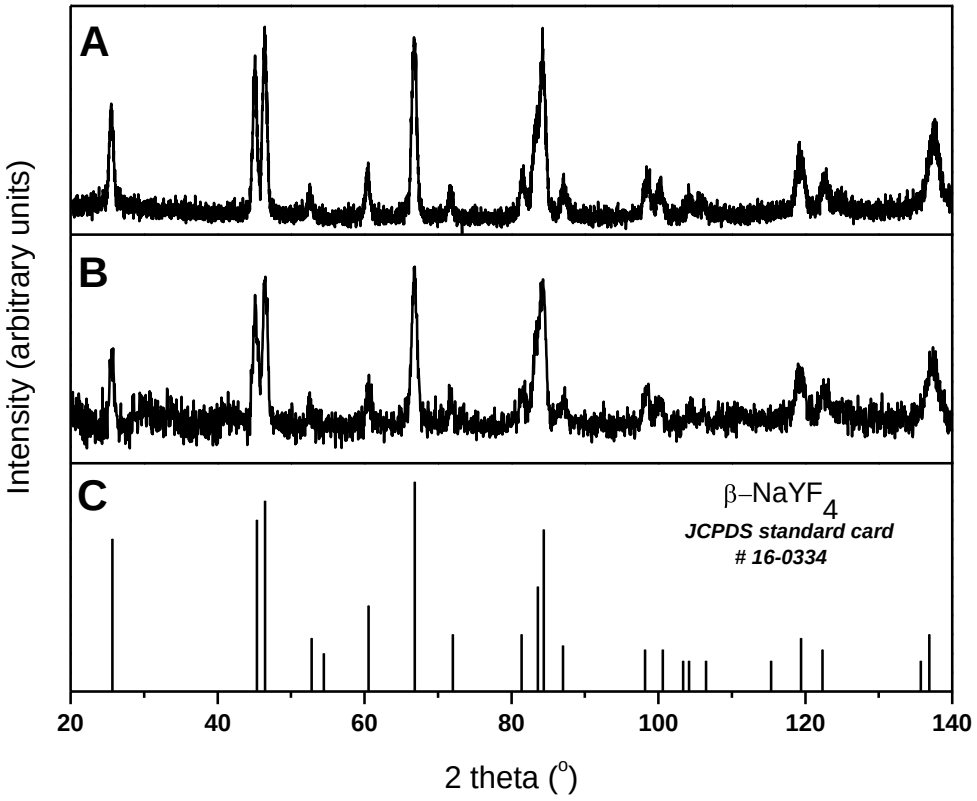

Figure 3.2. Powder X-ray diffraction pattern of $NaYF_4$:Yb^{3+}/Er^{3+} **(A)** oleate-stabilized, **(B)** ligand-exchanged with PVP, and **(C)** the corresponding reference pattern (JCPDS: #016-0334).

The TEM images (Figure 3.1B) of the PVP-stabilized NCs have the same morphology after exchange but did not show any long range ordering on the TEM grids as observed for the oleate-stabilized NCs. This indicates that the oleate ligands responsible for the packing of the hydrophobic NCs had been replaced successfully by PVP chains. The XRD pattern (Figure 3.2B) shows that the PVP-stabilized NCs retain their crystal phase after exchange. Comparison of the FT-IR spectra of the ligand-exchanged NCs with that of the oleate-stabilized NCs indicated that the oleates were exchanged with PVP. The FT-

IR spectrum of the oleate-stabilized NCs (Figure 3.4A) shows the carboxylate stretching vibrations at 1566 and 1465 cm^{-1}. On the other hand, the FT-IR spectra of the PVP exchanged NCs (Figure 3.4B) shows a strong carbonyl (C=O) stretching peak at 1651 cm^{-1} and a broad peak at 3500 cm^{-1} due to adsorbed water molecules. The appearance of the carbonyl stretching peak and the absence of the carboxylate stretching peaks indicates that the exchange of oleates with PVP was successful.

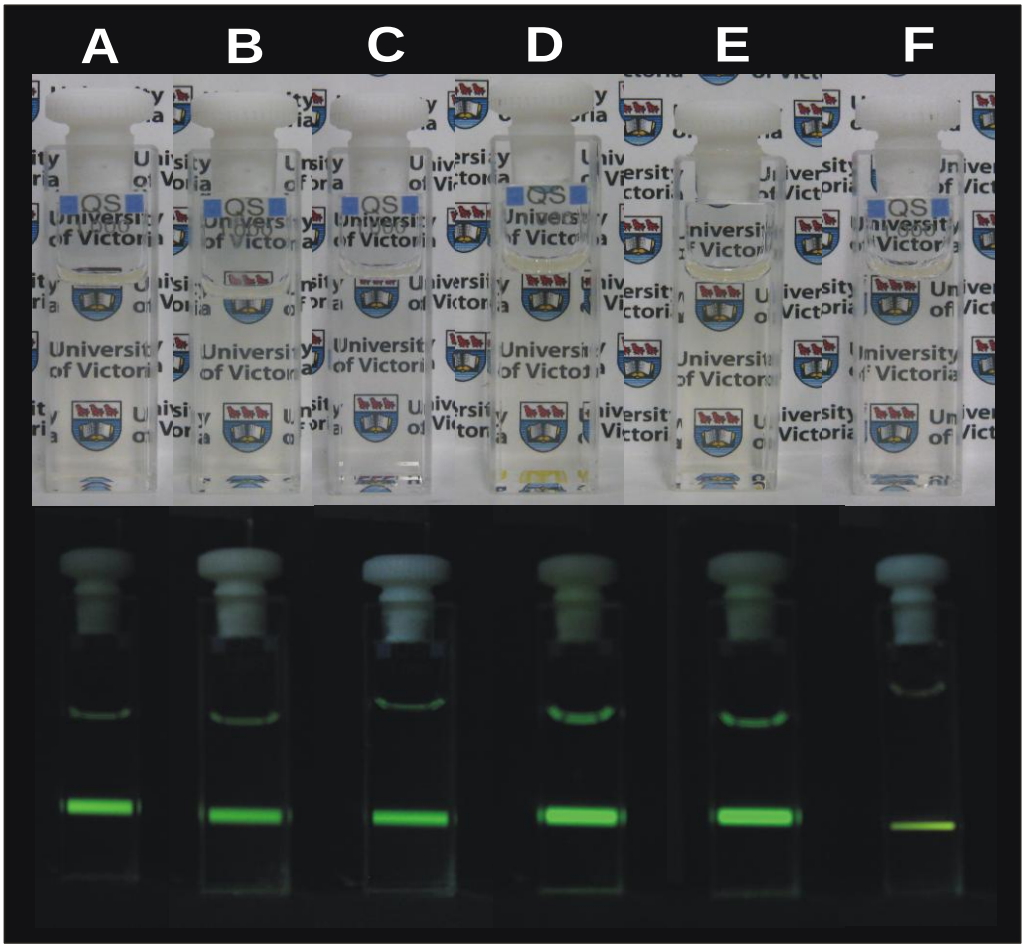

Figure 3.3. Colloidal dispersion of PVP-stabilized nanocrystals in different solvents (0.5 *wt%*) and their total fluorescence under 980 nm laser excitation (same power density). **(A)** chloroform, **(B)** DCM, **(C)** ethanol, **(D)** DMSO, **(E)** DMF, and **(F)** water.

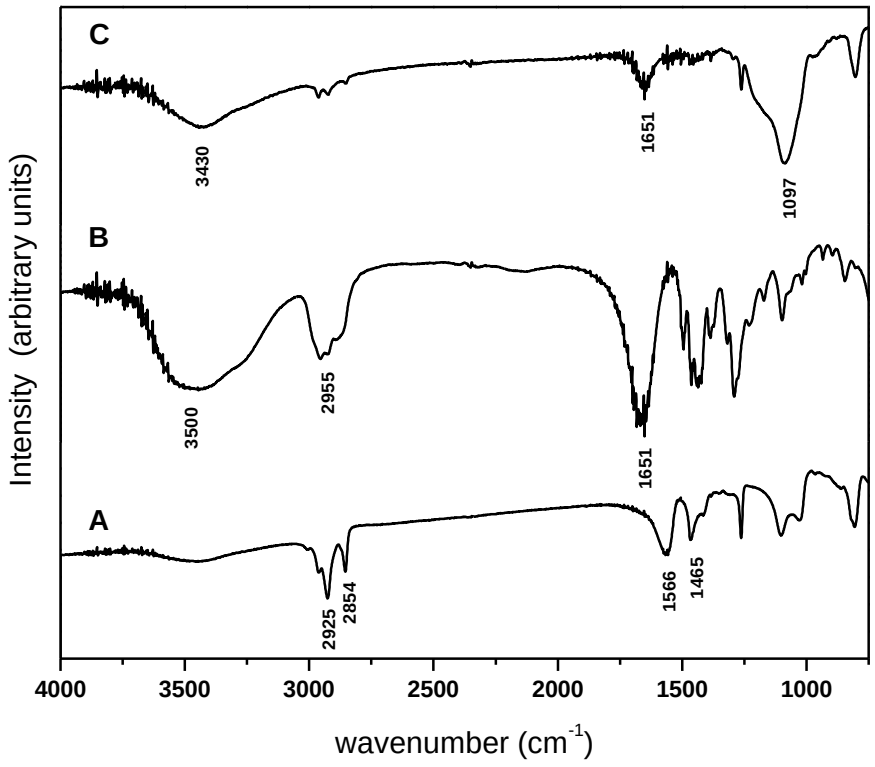

Figure 3.4. FT-IR spectra of β-$NaYF_4$:Yb^{3+}/Er^{3+} **(A)** oleate-stabilized NCs, **(B)** ligand-exchanged with PVP, and **(C)** silica-coated on the ligand-exchanged NCs.

3.2.2. Silica coating on PVP-stabilized β-$NaYF_4$: Yb^{3+}/Er^{3+} UCNCs

The affinity of PVP-stabilized NCs to silica is well documented.[118] In order to show that the exchange reaction with PVP was successful and aggregation of the UCNCs did not occur during the exchange reaction, PVP-stabilized NCs were coated with a thin shell of silica. The PVP-stabilized NCs were dispersed in ethanol and the silica shells were grown by a Stöber-like synthesis. PVP on the surface of the NCs allows for their stability in ethanol and their affinity to silica allows for uniform silica shell growth on the NC surface. The silica-coated NCs thus obtained have an average shell thickness of 9 nm

(Figure 3.5A-B) and there were few silica-coated NCs existing as dimers which can be attributed to the multidentate coordination of the PVP, which leads to some cross-linking between the NCs during exchange. The surface of the silica shells are rough, probably due to the silica nucleated PVP chains attached to the surface.[122,123] The excess PVP which is not coordinated to the NC surface acted as nucleation sites for silica growth, leading to the formation of some empty silica beads. This silica being less dense than the silica-coated NCs was easily removed by centrifugation at the end of the reaction. The FT-IR spectra of the silica-coated NCs (Figure 3.4C) shows the Si-O-Si stretching band at 1097 cm^{-1} and a small peak at 1651 cm^{-1} indicating the presence of some remnant PVP chains in the silica beads.

The reverse microemulsion route was also used to coat the hydrophobic NCs with a thin shell to compare with the silica coating on the PVP-stabilized NCs. The thin silica shell obtained by the reverse microemulsion route also had an average shell thickness of 9 nm. These silica-coated NCs have the same morphology when compared to the silica-coated PVP-stabilized NCs (Figure 3.5C). The excess surfactant used in the microemulsion route was hard to remove even by successive centrifugation and washing steps and the removal of the surfactants led to much higher necking between the silica beads (Figure 3.5D). The lower colloidal stability and aggregation tendency of thin silica shells grown in reverse microemulsion has been attributed to the dynamic nature of the reverse micelles and the presence of excess surfactants, by earlier reports.[120] The experimental studies demonstrated here also show the same features with respect to the silica-coated NCs grown in reverse micelles. Liu *et al*. have reported that the silica-coated $NaYF_4$ NCs from reverse micelles were stable for one day,[124] which implies that

they have a tendency to aggregate once removed from the stabilizing micelles which kept them apart during growth. NCs Silica-coated by reverse emulsion were mostly aggregated within one day after washing and storing in water (Figure A1 of the Appendix). On the other hand, the PVP-exchanged NCs coated with silica were individual particles with no aggregation after washing and storing for two days (Figure A2 of the Appendix). Some aggregation was noticeable after 5 days, and only after a week most of them were aggregated (Figure A3 of the Appendix).

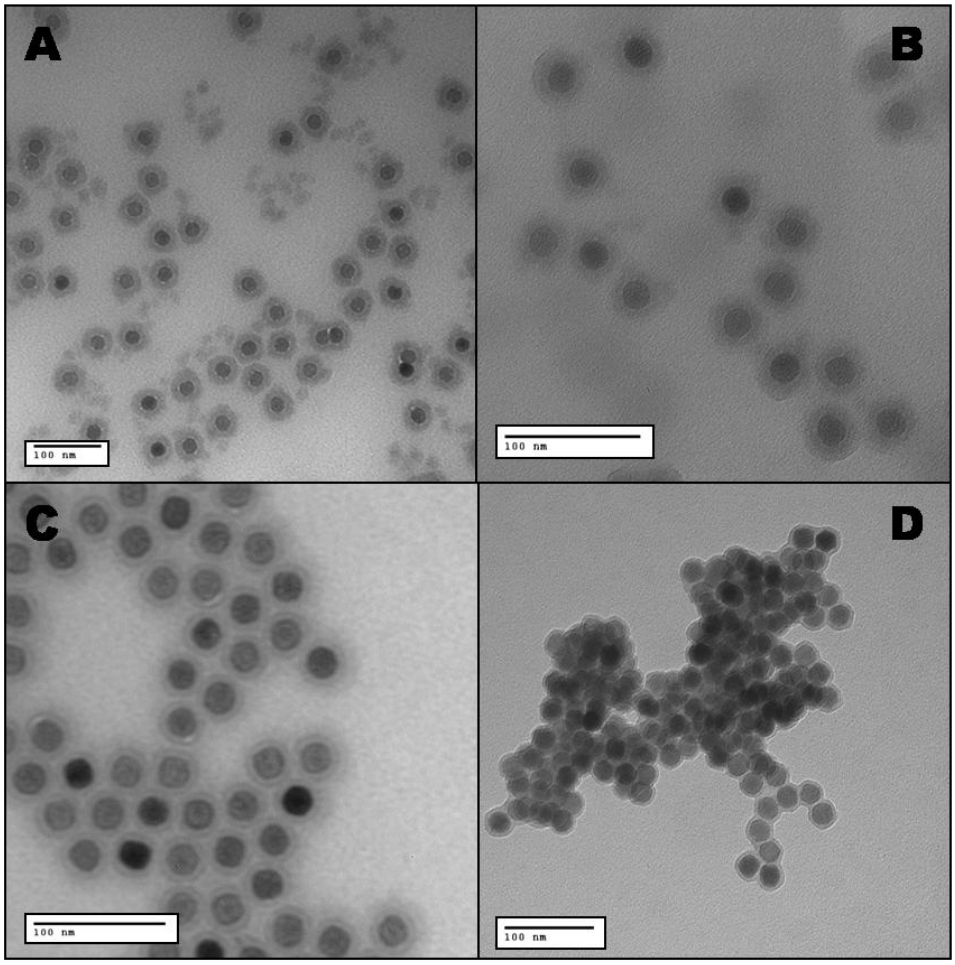

Figure 3.5. TEM images of silica-coated $NaYF_4$:Yb^{3+}/Er^{3+} NCs, **(A and B)** PVP-exchanged and subsequently coated, **(C)** from reverse microemulsion before washing, and **(D)** from reverse microemulsion showing aggregation and necking after washing to remove the excess surfactants.

Most of the biological studies require sterile samples, and attempts to filter the silica-coated NCs synthesized in reverse microemulsion through a 0.2 µm sterile syringe filter showed that they could not be filtered. This might be due to the excess surfactants clogging the pores and the aggregation resulting from the necking between the silica beads. On the other hand, the PVP-exchanged and subsequently silica-coated NCs could easily be filtered through 0.2 µm sterile syringe filters.

3.2.3. Optical properties of β-$NaYF_4$: Yb^{3+}/Er^{3+} UCNCs

The colloidal dispersion of the oleate-stabilized UCNCs in organic solvents showed bright green luminescence (Inset Figure 3.6) when excited with a 980 nm laser diode as observed by naked eye. The upconversion luminescence spectra (Figure 3.6) obtained from hexane and toluene dispersions show the characteristic green and red upconverted light with green being more intense than the red. The peaks at 520 and 540 nm are attributed to the transitions from the $^2H_{11/2}$, $^4S_{3/2}$ levels to the ground state ($^4I_{15/2}$), respectively. The peak at 654 nm corresponds to the transition from the $^4F_{9/2}$ to $^4I_{15/2}$ energy levels of the Er^{3+} doped in the NC matrix.

The ligand-exchanged NCs dispersed in water showed decreased upconversion luminescence when compared with the oleate-stabilized NCs dispersed in organic solvents. The high phonon energy of O–H groups in the water molecules can easily quench the upconversion luminescence by enhancing the non-radiative relaxation of the excited photons in Er^{3+} energy levels which account for the green and red emissions. The quenching of lanthanide excited states by O–H vibrations is well studied and has been reported to be highly effective compared to the C–H vibrational quenching of the excited states.[125] Hydrophilic upconverting NCs obtained by other pathways have also been

reported to show decreased luminescence intensity when dispersed in water.[50,101] Yi and Chow used a core-shell nanoparticle approach with an undoped $NaYF_4$ as a shell so that the emitting ions are shielded from the O–H vibrations.[101] Yet there was some quenching of upconversion emission when these core-shell NCs coated with amphiphilic PAA were dispersed in water. This shows that the upconversion emission is highly dependent on the environment or the solvent used.

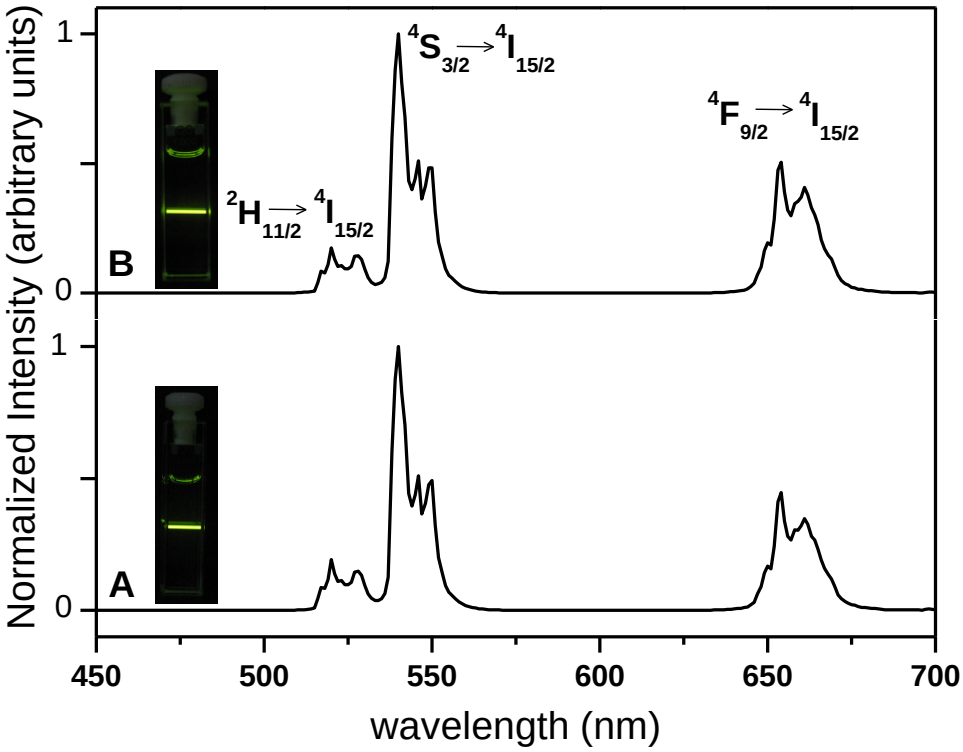

Figure 3.6. Upconversion emission spectra of oleate-stabilized β-$NaYF_4$:Yb^{3+}/Er^{3+} NCs (λ_{ex} = 980 nm) **(A)** in hexane, and **(B)** in toluene, *Inset*: upconversion emission from the colloidal dispersion under 980 nm diode excitation.

The PVP-exchanged NCs dispersed in water showed a different ratio of the green and red upconverted emission when compared with the oleate-stabilized NCs dispersed in organic solvents. While green upconverted emission was dominant in oleate-stabilized NCs, red upconverted emission was dominant in PVP-stabilized NCs dispersed in water (Figure 3.7A). Typical upconversion emission mechanism for β-$NaYF_4$: Yb^{3+}/Er^{3+} is shown in Figure 3.8. In the presence of O–H vibrations, the non-radiative relaxation of ($^2H_{11/2}$, $^4S_{3/2}$) to $^4F_{9/2}$ level and $^4I_{11/2}$ to $^4I_{13/2}$ are increased. The non-radiative relaxation of ($^2H_{11/2}$, $^4S_{3/2}$) to $^4F_{9/2}$ quenches the green emission and populates the red emitting level. In addition to that, as the probability of $^4I_{11/2}$ to $^4I_{13/2}$ non-radiative relaxation increases, the ions populating the $^4I_{13/2}$ can absorb another photon of 980 nm and eventually populate the red emitting level ($^4F_{9/2}$) . Thus, an increase in the non-radiative relaxation pathways in the presence of water enhances the red emission compared to the green. This effect has been observed from upconverting NCs dispersed in water.[50,126,127] The upconversion spectra of the silica-coated NCs in water shows that the coating was partially effective in shielding the high energy O–H vibrations as relatively equal amounts of green and red upconversion emission were observed (Figure 3.7B).

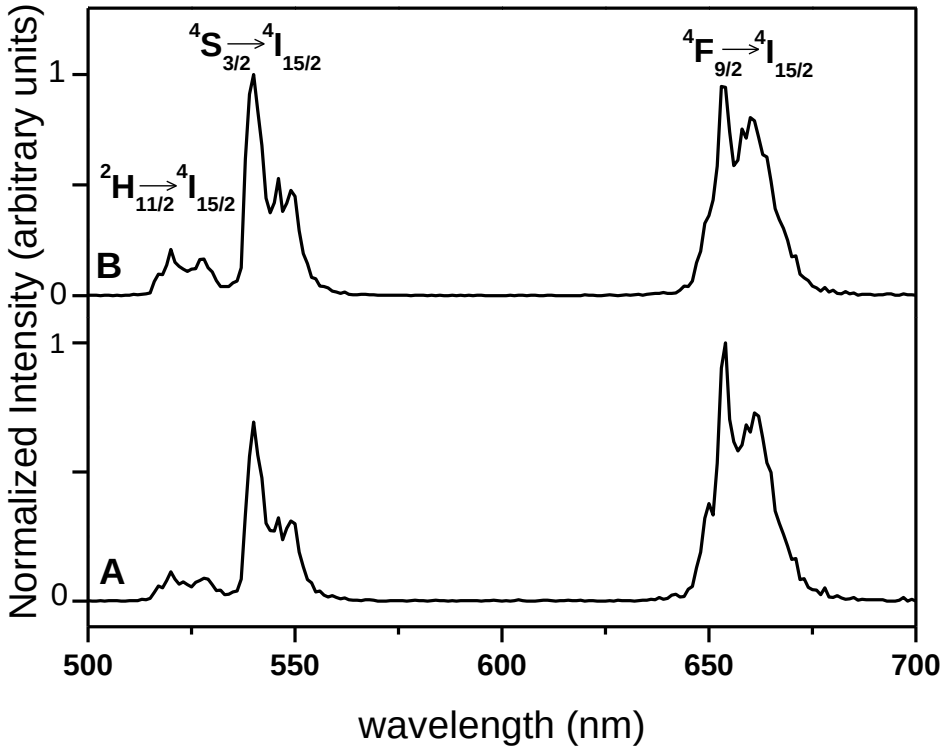

Figure 3.7. Upconversion emission spectra of β-$NaYF_4$:Yb^{3+}/Er^{3+} NCs (λ_{ex} = 980 nm) **(A)** PVP-stabilized in water, and **(B)** PVP-stabilized and subsequently silica-coated nanocrystals in water.

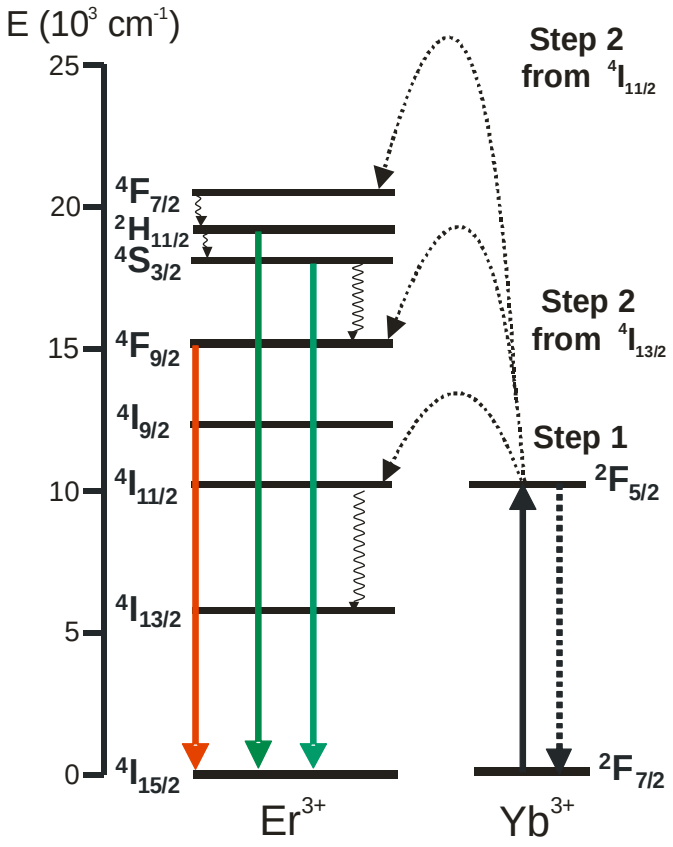

Figure 3.8. Upconversion emission pathway in β-$NaYF_4$:Yb^{3+} /Er^{3+} (λ_{ex} = 980 nm) NCs.

3.4. Conclusions

Highly monodisperse β-$NaYF_4$:Yb^{3+}/Er^{3+} UCNCs capped with oleates were successfully phase-transferred from organic solvent to water after ligand-exchange with a commercially available polymer, PVP. These PVP-stabilized NCs were used to grow thin silica shells to demonstrate the success of the PVP exchange reaction. The PVP-stabilized NCs were individually coated with a silica shell of ~ 9 nm showing that NC aggregation did not happen during the ligand exchange step. These NCs show decreased

upconversion emission in aqueous medium and the intensity of the red upconversion emission increases relative to the green due to increased non-radiative relaxation of Er^{3+} excitation levels in the presence of –OH phonons. This methodology of phase transfer and silica coating opens a different pathway for using these NCs in biological studies, as the silica aggregation and excess surfactant related problems as seen in the reverse emulsion-based silica shells are avoided. In the next chapter a modified strategy of using terminally functionalized PVP is described, which allows for direct bioconjugation of the PVP-exchanged NCs to specifically target human prostate cancer cells.

3.5. Experimental Section

Materials. All lanthanide chlorides ($YCl_3 \cdot 6H_2O$, $YbCl_3 \cdot 6H_2O$, $ErCl_3 \cdot 6H_2O$) (>99.99%), oleic acid (90%), 1-octadecene (90%), ammonium fluoride (99.99%), tetraethyl orthosilicate (TEOS) (99.99%), polyvinylpyrrolidone 10 kg/mol (PVP-10) and Igepal CO-520 were purchased from Sigma-Aldrich. Sodium hydroxide and dichloromethane (DCM) were obtained from ACP chemicals. Ethyl ether (anhydrous), dimethylformamide (DMF), toluene, cyclohexane and ammonium hydroxide (30 wt % in water) were from Caledon laboratories. All chemicals were used as received without further purification.

Synthesis of oleate-stabilized β-$NaYF_4$: Yb^{3+}/Er^{3+} NCs. The synthesis of β-$NaYF_4$ was done following a reported procedure with some modifications.[42] In a typical synthesis, 1 mmol of the lanthanide chlorides (0.78 mmol $YCl_3 \cdot 6H_2O$, 0.20 mmol $YbCl_3 \cdot 6H_2O$ and 0.02 mmol $ErCl_3 \cdot 6H_2O$) were taken in a 100 ml 3-necked flask and 15 ml of octadecene and 6 ml of oleic acid were added. The flask was then heated to 150 °C under vacuum and held at this temperature for 30 minutes to get a homogenous solution. Subsequently, the flask was cooled down to room temperature and 10 ml methanol solution containing

NH_4F (4 mmol) and NaOH (2.5 mmol) was added dropwise. The resulting solution was stirred at room temperature for 2 h and heated slowly to 70 °C until all the methanol evaporated. The reaction vessel was then brought under a gentle flow of argon and heated to 300 °C and held at that temperature for 90 min. The flask was then cooled to room temperature and the NCs were precipitated by adding ethanol (15 ml), centrifuged 4,500 rpm (Beckman Coulter Spinchron 15 - rotor F0630), and washed with ethanol. The isolated oleate-stabilized NCs were stored as 1 wt% dispersion in toluene.

Ligand Exchange of oleate-stabilized β-$NaYF_4$:Yb^{3+}/Er^{3+} with PVP. A dispersion of oleate-stabilized NCs in toluene (0.2 ml) was taken in a 100 ml round bottom flask and diluted with 5 ml of 1:1 DMF/DCM. To this, 75 mg of PVP was added and refluxed at 100 °C for 6 h. The reaction mixture was then added dropwise into ethyl ether (60 ml) to precipitate the polymer-stabilized NCs. The precipitate was washed once with ethyl ether and centrifuged at 4,500 rpm for 5 min. The precipitate was transferred to 6.5 ml of ethanol to yield a stable dispersion of the PVP-stabilized $NaYF_4$ NCs. The precipitate could also be dispersed in several other solvents like water, chloroform, dichloromethane, DMF, and DMSO to yield optically transparent dispersions.

Silica coating on PVP-stabilized $NaYF_4$:Yb^{3+}/Er^{3+} NCs. Ethanol dispersion of phase-transferred NCs (6.5 ml) was taken in a 15 ml vial and 0.28 ml of ammonium hydroxide (30 wt % in water) was added, followed by 65 µl of 10 vol % TEOS in ethanol solution. The vial was sealed and stirred for 15 h at room temperature. The silica-coated NCs were isolated by centrifugation at 12,000 rpm (Beckman Coulter Spinchron 15 - rotor F0630) for 15 min and washed with ethanol. The collected silica beads were dispersed in distilled water.

Silica coating on hydrophobic NCs through microemulsion route. Microemulsion-based silica coating was done by following a reported procedure.[63] Typically, ~7 mg of the oleate-stabilized NCs in cyclohexane was mixed with 6 ml cyclohexane and 0.1 ml of Igepal CO-520. To this, 0.4 ml Igepal CO-520 and 0.08 ml ammonium hydroxide (30 wt % in water) were added and the flask was sonicated until a transparent emulsion was obtained. TEOS (40 µl) was added and stirred for 2 days. The silica-coated NCs were precipitated by adding methanol and washed several times with ethanol/water, centrifuged at 4,500 rpm for 5 min and the collected silica beads were dispersed in distilled water.

TEM images of the NCs were obtained from Hitachi H-7000 microscope operating at 75 kV. The TEM grids (Formar Carbon on 300 mesh Cu) were coated with the NCs by drop casting a dilute dispersion of the NCs (hexane dispersions of hydrophobic NCs and ethanol dispersions of the hydrophilic NCs) and air dried before imaging. The size distribution was measured for an ensemble of ~ 100 particles.

X-ray diffraction (XRD) pattern of the NCs were acquired using a Rigaku Miniflex X-ray diffractometer with a Cr source (K_α λ = 2.2890 Å) operating at 30 kV and 15 mA. The XRD patterns were collected at a sampling width of 0.05° (2θ) and scan speed of 1°/min.

FT-IR spectra were obtained from a Perkin Elmer FT-IR spectrometer 1000 with a resolution of 2 cm^{-1} and averaged over four scans. The samples were taken as dry powder and pelletized with KBr and placed on the sample holder.

Optical measurements were done on the UCNCs using Edinburgh instruments FLS920 fluorimeter. The luminescence spectra were collected using a red-sensitive Peltier-cooled

Hamamatsu R955 PMT. A 980 nm laser diode (JDS Uniphase type 63-00342) coupled to a 100 μm core fiber was used as the excitation source. The output was collimated using a fiber coupler and a long band-pass filter (850 nm) was used on the excitation side and a short band-pass filter (800 nm) on the collecting end of the detector to remove the scattered excitation light. The optical measurements were done on toluene and hexane dispersions of oleate-stabilized NCs and water dispersions of the hydrophilic NCs (PVP-stabilized and silica-coated) taken in 1 cm path-length quartz cuvette. All upconversion emission spectra were measured at a resolution of 1 nm, using the same laser power density (150 W/cm^2) for excitation.

Chapter 4. End-group Functionalized Polyvinylpyrrolidone Coated Upconverting Nanocrystals for Immunolabeling of Human Prostate Cancer Cells (LNCaP)

This chapter describes the utilization of end-group functionalized polyvinylpyrrolidone as a single step route for direct bioconjugation of immunolabels to upconverting nanocrystals. The protocol described in Chapter 3 is modified to afford a simple synthetic approach to label effectively biomolecules to the nanocrystal surface, circumventing the challenges and issues of silica coating described in Chapter 3. Utilizing end-group functionalized polyvinylpyrrolidone this chapter demonstrates the specific targeting of upconverting nanocrystals to human prostate cancer cells (LNCaP), and also describes the ability to tune specifically the surface charge and functional group with this class of polymers.

4.1. Introduction

The advantages of using upconverting nanocrystals (UCNCs) in biological applications as described in the previous chapter are profound. However, modulating the surface properties of the NCs to integrate them in biological studies is challenging as multiple fundamental issues need to be addressed for efficient integration and utilization as bioprobes.[69] In general, the applicability of UCNCs in biological imaging and uptake by specific cells is often demonstrated by passive uptake of the NCs driven by surface charge or by prolonged incubation of the NCs with the cells.[52,53,86,128-131] These studies do not address the fundamental goal of utilizing the NCs in biolabeling, *i.e.* their active localization with high specificity in the region of interest, such as a tumor. The

conjugation of specific antibodies on UCNCs to target the over-expressed antigens on tumor cells *in vitro* has been addressed by few groups.[132-135] However, these groups do not take into consideration the biomimetic design consideration. For example, Wang *et al.* demonstrated the use of antibody conjugated silica-coated UCNCs for specific labeling of HeLa cells.[136] However, the silica surface is well-known for non-specific binding of plasma proteins (opsonization) and thus such *in vitro* studies may not be extended to potential *in vivo* applications. In a biomimetic design consideration the surface of UCNCs should be stabilized by a ligand which is both biocompatible and simultaneously suppress non-specific binding of biomolecules (for example plasma proteins). As mentioned earlier, silica coating is known for its biocompatibility but they are prone to non-specific binding of proteins, which can screen the surface bound antibody in potential targeting applications.[70,137] Polyethylene glycol (PEG) and polyvinylpyrrolidone (PVP) are well-known biocompatible polymers which are also known for their suitability in avoiding non-specific binding.[72,73,137] Integration of functionalized PEG based surface ligands for further bioconjugation of antibodies to UCNCs has recently been addressed using functionalized PEG-phospholipids.[58] However, the PEG-phospholipids are not easy to synthesize and are costly with respect to their wider utility. No studies on functionalized PVP as a surface ligand to conjugate biological tags and specifically target is reported to date. In this regard, end-group functionalized PVP synthesized by radical polymerization of 1-vinylpyrrolidone is demonstrated as a suitable ligand to further conjugate biological tags (antibody) to the UCNCs surface. In this study the over-expression of prostate specific membrane antigen

(PSMA) in human prostate cancer LNCaP cells is used as an *in vitro* model to target specifically anti-PSMA antibody conjugated UCNCs.

4.2. Results and Discussion

4.2.1. Synthesis of end-group functionalized polyvinylpyrrolidone

Polyvinylpyrrolidone functionalized at one end with either carboxylic acid (-COOH) or amino (-NH_2) groups were obtained by radical polymerization of 1-vinylpyrrolidone (VP) following previously reported protocols as shown in Figure 4.1.[138-141] The synthesis of polyvinylpyrrolidone with carboxylic acid at one end (PVP-COOH) was performed by a two-step procedure. The monomer 1-vinylpyrrolidone was polymerized in methyl *iso*butyrate acting both as solvent and chain transfer agent (CTA) in the presence of *2-2'*-azobis*iso*butyronitrile (AIBN) as radical initiator at 70 °C. The volume ratio of the CTA to monomer (CTA/VP) was 10 and the amount of initiator (AIBN) was 1 wt% of the monomer. The PVP-carbomethoxy derivative (PVP-$COOCH_3$) obtained from the first step was subsequently hydrolyzed with NaOH to give PVP-COOH. Polyvinylpyrrolidone with an amine moiety at one end (PVP-NH_2) was synthesized by radical polymerization of monomer 1-vinylpyrrolidone (0.125 mol) in dioxane with 2-mercaptoethylamine (0.4 mol/VP mol) as CTA and AIBN (0.06 mol/VP mol) as radical initiator at 60 °C.

The molecular weight of the synthesized polymers as determined from MALDI-MS (matrix assisted laser desorption ionization-mass spectrometry) analysis was about 1,500 g/mol (PVP-COOH) and 1,100 g/mol (PVP-NH_2), respectively as shown in Figure B1-B2 of the Appendix. If desired, end-group functionalized PVP with different molecular weights can be obtained by changing the ratio of monomer (VP) to CTA during

polymerization.[140,141] Thus this protocol allows for easy access to end-group functionalized PVP with tunable molecular weight and functionality.

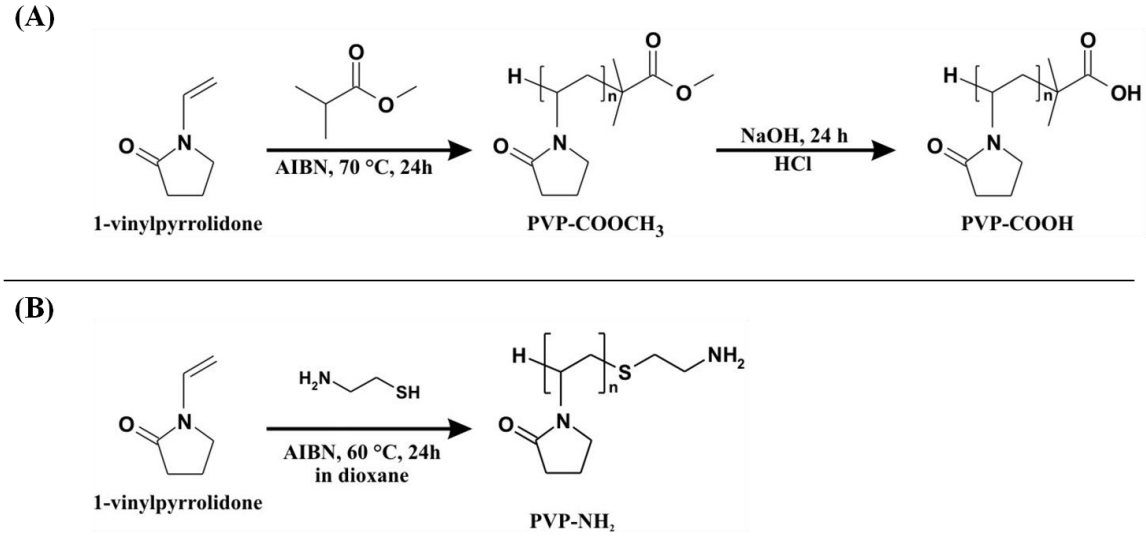

Figure 4.1. Reaction schemes for the synthesis of **(A)** carboxylic acid-terminated polyvinylpyrrolidone (PVP-COOH), and **(B)** amine-terminated polyvinylpyrrolidone (PVP-NH_2).

4.2.2. Core-shell upconverting nanocrystals (UCNCs)

Upconverting $NaYF_4$:Er^{3+} (2%), Yb^{3+} (20%) nanocrystals (UCNCs) were synthesized and subsequently an undoped shell of $NaYF_4$ was grown following previous reports.[46] The undoped shell protects the luminescent core NCs from solvent/ligand quenching and thus allows for enhanced luminescence efficiency. The core-shell NCs as shown in Figure 4.2A are highly monodisperse with an average size of 23.4 ± 0.8 nm (determined by measuring at least 100 NCs from the TEM image). The X-ray diffraction (XRD) pattern in Figure 4.2B shows that the core-shell NCs are of pure hexagonal crystal phase with no impurity. The crystallite size determined from the peak broadening in the XRD pattern using Scherrer equation was approximately 23 nm, consistent with the size determined from the TEM images. The synthesized core-shell UCNCs are coated with oleate ligands and thus form stable colloidal dispersions in organic solvents. A colloidal

dispersion of the UCNCs in toluene showing upconverted visible emission under 980 nm NIR excitation is shown in Figure 4.2A (*inset*). The upconversion emission mechanism is the same as discussed in Chapter 3 (Figure 3.8).

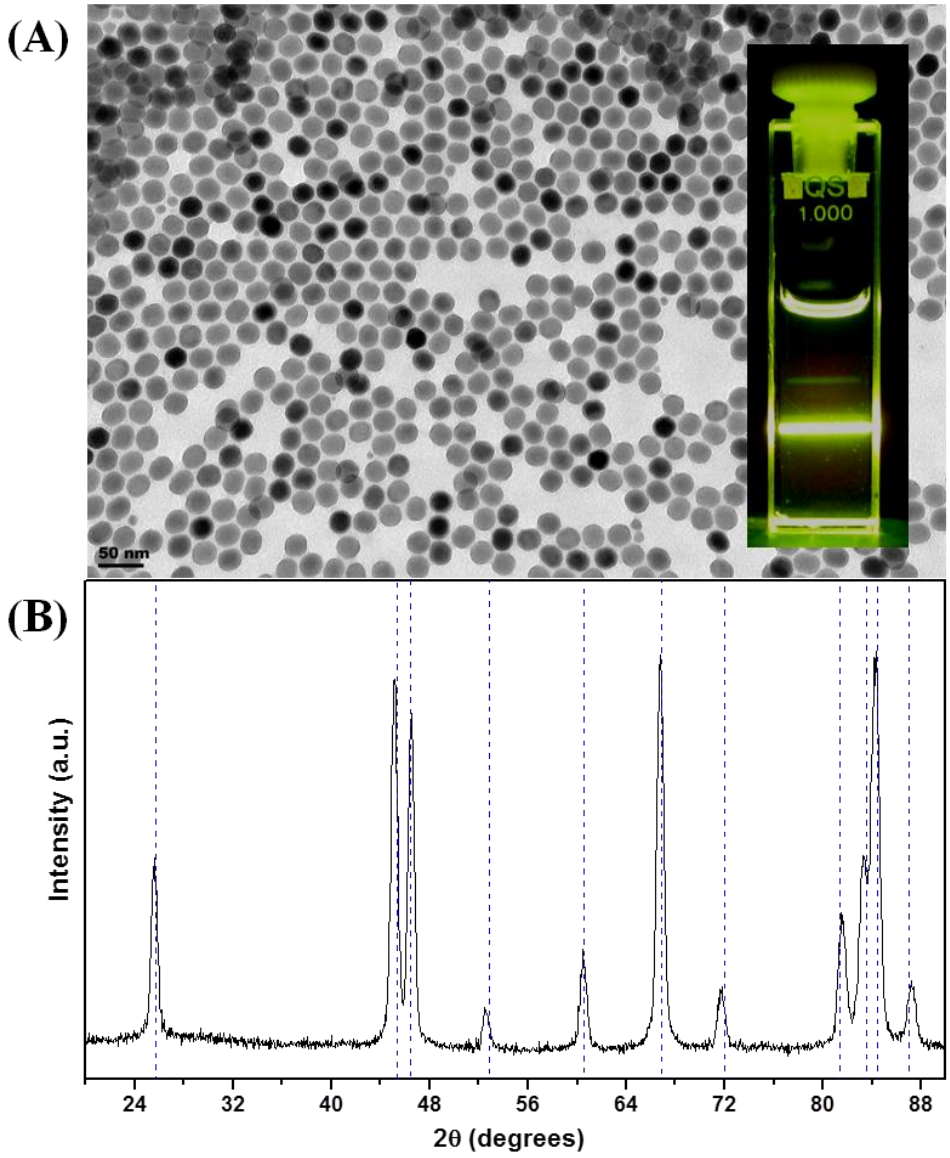

Figure 4.2. (A) TEM image of oleate-stabilized $NaYF_4:Yb^{3+},Er^{3+}/NaYF_4$ core/shell UCNCs (*Inset: Dispersion of UCNCs in toluene under 980 nm excitation*), and **(B)** X-ray diffraction pattern of the core/shell UCNCs and the standard reference lines (blue) of β-$NaYF_4$ (JCPDS: #016-0334).

4.2.3. Phase transfer of oleate-stabilized UCNCs to water using PVP-COOH

Following the protocol described in Chapter 3, but replacing the commercial unfunctionalized PVP with the synthesized end-group functionalized PVP-COOH, the oleate-stabilized core-shell UCNCs were transferred to water as illustrated in Figure 4.3A. The colloidal dispersion of the phase-transferred NCs in water shown in Figure 4.3B confirms the successful exchange of UCNCs to water. Moreover, the TEM image of the phase-transferred NCs (Figure B3 of the Appendix) confirms that no agglomeration had happened during the ligand exchange step. To confirm further the even distribution of NCs after phase transfer in water, $NaYF_4$:Ce^{3+},Tb^{3+}/$NaYF_4$ core/shell NCs were synthesized and transferred to water similar to the UCNCs. The Tb^{3+} green emission upon 256 nm UV excitation shown in Figure 4.3C illuminates the whole dispersion, confirming that no precipitation of phase-transferred NCs occurs.

The carboxylic groups (-COOH) are well-known to have a strong affinity to lanthanide-based NCs,[48] and this along with the coordination of carbonyl groups of the PVP chains as demonstrated earlier in Chapter 3, result in effective transfer of the UCNCs. The multidentate coordination of PVP-COOH ligand should also allow for free surface carboxylic groups that are not coordinated to the NCs surface for further bioconjugation. Thus, one only needs functional group at one end of the PVP chain for further bioconjugation. The ability to conjugate bi-functionalized molecules to the surface carboxylic groups, to generate multiple functionality, and surface charge tunability is discussed in the next section.

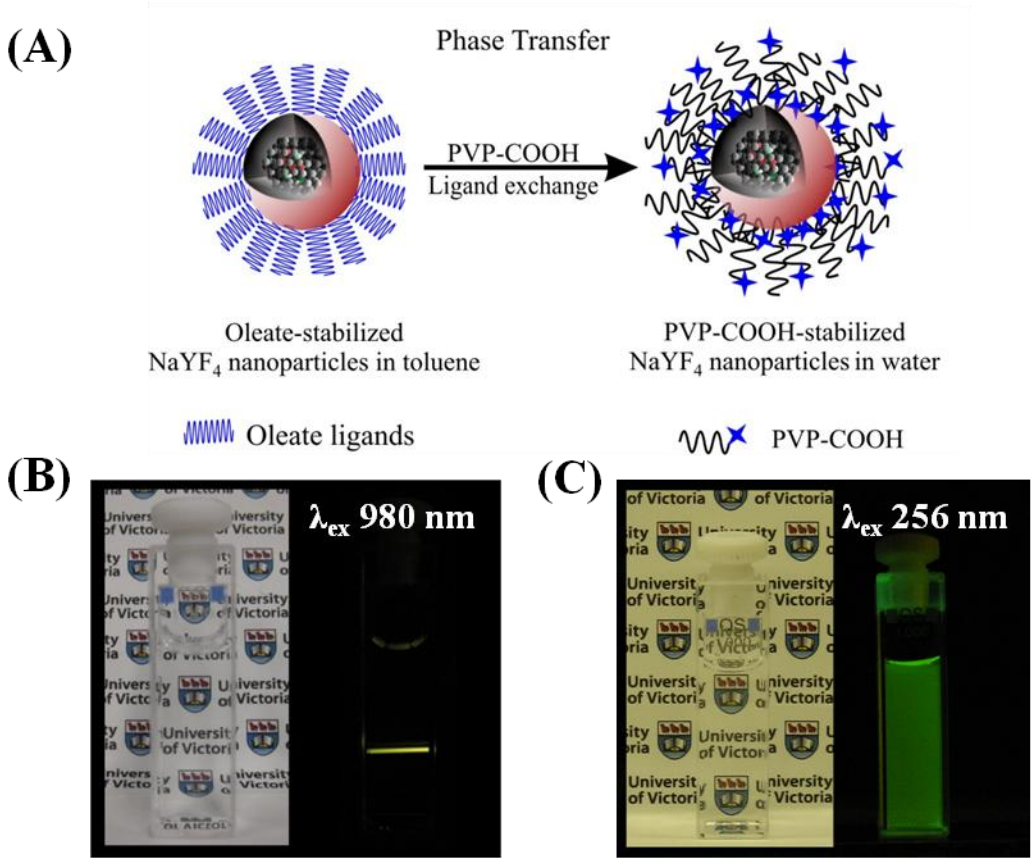

Figure 4.3. (A) Illustration of the ligand exchange in UCNCs, replacing the surface oleates with end-group functionalized polyvinylpyrrolidone, **(B)** colloidal dispersion of phase-transferred UCNCs in water and upconverted emission under NIR (980 nm) excitation, and **(C)** colloidal dispersion of phase-transferred $NaYF_4:Ce^{3+},Tb^{3+}/NaYF_4$ core/shell NCs in water and Tb^{3+} emission under UV (256 nm) excitation.

4.2.4. Reactivity of PVP-COOH stabilized UCNCs with bi-functional molecules

The PVP-COOH stabilized UCNCs described earlier were analyzed for the reactivity of the surface carboxylic acid groups for further coupling reactions. The availability of surface carboxylic groups after phase transfer was confirmed by zeta-potential measurements shown in Figure 4.4. The oleate-stabilized UCNCs do not have a surface charge as the -COOH group of the oleate ligand is coordinated to the surface lanthanide ions. The small positive charge is ascribed to the slight excess of lanthanide ions on the NCs surface. After ligand exchange with PVP-COOH the phase-transferred UCNCs have

a net negative surface charge confirming the effective replacement of oleate chains and the availability of carboxylic groups for further coupling reactions.

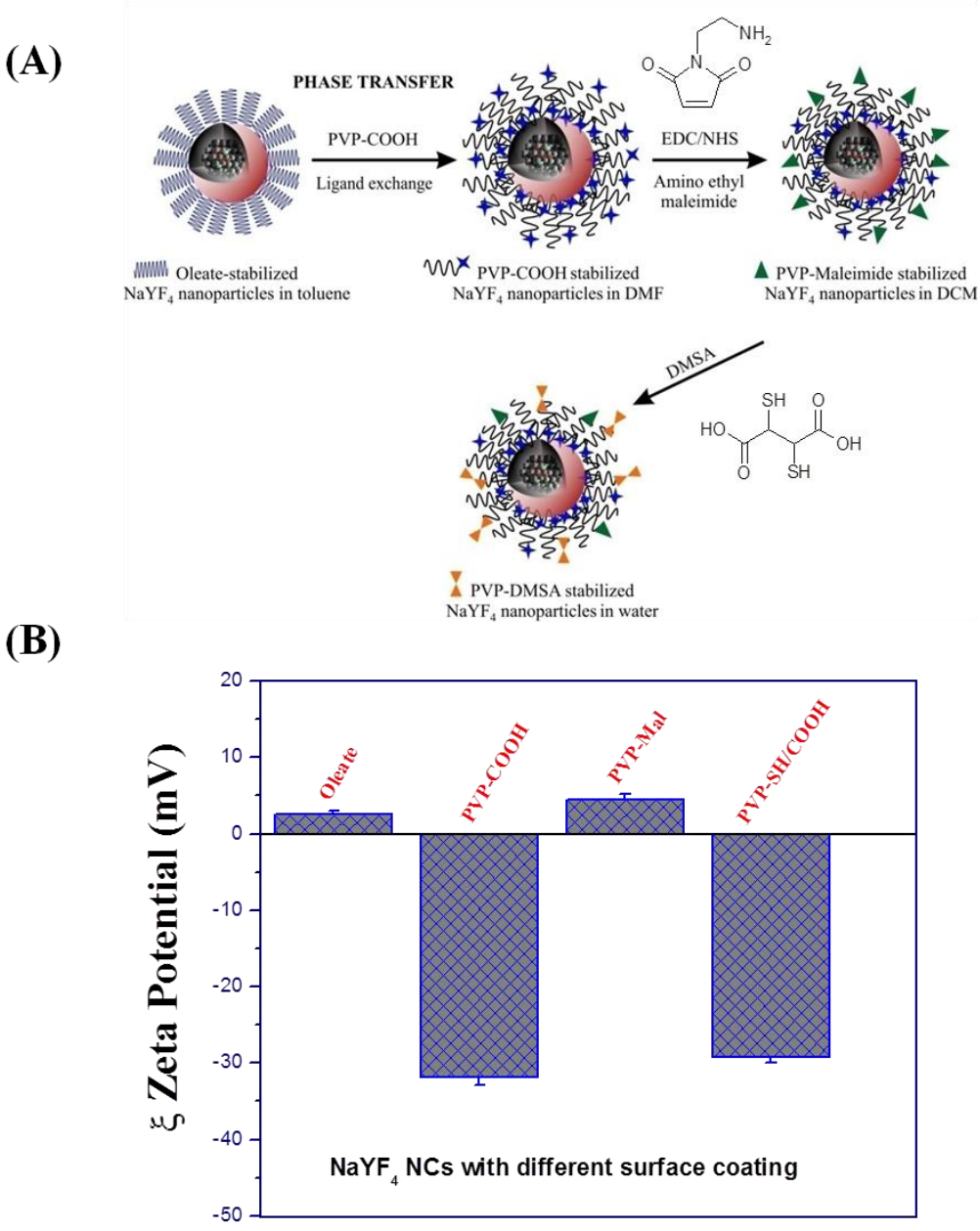

Figure 4.4. (A) Schematic illustration of the derivatization of the surface carboxylic acid groups of PVP-COOH stabilized UCNCs with bi-functional molecules, and **(B)** Zeta-potential of the UCNCs with different surface functional coating.

The carboxylic group (-COOH) groups on the UCNCs allows for a highly reactive site for further conjugation reactions, and thus allows for validating the reactivity of the surface bound PVP-COOH ligands. To demonstrate the reactivity of the surface PVP-COOH ligands of UCNCs two successive conjugation steps were performed such that the net surface charge also changes upon each step. In the first step, the reactivity of the carboxylic acid moiety with amino groups was utilized to conjugate aminoethylmaleimide to the surface of the PVP-COOH stabilized UCNCs. Utilizing *N*-(3-dimethylaminopropyl)-*N'*-ethylcarbodiimide hydrochloride (EDC) and *N*-hydroxysulfosuccinimide sodium salt (NHS), the surface carboxylic acid groups were modified into activated esters. The activated ester readily reacts with primary amine groups of the aminoethylmaleimide forming amide linkages resulting in maleimide-terminated UCNCs as shown in Figure 4.4A. The maleimide groups on the surface result in a net loss of the negative surface charge as shown in Figure 4.4B, confirming that the surface carboxylic acid groups have been derivatized with maleimide functionality. The maleimide moiety is highly reactive towards thiols (-SH) and undergoes spontaneous Michael addition, a general route often used to conjugate the thiol groups of biological molecules such as proteins and antibodies. To validate that such a spontaneous reactivity is possible on the surface of UCNCs, the surface maleimide groups were reacted with dimercaptosuccinic acid (DMSA) as shown in Figure 4.4A. The UCNCs after DMSA coupling show a net negative surface charge similar to the starting PVP-COOH functionalized UCNCs confirming the presence of surface carboxylic acid groups. These two successive steps clearly demonstrate the ability to perform surface chemistry on the PVP-COOH stabilized UCNCs to generate easily tunable surface functionality.

Similar to the high biological relevance of carboxylic acid moiety, amino groups are also versatile for performing bioconjugation reactions. In this regard, utilizing the PVP-NH_2 polymer the oleate-stabilized UCNCs were transferred to water and the resulting surface charge after exchange was determined by zeta-potential analysis. The PVP-NH_2 stabilized UCNCs because of their amino-group rich surface showed a net positive surface charge of ~ +20 mV, confirming the ability to tune both the surface charge and functionality using end-group functionalized PVP.

4.2.5. Immunolabeling of PVP-COOH stabilized UCNCs to human prostate cancer cells

The PVP-COOH stabilized UCNCs were studied for their ability to target specifically human prostate cancer cells. LNCaP cells are human prostate adenocarcinoma cells which over-express prostate specific membrane antigen (PSMA).[68] The anti-PSMA antibody is known to detect specifically PSMA, and was conjugated to the surface of PVP-COOH stabilized UCNCs. The antibody conjugated UCNCs (UCNCs-anti-PSMA) were synthesized by condensation of the surface carboxylic acid groups of PVP-COOH stabilized UCNCs with amino groups of the antibody as shown in Figure 4.5A, following the EDC/NHS protocol discussed earlier. To validate the specificity of the anti-PSMA conjugated UCNCs to LNCaP cells, PSMA (-) negative human prostate cancer PC3 cells, which do not over-express, were employed as negative control.[68] The antibody conjugated UCNCs (UCNCs-anti-PSMA) were then incubated with the cultured LNCaP and PC3 cells *in vitro* under the same conditions and then washed and fixed. The cells were then incubated in 4',6-diamidino-2-phenylindole (DAPI), a nuclear fluorescent probe, and the cover slip with the cells was then transferred to a glass slide and examined with a Leica compound epifluorescence microscope.

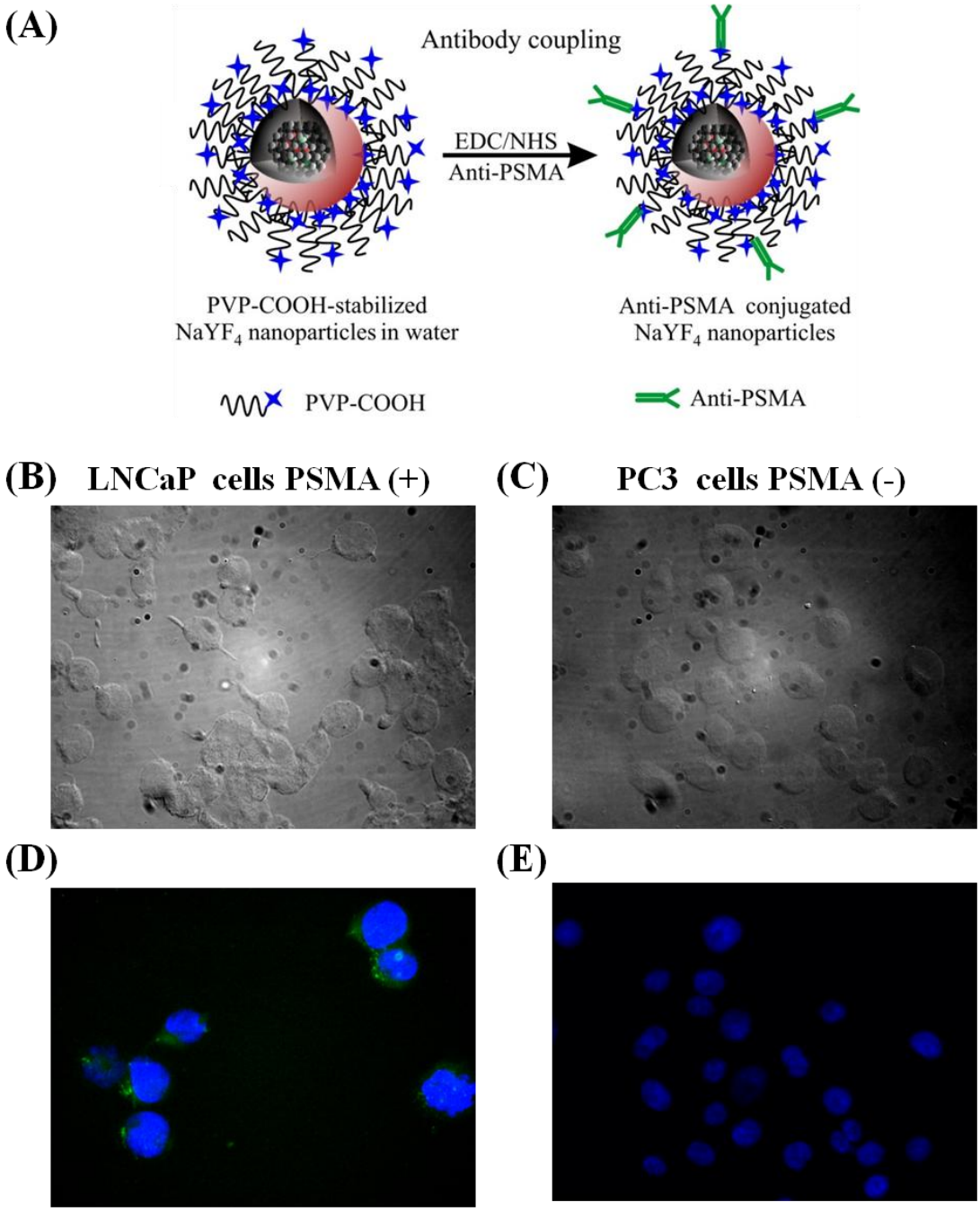

Figure 4.5. (A) Schematic illustration of the conjugation of anti-PSMA antibody to PVP-COOH functionalized UCNCs, **(B,C)** Bright field differential interference contrast image showing the morphology of fixed PSMA (+) LNCaP cells, and PSMA (-) PC3 cells, respectively, and **(D,E)** overlay of upconverted emission (green) from UCNCs and DAPI (nuclei stain) emission (blue) of LNCaP and PC3 cells, respectively.

The incubated cells were imaged both for the upconverted emission from the UCNCs and the DAPI emission from the nuclei stain. The overlay of the upconverted emission and DAPI emission from the stained LNCaP and PC3 are shown in Figure 4.5D,E. It is clearly evident from the images that the targeting of anti-PSMA conjugated UCNCs is specific to the PSMA (+) LNCaP cells, an no upconverted emission from the PSMA (-) PC3 cells was observed. The upconverted green emission from the LNCaP cells is mostly localized around the nucleus confirming the preferential binding to the PSMA rich cell membrane of the cells. Further confirmation of the green emission resulting from the upconversion of the cell bound UCNCs was done by imaging a specific cell with the excitation (980 nm) preferentially turned on and off as shown in Figure B4 of the Appendix. There are no known biological molecules that can be illuminated under NIR (980 nm) excitation, which clearly confirms the presence of cell bound UCNCs. These results demonstrate that end-group functionalized PVP can potentially be used as functional surface ligand to integrate biological probes onto UCNCs for detection and easy diagnosis of specific human cancer cells.

4.3. Conclusions

Utilizing end-group functionalized polyvinylpyrrolidone water-dispersible β-$NaYF_4$:Er^{3+} (2%), Yb^{3+} (20%)/$NaYF_4$ core/shell upconverting nanocrystals (UCNCs) were obtained by replacing the oleate ligands on the hydrophobic UCNCs. The generality of replacing the surface ligands to generate different surface functional groups was validated utilizing both PVP-COOH and PVP-NH_2 synthesized by radical polymerization of 1-vinylpyrrolidone. Moreover, the successive functionalization reaction to tune the surface functional group and surface charge demonstrates the high flexibility in surface

conjugation reactions utilizing end-group functionalized PVP. The ability to target specifically PSMA (+) positive LNCaP cells, without any specific binding to PSMA (-) PC3 cells confirm the high degree of specificity of the anti-PSMA conjugated UCNCs. The advantage of the developed protocol is that the PVP backbone is known to avoid non-specific binding of proteins and biomolecules to the NC surface, and thus could be ideal for integration in highly specific labeling and targeting biological applications.

4.4. Experimental Section

Materials. All lanthanide chlorides ($YCl_3 \cdot 6H_2O$, $YbCl_3 \cdot 6H_2O$, $ErCl_3 \cdot 6H_2O$) (>99.99%), oleic acid (90%), 1-octadecene (90%), ammonium fluoride (99.99%), 1-vinylpyrrolidone, methyl*iso*butyrate, *N*-(3-dimethylaminopropyl)-*N'*-ethylcarbodiimide hydrochloride (EDC), *N*-hydroxysulfosuccinimide sodium salt (NHS), 2-2'-azobis*iso*butyronitrile (AIBN), 1,4-dioxane, mercaptoethylamine, and dimercaptosuccinic acid (DMSA) were purchased from Sigma-Aldrich. Antibody (anti-PSMA) was purchased from Abcam. Sodium hydroxide and dichloromethane (DCM) were obtained from ACP chemicals. Ethyl ether (anhydrous), dimethylformamide (DMF), toluene, cyclohexane and ammonium hydroxide (30 wt % in water) were from Caledon laboratories. All chemicals were used as received except the following: 1-vinylpyrrolidone was vacuum distilled at 100 °C (P_{max} 8 mbar) before polymerization to remove the inhibitor, AIBN was recrystallized twice from methanol and dried, and methyl*iso*butyrate was distilled at 100 °C.

Synthesis of carboxylic acid-terminated polyvinylpyrrolidone (PVP-COOH). Vinylpyrrolidone (20 ml), methyl*iso*butyrate (200 ml), and AIBN (200 mg) was taken in a three-neck flask and purged with argon and degassed alternatively multiple times at

room temperature. Subsequently, the flask was sealed with argon and heated at 70 °C for 24 h. The reaction mixture was then cooled to room temperature and the polymer was precipitated into ether and filtered. The obtained polymer with a terminal ester residue (PVP-carbomethoxy derivative) was dissolved in ethanol and the ethanol and residual ether was removed by rotary evaporation. The oily polymer layer at the bottom was dissolved in distilled water (100 ml) and NaOH (1 g) was added and stirred at room temperature for 48 h to convert the ester residue to the sodium salt. The solution was then heated at 50 °C for 2 h and at room temperature the pH of the solution was reduced to ~3 using conc. HCl and stirred for 2 h. The solution was then transferred to a 1,500 MWCO dialysis tube and dialysed against distilled water for a day (replacing the water every 3 h). The contents in the dialysis tube were then transferred to a flask and water was removed by rotary evaporation. The final oily polymer was freeze dried overnight to obtain PVP-COOH as white dry powder.

Synthesis of amine-terminated polyvinylpyrrolidone (PVP-NH_2). Vinylpyrrolidone (14 ml), mercaptoethylamine (960 mg), AIBN (1.2 g), and 1,4-dioxane (50 ml) was taken in a three-neck flask and purged with argon and degassed alternatively multiple times at room temperature. Subsequently, the flask was refluxed under argon at 60 °C for 24 h. The reaction mixture was then cooled to room temperature and the polymer was precipitated into ether and filtered. The obtained polymer (PVP-NH_2) was dissolved in ethanol and the ethanol was removed by rotary evaporation. The oily polymer was freeze dried overnight to obtain PVP-NH_2 as white dry powder.

Synthesis of oleate-stabilized $NaYF_4$: Yb^{3+}/Er^{3+} core and core-shell NCs. The synthesis of core NCs was performed as described in Chapter 3 with no specific

modifications. The purified core NCs from the reaction mixture were dispersed in 10 ml hexanes and used for growing an undoped shell of $NaYF_4$ following a published procedure.[46] In a typical core-shell synthesis, 1 mmol of $YCl_3{\cdot}6H_2O$ was taken in a 100 ml 3-neck flask and 15 ml of octadecene and 6 ml of oleic acid were added. The flask was then heated to 150 °C under vacuum and held at this temperature for 45 min to get a homogenous clear solution. The flask was cooled down to 70 °C and brought to atmospheric pressure by removing the vacuum. To this reaction mixture, the hexane dispersion of core NCs was added and stirred under a gentle flow of argon to remove the hexanes completely. Subsequently, the reaction mixture was further cooled down to 50 °C and 10 ml methanol solution containing NH_4F (4 mmol) and NaOH (2.5 mmol) was added dropwise. The resulting mixture was stirred for 30 min and heated slowly to 70 °C until all methanol had evaporated. The reaction vessel was then heated to 300 °C under a gentle argon flow and held at that temperature for 90 min. The flask was then cooled to room temperature and the NCs were precipitated and washed with ethanol. The isolated core-shell NCs were stored as ~1 wt% dispersion in toluene.

Ligand exchange of oleate-stabilized upconverting core-shell NCs. Oleate-stabilized upconverting NCs in toluene (0.2 ml) were taken in a 100 ml round bottom flask and diluted with 5 ml of 1:1 DMF/DCM. To this mixture, 75 mg of PVP-COOH (or PVP-NH_2) in 5 ml 1:1 DMF/DCM was slowly added and refluxed at 100 °C for 6 h. The reaction mixture was then added dropwise into ethyl ether (100 ml) to precipitate the polymer-stabilized UCNCs. The precipitate was then centrifuged and the collected polymer-stabilized UCNCs were dried under vacuum at 70 °C overnight. The dried particles were then dispersed in distilled water (5 ml) and excess polymer was removed

by centrifugation (12,000 rpm/~10,000 g for 10 min). The collected pellet was then redispersed in 5 ml of 0.001 N NaOH (PVP-COOH stabilized) or 0.001 N HCl (PVP-NH_2) and centrifuged. The final pellet was dispersed in 5 ml distilled water for further antibody labeling or stored as dry pellet for further conjugation with bi-functional molecules.

Derivatization of surface carboxylic acid groups on UCNCs with bi-functionalized molecules. *Functionalization with aminoethyl maleimide*. PVP-COOH functionalized UCNCs was dispersed in DMF (3 ml) and sonicated to get a clear dispersion. To this mixture, 0.1 M EDC (100 µl) was added and stirred for 20 min, followed by addition of a DMF solution (1 ml) of aminoethylmaleimide (5 mg). The solution was subsequently stirred at room temperature overnight and then centrifuged (12,000 rpm/~10,000 g, for 10 min). The obtained maleimide-functionalized UCNCs were dispersed in 3 ml DCM for further derivatization.

Functionalization with dimercaptosuccinic acid. To the maleimide-functionalized UCNCs in DCM (3 ml), DMSA (5 mg in 0.5 ml DMSO) was added along with triethylamine (2 µl) and the mixture was stirred at room temperature. The DMSA functionalized UCNCs were then centrifuged (12,000 rpm/~10,000 g, for 10 min) and dispersed in distilled water (5 ml). The dispersion was then finally filtered through a 0.2 µm sterile syringe filter and stored as such.

Conjugation of carboxylic acid functionalized UCNCs with anti-PSMA antibody. A solution of PVP-COOH stabilized UCNCs (300 µl of 1 mg/ml) was taken and diluted with distilled water to 1 ml. To this dispersion, 50 µl of 0.2 mg/ml EDC and 25 µl of 0.2 mg/ml NHS were added and the mixture was stirred at room temperature for 30 min. To

this reaction mixture, 200 µl of 0.1 mg/ml anti-PSMA antibody was added and continued stirring for 2 h. The anti-PSMA conjugated UCNCs were centrifuged and washed twice with water and dispersed in RPMI-1640 growth media (2 ml) supplemented with 10% fetal bovine serum (FBS).

Cell culture and immunolabeling of human prostate cancer cells with UCNCs. Human prostate cancer cells (LNCaP and PC3) were grown in tissue culture treated dish (100 × 20 mm^2) with 10% FBS supplemented RPMI-1640 growth medium. The cells were detached at 60- 70 % confluency and seeded on a 22 × 22 mm^2 sterilized glass coverslip placed in a six-well culture plate. The cells were allowed to grow for 2 days and then carefully washed multiple times with PBS. The cells were then incubated with PSMA-antibody conjugated UCNCs at 4 °C for 1 h. After incubation the cells were washed thoroughly with PBS and fixed with cold methanol (10 min) and dried. The coverslip was then inverted and mounted onto a glass slide for imaging.

Upconversion cell imaging by fluorescence microscopy. Imaging of the LNCaP and PC3 cells incubated with antibody conjugated UCNCs were done using a Leica DM 6000B microscope. A Leica 50X 0.5NA long working distance lens as objective was used to image the cells with the excitation at 980 nm using a JDS Uniphase laser diode coupled to a 105 µm core fiber. The power density was ~ 5 W/cm^2 in front of the lens. A Hamamatsu digital camera (C47420-80-12AG) was used to collect the green emission from the UCNCs. A band-pass filter (527/30 nm) from Leica was employed to filter the scattered excitation light. The nucleus of the cells was stained with 4',6-diamidino-2-pheylindole (DAPI) before imaging. Images of DAPI stained cells were obtained with a 40X 0.75NA Leica lens, with excitation (360/40 nm) and emission (470/40 nm) band

pass filters from Leica. The DAPI were obtained with 358 nm (UV) excitation and the blue emission was collected at 460 nm.

Characterization. Transmission electron microscopy (TEM) images were obtained from a JEOL JEM-1400 microscope operating at 80 kV. The UCNCs stabilized with oleate/PVP-COOH ligands were drop cast on a formvar carbon-coated grid (300 mesh Cu) and air-dried before imaging, size analysis of NCs from the images were obtained by measuring at least 100 particles and averaged. X-ray diffraction (XRD) patterns with a resolution of 0.05° (2θ) and a scan speed of 1 °/min, were collected using a Rigaku Miniflex diffractometer with a Cr source (Kα radiation, λ=2.2890 Å) operating at 30 kV and 15 mA. Zeta-potential analysis to determine the surface charge on the UCNCs were acquired using Zeta-PALS zeta-potential analyzer from Brookhaven Instruments Corp. equipped with a 15 mW solid-state laser (658 nm). Three runs of 30 cycles each were performed to determine the standard deviation of the measured zeta-potential values.

Chapter 5. Size-Tunable, Ultra-small $NaGdF_4$ Nanocrystals: Insights into their T_1 MRI Contrast Enhancement

(This chapter is reproduced with permission from Ref.[142] Copyright 2011 American Chemical Society)

5.1. Introduction

Nanomaterials show unique properties and are widely explored for a variety of applications.[143-146] Lanthanide-based nanomaterials have versatile utility in biological applications, as they can be made either as luminescent, magnetic, or as dual probe by selective doping of lanthanide ions.[147] In particular, paramagnetic Gd^{3+}-doped NCs show tremendous potential as contrast agents (CAs) for magnetic resonance imaging (MRI).[29,74] MRI is a powerful medical diagnostic tool, where the relaxation of water protons exposed to an external magnetic field is used to obtain morphological and anatomical information with unlimited tissue penetration and yet high spatial resolution.[16] CAs are used to improve the sensitivity, as they interact with the surrounding water protons and shorten their relaxation time to provide better contrast. Two types of CAs are clinically prevalent: i) paramagnetic Gd^{3+} chelates which affect the longitudinal relaxivity (r_1), and are termed positive (T_1) CAs as they enhance the contrast,[148] and ii) superparamagnetic iron oxide (SPIO) NPs, which affect transverse relaxivity (r_2), and are referred to as negative (T_2) CAs because they diminish the signal intensity at the region of interest.[74,81] T_1 contrast agents are preferred over the T_2 agents as their enhanced brightening effect can easily be used to differentiate the signal from other pathogenic or biological conditions.[74]

Gd^{3+} chelates that are used clinically have very low body circulation time because of their low molecular weight and therefore show limitations as molecular probes for long-term tracking.[29] They also provide very low local contrast as each chelate has only one Gd^{3+} ion. To increase the local contrast and relaxivity, second generation agents have been developed by covalently anchoring Gd^{3+} chelates to different nanostructure frameworks,[78] or bundling multiple Gd^{3+} chelates together using polymers, dendrimers, liposomes, and viral capsids.[149] These structures have been shown to have high relaxivity and increased local contrast as multiple Gd^{3+} ions are coupled to a single nanostructure. The main disadvantage of this class of agents concerns with their functionalization, which is tedious (multistep reactions), expensive, and the number of ions that can be loaded to a nanostructure is further limited by the number of anchoring sites available. Moreover, some of these aggregates are too large to be clinically useful.[29,74] Recently, inorganic Gd^{3+}-doped NCs have been explored as a new class of T_1 CAs partly because of their ease of synthesis, smaller size, and potential for improvement in contrast over currently used Gd^{3+} chelates. Other distinct advantages of this class of CAs are i) dramatic increase in the local gadolinium ion concentration at the region of interest, ii) ease of functionalization without compromising Gd^{3+} binding, iii) increased tumbling time and consequent improvement in relaxivities, and iv) control of targeting and clearance through their size.

Synthesis of inorganic Gd^{3+}-based NCs generally follows one of two protocols: i) direct nanoprecipitation in water or polyol using a stabilizing agent which allows for crystal growth, followed by extraction and exchange with a more robust stabilizing agent;[82,83,85,150-152] ii) preparation of hydrophobic NCs in high-boiling organic solvents

and subsequent transfer of the NCs into water using a hydrophilic ligand to render them water-soluble.[87,88,153-155] While the first approach is simpler and direct, synthetic methods employing high-boiling organic solvents yield improved size control and uniformity.[156,157] Several studies have shown that the particle size is directly related to biodistribution, clearance rate,[158-160] and MRI contrast capabilities.[83] This fact imposes a restriction on the permissible polydispersity of the NCs used as CAs, if control over the aforementioned parameters is desired. Hence, NCs developed as CAs for clinical use are required to be highly monodisperse.

Inorganic Gd^{3+}-based NCs such as GdF_3,[82] Gd_2O_3[83,150-152] and $GdPO_4$[84], have shown 2-3 fold higher ionic relaxivity (*i.e.* per Gd^{3+} ion) than clinical complexes. These NCs are synthesized in water or polyol solutions with poor size control, which limits their suitability for clinical usage. Moreover, there are differing views on the individual contributions of the core,[82,83] and surface Gd^{3+} ions[151] to the observed relaxivity enhancement and a systematic study is required to resolve the issue. These concerns were clearly articulated in reviews by Hyeon *et al.* who stated, "uniformly sized nanoparticles of gadolinium or related lanthanide compounds have not yet been demonstrated"[74] and "the synthesis of most materials has not been fully optimized yet, and the contrasting mechanisms of many of these materials still remains unclear".[29] Moreover, previous efforts to understand the contrasting mechanism utilized polydisperse NCs synthesized in polyol/water medium from different synthetic methods, and the relaxivity measured at different magnetic field strengths were compared.[151] Such factors are known to affect the observed relaxivity and do not allow for a complete understanding of the relaxivity

enhancement. Although such studies are informative, they provide only circumstantial evidence rather than a direct one for the enhancement factor.

Theoretically, NCs of sizes below 10 nm show a dramatic increase in the ratio of surface to core ions with decrease in size. Therefore, particles in this size regime are ideal for gaining insights into their relaxivity enhancement. NCs used for such study should also be uniform in size, shape, and phase (crystal structure) as these parameters can impact the observed relaxivity. However, there are no known reported procedures for size-tunable synthesis of lanthanide NCs meeting all these criteria below 10 nm. In this chapter the synthesis of monodisperse $NaGdF_4$ NCs of sizes between 2.5 – 8.0 nm by optimizing the reaction parameters associated with both the nucleation and growth phases in a high-boiling binary solvent mixture is described followed by a detailed analysis and insights into the parameters affecting the T_1 MRI contrast enhancement.

5.2. Results and Discussion

5.2.1. Size-tunable, ultra-small β-$NaGdF_4$ nanocrystals

Attempts to prepare β-$NaGdF_4$ NCs by following the synthetic protocol used for β-$NaYF_4$ NCs[42] yields particles that show both size and shape dispersity (Figure C1 of the Appendix). The growth mechanism of β-$NaGdF_4$ NCs in oleic acid and octadecene significantly differs from that of β-$NaYF_4$.[39,42-44] It is clearly evident that Ostwald ripening of NCs dominates when gadolinium salts are used instead of yttrium salts, following the $NaYF_4$ synthesis protocol. In order to tune the NC size and restrict Ostwald ripening, modified protocols to synthesize uniform β-$NaGdF_4$ have been described previously.[41,50,161,162] These protocols give access to NC sizes above 10 nm, and this

section discusses the parameters to obtain β-$NaGdF_4$ NCs below 10 nm with high size tunability and uniformity. There are no known reports for such β-$NaLnF_4$ NC synthesis.

Based on the LaMer nucleation-growth model, the growth of uniform NCs is mainly governed by a temporally discrete nucleation stage and followed by a controlled slow growth of the existing nuclei.[8] During NC growth, if the growth phase is fast or the nucleation stage is delayed (*i.e.* if nucleation and growth phases overlap), the resulting NCs are polydisperse and control over their size is hard to achieve. In a previous detailed study on the growth of $NaLnF_4$ NCs it has been shown that Ostwald ripening is dominant in the case of $NaGdF_4$ in oleic acid & octadecene binary solvent mixtures and that the energy barrier between the nucleation and growth stages is relatively low.[39] This clearly shows that the nucleation and growth phase are highly overlapped in Gd^{3+}-based reactions. To tune the synthesis to obtain uniform Gd^{3+}-based NCs with controllable sizes, the separation of these two phases in the reaction should be an important criteria.

The process of nucleation is strongly dependent on the concentration of stabilizing agent (*i.e.* oleic acid) which is related inversely to the number of nuclei formed. It has been suggested that, when a large excess of oleic acid is present, fewer nuclei are formed and these nuclei grow very rapidly and indiscriminately leading to polydisperse NCs.[163,164] As $NaGdF_4$ NCs are known to grow faster,[39] the critical step should be to control the nucleation stage and enable enough nuclei formation to suppress the indiscriminate growth. Following this hypothesis, the concentration of oleic acid was systematically reduced to control nucleation with a simultaneous reduction of the reaction temperature to control the growth of those existing nuclei. Thus, when the ratio of oleic acid to gadolinium salt was decreased from 19:1 to 13:1, at a decreased reaction

temperature of 270 ºC (300 ºC is used for $NaYF_4$ synthesis), highly uniform NCs of 4.0 ± 0.3 nm were obtained. Increasing the number of nuclei formed during the nucleation stage results in increased number of NCs growing at the same time, directly resulting in the decrease of the average NC size. Transmission Electron Micrograph (TEM) of these NCs (Figure 5.1), indicates that the size distribution is excellent leading to the self-assembly of these NCs into hexagonal close-packed structure on the carbon-coated copper grid. The presence of oleate ligands on the NC surface leads to an average ~2.5 nm interparticle distance.

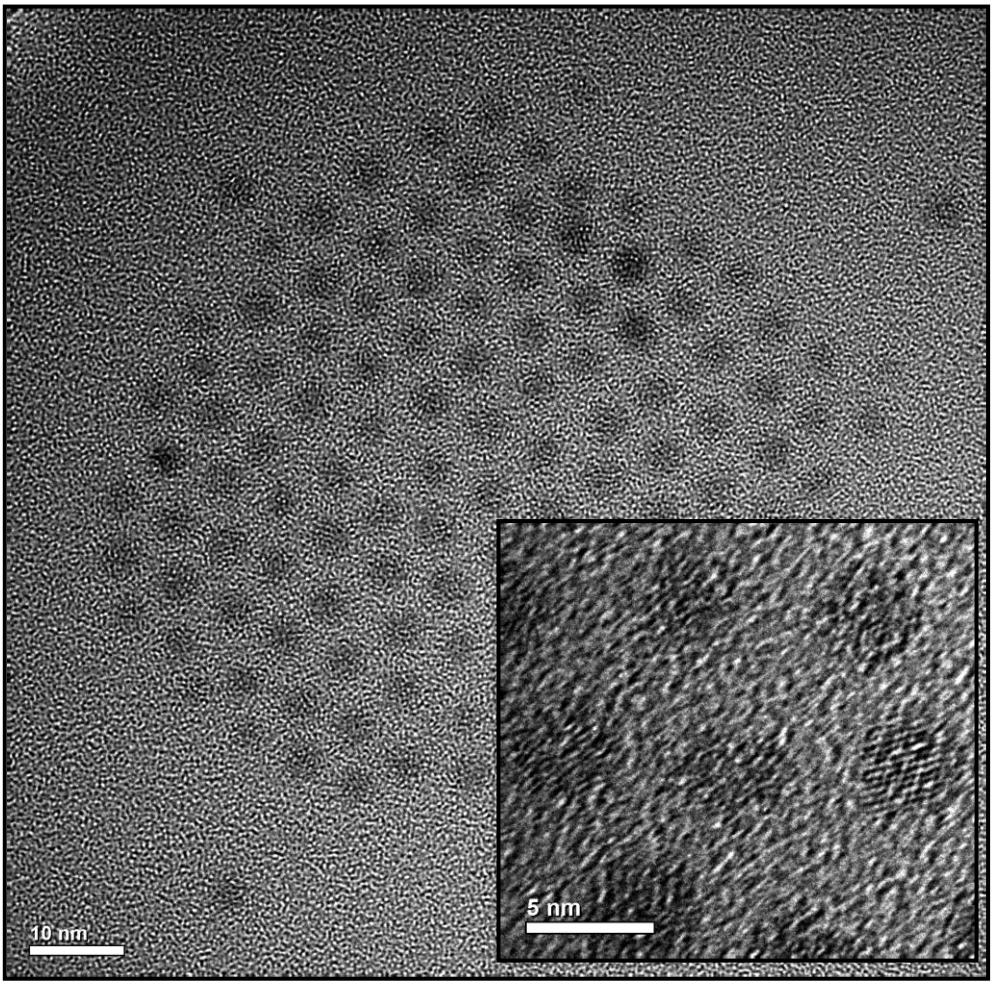

Figure 5.1. TEM image of 4.0± 0.3 nm oleate-stabilized $NaGdF_4$ NCs, *inset* shows the respective HR-TEM image.

By tuning the growth rate further, it was possible to achieve reproducibly monodisperse $NaGdF_4$ NCs, of four sizes *viz*., 2.5 ± 0.3, 4.0 ± 0.3, 6.5 ± 0.5, 8.0 ± 0.5 (Figure 5.2A-D and Figure C2 of the Appendix). The size of the NCs can precisely be controlled by careful choice of the reaction time and temperature and these parameters are tabulated in Table 5-1. Powder X-ray Diffraction (XRD) spectra of the NCs indicates that all the NCs are highly crystalline hexagonal phase $NaGdF_4$. There is a regular, consistent broadening of the XRD peaks with decrease in NC size (Figure 5.2E). The NC sizes calculated from the XRD peak widths using the Scherrer equation agree well with the sizes determined from TEM analysis. High-Resolution TEM (HR-TEM) shown in Figure 5.3, further confirms the crystalline nature of the NCs.

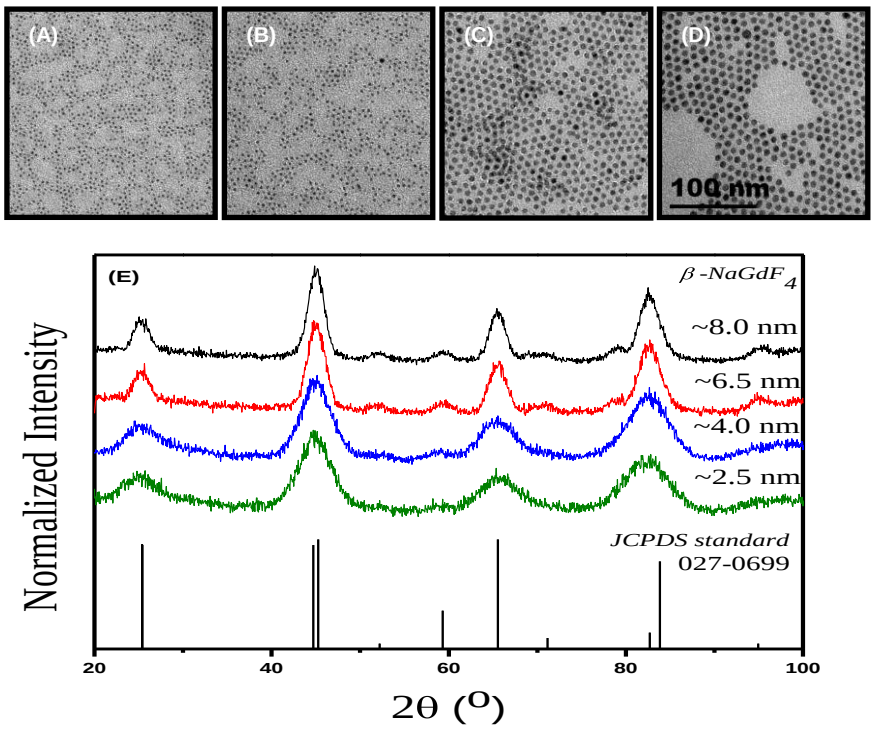

Figure 5.2. TEM images of oleate-stabilized $NaGdF_4$ NCs **(A-D)** of sizes 2.5, 4.0, 6.5, and 8.0 nm respectively (Scale bar is the same for all images), and **(E)** Powder X-ray diffraction pattern of the NCs (sizes are average numbers from TEM) overlaid with the reference pattern.

Table 5-1. Parameters for controlling the growth phase and the size distribution of NCs obtained from TEM & XRD analysis.

Temperature (°C)	Time (min)	TEM size (nm)	XRD size (nm)
260	10	2.5 ± 0.3	2.6 ± 0.2
270	40	4.0 ± 0.3	3.8 ± 0.2
280	90	6.5 ± 0.5	7.2 ± 0.2
285	100	8.0 ± 0.5	8.1 ± 0.2

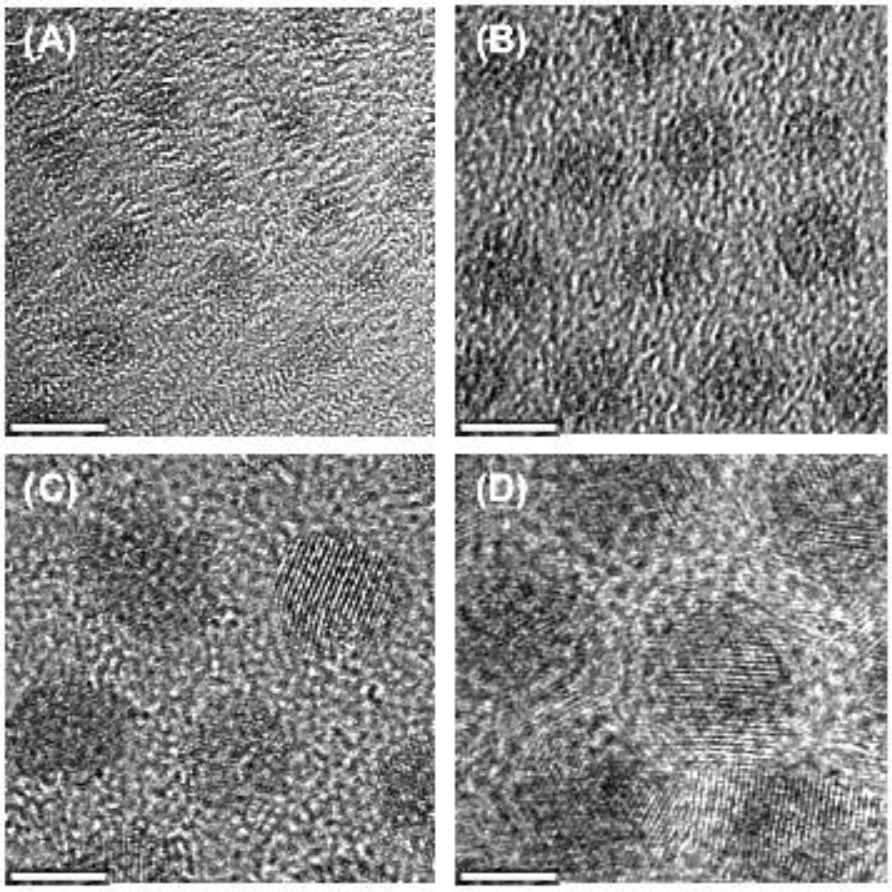

Figure 5.3. HR-TEM images of oleate-stabilized $NaGdF_4$ NCs **(A-D)** of sizes 2.5, 4.0, 6.5, and 8.0 nm respectively. Scale bar in all images is equal to 5 nm.

The synthesis outlined here using a simple modification in reaction conditions not only allows for tunable NCs below 10 nm, but also yields the thermodynamically stable crystal structure (β-phase). This is in stark contrast to previous claims that such stable structures (β-phase) can only be synthesized above 10 nm.[39] There are no known reported procedures to make NCs below 10 nm for this crystal phase and this synthetic protocol allows for access to these size ranges with size-tunability down to 2.5 nm.

5.2.2. Surface modification of β-$NaGdF_4$ nanocrystals

The synthesized oleate-stabilized $NaGdF_4$ NCs were transferred from toluene to water by exchanging the oleate ligands with polyvinylpyrrolidone (PVP-10), following the exchange protocol described in Chapter 3 of this dissertation.[89] PVP is an ideal colloidal stabilizer for NC based CAs due to its high biocompatibility, non-toxicity, longer blood circulation times, and low accumulation in vital organs.[71,117] TEM and dynamic light scattering (DLS) analysis were performed to confirm that the NCs had maintained their morphology and were not aggregated in water after exchange with PVP. The TEM images (Figure C3 of the Appendix) show random distribution of individual NCs without any long-range ordering typically observed for the oleate-coated NCs. This is consistent with the fact that the oleates on the NC surface have been replaced with random coils of PVP. The hydrodynamic diameter measured by DLS (Figure 5.4) was between 10 – 17 nm for the four different core sizes with a low polydispersity in all cases. Considering PVP-10 with a hydrodynamic size of ~4 nm in water,[118] the observed DLS data further confirms that the NCs are coated with random coils of PVP chains.

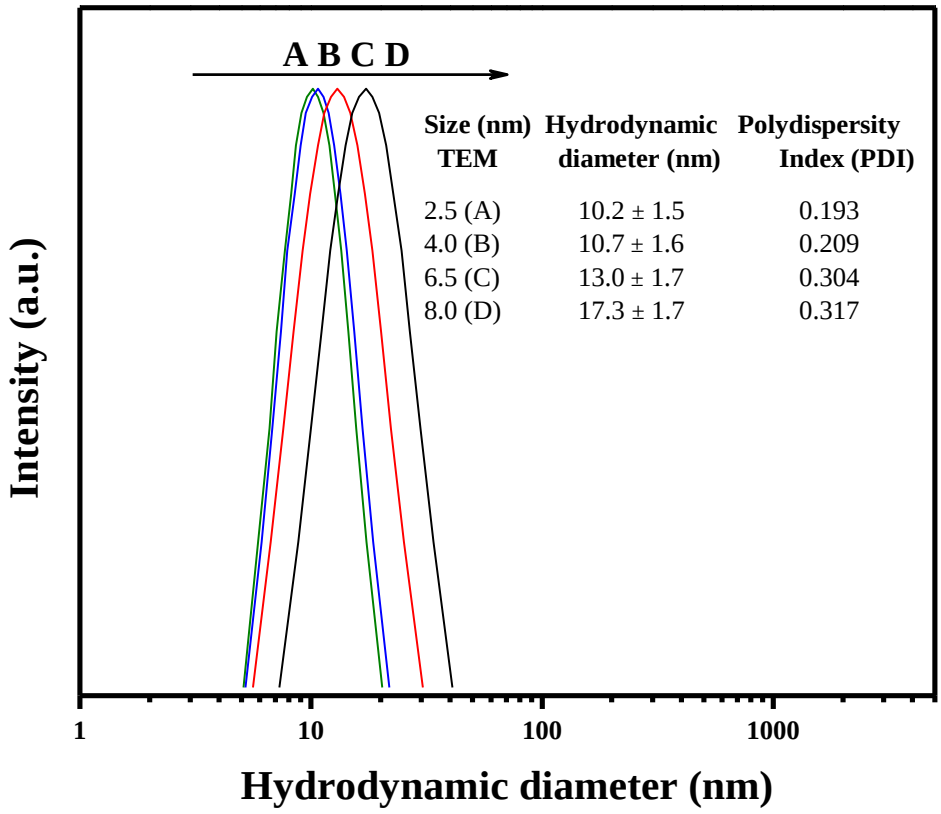

Figure 5.4. Dynamic Light Scattering (DLS) data showing the hydrodynamic diameter and polydispersity index for the phase-transferred $NaGdF_4$ NCs in water.

5.2.3. Size dependent T_1 relaxivity of $NaGdF_4$ nanocrystals

The concentration dependent T_1 relaxation of water protons at 1.5 T was determined for the aqueous dispersions of the four sizes of NCs prepared. To evaluate the ionic relaxivities, the gadolinium ion concentration of the NC dispersions was determined using ICP-MS, after digesting the NCs in concentrated nitric acid. The ionic relaxivity (r_1) (*i.e.* per Gd^{3+} ion concentration), was obtained from the slope of the linear regression fit from the relaxivity plots shown in Figure 5.5 and the values are tabulated in Table 5-2.

The increase in slope corresponds to enhancement of T_1 ionic relaxivity. Ionic relaxivities increase dramatically with decreasing NC size from a value of 3.0 $mM^{-1}s^{-1}$ for the 8.0 nm NCs to 7.2 $mM^{-1}s^{-1}$ for the smallest, *i.e.* 2.5 nm, NCs. The clinical standard Gd-DTPA (Magnevist®) has an ionic relaxivity of 3.7 $mM^{-1}s^{-1}$ at 1.5 T.[16] While the ionic relaxivity for the larger 6.5 and 8.0 nm NCs are on par with the clinical CA, it is almost twice for the smallest NCs. The relaxivity based on the mass concentration of NCs (r_1/M), concentration of NCs or contrast agent (r_1/NC) and unit surface area of NC (r_1/SA) were calculated from the ionic relaxivity ($r_1/[Gd^{3+}]$) (Table 5-2, Appendix C for calculation), to further analyze the observed enhancement of ionic relaxivity with decrease in NC size.

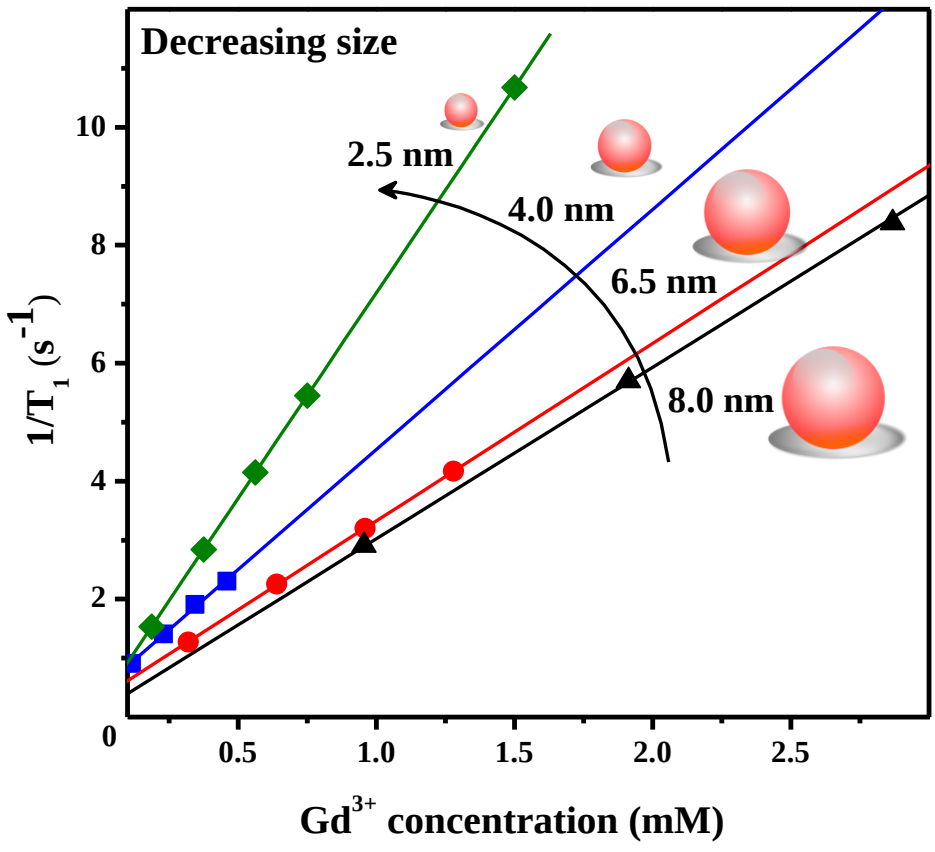

Figure 5.5. T_1 ionic relaxivity plot for $NaGdF_4$ NCs of different sizes in water (1.5 T) (where T_1 is the longitudinal relaxation time of water protons).

Table 5-2. Size dependent relaxivity data for $NaGdF_4$ NCs at 1.5 T.

Size (nm)	Ionic Relaxivity $r_1/[Gd^{3+}]$ $(mM^{-1}s^{-1})$	Mass Relaxivity r_1/M $(mg/ml)^{-1}s^{-1}$	Nanocrystal Relaxivity r_1/NC $(mM^{-1}s^{-1})$	Surface Area Relaxivity r_1/SA (ms^{-1})
2.5	7.2 ± 0.2	28	770	65
4.0	4.5 ± 0.2	18	2,100	69
6.5	3.3 ± 0.2	13	6,200	79
8.0	3.0 ± 0.2	12	11,000	88

The r_1/NC values correspond to per CA relaxivity and the relaxivity increases from 770 $mM^{-1}s^{-1}$ for the 2.5 nm particle to 11,000 $mM^{-1}s^{-1}$ for the 8.0 nm particles. As the total number of gadolinium ions is higher in larger particles, the r_1/NC values increase with size. Clinical complexes typically contain one Gd^{3+} ion per CA and their unit CA relaxivity is the same as their ionic relaxivity. Thus the relaxivity offered by each $NaGdF_4$ NCs described here is about 200 – 3,000 times than that of clinical agents. This allows for enhanced local contrast while using NC based CAs, which would be highly beneficial for targeted imaging. Moreover, bundling of multiple gadolinium ions in a crystalline NC affords rigid binding of the ions and leaching of gadolinium ions from the materials is less likely if they are stabilized with a protective ligand. ICP-MS analysis of the bulk water after dialysis of the NCs showed no appreciable amount of free gadolinium ions in solution, indicating that no leaching of ions from the NC occurred. The detection limit of the analysis for gadolinium ion concentration was about 1.5 ng/l (~10 pM). Thus these NCs are good scaffolds for integrating multiple gadolinium ions without compromising on the Gd^{3+} binding.

The ability of contrast agents to be used as positive T_1 agents is governed by the ratio of their transverse relaxivity (r_2) to longitudinal relaxivity (r_1), and low r_2/r_1 ratios are considered to be ideal. The r_2/r_1 ratio for the smallest 2.5 nm NCs was ~3.2 (Figure C4 of the Appendix). Moreover, the relaxivity values for these ultra-small NCs are much higher than the reported r_1 values of uniformly synthesized Gd^{3+}-based NCs developed to date as summarized in Table 5-3. It should be noted that a fairly long chain polymer (10,000 g/mol) was used for this study and a careful screening of ligands with shorter length to enhance water access to the surface ions may yield much better values for these NCs.

Table 5-3. Comparison of ionic relaxivity (r_1) values of uniformly synthesized Gd^{3+}-based NCs.

Nanocrystals	Size (nm)	Surface coating	r_1 ($mM^{-1}s^{-1}$)	field (T)
β-$NaGdF_4$	2.5	PVP[142]	7.2	1.5
α-$NaGdF_4$:Yb^{3+}:Er^{3+} /$NaGdF_4$ core/shell	20	PEG-phospholipid[88]	1.40	1.5
α-$NaGdF_4$:Yb^{3+}:Er^{3+} /$NaGdF_4$ core/shell	41	PEG-phospholipid[88]	1.05	1.5
β-$NaGdF_4$:Yb^{3+}:Er^{3+}	10	Octylamine-PAA[87]	0.99	4.7
β-$NaGdF_4$:Yb^{3+}:Er^{3+}	40	Octylamine-PAA[87]	0.47	4.7
β-$NaYF_4$:Yb^{3+}:Er^{3+}/ $NaGdF_4$ core/shell	28	Silica[155]	0.48	3.0
Gd_2O_3 Yb^{3+}/Er^{3+} nanorods	2.5×18.0	Silane[154]	1.5	9.4

5.2.4. Analysis of T_1 relaxivity enhancement

The fraction of surface ions increases relative to the core ions with decreasing NC size, and there is a striking similarity in the dependence of NC S/V ratio and ionic relaxivity values with NC size (Figure 5.6A-B). This signifies that the gadolinium ions on the

surface are the major contributors towards the relaxation of water protons and gadolinium ions in the NC core do not show any significant effect towards relaxivity enhancement. To make sure this is indeed the case and to determine the extent to which gadolinium ions on the surface of different sized NCs affect the relaxivity, the relaxivity per NC or contrast agent (r_1/NC), and the relaxivity per unit surface area of the NCs (r_1/SA) were analyzed (Figure 5.6C-D respectively). When the r_1/NC values are compared between the 2.5 and 8.0 nm NCs, the 8.0 nm NCs show a 14-fold relaxivity enhancement (770 → 11,000 $mM^{-1}s^{-1}$) while the surface area increases by only 10-fold (20 → 200 nm^2). If surface ions on the NCs were contributing evenly towards the relaxivity enhancement, the increase in r_1/NC values should have a linear dependence with increase in NC surface area. This deviation is further substantiated by the relaxivity per unit surface area of the NCs (r_1/SA). If the gadolinium ions on the surface are the only contributors and affect the relaxivity uniformly, the r_1/SA should have remained the same regardless of NC size (*i.e.* a straight line relative to the size (x-axis) in Figure 5.6D). The r_1/SA values show an increasing trend with increase in NC size. In short, the surface gadolinium ions on a bigger NC affect the relaxivity more strongly than the surface gadolinium ions on a smaller NC.

These observations are comparable with results reported by Hyeon *et al*. on uniformly synthesized 20 nm and 41 nm α-$NaGdF_4$ NCs, which show a similar deviation in relaxivity values.[88] While the NC S/V ratio decreases by ~50% from 20 nm to the 41 nm particles, the relaxivity values drop only by ~25% (1.40 $mM^{-1}s^{-1}$ and 1.05 $mM^{-1}s^{-1}$ for 20 and 41 nm particles, respectively). These observations suggest that other parameters play

a role, even though less significant than the increase in S/V ratio. To account for this deviation other known factors which affect the T_1 relaxivity are analyzed.

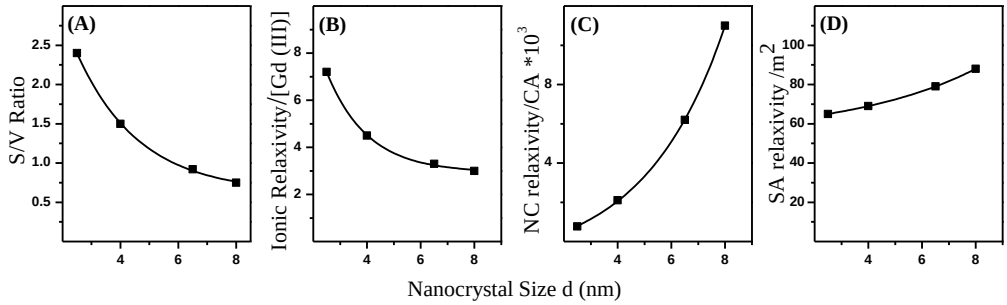

Figure 5.6. NC size-dependent plots of **(A)** surface to volume ratio, **(B)** ionic relaxivity, **(C)** per nanoparticle relaxivity, and **(D)** relaxivity per m^2 surface area.

The ability of a contrast agent to affect the relaxation of water protons can be classified into inner sphere (IS), secondary sphere (SS) and outer sphere (OS) contributions.[165] These individual contributions add up to the observed relaxivity, equation (1).

$$r_1^{obs} = r_1^{IS} + r_1^{SS} + r_1^{OS} \quad (1)$$

The second and outer sphere contributions are mainly from the relaxation of water molecules hydrogen-bonded to the ligands and their exchange with bulk water. The ligand employed in this study for all the NCs are the same and hence their outer sphere effects may be considered to be similar. So, any difference in contribution from the outer shell may be neglected, and such assumptions have been used previously for similar Gd^{3+}-complexes to understand the factors determining relaxivity enhancement.[166] The

inner sphere contributions is dependent on the residence time of bound water (τ_M), the electron paramagnetic relaxation (T_{1e} and T_{2e}) and the molecular reorientation or the tumbling time of the contrast agent (τ_R). The first two factors τ_M, T_{1e} and T_{2e} are frequency dependent and their contributions are insignificant at low field strengths (0.5 – 1.5 T).[16,76] The main contribution for the relaxivity at low field strengths is therefore the tumbling time of the CA and the second generation CAs were developed based on this basic concept by anchoring the Gd^{3+}-complexes to more slowly tumbling nanostructures. In short, more slowly tumbling CAs enhance the relaxivity of water molecules and at clinically relevant field strengths, tumbling times in the nanosecond time scale are said to be ideal.[77-79]

The tumbling time (τ_R) of spherical CAs can be deduced from the classical Debye-Stokes equation[77] (calculation details in Appendix C). The tumbling time of the NCs were calculated from the hydrodynamic radius determined by DLS and were found to be ~139, 161, 288, and 678 ns for 2.5, 4.0, 6.5, and 8.0 nm NCs, respectively. Evidently, bigger NCs have longer tumbling times (τ_R), *i.e.* surface ions on bigger NCs tumble more slowly than on the smaller NCs. This fact accounts for the increase in r_1/SA values with increase in NC size. Gd^{3+}-complexes coupled to different sizes of gold NCs have shown this effect,[167] and surface gadolinium ions on inorganic NCs can be visualized to be similar to one such structure.

To summarize, i) relaxivity enhancement shows a clear dependence on S/V ratio, *i.e.* the increase in surface gadolinium ions relative to the core ions as the NC size decreases. Hence smaller NCs show high ionic relaxivity values relative to the larger NCs, ii) the increase in tumbling time (τ_R) with NC size increase, counteracts the effect of S/V ratio

and makes the surface ions on a larger NC to affect the relaxivity more strongly than the ions on a smaller NC.

The enhancement of ionic relaxivity for the 2.5 nm NCs over clinical complexes can be attributed to the difference in their tumbling times. The clinical complexes tumble on a picosecond time scale (Gd-DTPA ~54 ps),[168] while the 2.5 nm NCs tumble on a nanosecond time scale (~139 ns). These findings, based on uniformly synthesized NCs, show that the previous suggestions of core gadolinium ions cooperatively enhancing the relaxivity,[82,83] and cooperative effect of surface gadolinium ions,[151] are not the main factors affecting the relaxivity. There is a clear relaxivity enhancement with the increase in the number of surface ions relative to core ions as the NC size decreases and any contributions from core ions may be disregarded. The cooperative effect of surface gadolinium ions is also not a major factor, as for a given unit surface area of NC the relaxivity values should have remained the same irrespective of their size.

5.2.5. Upconverting $NaGdF_4$ core-shell nanocrystals

The synthesis of $NaGdF_4$ NCs presented here yields thermodynamically stable hexagonal crystal phase, one of the best known matrix for upconversion emission to date.[100] Nanoparticles below ~10 nm are reported to have efficient body clearance[169] and previously reported sub-10 nm upconverting $NaLnF_4$ NCs were of α-phase (kinetic product),[170-172] and upconversion emission in this phase is an order of magnitude less than the β-phase. Using this synthetic route, β-$NaGdF_4$ NCs doped with Yb^{3+} and Tm^{3+} ions with a size of ~3.5 nm were synthesized, and the dopants did not hinder the formation of ultra-small particles. When excited with a 980 nm diode laser, these NCs exhibit near-infrared (NIR) upconversion emission at 800 nm. Both the excitation and the

emission peaks fall in the biological window, where biological tissues scatter the least, allowing for enhanced penetration depth. An undoped $NaGdF_4$ shell was grown on these upconverting NCs to enhance their emission efficiency and this resulted in the increase of NC size to ~ 6 nm (Figure 5.7 and Figure C5 of the Appendix). The emission intensity of the core-shell NCs, increased ten-fold as compared to the core NCs (Figure 5.7) consistent with other published works.[52,101,162]

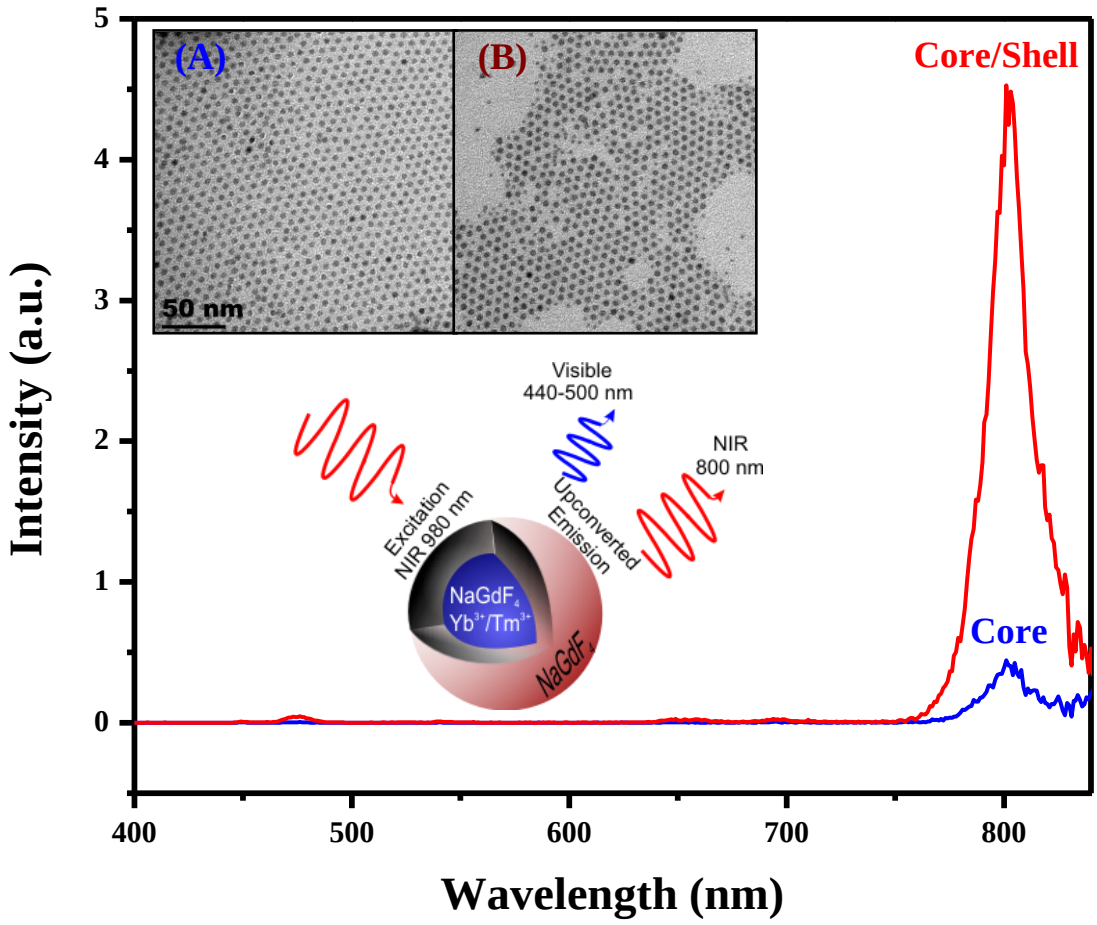

Figure 5.7. Upconversion emission spectra of $NaGdF_4$ Yb^{3+} (24%) /Tm^{3+} (1%) core and $NaGdF_4$ Yb^{3+} (24%) /Tm^{3+} (1%) core / undoped $NaGdF_4$ shell NCs in toluene excited with a 980 nm laser diode at 150 Wcm^{-2} (*Inset*: **(A)** TEM images of core, and **(B)** core-shell NCs, Scale bar is same for both images).

5.3. Conclusions

A simple size-selective synthesis of paramagnetic $NaGdF_4$ NCs of four sizes between 2.5 – 8.0 nm applicable as MRI T_1 contrast agents was developed. These NCs are the first evidence of size tuned synthesis of uniform lanthanide-based NCs below 10 nm. This was accomplished by controlling the NC growth dynamics, such as the nucleation and growth rate. The amount of the coordinating ligand used in the synthesis was reduced to have increased nucleation and then the growth stage was controlled by carefully altering the reaction time and temperature. These NCs show effective shortening of water protons T_1 relaxation time, depending on their sizes, with the smallest 2.5 nm particles showing higher relaxivities compared to clinical Gd^{3+}-complexes. Correlations based on NC sizes and their relaxation rates show that the contributions from surface to volume (S/V) ratio decrease with increasing NC size, while contributions from rotational correlation time (τ_R) increase with increasing size, with the S/V ratio being the dominant factor. The relaxivity offered by these NCs can be improved through judicious approaches such as confining in nanoporous structures,[168] controlled aggregation,[173] and tuning the surface ligands to allow enhanced water access, which will help to realize the true potential of these size-tunable NCs.

These NCs can be extended as a potential bi-modal probe (upconverting and paramagnetic) without compromising on their ultra-small size. However the upconversion emission from these NCs because of their small size is predominantly lower than the larger NCs discussed in chapters 3 and 4. It is evident that for upconversion larger NCs with minimal S/V ratio are ideal, while for T_1 relaxivity enhancement smaller NCs with larger S/V ratio is ideal. Moreover, as only the surface

Gd^{3+} ions account for relaxivity enhancement, a modified core-shell structure with a gadolinium free upconverting core coated with a thin shell (~ 1 monolayer) of gadolinium rich surface should be ideal to realize an efficient bi-modal structure. To achieve such precise manipulation of shell growth in nanometer precision, a unique technique utilizing a fundamental colloidal phenomenon of ripening is discussed in Chapter 6.

5.4. Experimental Section

Materials. All chemicals were from Sigma-Aldrich except sodium hydroxide, dichloromethane (DCM) from ACP chemicals, ethyl ether (anhydrous), dimethylformamide (DMF), and toluene from Caledon laboratories. .

Synthesis of ultra-small β-$NaGdF_4$ NCs. Gadolinium chloride hexahydrate (1 mmol), oleic acid (4 ml) and octadecene (15 ml) were mixed together and heated to 140 °C under vacuum until a clear solution formed, after which the solution was cooled to room temperature. A solution of NaOH (2.5 mmol) and ammonium fluoride (4 mmol) in methanol (10 ml) was added dropwise to this and the mixture stirred overnight (~15 hrs). The reaction mixture was then heated at 70 °C to remove the methanol and placed under a gentle argon flow. Afterwards the solution was heated rapidly to the desired temperature (~10 °C/minute) and maintained for a constant time depending on the desired NC size. Subsequently, the solution was cooled to room temperature and the NCs were precipitated using ethanol, centrifuged (4,500 rpm, Beckman Coulter Spinchron 15 - rotor F0630) and washed twice with ethanol. The NCs were finally dispersed in 5 ml toluene centrifuged and the supernatant was stored. (No modifications in purification steps were made for the synthesis described below).

Synthesis of β-$NaYF_4$ and β-$NaGdF_4$ NCs. Yttrium chloride hexahydrate (1 mmol) for β-$NaYF_4$ synthesis, or gadolinium chloride hexahydrate (1 mmol) for β-$NaGdF_4$, was mixed with 6 ml oleic acid and 15 ml octadecene. Other reagents and reaction conditions were same as explained above except that the reaction mixture was heated to 300 °C for 90 minutes. The NCs were precipitated, washed and stored in 5 ml toluene.

Synthesis of upconverting core-shell β-$NaGdF_4$ NCs. Gadolinium chloride hexahydrate (0.75 mmol), ytterbium chloride hexahydrate (0.24 mmol), and thulium chloride hexahydrate (0.01 mmol) were mixed with oleic acid (4 ml) and octadecene (15 ml) and heated to 140 °C under vacuum until a clear solution was formed, after which the clear solution was cooled to room temperature. To this, a solution of NaOH (2.5 mmol) and ammonium fluoride (4 mmol) in methanol (10 ml) was added and the mixture was stirred overnight (~15 hrs). The reaction mixture was then heated at 70 °C to remove the methanol and then placed under a gentle argon flow. Subsequently, the solution was heated to 270 °C (~10 °C/minute) and maintained at this temperature for 45 minutes. After this, the solution was cooled down to room temperature and the core NCs were precipitated and washed with ethanol before storing in 5 ml cyclohexane. For the shell synthesis, gadolinium chloride hexahydrate (1 mmol), oleic acid (8 ml) and octadecene (15 ml) were mixed together and heated to 140 °C under vacuum until a clear solution formed, after which the clear solution was cooled to 80 °C. The cyclohexane dispersion of core NCs was injected and cyclohexane removed under continuous stirring. Subsequently, the solution was cooled to 50 °C and NaOH (2.5 mmol) and ammonium fluoride (4 mmol) in methanol (10 ml) were added and stirred for 2 hrs, followed by removing the methanol at 70 °C and the reaction mixture placed under a gentle argon

flow. The temperature was raised to 270 °C (~10 °C/minute) and maintained for 30 minutes. Subsequently, the solution was cooled down to room temperature and the NCs precipitated and washed with ethanol before dispersing in 5 ml toluene.

Phase transfer of hydrophobic NCs to water. Oleate ligands on the NCs were exchanged with polyvinylpyrrolidone (PVP-10) (M.Wt. 10,000 g/mol) in a dichloromethane and dimethylformamide solvent mixture. The amount of polymer for exchange was based on the NC size and calculated such that there were ~60 PVP molecules per square nm surface (calculation details in Appendix C). After the exchange, the NCs coated with PVP-10 were dispersed in distilled water and dialyzed (Dialysis Membrane 25,000 MWCO, Spectrum labs) against water for 6 hrs. The water was changed every 2 hrs. The water from the dialyzed dispersion of NCs was removed by rotary evaporation (40 °C, P_{max} 8 mbar) and the NCs were then re-dispersed in fresh deionized water for relaxivity measurements. .

TEM images of the NCs were obtained after drop casting on a formvar carbon-coated grid (300mesh Cu), and air dried before imaged. Low resolution TEM images were obtained from a Hitachi H-7000 microscope operating at 75 kV and a JEOL JEM-1400 microscope operating at 80 kV. High Resolution (HR-TEM) images were from FEI Tecnai Field Emission Scanning Transmission Electron Microscope at 200 kV. The size distribution was obtained from averaging a minimum of 50 NCs.

X-ray diffraction (XRD) patterns of the NCs were collected with a resolution of 0.05° (2θ) and a scan speed of 1°/min, using a Rigaku Miniflex diffractometer with a Cr source (K_α λ = 2.2890 Å) operating at 30 kV and 15 mA. The average NC size was determined

using Scherrer equation for the single peaks at ~25° (*2θ*) and ~65° (*2θ*), the deviation in calculated crystallite size was less that ± 0.2 nm for all cases.

Dynamic Light Scattering (DLS) measurements were done using Brookhaven Zeta PALS instrument with 90Plus/BI-MAS Multi Angle Particle Sizing option, equipped with a 15 mW solid state laser (658 nm). All data were obtained at a single scattering angle (90°) and averaged over five scans.

Inductively Coupled Plasma Mass Spectroscopy (ICP-MS) analysis was carried out using a Thermo X-Series II (X7) quadrupole ICP-MS to determine the Gd^{3+} ion concentration on the NC stock solution used for relaxivity measurements. The water dispersion of NCs were digested in concentrated nitric acid at 135 °C in sealed Teflon vials for 3 days and diluted with ultrapure water before analysis. Calibration was done by analyzing serial dilutions of a mixed element synthetic standard containing known amount of gadolinium. Each sample, standard and blank, were spiked with indium (to a concentration of about 7 ppb) as the internal standard to correct for signal drift and matrix effects. Accuracy was confirmed by analysis of a standard reference material (SLRS-4).

Magnetic Resonance (MR) T_1 relaxation measurements at 1.5 T were performed using a clinical MRI scanner (GE Signa, GE Medical Systems, Milwaukee, WI) and a standard inversion recovery spin echo sequence, with a repetition time (TR) of 4000 ms, an echo time (TE) of 9 ms, and seven inversion recovery times, (TI = 50, 104, 215, 444, 921, 1907 and 3950 ms); the field of view was 12 × 6 cm^2, and image plane was 128 × 128 with a slice thickness of 5 mm allowing simultaneous imaging of up to 50 vials (1.5 ml). The regions of interest were then drawn for each of the vials at TI = 3950 ms, and the signal containing an average of 20 voxels for each TI was evaluated. The signal-to-noise

ratio was ~200. The deviation was 1% on the measured relaxation times and the best linear fit was used to determine the relaxivity from the concentration dependent plot measured at four different concentrations. The error in the relaxivity values was estimated from the deviations in the linear fit.

Optical measurements were carried out using an Edinburgh instruments FLS920 fluorimeter with a 980 nm laser diode (JDS Uniphase type 63-00342) coupled to a 100 μm core fiber as excitation source. The output from the laser was collimated using a fiber coupler and a long band-pass filter (850 nm) was used on the excitation side and a short band-pass filter (900 nm) on the collecting end of the red-sensitive Peltier-cooled Hamamatsu R955 PMT detector. Both core and core-shell NCs in toluene (approximately equal number of NCs) were taken in a 1 cm path-length quartz cuvette and upconversion emission spectra measured at 2 nm resolution with the same laser power density (150 W cm^{-2}) and corrected for the instrument sensitivity.

Chapter 6. Self-focusing by Ostwald Ripening: A Strategy for Layer-by-Layer Epitaxial Growth on Upconverting Nanocrystals

(This chapter is reproduced with permission from Ref.[174] Copyright 2012 American Chemical Society.)

6.1. Introduction

Epitaxial shell growth on colloidal nanocrystals (NCs) is a widely employed strategy to separate spatially the optically active core from the surrounding environment, or to generate NCs with multi-functionality. In case of lanthanide-based upconverting NCs, shell growth is an attractive option for enhancing the inherently low quantum yield of the upconversion (UC) process.[46,88,101,162,175,176] The unique UC process, which converts multiple low-energy photons to a high-energy photon facilitated by the Ln^{3+} dopants in $NaLnF_4$ NCs, is attractive for a wide range of applications.[48,147,177,178] These multi-photon absorption and relaxation processes are easily quenched by the high-energy vibrations of solvent molecules, and epitaxial shell growth has been shown to enhance the efficiency of the UC process. While in principle thick shells are ideal for enhanced UC efficiency, integrating the UC process for other applications such as luminescence resonance energy transfer (LRET), energy migration-mediated upconversion (EMU), metal-enhanced luminescence, photo-switches, and optically driven actuators requires modulation of the thickness of the epitaxial layers to facilitate efficient energy transfer/enhancement.[179-183] As these applications are highly dependent on the spatial separation of the organic molecules/metal centers/dopant ions from the UC core, a highly tunable layer-by-layer

epitaxial growth becomes particularly important. Moreover, as emphasized in Chapter 5, integrating T_1 MRI contrast enhancement and UC properties an epitaxial layer growth tunable down to a monolayer (ML) thickness control is a necessity.

While there has been promising progress in epitaxial growth, fundamental limitations and challenges in generating easily tunable shell growth are not fully addressed. In the widely used seed-mediated shell growth on β-$NaYF_4$ as that described in Chapter 4 only one shell thickness can be achieved based on the starting ratio of core NCs to molecular shell precursors. To grow different shell thickness, the core to shell precursors have to be varied and multiple growth parameters need to be tuned simultaneously for each reaction conditions. The fact that the rate of active monomer formation will vary with the molecular precursor concentration which is directly related to time and temperature makes it cumbersome to tune shell growth, as this relies on a trial-and-error approach.[181]

In seed-mediated shell growth the pre-synthesized core NCs (β-$NaYF_4$) are mixed with the shell precursors at room temperature and subsequently heated to 300 °C for the growth of an epitaxial shell. The pre-synthesized core NCs are believed to act as seeds or nuclei to direct the crystallization of the shell precursors resulting in an epitaxial shell on the core NCs.[46] If this generalized assumption is true, different shell thicknesses can be achieved by just stopping the reaction at different time intervals, and not necessarily require multiple growth conditions (such as varying core NCs to shell precursor ratio) and multiple reactions as mentioned above. In this regard the well established seed-mediated shell growth process was first analyzed by retrieving aliquots of reaction mixture at different time intervals of shell growth. The first part of this chapter demonstrates that contrary to the generally assumed mechanism of the core NCs acting as

nuclei/seeds for subsequent growth, the shell precursors preferentially nucleate as α-$NaYF_4$ NCs (kinetic product) and a ripening-mediated process leads to core-shell NCs. This deviation from the conventional growth mode greatly restricts the ability to tune the layer thickness as multiple parameters need to be controlled precisely and simultaneously. To overcome these limitations, a novel approach of self-focusing by Ostwald ripening for achieving layer-by-layer growth directly onto the core NCs is demonstrated. The method described in the second part based on the above observations eliminates the need for precise control of multiple parameters/reactions to obtain tunable shell growth.

In colloidal systems, larger particles with smaller surface to volume ratios are favored over the energetically less stable smaller particles, resulting in the growth of larger particles at the expense of smaller ones, referred to as Ostwald ripening. Ripening typically leads to size broadening, and one usually aims to avoid ripening so as to obtain NCs with a narrow size distribution. However, theoretical studies on ripening in an ensemble of differently sized NCs have shown that the ensemble size focuses unlike the asymmetric broadening predicted by LSW (Lifshitz-Slyozov-Wagner) theory.[184] While it has been more than a decade since these theoretical studies, reports on ripening-mediated self-focusing have been limited to observations of such a pathway during growth of various semiconductor/inorganic NCs.[185-188] To date, no reports on the deliberate use of this unique self-focusing process as a synthetic tool to tune the structure/property of NCs has been realized. In this context, the unique self-focusing process is utilized as a potential tool for easily tunable epitaxial shell growth. Deliberate injection of small sacrificial NCs (SNCs) as shell precursors into larger core NCs (defocusing) results in the

rapid dissolution of the SNCs and their deposition onto the larger core NCs (self-focusing) to yield core-shell structured NCs. Exploiting this NC size dependent dissolution/growth, the shell thickness can be controlled either by manipulating the number of SNCs injected or by successive injection of SNCs. In either of these approaches the NCs self-focus from an initial bimodal distribution to a unimodal distribution (σ <5%) of core-shell NCs, without the need for any stringent requirements in generating tunable epitaxial layer growth. The protocol described in this chapter is the first experimental evidence of deliberate defocusing and subsequent self-focusing demonstrated for any colloidal NCs, and exploration as a strategy for epitaxial layer growth.

6.2. Results and Discussion

6.2.1. Core-shell NCs by seed-mediated heat-up method

The growth kinetics of the core-shell upconverting nanocrystals (UCNCs) by the seed-mediated heat-up method from published protocols[46] were systematically evaluated by retrieving aliquots of reaction mixture at different reaction times and analyzed by TEM and XRD. The hexagonal phase UCNCs (β-$NaYF_4$: Yb^{3+}/Er^{3+} (15/2%) as core was pre-synthesized and mixed with yttrium precursors at room temperature and subsequently heated to obtain undoped $NaYF_4$ shell. The TEM & XRD patterns shown in Figure 6.1 clearly demonstrate the growth of the kinetic product (cubic α NCs) at early stage of the reaction (250˚C) and more pronounced at elevated temperatures (280 ˚C and 300 ˚C for 20 min). Due to the presence of large number of small cubic NCs at these temperatures the TEM images were obtained from well diluted dispersions. The XRD patterns for the temperature regime 250˚C, 280 ˚C, and 300 ˚C for 20 min, clearly show a broad peak at

42˚ and 73˚ (2θ) pertaining to the presence of really small cubic NCs, which is completely absent in the core and late stage core-shell NCs. Moreover, the core NCs almost remains the same size at the early stage (250˚C, 280 ˚C, and 300 ˚C for 20 min) which later increases in size (300 ˚C for 60 min) confirming the ripening-mediated core-shell growth and that the process is not a nuclei/seed-mediated growth as often assumed in literature.

The growth mechanism of $NaLnF_4$ (Ln: Pr to Lu, Y) NCs is known to vary along the series, while the light lanthanides favor hexagonal phase (β), the cubic phase (α) is preferred in heavy lanthanides. Liu *et al.* used this fundamental property to control simultaneously the size and phase of $NaYF_4$ NCs.[41] Here, in the seed-mediated growth conditions the cubic phase of $NaYF_4$ is favored over the direct crystallization of yttrium precursors as hexagonal layers on the core β-$NaYF_4$: Yb^{3+}/Er^{3+} (15/2%) UCNCs. This fundamental limitation in the core-shell growth demonstrates the necessity to utilize multiple growth conditions to obtain different shell thickness as the core UCNCs do not act as seeds or nuclei. This deviation from conventional expectation of a seeded growth process makes it challenging to obtain tunable shell growth without the need for manipulating multiple growth parameters.

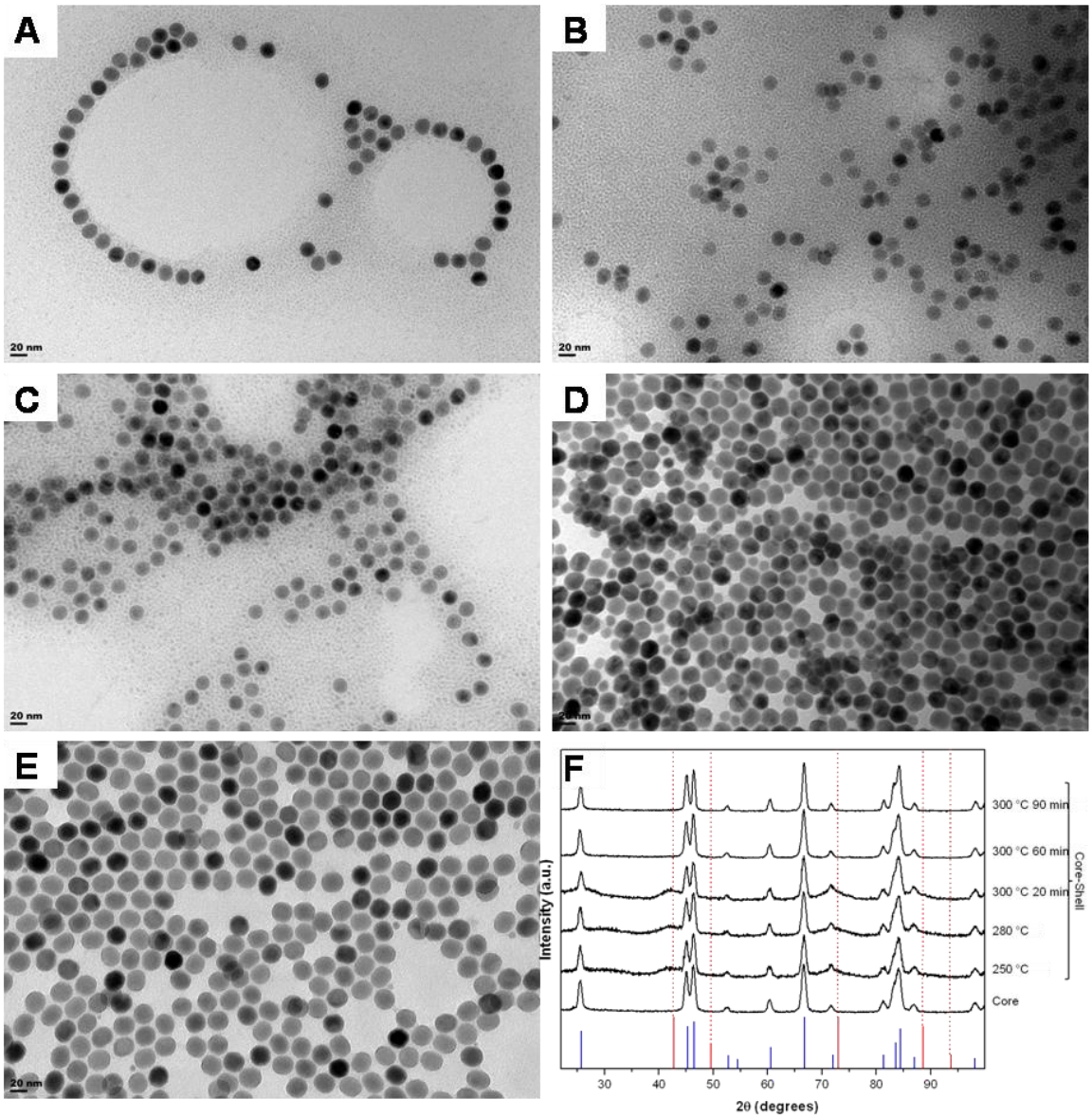

Figure 6.1. TEM images of core-shell NCs at different reaction times/temperature **(A)** 250 ˚C, **(B)** 280 ˚C, **(C)** 300 ˚C for 20 min, **(D)** 300 ˚C for 60 min, **(E)** 300 ˚C for 90 min, and **(F)** XRD pattern of the core and the core-shell NCs at different reaction time/temperature, and the standard reference pattern of α-$NaYF_4$ (red), and β-$NaYF_4$ (blue) (JCPDS- 06-0342: α-$NaYF_4$, 016-0334: β-$NaYF_4$).

6.2.2. Core-shell NCs by ripening-mediated self-focusing method

Based on the observations described above, a ripening-mediated approach to deposit easily epitaxial layers on upconverting core NCs was investigated. If the core-shell growth by the heat-up method is driven by a ripening process, one should be able to control explicitly the ripening process by deliberately introducing the shell component as small sacrificial NCs (SNCs) directly into the reaction of core NCs, and the NCs should spontaneously self-focus as core-shell NCs. Undoped α-$NaYF_4$ NCs (~6.5 nm) were synthesized and used as SNCs[45] (Figure D1 of the Appendix). Using lanthanide ions in appropriate molar ratio, upconverting β-$NaYF_4$:Yb^{3+}, Er^{3+} NCs were synthesized at 300 ˚C for 1 h.[43] After 1 h at 300 ˚C when core NCs had formed, calculated amounts of SNCs (0.65 mmol) in 1-octadecene (1 ml) were injected and allowed to ripen (10 min) before cooling the mixture to room temperature. Aliquots of reaction mixture: core NCs (t=0), right after SNC injection (t=5 sec), and the final product (t=10 min) were retrieved, washed and dispersed in hexane for analysis by transmission electron microscopy (TEM) and X-ray diffraction (XRD). The TEM images and the corresponding NC size distributions are shown in Figure 6.2 and uncropped TEM images and the corresponding XRD pattern are shown in Figure D2 of the appendix.

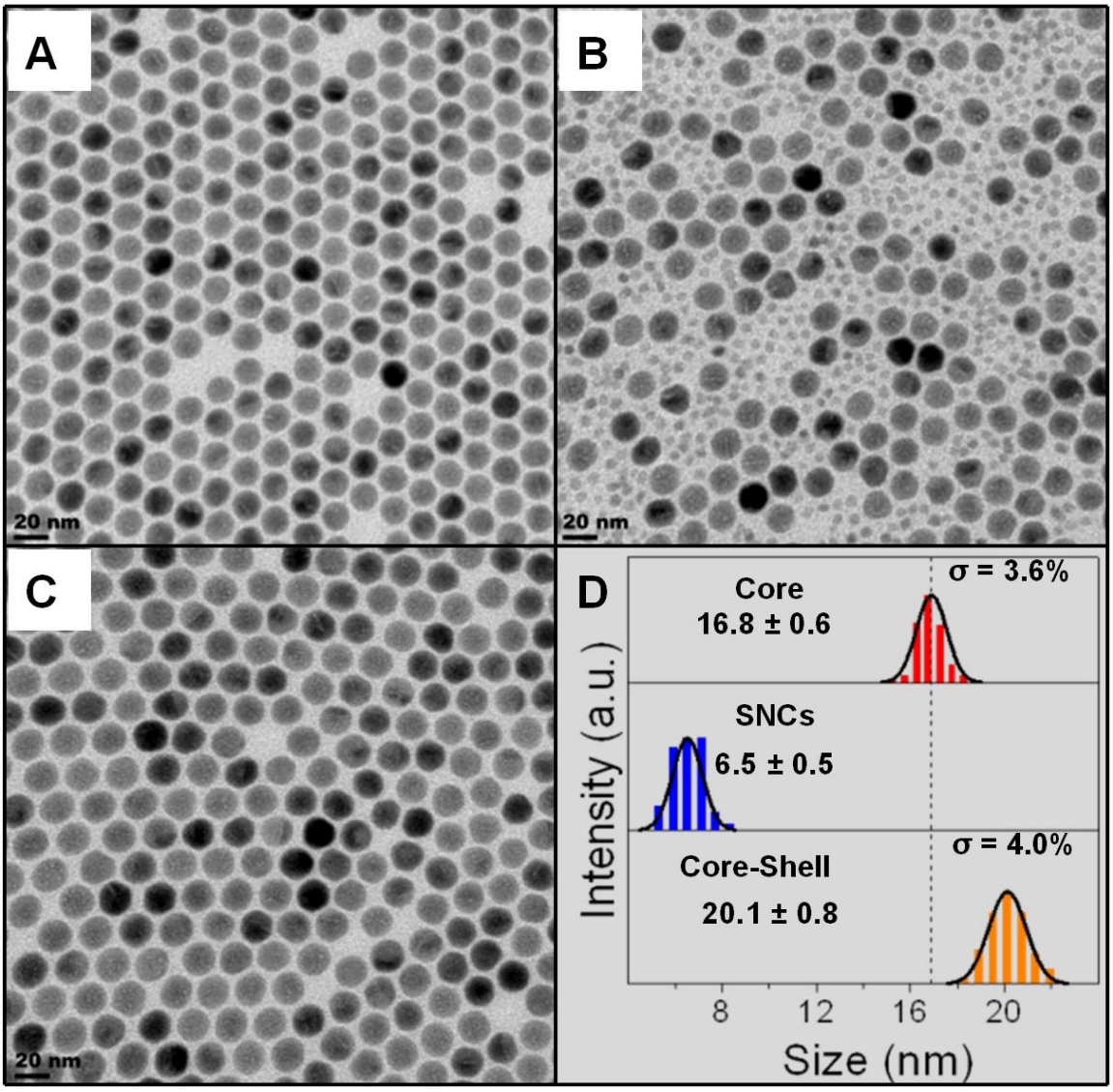

Figure 6.2. (A-C) Transmission Electron Micrographs of $NaYF_4$: Yb^{3+}/Er^{3+} (15/2%) core NCs (@t=0), after injection of sacrificial α-$NaYF_4$ NCs (@t=15 sec), and after self-focusing $NaYF_4$: Yb^{3+}/Er^{3+} (15/2%) core/$NaYF_4$ shell NCs (@t=10 min) respectively, and **(D)** size distribution of the NCs.

The TEM analysis (Figure 6.2 and Figure D2 of the Appendix) of the three aliquots confirms the complete dissolution and deposition of the SNCs on core NCs. The core NCs 16.8 ± 0.6 nm has grown into a unimodal size distribution of larger 20.1 ± 0.8 nm NCs after 10 min ripening. The aliquot retrieved right after SNC injection shows a

bimodal distribution (Figure 6.2B), corresponding to the presence of core NCs and injected SNCs. Importantly, the size increase strictly correlates to the amount of SNCs injected, accounting for the mass balance during the dissolution/growth process. The XRD patterns indicate (Figure D2 of the Appendix) that the core NCs are of hexagonal phase, and after SNC (cubic NCs) injection in the bi-modal size regime a small peak arising from the 111 plane of cubic SNCs (42˚2θ), completely vanished after ripening to yield hexagonal phase NCs. During ripening the cubic SNCs dissolve and deposit as hexagonal layers on the core NCs, the monomers/adatoms released from the SNCs adapt to the NC surface onto which they deposit. The epitaxial layer thickness can readily be tuned by simply manipulating the amount of SNCs injected (Figure D3 of the Appendix). This approach for epitaxial growth does not require precise control over the introduction of shell components (injection rate), as often needed with the molecular precursor injection and growth (hot-injection method).[88,176] In molecular precursor mediated epitaxy by the hot-injection method, to eliminate homogeneous nucleation of the shell precursors and to maintain the narrow temperature window for the precursor decomposition imposes a highly controlled addition step (using a mechanical pump). These variables will lead to difficulties in generating reproducible and tunable epitaxial layer growth.[177]

To gain insights into the dissolution/growth process, the growth of core NCs was first studied. The solution growth of β -$NaYF_4$ NCs is known to grow in a monomer-depleted regime, where the kinetic product (α-$NaYF_4$) formed at lower temperature dissolves at elevated temperature to nucleate into the thermodynamic phase, followed by inter-particle ripening to yield uniform β -$NaYF_4$ NCs.[39,40,45] To confirm that this is also the

case in this system, core UCNCs were synthesized and multiple aliquots at different reaction time and temperature were retrieved and analyzed by TEM and XRD (Figure 6.3). The TEM & XRD patterns clearly demonstrate the growth of the kinetic product (cubic α NCs) at early stage of the reaction and after aging for 30 min at 300 ºC the thermodynamic product (hexagonal β NCs) evolves. The thermodynamic product subsequently grows at the expense of less stable cubic NCs by ripening to yield single phase hexagonal β NCs. Furthermore, the yields of the inorganic NC growth carried out for different reaction times (30 min and 1 h) were almost the same at >80%, confirming the monomer depleted inter-particle ripening-mediated growth (Figure D4 of the Appendix).

The growth rate of a particle with size *r* in this diffusion controlled regime is given by the following equation (1)

$$dr/dt = K\,(1/r + 1/\delta)\,(1/r^{*}-1/r) \qquad (1)$$

where, K is constant proportional to the diffusion constant of the monomer, and δ is the thickness of the diffusion layer.[189] NCs smaller than the critical radius (r*) dissolve while NCs larger than the critical radius grow at their expense. The critical radius in an ensemble of NCs is the average size number of the ensemble,[190] which increases as the smaller particles are depleted by dissolution/deposition on the larger NCs. When the core NCs focus into a unimodal size distribution, the critical radius (r*) is about the same as the average size. Thus, deliberately defocusing the ensemble by introducing small SNCs (α-$NaYF_4$) shifts the critical radius to a smaller size. Under this condition, the SNCs

rapidly dissolve as they are smaller than the critical radius, and deposit on the larger core NCs, *i.e*. the ensemble refocuses to a narrow unimodal size distribution ($\sigma < 5\%$). Remarkably, the core NCs (Figure 6.2A) after ripening (Figure 6.2C) had increased by 70% in volume in just 10 minutes confirming the rapid dissolution/growth process.

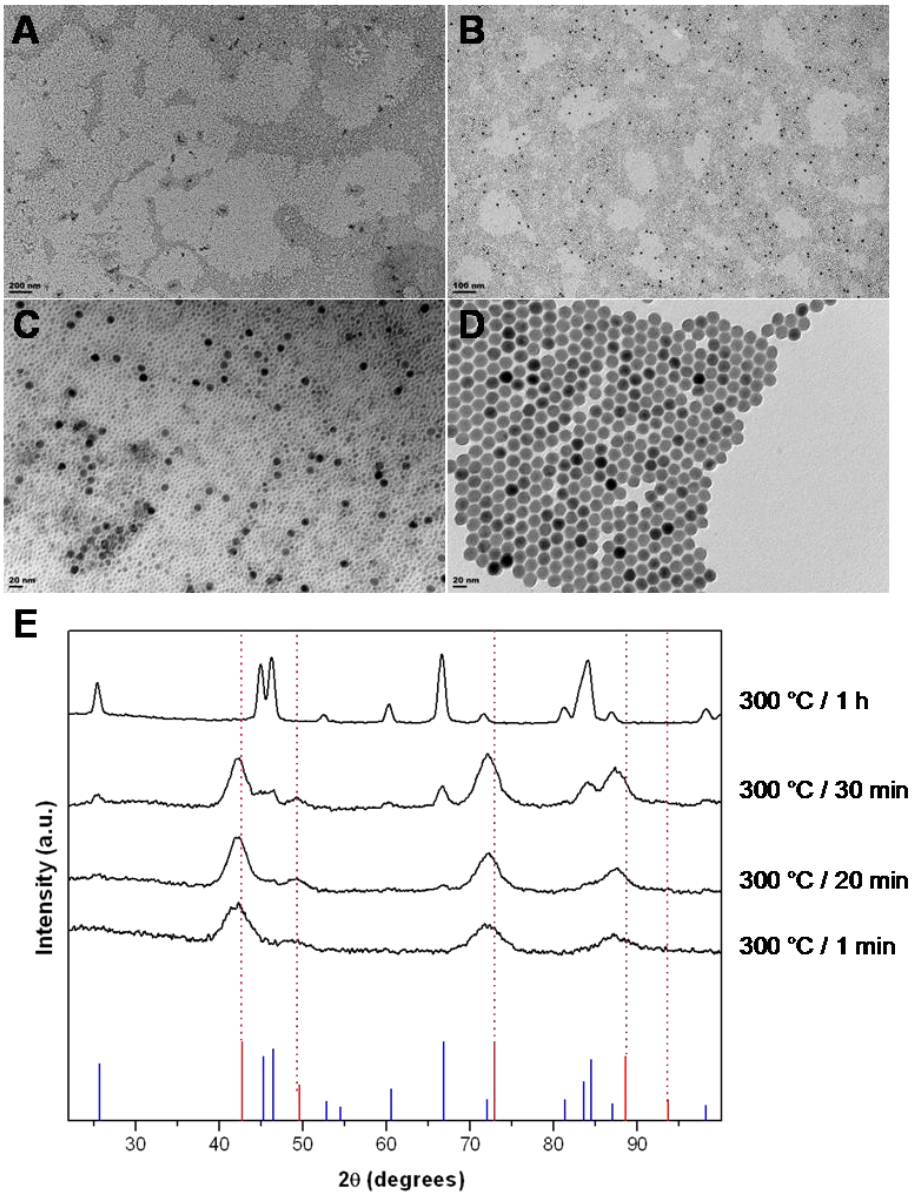

Figure 6.3. TEM images of core NCs @ 300 ˚C **(A)** 1 min, **(B)** 20 min, **(C)** 30 min, **(D)** 60 min, and **(E)** XRD pattern of the NCs at different reaction times corresponding to the TEM images (standard reference pattern of α-$NaYF_4$ (red), and β-$NaYF_4$ (blue) (JCPDS- 06-0342: α-$NaYF_4$, 016-0334: β-$NaYF_4$).

The defocusing and self-focusing cycle can be repeated multiple times to generate layer-by-layer shell growth. TEM images shown in Figure 6.4A-E and Figure D5-7 of the Appendix demonstrate the easy control offered by this method in shell thickness tuning, which was achieved by four successive SNC injection (0.2 mmol) and ripening cycles. Varying the quantity of SNCs injected (0.25 mmol) resulted in increased layer thickness in each cycle (Figure D8 of the Appendix).

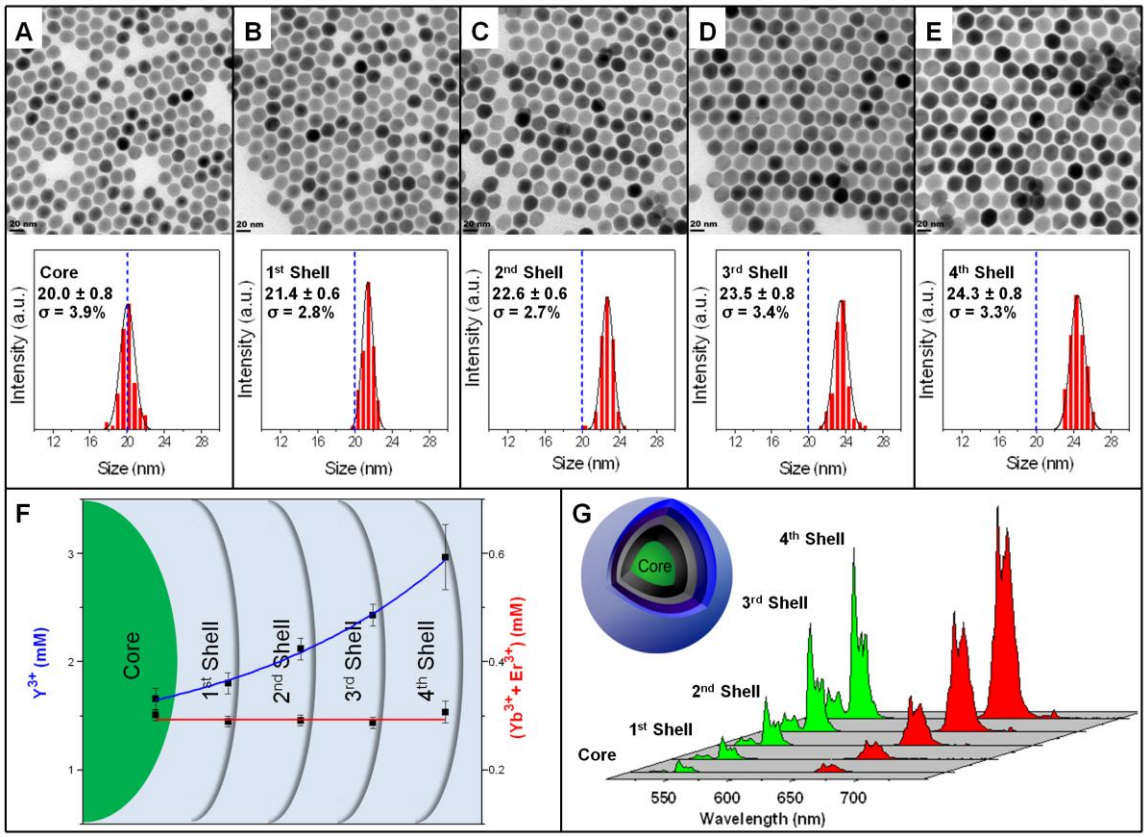

Figure 6.4. (A-E) TEM images and size distribution of $NaYF_4$: Yb^{3+}/Er^{3+} (15/2%) core NCs (@t=0), $NaYF_4$: Yb^{3+}/Er^{3+} (15/2%) core/$NaYF_4$ shell NCs after successive layer-by-layer epitaxial growth @ t= 5, 10, 15,and 20 min respectively, **(F)** ICP-MS elemental analysis of the core and core-shell NCs with same number concentration of NCs, **(G)** Upconversion emission spectra of the hexane dispersions of core and core-shell NCs with same number concentration of NCs under 980 nm excitation.

The successive growth of epitaxial shells with each cycle is confirmed by the elemental analysis (ICP-MS) of NC dispersions containing the same number of NCs (see Appendix for details). Figure 6.4F clearly shows the increase in Y^{3+} while the optically active ions (Yb^{3+} and Er^{3+}) remain the same. The increase in the amount of Y^{3+} after four cycles correlates excellently to the total amount of SNCs injected (see Table D1 in Appendix for details), confirming the mass balance throughout the ripening cycle. The consistent increase in upconversion emission intensity of both green and red emissions with increasing layer thickness (Figure 6.4G) with the optically active ion concentration (Yb^{3+} and Er^{3+}) remaining constant further confirms the epitaxial shell growth. Considering the distance dependent Förster mechanism ($1/r^6$) in solvent quenching, the spatial screening of the luminescent core from the solvent environment with each additional layer leads to luminescence enhancement (Figure 6.5 shows relative increase in intensities and dispersion photographs of the core and successive shell growth under 980 nm excitation). The size increase from the TEM analysis, alongside the ICP-MS and upconversion emission profiles unequivocally demonstrate the ability to generate core-shell NCs with tunable shells through a layer-by-layer growth by deliberate defocusing of the system and self-focusing by ripening in multiple cycles.

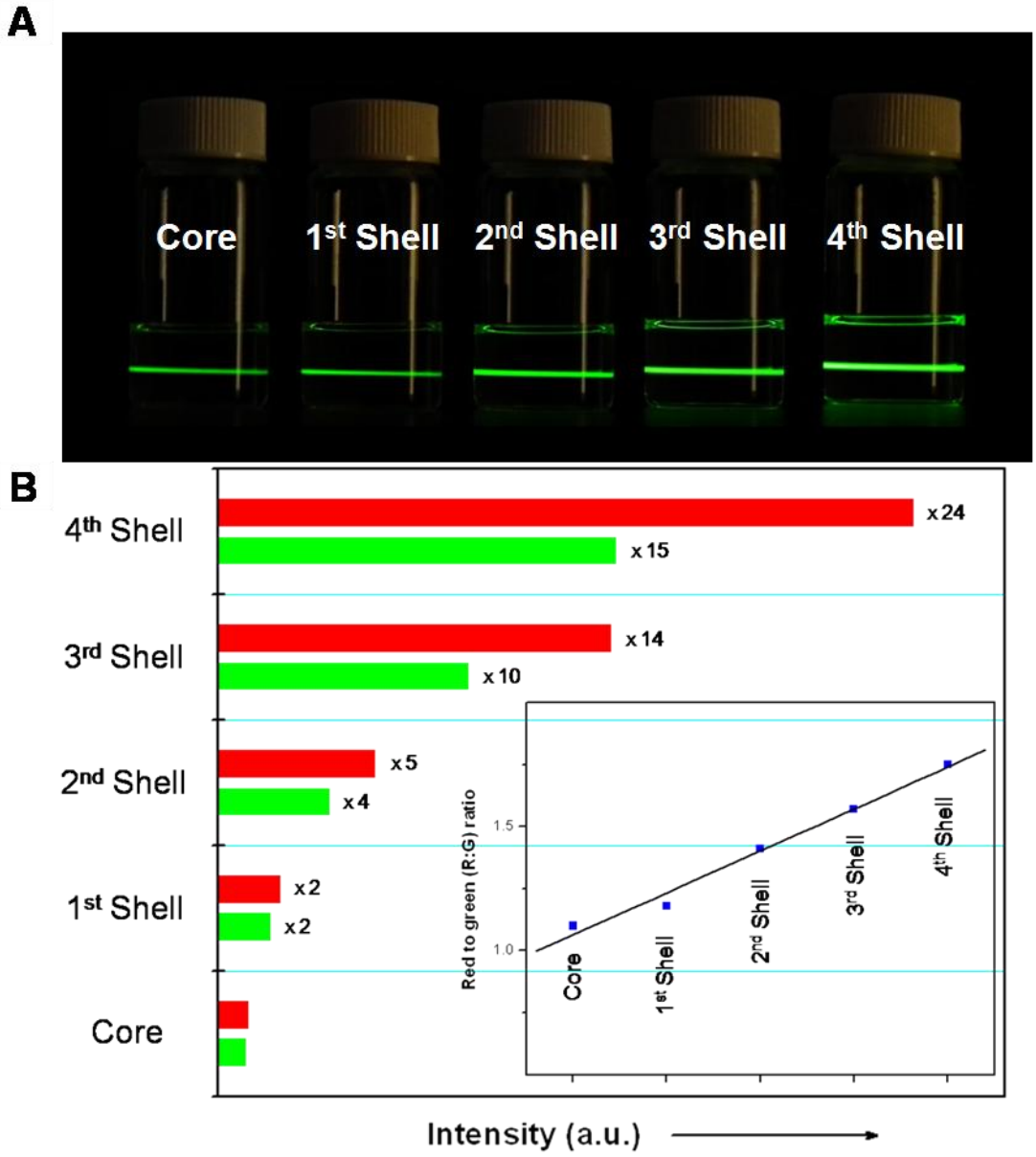

Figure 6.5. (A) Colloidal dispersions of upconverting core, and core-shell NCs with successive shell growth with same number concentration of NCs (constant optically active ion concentration (Yb^{3+}/Er^{3+}) in each dispersion) in hexane under 980 nm laser diode excitation, and **(B)** enhancement of red and green emission intensities with successive shell growth (*Inset*: ratio of red to green emission intensity with successive shell growth).

This protocol is versatile and can easily be extended to obtain core-shell NCs of different composition and also to orient spatially dopant ions and layers with variable compositions. A thin layer of $NaGdF_4$ as shell is ideal for integrating magnetic resonance imaging (MRI) and upconversion properties into a single NC, as only the surface gadolinium ions are known to affect the relaxation of water protons.[142,191] $NaYF_4$/$NaGdF_4$ core-shell NCs could be obtained by injection of hexagonal β-$NaGdF_4$ (5 nm) SNCs into a solution of core β-$NaYF_4$ NCs, and ripening. The size increase of the NCs after ripening (Figure 6.6A-B and Figure D9 of the Appendix) and the absence of the SNCs demonstrate the ability to deposit epitaxial layers of choice by ripening, and that the SNCs of any composition/crystal phase can be utilized in the process. The difference in chemical composition of the core (Y^{3+}) and shell (Gd^{3+}) allowed for 2D-elemental mapping by electron energy-loss spectroscopy (EELS) to confirm the dissolution and deposition of $NaGdF_4$ on the $NaYF_4$ core NCs (Figure 6.6C-D and Figure D10 of the Appendix).

As a proof-of-principle, dual-mode emitting NCs were obtained using this protocol either by spatially orienting different dopant ions in the same matrix (Figure D11 of the Appendix) or by simultaneously varying both the matrix and dopant ions (Figure D13 of the Appendix). This further demonstrates the utility of this self-focusing by ripening approach to orient easily dopant ions and layers of variable compositions without any deleterious cross-relaxation as observed with co-doped NCs of the same dopant concentrations (Figure D12 and D14 of the Appendix). This self-focusing approach to generate core-shell NCs can be extended for relatively smaller sized core NCs as

demonstrated using upconverting $NaGdF_4$ NCs shown in Figure D15 and D16 of the Appendix.

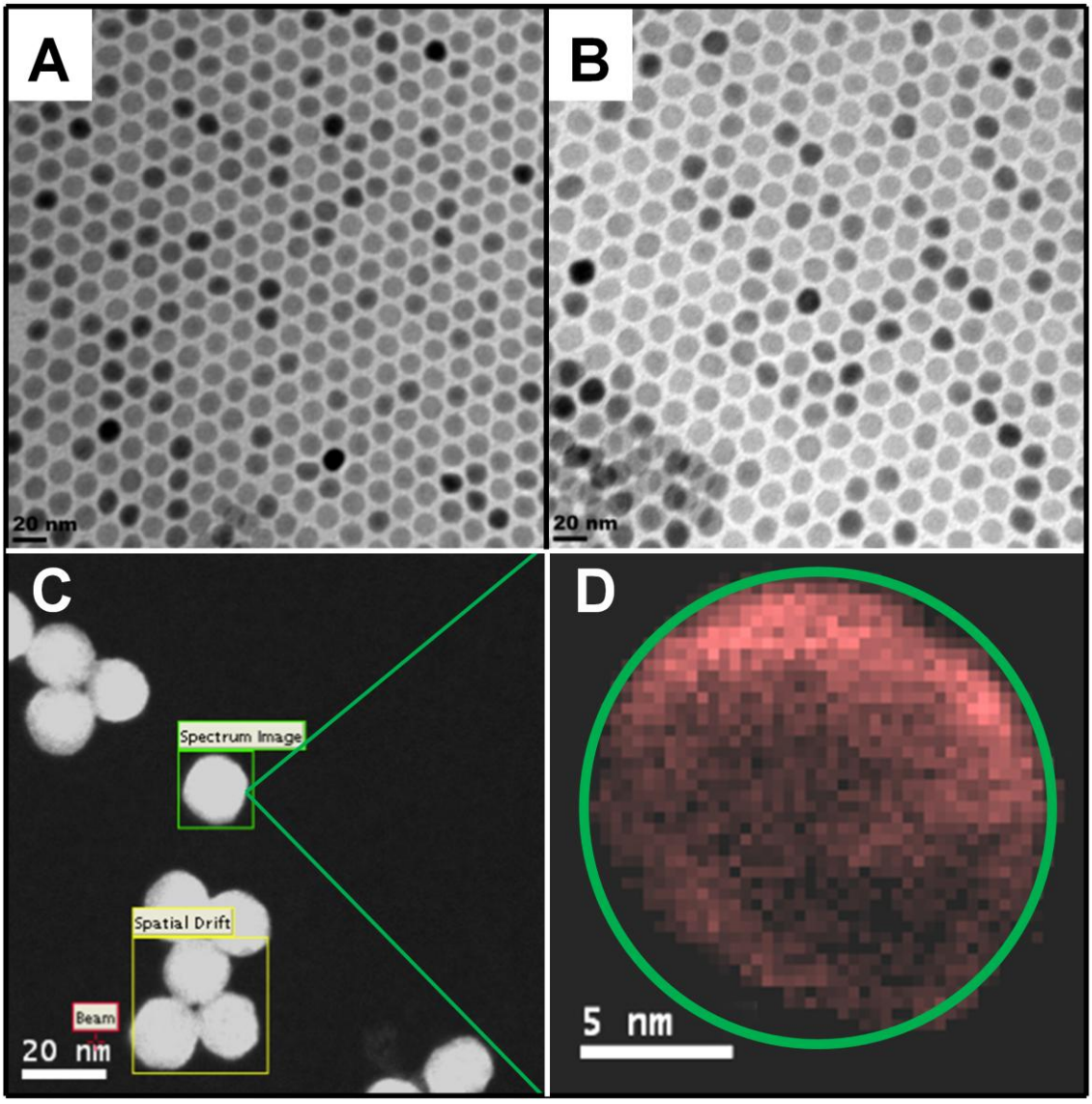

Figure 6.6. TEM images of **(A)** $NaYF_4$ core NCs, **(B)** $NaYF_4$ core /$NaGdF_4$ shell NCs, and **(C, D)** EELS 2D-mapping of gadolinium confirming the deposition of $NaGdF_4$ shell.

6.3. Conclusions

In summary, a versatile epitaxial growth technique is demonstrated based on a common physical phenomenon of ripening in colloids to grow shells tunable both in thickness and composition. The protocol is flexible and allows to deposit easily multiple layers by successive defocusing and self-focusing cycle without the need for multi-step process. Moreover, the ripening-mediated epitaxial growth facilitates NCs with narrow size distribution, as the NCs spontaneously self-focus by dissolution of the energetically less favored SNCs in the ensemble. This approach does not necessitate any external control over the introduction of shell components as needed for precursor injection and shell growth. This added advantage should allow for easy automation and scaled-up synthesis of high quality core-shell NCs as their scope widens in various applications. Finally, as this approach relies on a fundamental colloidal property, it is pertinent for NCs in general to overcome the limitations of conventional shell growth techniques.

6.4. Experimental Section

Materials. All chemicals were purchased from Sigma-Aldrich except oleylamine (97%) from Acros, anhydrous ethanol from Commercial Alcohols and methanol from Caledon. All chemicals were used as received.

Synthesis of sacrificial nanocrystals (SNCs)

Synthesis of cubic (α) $NaYF_4$ nanocrystals. Cubic $NaYF_4$ SNCs were synthesized based on a previously reported procedure.[45] In a typical synthesis Y_2O_3 (1 mmol) was mixed with 10 ml of 50 % aqueous trifluoroacetic acid and refluxed at 85 ˚C overnight. Yttrium trifluoroacetate precursor ($Y(CF_3COO)_3$) was then obtained after removing excess trifluoroacetic acid and water by evaporation at 65 ˚C. Sodium trifluoroacetate (2

mmol) was added to the precursor along with oleic acid (6 ml), oleylamine (6 ml), and 1-octadecene (10 ml) and heated to 120 ˚C under vacuum for 45 min to remove residual water and oxygen. The obtained transparent solution was subsequently heated to 290 ˚C (~15˚C/min) under argon and vigorously stirred for 45 min and cooled down to room temperature. The NCs were precipitated by addition of ethanol, collected by centrifugation, washed with ethanol and finally dispersed in hexane (10 ml).

Synthesis of cubic (α) $NaYF_4$ (1 mol% Tm^{3+}, 15 mol% Yb^{3+} doped). The synthesis was carried out exactly as outlined for undoped cubic (α) $NaYF_4$ SNCs mentioned above, except that the precursors were taken in the ratio of Y_2O_3 (0.84 mmol), Yb_2O_3 (0.15 mmol), and Tm_2O_3 (0.01 mmol). The obtained NCs were dispersed in 10 ml hexane.

Synthesis of cubic (α) $NaYF_4$ (5 mol% Tb^{3+}, 15 mol% Ce^{3+} doped). The synthesis was carried out exactly as outlined for undoped cubic (α) $NaYF_4$ SNCs mentioned above, except that the precursors were taken in the ratio of Y_2O_3 (0.80 mmol), $Ce_2(CO_3)_3.xH_2O$ (0.15 mmol), and Tb_2O_3 (0.05 mmol). The obtained NCs were dispersed in 10 ml hexane.

Synthesis of hexagonal (β) $NaGdF_4$ nanocrystals. $Gd(CH_3CO_2)_3.xH_2O$ (0.8 mmol), oleic acid (8 ml), oleylamine (8 ml), and 1-octadecene (16 ml) were added to a 100 ml flask and heated to 120 ˚C for 45 min under vacuum and cooled to room temperature. To this solution at room temperature, methanol solution (10 ml) of ammonium fluoride (4 mmol) and sodium hydroxide (2.5 mmol) was added dropwise and stirred for 30 min. The reaction vessel was then heated to 70 ˚C to remove methanol and subsequently heated to 300 ˚C (~10 ˚C/min) under argon and maintained for 60 min, followed by raising the temperature to 320 ˚C (~5 ˚C/min) and maintained for 20 min. The reaction mixture was

then cooled to room temperature and the NCs were precipitated by addition of ethanol, collected by centrifugation and washed with ethanol before dispersing them in hexane (10 ml).

Synthesis of hexagonal (β) $NaGdF_4$ (5 mol% Eu^{3+}, 2 mol% Ce^{3+} doped) nanocrystals. The synthesis was carried out exactly as outlined for undoped hexagonal (β) $NaGdF_4$ NCs mentioned above, except that the lanthanide salts were added in the ratio of $Gd(CH_3CO_2)_3.xH_2O$ (0.744 mmol), $Eu(CH_3CO_2)_3.xH_2O$ (0.04 mmol), and $Ce(CH_3CO_2)_3.xH_2O$ (0.016 mmol). The obtained NCs were dispersed in 10 ml hexane.

Synthesis of core nanocrystals

Synthesis of hexagonal (β) $NaYF_4$ upconverting core nanocrystals (2 mol% Er^{3+}, 15 mol% Yb^{3+} doped). The synthesis was adapted from a reported procedure with slight modifications.[43] $Y(CH_3CO_2)_3.xH_2O$ (0.83 mmol), $Yb(CH_3CO_2)_3.xH_2O$ (0.15 mmol) and $Er(CH_3CO_2)_3.xH_2O$ (0.02 mmol) were added to a 100 ml flask containing oleic acid (6 ml) and 1-octadecene (15 ml) and heated to 125 ˚C under vacuum for 45 min and cooled to room temperature. To this solution at room temperature, methanol solution (10 ml) of ammonium fluoride (4 mmol) and sodium hydroxide (2.5 mmol) was added dropwise and stirred for 30 min. The reaction vessel was then heated to 70 ˚C to remove methanol and subsequently heated to 300 ˚C (~10˚C/min) under argon and maintained for 60 min. The reaction mixture was then cooled to room temperature and the NCs were precipitated by addition of ethanol, collected by centrifugation and washed with ethanol before dispersing them in hexane (10 ml).

Growth kinetics of core NCs. During the course of the reaction, aliquots of the reaction mixture (1 ml) were retrieved at different time to monitor the growth kinetics of the core

NCs. The retrieved aliquots were purified and dispersed in hexane (1 ml) as described above.

Determination of inorganic crystal yield at different reaction times. For determining the inorganic crystal yield at different reaction times, two such reactions were carried out with one for the complete 60 min and the other for 30 min. Both the reaction products were purified as described above and dispersed in 10 ml hexane.

Synthesis of hexagonal (β) $NaYF_4$ core nanocrystals. The synthesis was carried out exactly as outlined for doped hexagonal (β) $NaYF_4$ NCs mentioned above, except that the $Y(CH_3CO_2)_3.xH_2O$ (1.0 mmol) was used.

Synthesis of core-shell nanocrystals

Synthesis of hexagonal (β) $NaYF_4$ upconverting core (2 mol% Er^{3+}, 15 mol% Yb^{3+} doped) / $NaYF_4$ shell nanocrystals (Seed-mediated heat-up method). The core-shell synthesis was based on a previously reported procedure.[46] The synthesis of the core upconverting NCs was done as described above and used as seeds for the core-shell reaction. Using $Y(CH_3CO_2)_3.xH_2O$ (1.0 mmol) as shell precursors following the published protocol the core-shell NCs were synthesized. During the reaction, aliquots of reaction mixture were retrieved at different time/temperature. The NCs from different aliquots were then precipitated and washed as mentioned for core NCs and dispersed in hexane (1 ml).

Synthesis of hexagonal (β) $NaYF_4$ upconverting core (2 mol% Er^{3+}, 15 mol% Yb^{3+} doped) / $NaYF_4$ shell nanocrystals (Ripening-mediated self-focusing method).

Single step epitaxial shell growth. The synthesis of the core upconverting NCs was done as described above, and after 60 min at 300 ˚C about 1 ml of reaction mixture was retrieved (t = 0 core) and immediately calculated amount (see table D2 of the Appendix for details) of sacrificial NCs (SNCs) (α-$NaYF_4$) in 1 ml octadecene was injected (*no precise control on injection is necessary, the SNCs were taken in a syringe with a stainless steel cannula and injected in one-shot ~1 sec for the injection volume of 1 ml*) into the reaction mixture and ripened to yield core-shell NCs. Immediately after injection of SNCs the temperature of the reaction mixture dropped to about 290 ˚C and increased back to 300 ˚C in the next 2-3 min, and no careful temperature control was necessary to obtain unimodal size distribution of core-shell NCs. The ripening time for different amount of SNCs was either 5 min (< 0.25 mmol) or 10 min (> 0.25 mmol) and no other specific changes were made. After ripening the solution was cooled down to room temperature and the core-shell NCs were precipitated and washed as outlined for core NCs and dispersed in hexane (10 ml).

Layer-by-layer successive epitaxial shell growth. The same procedure outlined for single step epitaxial shell growth was performed, and calculated amount (see Table D2 of the Appendix for details) of SNCs (α-$NaYF_4$) in 1 ml octadecene was injected into the reaction mixture and ripened for 5 min followed by injection of SNCs and ripening cycles for each additional layer growth. Injection of SNCs and ripening cycles were performed to a total of four cycles. The ripening time between each cycle was kept constant at 5 min. During the course of the reaction, 1 ml aliquots of reaction mixture was retrieved

just before each SNC injection and ripening cycle, and NCs from each aliquot were precipitated and washed as described above and dispersed in hexane (1 ml).

Synthesis of hexagonal (β) $NaYF_4$ core / $NaGdF_4$ shell nanocrystals. The synthesis of the core undoped β-$NaYF_4$ NCs was done as described above, and at 300 ˚C after 60 min calculated amount (see Table D2 of the Appendix for details) of SNCs (β-$NaGdF_4$) in 1 ml octadecene was injected into the reaction mixture and ripened to yield core-shell NCs. The core-shell NCs were precipitated and washed as described above and dispersed in hexane (10 ml).

Synthesis of hexagonal (β) $NaYF_4$ upconverting core (2 mol% Er^{3+}, 15 mol% Yb^{3+} doped) / $NaYF_4$ (1 mol% Tm^{3+}, 15 mol% Yb^{3+} doped) shell/ $NaYF_4$ (5 mol% Tb^{3+}, 15 mol% Ce^{3+} doped) shell nanocrystals. The synthesis of the core upconverting NCs was done as described above, and after 60 min at 300 ˚C calculated amount (see Table D2 of the Appendix for details) of SNCs (α-$NaYF_4$ (1 mol% Tm^{3+}, 15 mol% Yb^{3+} doped)) in 1 ml octadecene was injected into the reaction mixture and ripened to yield core/shell NCs. After ripening of the first shell calculated amount (see Table D2 of the Appendix for details) of SNCs (α-$NaYF_4$ (5 mol% Tb^{3+}, 15 mol% Ce^{3+} doped)) in 1 ml octadecene was injected into the reaction mixture and ripened to yield core/shell/shell NCs. After ripening the solution was cooled down to room temperature and the core/shell/shell NCs were precipitated and washed as described above and dispersed in hexane (10 ml).

S*ynthesis of hexagonal (β) $NaYF_4$ upconverting core (2 mol% Er^{3+}, 15 mol% Yb^{3+} doped) / $NaGdF_4$ (5 mol% Eu^{3+}, 2 mol% Ce^{3+} doped) shell nanocrystals.* The same protocol used for undoped hexagonal (β) $NaYF_4$ core / $NaGdF_4$ shell nanocrystals was

followed except that the core and the shell were doped as mentioned above. The obtained core-shell NCs were dispersed in hexane (10 ml).

Synthesis of hexagonal (ß) $NaGdF_4$ upconverting core (2 mol% Er^{3+}, 25 mol% Yb^{3+}, 10 mol% Y^{3+} doped) / $NaYF_4$ (5 mol% Tb^{3+}, 15 mol% Ce^{3+} doped) shell nanocrystals. The upconverting core $NaGdF_4$ nanocrystals were synthesized following a previously reported procedure.[142] Chloride salts of the lanthanide ions to a total of 0.5mmol were added to a 50 ml flask containing oleic acid (2 ml) and 1-octadecene (8 ml) and heated to 140 °C under vacuum for 60 min and cooled to room temperature. To this solution at room temperature, methanol solution (5 ml) of ammonium fluoride (2 mmol) and sodium hydroxide (1.25 mmol) was added and stirred for 30 min. The reaction vessel was then heated to 70 °C to remove methanol and subsequently heated to 280 °C (~10°C/min) under argon and maintained for 90 min. To this SNCs (α-$NaYF_4$ (5 mol% Tb^{3+}, 15 mol% Ce^{3+} doped)) in 1 ml octadecene was injected and ripened to yield core-shell NCs. After ripening the solution was cooled down to room temperature and the core-shell NCs were precipitated and washed as described above and dispersed in hexane (5 ml).

Determination of crystal yield of SNCs and amount injected for core-shell growth. The SNCs synthesized and dispersed in hexane were taken, and measured volume of the dispersion was transferred to a pre-weighed vial and the hexane then removed by bubbling with argon. The SNCs in the vial were dried over-night at 70 ºC under vacuum, and the vial was then weighed to determine the total organic and inorganic content (ligand+SNCs). The percentage of organic ligands were then determined by Thermogravimetric Analysis (TGA) and subtracted to obtain the total inorganic content in a given volume and the crystal yield. Three such measurements were done, averaged

and utilized for calculating the amount of SNCs injected (see Table D2 of the Appendix for details). The average inorganic crystal yield for the cubic (α) SNCs was between 70-80 %, and 80-90 % for the hexagonal (β) SNCs.

Characterization. Transmission electron microscopy (TEM) images were obtained from a JEOL JEM-1400 microscope operating at 80 kV and High-resolution (HR-TEM) images from a FEI Tecnai field-emission scanning transmission electron microscope operating at 200 kV. Hexane dispersions of the NCs were drop cast on a formvar carbon-coated grid (300 mesh Cu) and air-dried before imaging, size analysis of NCs from the images were obtained by measuring atleast 100 particles and averaged. TEM images of 2-D self-assembled NCs were obtained following a published procedure.[44] X-ray diffraction (XRD) patterns with a resolution of 0.05° (2θ) and a scan speed of 1 °/min, were collected using a Rigaku Miniflex diffractometer with a Cr source (Kα radiation, λ=2.2890 Å) operating at 30 kV and 15 mA. Thermo-gravimetric analysis was done using TA Instruments (SDT Q600), and the weight loss analyzed by heating from room temperature to 600 °C at the rate of 10 °C/min. Light scattering experiments were performed on a Brookhaven Instruments photon correlation spectrometer with a BI-200SM goniometer, a BI-9000AT digital autocorrelator, and a Melles Griot He-NE laser (632.8 nm) at a single scattering angle of 90°. Inductively coupled plasma mass spectroscopy (ICP-MS) analysis to determine the ratio of lanthanide ion concentration was carried out using a Thermo X-Series II (X7) quadrupole ICP-MS. Measured volume of hexane dispersion of NCs were carefully dried in a Teflon vial, then sealed and digested in concentrated nitric acid at 135 °C for 3 days and diluted with ultrapure water for ICP-MS analysis. Optical measurements were done using an Edinburgh Instruments

(FLS920) fluorimeter, a 980 nm laser diode coupled to a 100 µm core fiber and a xenon lamp were used as NIR, and UV excitation source respectively. The output from the laser diode was collimated using a fiber coupler and focused (power density 150 Wcm^{-2}) onto the NC dispersions held in a 1 cm path length quartz cuvette. All the obtained spectra were corrected for instrument sensitivity. High-angle annular dark-field (HAADF) images combined with electron energy-loss spectroscopy (EELS) were acquired on a FEI Titan 80-300 TEM (FEI company, Eindhoven, Netherlands), equipped with a CEOS image corrector and operated at 300 kV with a Gatan Tridiem ER energy filter (GIF) (Gatan Inc, Pleasanton, CA). EELS mapping was performed in STEM mode with a convergence angle of 8 mrad, and the collection angle was 15 mrad. The energy resolution of the system was 0.8 eV. Spectrum image acquisition and post-processing was done using the Gatan Digital Micrograph Software. STEM micrograph collection was performed using the FEI TIA software. NCs in solution were deposited directly onto ultrathin carbon film supported on a copper mesh grid (Ted Pella, Inc, Redding, CA) Samples were plasma cleaned for 40 sec to remove hydrocarbon contaminations using a O_2/H_2 gas mixture. The object pixel size for the EELS spectrum images was 3 Å with an acquisition time of 0.2 seconds per pixel, the dispersion per channel was 0.2 eV. During acquisition, the spatial drift of the specimen was compensated every 60 seconds.

Chapter 7. Hetero-Epitaxy in Colloidal Nanocrystals: Compressive *vs.* Tensile Strain Asymmetry

The fundamental rule of minimal lattice-mismatch between the substrate (here the core) and epilayer (here the shell) to generate conformal/isotropic core-shell nanocrystals (NCs), does not take into account the sign of mismatch caused by a compressive/tensile strained epitaxial layer. Exploiting the lanthanide contraction along the series, multiple compressive and tensile strained epitaxial hetero-structures of $NaLnF_4$ NCs have been investigated in this chapter. This rule breaks down when the sign of mismatch is taken into account and a strong asymmetric effect is observed between the compressive and tensile strained epitaxial growth. While the compressive strained shell growth is not conformal even with minimal mismatch, the tensile strained shell is conformal and pseudomorphic to the core, even with a relatively larger lattice mismatch. This chapter demonstrates the necessity of including the sign of mismatch as *a priori* design consideration in conformal thick epitaxial growth of colloidal core-shell NCs.

7.1. Introduction

Epitaxial growth of thin films revolutionized the semi-conductor industry in the past decades with a profound impact on everyday life. Recently, the greater interest of miniaturization has focused on materials in nanodimensions and a colloidal bottom-up approach to generate hetero-structured nanocrystals (NCs) is of high technological relevance in developing functional materials for diverse applications. These hetero-structured NCs can be developed either as a core-shell architecture, where one structure is spatially confined within the other or as anisotropic hetero-dimers and higher-order

organization without spatial confinement but fused along a common crystal plane.[192-194] The generality of obtaining such architectures are known to be driven by the magnitude of the lattice mismatch between the structures, where minimal mismatch allows for conformal overgrowth (core-shell) and anisotropic non-conformal structures with larger mismatch.[195] The core-shell conformal growth is unique as it allows for both integration and spatial confinement of different materials. Here, the minimal lattice mismatch rule for obtaining conformal growth (core-shell) is revisited which generally considers only the magnitude of the mismatch, but not the sign.

In hetero-epitaxy with lattice mismatched core (substrate) and shell (epilayer), the shell adapts to the lattice parameters of core and thus conformal overgrowth is possible when the mismatch is minimal and thus induces minimal strain. Theoretically, the general rule of minimal lattice mismatch for conformal overgrowth arises from this fact, but does not consider the sign of mismatch. The lattice mismatch of the core and shell in hetero-epitaxy is given by the following equation: $f = (a_c - a_s)/a_s$, where a_s, and a_c are the lattice parameter of the shell and core respectively. During epitaxy, the lattice parameter of the shell undergoes either a compressive strain ($a_s > a_c \rightarrow f < 0$), or a tensile strain ($a_s < a_c \rightarrow f > 0$) to adapt pseudomorphically to the core lattice parameter. Such adaptation for pseudomorphic growth causes a considerable interfacial strain which increases with each additional layer, and beyond a critical thickness pseudomorphic growth is no longer possible resulting in strain relaxation and deterioration of the core-shell structure. The effect of strain on the epitaxial thin film growth on flat substrates (2D structures) is documented, and is known to be significantly different between the compressive and tensile strain. For example, in the widely studied silicon-germanium (SiGe) system, a

tensile strained Si layer on $Ge_{0.30}Si_{0.70}$ produces a flat/smooth surface, whereas a compressive strained Ge layer on $Ge_{0.60}Si_{0.40}$ results in a rough surface due to strain relaxation by island formation.[196] In epitaxial growth with larger misfits (> 5%) as in Cu-Pd heteroepitaxy, the tensile strained Cu conformally grows on Pd for about 9 monolayers (MLs) while the compressive strained Pd on Cu substrate relaxes due to strain within 1-2 MLs.[197-199] In this context it is not clearly established how the sign of misfit affects hetero-epitaxial growth in zero-dimensional (0D) colloidal NCs and it is generally not considered as a parameter in core-shell design.

Unlike the advancement and availability of multiple growth techniques for 2D thin film epitaxial growth, the choice of hetero-structured colloidal NCs (0D) that can be synthesized under the same reaction conditions, while simultaneously allowing for tuning the magnitude and sign of epilayer mismatch is limited and challenging. To overcome this fundamental challenge and taking advantage of the unique properties of lanthanide series, lanthanide-based NCs are utilized to investigate the compressive/tensile strain effect on hetero-epitaxial growth. Lanthanide elements along the series have very similar chemical properties while their ionic radii gradually decreases with increasing atomic number from lanthanum to lutetium (La^{3+} r = 1.300 Å to Lu^{3+} r = 1.117 Å), generally referred as the lanthanide contraction. This unique property of lanthanides with similar chemical identity and a gradual change in their physical property along the series allows for a highly flexible template to investigate the hetero-structure growth under identical growth conditions that cannot be pursued with any other combinations in the Periodic Table. The change in ionic radii result in a gradual decrease of the crystal lattice parameters with increasing atomic number providing a suitable handle for precise

manipulation of both the magnitude and sign of the epilayer mismatch. Yttrium (Y^{3+}) is chemically similar to the lanthanides and its ionic radii (r = 1.159 Å) is between that of dysprosium (Dy^{3+} r = 1.167 Å) and holmium (Ho^{3+} r = 1.155 Å). Utilizing the hexagonal phase (β) $NaYF_4$ as core NCs, epitaxial layers of $NaLnF_4$ (Ln: Gd, Tb, Dy, Tm, Yb, Lu) can be generated with increasing tensile/compressive strain (from ± 0.5% to ± 2%) as illustrated in Table 7-1. While the epitaxial growth of larger lanthanides (Gd, Tb, and Dy) results in compressive strain, the smaller lanthanides (Tm, Yb, and Lu) undergo a tensile strain relative to the $NaYF_4$ core.

Table 7-1. Ionic radii of Ln^{3+} ions,[200] the unit cell parameters of hexagonal phase (β) $NaLnF_4$ employed in the study, and the percentage of compressive/tensile strain lattice mismatch relative to the core $NaYF_4$ NCs.

		Gd	Tb	Dy	Y	Tm	Yb	Lu
● Ln^{3+} Ionic radius* (Å)		1.193	1.180	1.167	1.159	1.134	1.125	1.117
β-$NaLnF_4$ unit cell 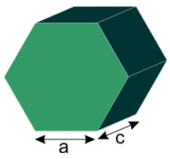	Volume (Å³)	113.0	111.9	110.3	108.6	107.2	105.7	104.1
	a (Å)	6.020	6.008	5.985	5.960	5.953	5.929	5.901
	c (Å)	3.601	3.580	3.554	3.530	3.494	3.471	3.453
		Compressive Epilayer  Substrate				Tensile Epilayer  Substrate		
% Lattice mismatch with β-$NaYF_4$	a	-1.01	-0.81	-0.42		+0.12	+0.52	+0.99
	c	-2.01	-1.42	-0.68		+1.02	+1.68	+2.18
		⟸ Increasing Compressive Strain				⟹ Increasing Tensile Strain		

* Ln^{3+} ionic radii for eight coordinate species.

The experimental conditions for the core β-$NaYF_4$ NCs, and epitaxial overgrowth were designed to be identical irrespective of the magnitude/sign of mismatch to determine the interfacial strain dependent effect on hetero-epitaxial growth.

i. β-$NaYF_4$ core NCs were synthesized at 300 ˚C following published procedures;[42,43]

ii. Epitaxial overgrowth was performed directly on the core NCs at 300 ˚C by a successive injection and self-focusing approach (demonstrated in Chapter 6),[174] utilizing respective cubic (α)-$NaLnF_4$ (Ln: Gd, Tb, Dy, Tm, Yb, Lu) sacrificial nanocrystals (SNCs);

iii. To β-$NaYF_4$ core NCs (1 mmol), SNCs to a total of 1.5 mmol were injected and epitaxial shell growth achieved by successive defocusing and self-focusing cycles (0.5 mmol × 3), the focusing time between each cycle was 10 min.

The effect of compressive/tensile strain and the magnitude of lattice mismatch between the core and the shell material on the epitaxial growth properties are discussed below.

7.2. Results and Discussion

7.2.1. Compressive/tensile epitaxial growth with minimal lattice mismatch

The lattice parameters of $NaDyF_4$ and $NaTmF_4$ are almost identical to that of $NaYF_4$ (mismatch < 1%) as shown in Table 7-1, and based on the minimal lattice mismatch rule epitaxial growth for both should be possible. Epitaxial shell growth of $NaDyF_4$ and $NaTmF_4$ on $NaYF_4$ core NCs was performed under identical growth conditions and the TEM images of the respective core and core-shell NCs synthesized are shown in Figure 7.1. The core $NaYF_4$ NCs (Figure 7.1A-B) are highly monodisperse and quasispherical in shape. However, in case of core-shell NCs, only the tensile strained $NaTmF_4$ shell growth

(Figure 7.1C) resulted in the same morphology as the core NCs (*i.e.* quasispherical), while the compressive strained $NaDyF_4$ shell (Figure 7.1D) resulted in anisotropic growth. Given the almost identical mismatch relative to the core lattice parameters and also being very minimal, these two different morphologies of the core-shell NCs are quite intriguing, as anisotropic growth due to strain relaxation is generally known to happen only with relatively larger mismatch.[195]

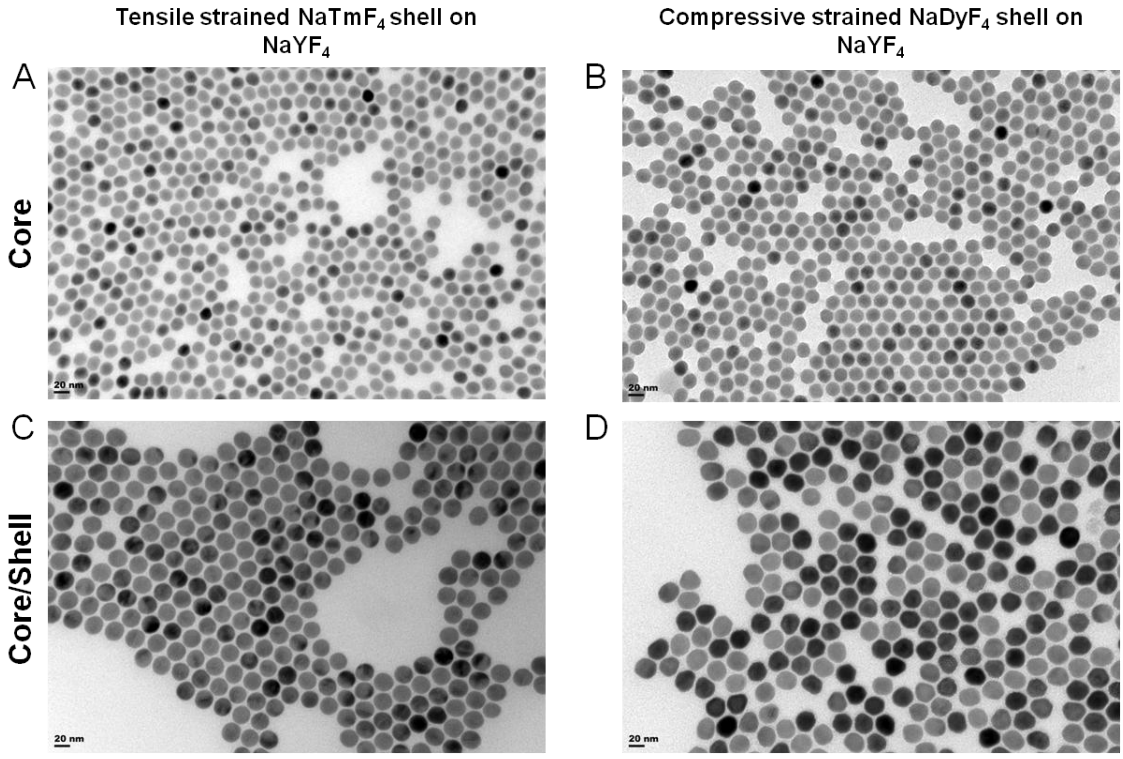

Figure 7.1. TEM images of **(A,C)** $NaYF_4$ core, and tensile strained $NaTmF_4$ shell on $NaYF_4$ core NCs respectively, and **(B,D)** $NaYF_4$ core, and compressive strained $NaDyF_4$ shell on $NaYF_4$ core NCs respectively. (All images are of same magnification 300K).

The shell growth was performed by three successive defocusing and self-focusing cycle following the procedure, as described in Chapter 6. To understand the shape evolution during shell growth, the core-shell NCs after each cycle was analyzed. The tensile shell growth of $NaTmF_4$ on $NaYF_4$ core NCs shows a uniform quasispherical

shape after each cycle (Figure E1 of the Appendix), and almost identical to the core NCs. However, in case of the compressive shell growth of $NaDyF_4$ on $NaYF_4$ core NCs the shape deteriorates to anisotropic structures after each cycle (Figure E2 of the Appendix). This demonstrates that the epitaxial growth and strain relaxation of $NaDyF_4$ and $NaTmF_4$ on $NaYF_4$ are not the same even with such minimal lattice mismatch.

To gain insights into the core-shell structure, high-angle annular dark-field (HAADF) images were obtained for the $NaYF_4$/$NaTmF_4$ and $NaYF_4$/$NaDyF_4$ core/shell NCs shown in Figure 7.2. The HAADF images show a clear contrast between the core (dark) and shell (bright) attributed to the much larger atomic number of the lanthanide ion in the shell (Tm and Dy) compared with the yttrium in the core. The $NaYF_4$/$NaDyF_4$ core/shell NCs show that, in spite of shell growth the NCs are highly anisotropic in shape when compared with the $NaYF_4$/$NaTmF_4$ core/shell NCs. In case of the $NaYF_4$/$NaTmF_4$ core/shell NCs higher resolution images as shown for the $NaYF_4$/$NaDyF_4$ core/shell NCs could not be obtained, as they were more prone to beam damage (the reasons are discussed in detail in section 7.2.3). However, the HAADF image of $NaYF_4$/$NaTmF_4$ core/shell NCs still shows an appreciable contrast between the substrate and epitaxial layer confirming their core-shell morphology. To confirm further the highly uniform quasispherical shape of the $NaYF_4$/$NaTmF_4$ core/shell NCs a low resolution HAADF image is shown in Figure 7.3. The packing of these $NaYF_4$/$NaTmF_4$ core/shell NCs as hexagonal close-packed arrays demonstrate the highly uniform size and shape, compared to that of $NaYF_4$/$NaTmF_4$ core/shell NCs. Although the lattice mismatch was relatively small in these core-shell NCs, the analysis demonstrates that the growth and shape evolution are not the same between the tensile/compressive strained shell growth.

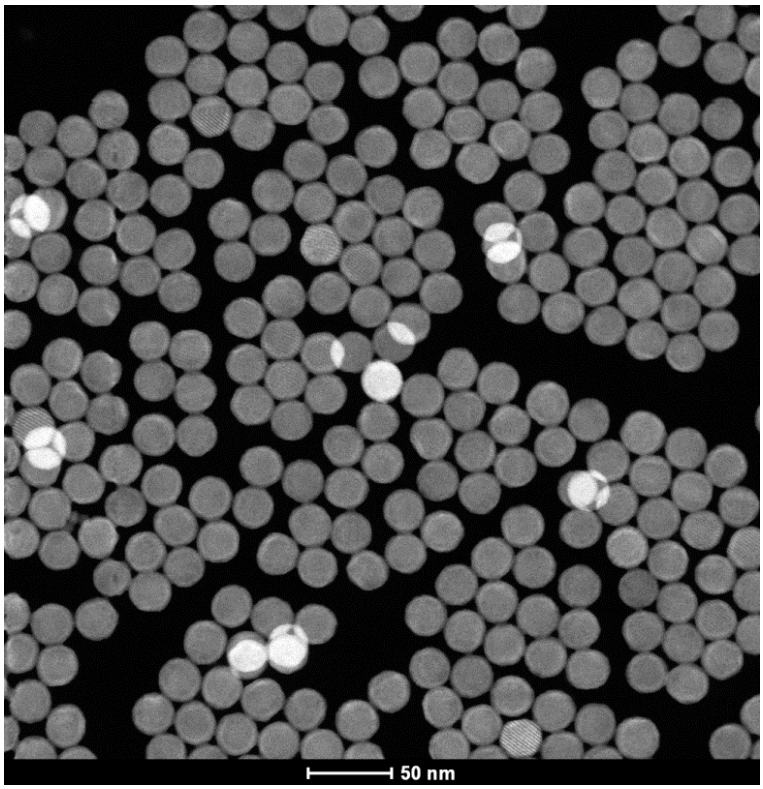

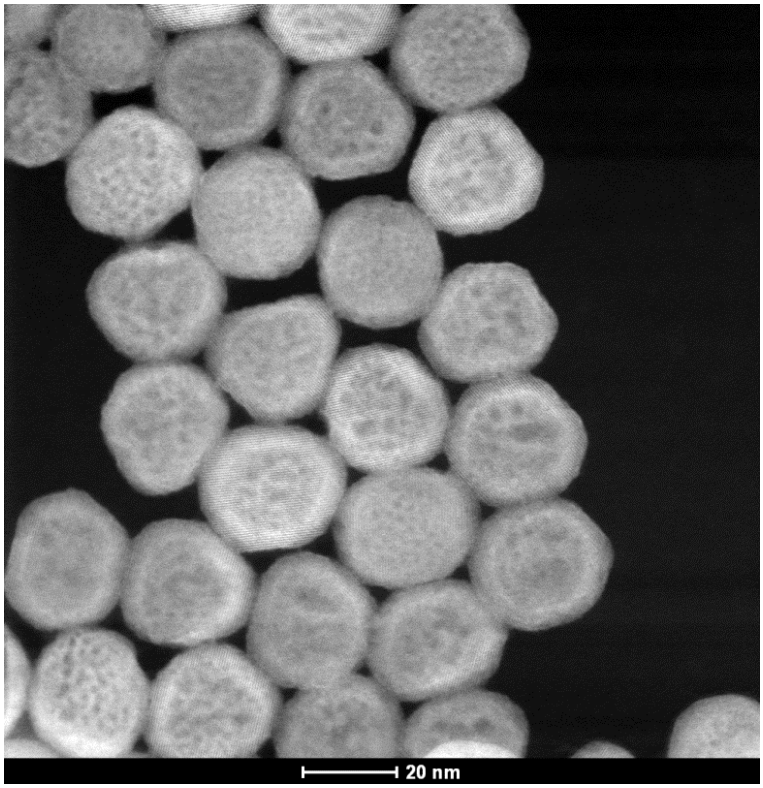

Figure 7.2. HR-HAADF images of $NaYF_4/NaTmF_4$ core/shell NCs **(top)**, and $NaYF_4/NaDyF_4$ core/shell NCs **(bottom)**.

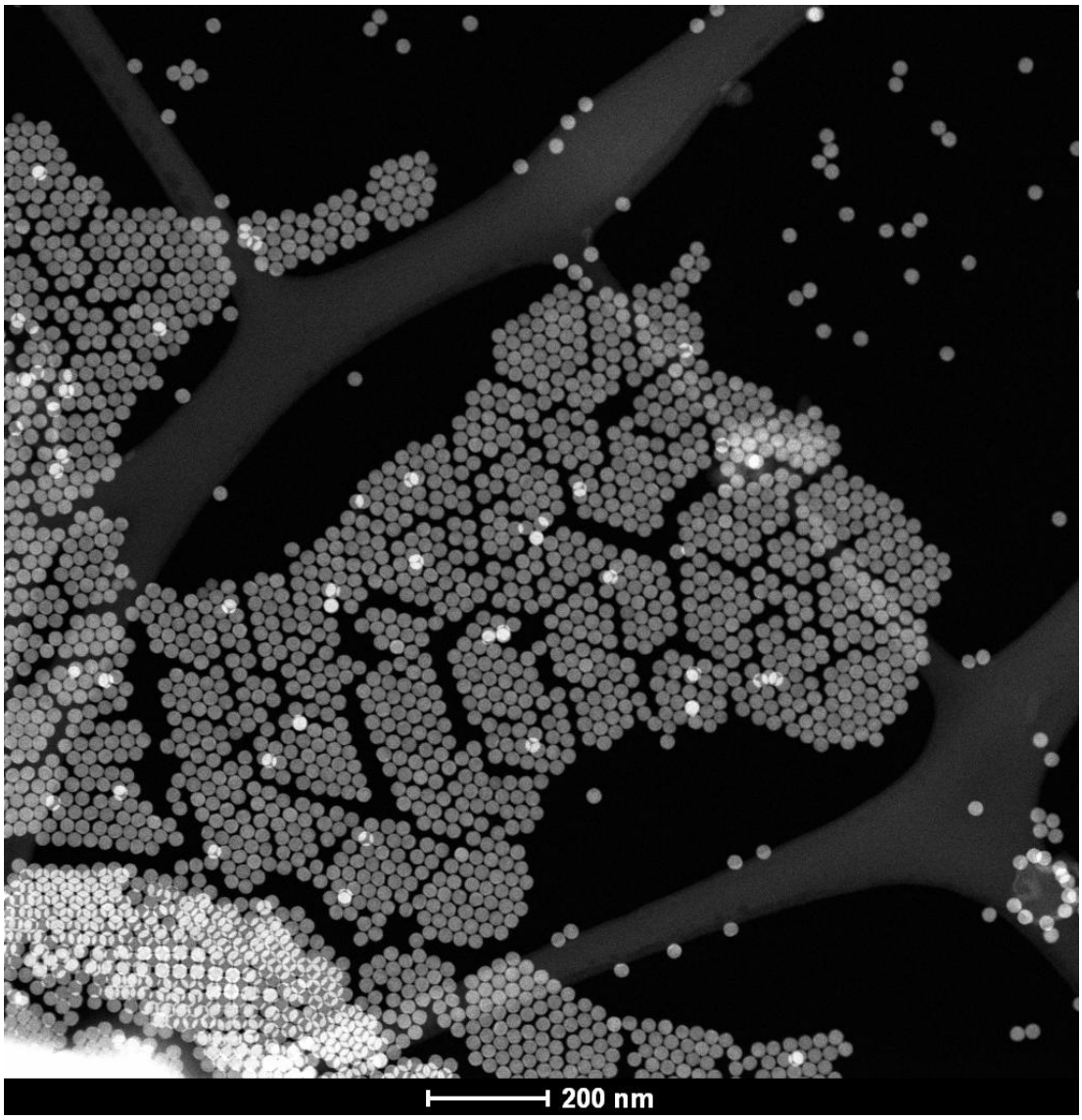

Figure 7.3. Low-magnification HAADF image of $NaYF_4/NaTmF_4$ core/shell NCs.

7.2.2. Compressive/tensile epitaxial growth with larger lattice mismatch

Compared to other colloidal hetero-structures, the advantage of the lanthanide series is the gradual contraction of the size of lanthanide ions along the series. Utilizing this unique advantage, relatively larger lattice mismatched core-shell NCs were investigated employing $NaYF_4$ as core NCs. Tensile strained ($NaYbF_4$ and $NaLuF_4$), and compressive strained shells ($NaTbF_4$ and $NaGdF_4$) with increasing lattice mismatch relative to the

$NaYF_4$ core NCs (as shown in Table 7-1) were synthesized under identical growth conditions as described above.

The tensile strained epitaxial growth of $NaYbF_4$ and $NaLuF_4$ on $NaYF_4$ core NCs (Figure 7.4 A and C respectively) resulted in uniform quasispherical core-shell NCs. The increase in lattice mismatch did not affect the isotropic shape of the core-shell NCs in both the tensile strained epitaxial growth. However, in case of the compressive strained epitaxial growth of $NaTbF_4$ and $NaGdF_4$ on $NaYF_4$ core NCs (Figure 7.4 B and D respectively) resulted in anisotropic core-shell NCs. Especially, the $NaYF_4/NaGdF_4$ core/shell NCs with larger compressive strain are highly anisotropic compared to all other core/shell structures investigated.

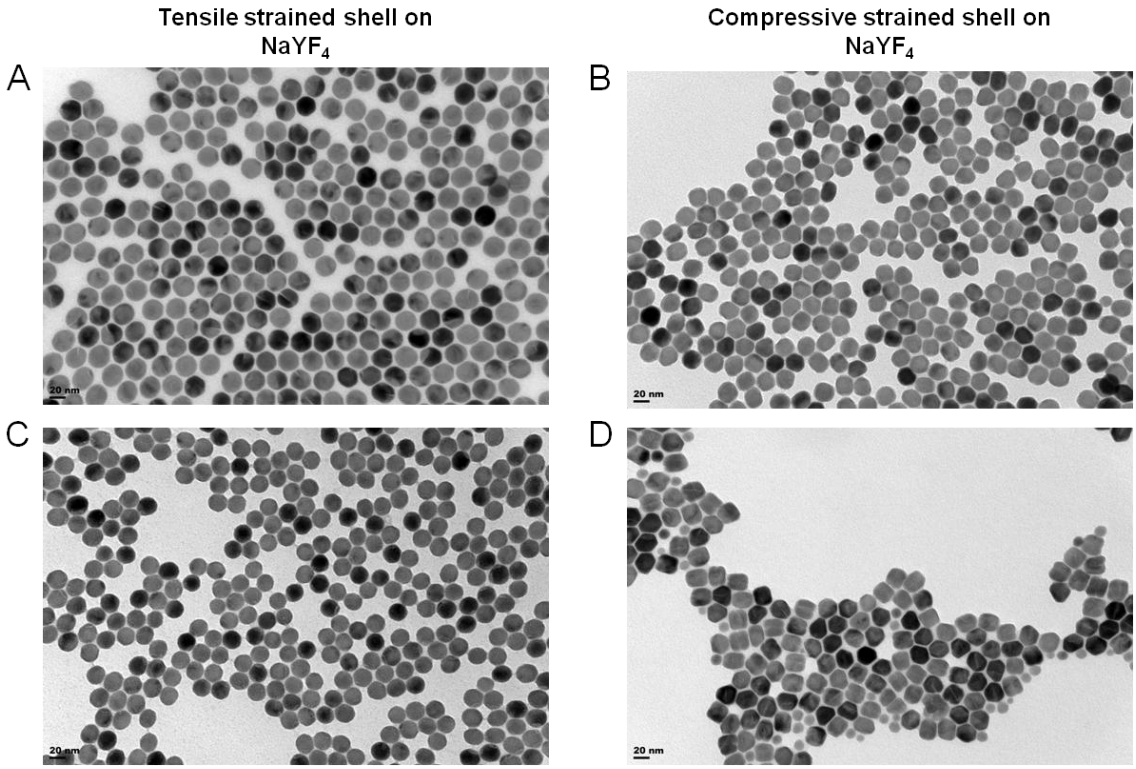

Figure 7.4. TEM images of **(A, C)** tensile strained $NaYbF_4$ shell, $NaLuF_4$ shell on $NaYF_4$ core NCs respectively, and **(B, D)** compressive strained $NaTbF_4$ shell, $NaGdF_4$ shell on $NaYF_4$ core NCs respectively. (All images are of same magnification, 300K).

The HAADF images for the tensile strained shell growth shown in Figure 7.5, show a clear contrast between the core (dark) and shell (bright). Moreover, the increase in lattice mismatch did not show any deteriorating effect on the shape of the core-shell NCs which remained quasispherical. The HAADF images for the compressive strained shell growth shown in Figure 7.6, show the core and shell morphology of the NCs. However, the core-shell NCs are heavily deformed and especially in case of the $NaGdF_4$ shell with the largest percentage of compressive mismatch. $NaLuF_4$ (tensile strained), and $NaGdF_4$ (compressive strained) both have relatively equal magnitude of mismatch with $NaYF_4$ (Table 7-1), but show uniquely different growth behavior. Low resolution images (Figure E3 of the Appendix) show that the $NaYF_4$/$NaLuF_4$ core/shell NCs are highly uniform, while the $NaYF_4$/$NaGdF_4$ core/shell NCs are anisotropic along with a large excess of SNCs that have not deposited on the core NCs (discussed in section 7.2.3). This further confirms the asymmetric growth of the epitaxial layers between the compressive and tensile strained growth.

The analysis described thus far explicitly addresses the shape evolution of the core-shell NCs by varying both the magnitude and sign of the epitaxial layer mismatch. The increase in lattice mismatch with tensile strained epitaxial growth did not affect the shape of the core-shell NCs (quasispherical) resulting in uniform shell growth. In case of compressive strained epitaxial growth, even with minimal lattice mismatch, the shell growth resulted in anisotropic core-shell NCs, which deteriorates with increase in the magnitude of mismatch.

In the next section, the analysis of coherent/pseudomorphic growth of the epitaxial layer to that of the core (substrate) NCs is further discussed.

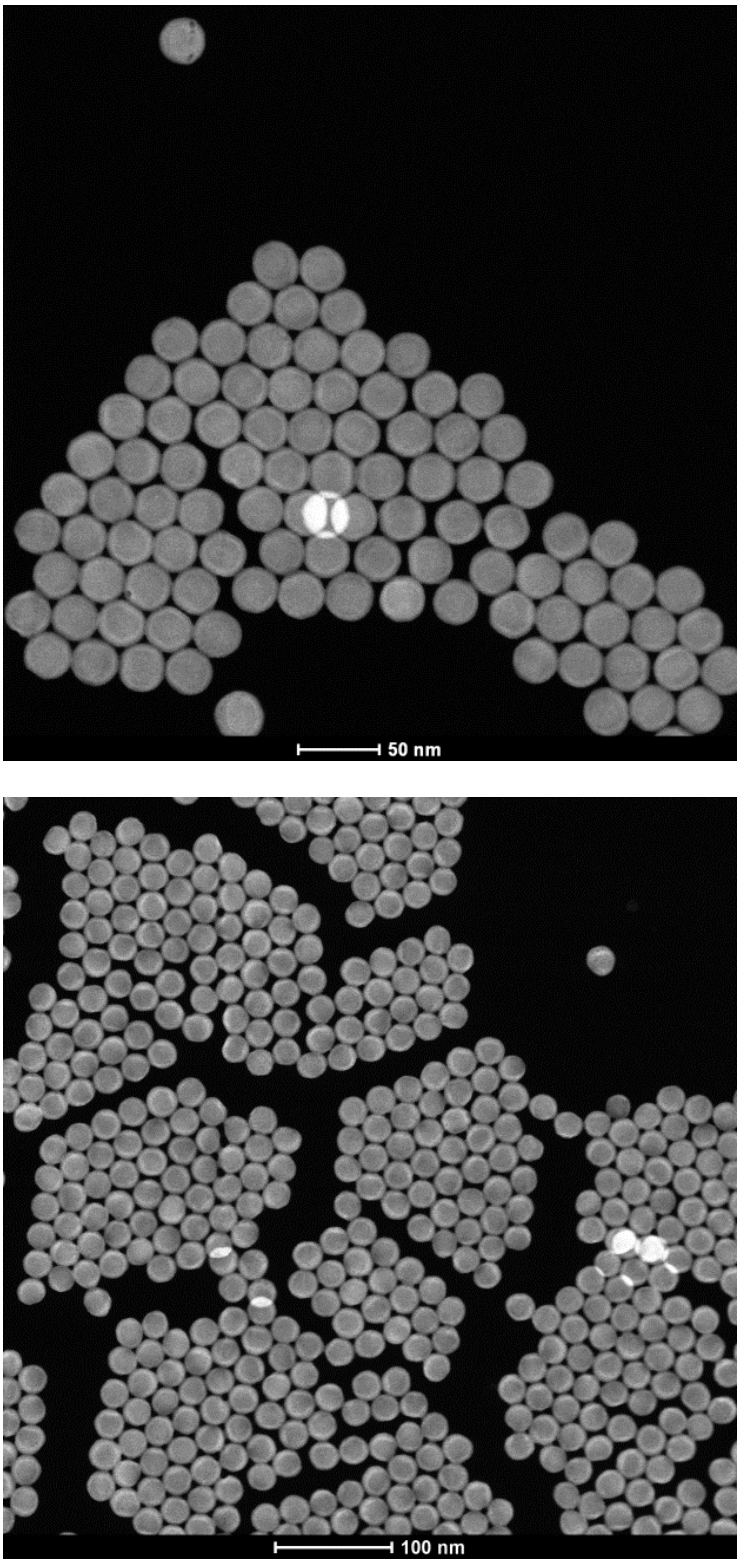

Figure 7.5. HR-HAADF images of $NaYF_4/NaYbF_4$ core/shell NCs **(top)**, and $NaYF_4/NaLuF_4$ core/shell NCs **(bottom)**.

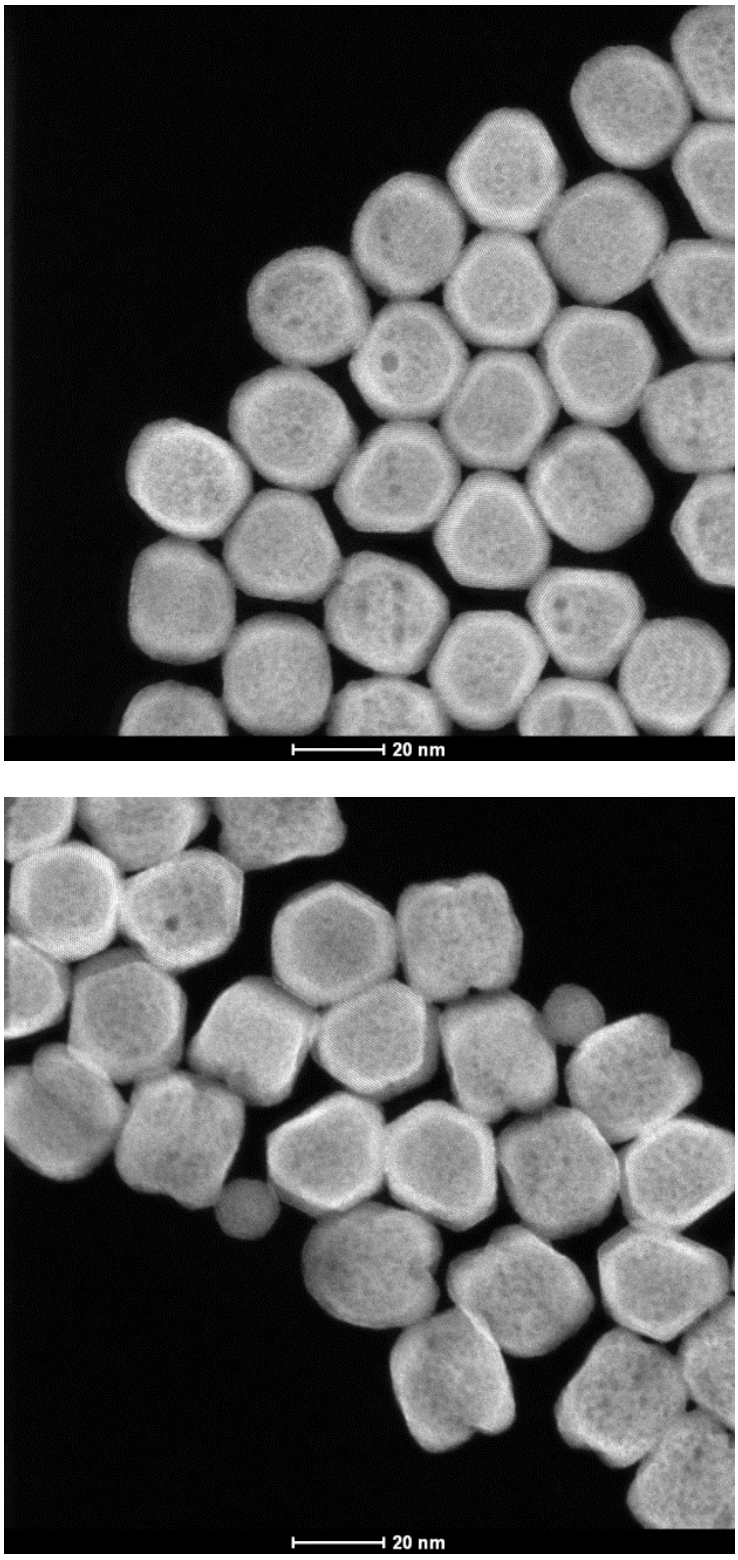

Figure 7.6. HR-HAADF images of $NaYF_4/NaTbF_4$ core/shell NCs **(top)**, and $NaYF_4/NaGdF_4$ core/shell NCs **(bottom)**.

7.2.3. Pseudomorphic epitaxial shell growth

In lattice mismatched epitaxial growth, the epitaxial layer adapts to the lattice parameter of the substrate (core) and grows coherently (pseudomorphic) to the substrate, referred as pseudomorphic epitaxial growth. When the mismatch is larger, the interfacial strain due to this adaptation results in larger interfacial strain, and pseudomorphic growth is not possible.[201] Considering that the hetero-epitaxial growth studied here is well within the minimal mismatch rule (< 2%), it should be safe to presume that pseudomorphic epitaxial growth could be possible with these core-shell structures.

The core-shell NCs studied here are all of the same hexagonal (β) crystal structure. The X-ray diffraction peaks of the epitaxial layers are identical to the core (β-$NaYF_4$), but shift either to smaller/larger angles (2θ) depending on the unit-cell size. For the smaller lanthanides (Gd/Tb/Dy) relative to that of yttrium, the peak shifts to smaller 2θ values with decrease in size, and vice versa for the larger lanthanides (Tm/Yb/Lu). The core-shell NCs synthesized have more of the shell material (1.5 mmol) than the core (1 mmol) and thus should dominate the X-ray diffraction peaks.

The synthesized core-shell NCs were analyzed and the X-ray diffraction patterns are shown in Figure 7.7 A-B. In case of the tensile strained epitaxial growth, all the peaks clearly align with the reference pattern of β-$NaYF_4$ (core) confirming a pseudomorphic epitaxial growth without any interfacial strain induced relaxation. For the compressive strained epitaxial growth, none of the peaks align with the reference pattern of β-$NaYF_4$ (core) and are shifted to smaller angles relative to the shell lattice parameter. Comparison of the peaks with the core and shell reference pattern for each of the hetero-structured core-shell NCs is provided in Figure E4-5 of the Appendix.

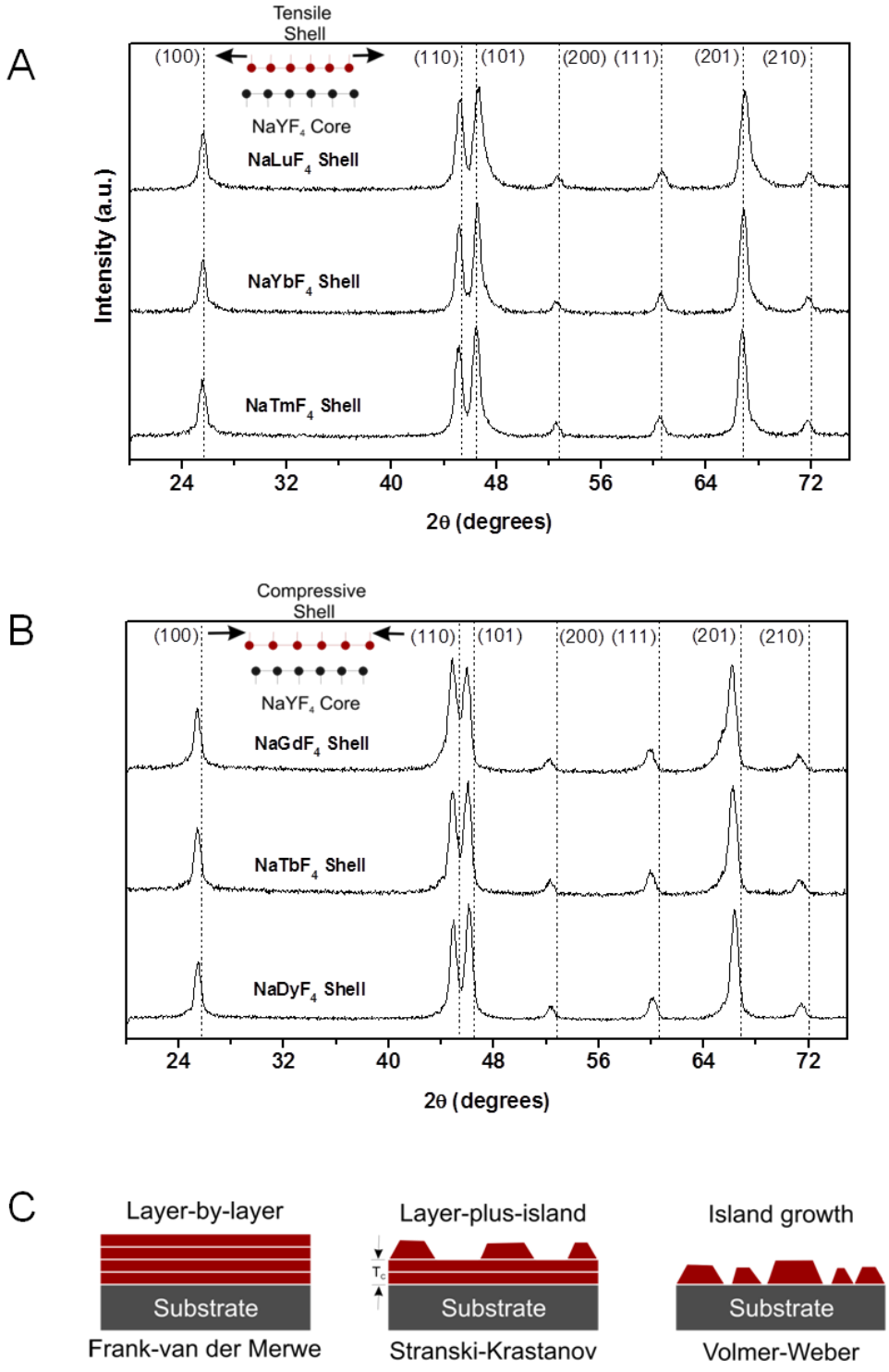

Figure 7.7. (A) XRD patterns of core-shell NCs with tensile strained shell on $NaYF_4$ core NCs, **(B)** XRD patterns of core-shell NCs with compressive strained shell on $NaYF_4$ core NCs, (*black dotted lines in both the patterns are the standard reference lines of β-$NaYF_4$: JCPDS 016-0334*), and **(C)** Schematic illustration of the three different growth modes in epitaxial growth.

The deviation in the growth mechanism between the compressive and tensile strained epitaxial layers can be discussed based on the different growth modes illustrated in Figure 7.7C. For the tensile strained epitaxial growth, the shell growth is both conformal (isotropic) and pseudomorphic (coherent/commensurate) to the core NCs. The increase in lattice mismatch (magnitude) did not affect the growth of uniform shell on the core $NaYF_4$ NCs. Thus, the tensile strained epitaxial core-shell growth is an ideal layer-by-layer growth process as that illustrated by the FM (Frank-van der Merwe) growth mode.[202] In case of the compressive strained epitaxial core-shell growth, the shell growth is both non-conformal (anisotropic) and non-pseudomorphic (incoherent) to the core NCs. This is the case even with minimal mismatch and it deteriorates with increasing mismatch (magnitude). However, considering that they still show core-shell morphology, the growth mode is a combined layer-by-layer and island growth mode as that illustrated by the SK (Stranski-Krastanov) growth mode (layer-plus-island).

The deviation of the compressive strained epitaxial growth to the SK growth mode, compared to the tensile strained epitaxial growth which follows the FM growth mode, confirms the asymmetric growth of compressive and tensile strained epitaxial layers. This deviation in growth mode arises from the anharmonicity in the interatomic interactions. Interatomic interactions between the attractive and repulsive part are not harmonic, and the resistance to compression is stronger than tension. Thus the interfacial strain during hetero-epitaxy is anharmonic, and is heavily influenced by the sign of mismatch between the core and epitaxial layer as illustrated in Figure 7.8. The stronger resistance to compression causes the interfacial strain between the core and epitaxial layer to increase

substantially resulting in strain induced shape deformation, which is ideally not the case with the tensile strained epitaxial growth.

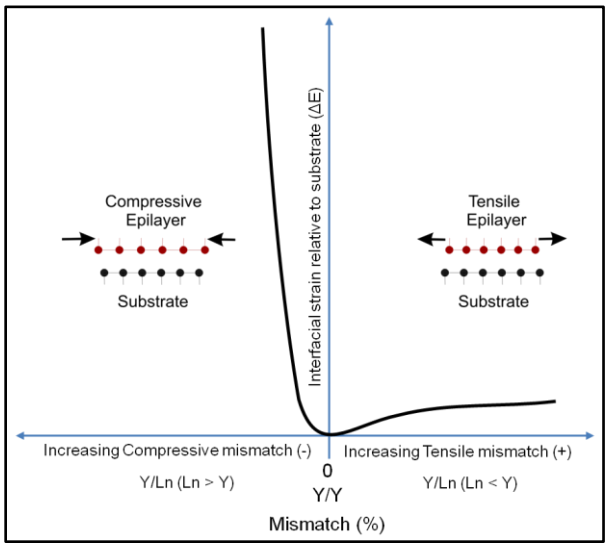

Figure 7.8. Schematic illustration of the anharmonicity in interfacial strain between the substrate ($NaYF_4$) and compressive/tensile mismatched epitaxial layers.

In case of compressive strained shell growth the interfacial strain is much larger (even with minimal mismatch), the adatoms depositing on the surface diffuse to energetically favorable sites thus restricting layer-by-layer growth. The diffused adatoms form islands (hill-lock formation) and grow as relaxed islands on the substrate, which addresses both the anisotropic and incoherent growth observed with the compressive strained shell.[47] Especially for the case of $NaYF_4/NaGdF_4$ core/shell NCs with larger compressive mismatch, the adatoms deposition needs to compete heavily with the surface diffusion and relaxation process caused by much larger interfacial strain. Thus the growth is no longer diffusion-limited, but reaction-limited which explains the presence of large excess of smaller SNCs after the same reaction time (Figure E3A of the Appendix).

The tensile strained epitaxial growth on the other hand experiences only a minimal interfacial strain even with increasing lattice mismatch (magnitude). This affords both

isotropic and pseudomorphic epitaxial layer growth. However, the interfacial strain still remains and when exposed to high energy electron beam they relax and undergo heavy and rapid beam damage. The TEM images of the $NaYF_4/NaLuF_4$ core/shell NCs in Figure E6 of the Appendix clearly show beam damage *along* the core-shell interface. Hence it still remains a challenge to image these core-shell NCs at very high resolution. A very recent study exploited the use of cryo-TEM to overcome the beam damage issues with core-shell NCs, which might potentially help to characterize further these core-shell NCs.[203]

7.2.4. Generality of the compressive *vs.* tensile strain asymmetry

Colloidal hetero-epitaxy in various structures has been investigated in literature. However, as discussed previously only the magnitude of lattice mismatch is highlighted and not the sign. Evidence from previous literature show that all the well-established hetero-epitaxial growth (with strong evidence of isotropic/conformal growth) are indeed with a tensile strained epitaxial shell, and none with a compressive strained epitaxial shell. For example, Yang and coworkers demonstrated the isotropic/conformal growth of Pd on Pt, where the mismatch is only 0.77% (Pd is smaller than Pt and undergoes a tensile strain).[195] In spite of the minimal mismatch, to date no convincing evidence of isotropic/conformal growth of Pt on Pd (compressive strained shell) has been reported. A recent computational study on the Pt and Pd core-shell combination has revealed that the Pd-core/Pt-shell structures are the least structurally stable, while the inverted Pt-core/Pd-shell are more stable.[204] Atomic resolution structural characterization of Pt-Pd core-shell nanocrystals by Nuzzo and coworkers has also reported discontinuous and non-isotropic

Pt shell growth on Pd nanocrystals, which further confirms the observation reported in this chapter with respect to compressively strained shells. [205]

In case of large-mismatched hetero-epitaxial growth, there is convincing evidence of isotropic/conformal growth with tensile strained epitaxial shells. Conformal epitaxial growth of Pd on Au with large lattice mismatch of 4.71% has been reported, where Pd which is smaller than Au undergoes a tensile strain.[206,207] Xia and coworkers demonstrated the epitaxial growth of Cu on Pd with a lattice mismatch of 7.1%.[208] Based on their success, they suggested that the requirement of minimal lattice mismatch should be examined again. Considering that Cu is smaller than Pd and undergoes tensile strain, the successful demonstration of Cu on Pd is clearly due to the compressive *vs.* tensile strain asymmetry. Tensile strained epitaxial shell with very large mismatch as in Au-core/Ni-shell (13.6%) has also been reported.[209] Uniquely, for all these structures discussed above no evidence of the inverted structures are known to date (*i.e.* with compressive strained shells).

7.3. Conclusions

In summary, the general rule of minimal lattice mismatch to grow epitaxial core-shell hetero-structures have been analyzed in $NaLnF_4$ NCs. The contraction of lanthanides along the series allowed for a flexible template to tune simultaneously the magnitude and sign of lattice mismatch relative to the core NCs. The results demonstrate the asymmetric effect in core-shell growth between the compressive and tensile strained shells. While the tensile strained shell growth (+ mismatch) is conformal and pseudomorphic to the core NCs even with a larger mismatch, the compressive strained shell growth (- mismatch) were not, even with a minimal mismatch. These results demonstrate that for

isotropic/pseudomorphic core-shell design the sign of lattice mismatch is the important parameter, and not the widely employed rule of minimal mismatch which only considers the magnitude of the mismatch. In general, for any two combinations of lattice mismatched materials, the smaller lattice parameter material as a shell should allow for isotropic/pseudomorphic core-shell growth, and the reverse configuration is not possible. The study performed here explicitly focused on thick shell growth and the importance of the sign of mismatch on epitaxial growth. In case of compressive strained shells, thin shells of 1-2 MLs are still possible when the lattice mismatch (magnitude) is minimal. It might however, also vary with the size of core NCs, which needs further attention and exploration. However, at any given condition it is easier to grow tensile strained shells of multiple MLs (> 2), which is both conformal and pseudomorphic to the core NCs, than a compressive strained shell.

7.4. Experimental Section

The synthesis of all the core-shell NCs described in Chapter 7, were performed following the self-focusing by ripening procedure described in Chapter 6. All the sacrificial NCs used were synthesized following the cubic SNCs synthesis described in Chapter 6. Undoped core NCs β-$NaYF_4$ (1 mmol) was synthesized following published procedure. The core-shell synthesis was performed by a layer-by-layer growth process directly on the core NCs, employing 0.5 mmol of SNCs (α-$NaLnF_4$, Ln: Gd, Tb, Dy, Tm, Yb, Lu) in each step growth, and repeated 3 times (total 1.5 mmol SNCs). The final core-shell samples were retrieved and washed as described in Chapter 6, before dispersing them in 10 ml hexanes for further analysis. The characterization by TEM, XRD, and HAADF of the core-shell samples were performed as described in Chapter 6.

Chapter 8. Conclusions and Possible Future Work

8.1. Conclusions

The synthesis and potential application of colloidal sodium lanthanide fluoride nanocrystals as nano-bioprobes have been investigated in this dissertation. The utilization of these nanocrystals as optical-imaging probes for targeted diagnosis of cancer cells, and as T_1 relaxivity enhancement magnetic resonance imaging (MRI) probes are demonstrated in Chapters 3, 4, and 5. The challenges in controlled growth of core-shell nanocrystals with well-defined and tunable epitaxial layers have been addressed with a novel synthetic strategy utilizing the common physical phenomenon of ripening (Chapter 6). Finally, in Chapter 7 the established rule of minimal lattice mismatch to grow epitaxial layers is revisited, and the effect of the sign of lattice mismatch in generating conformal/isotropic shell growth is demonstrated. The developed strategy in Chapter 6 can potentially be used for colloidal nanocrystals in general, and the effect of the sign of lattice mismatch demonstrated in Chapter 7 is universal for epitaxial shell growth in any colloidal nanocrystal.

Chapter 1 provides a general introduction to colloidal nanocrystals, and the significance of size control and surface properties are highlighted. The requirements of controlled epitaxial shell growth to generate core-shell nanocrystals have been discussed.

Chapter 2 describes in detail the synthesis of colloidal nanocrystals, and especially that of colloidal lanthanide fluoride nanocrystals and their surface modification techniques. Their potential use in optical imaging and magnetic resonance imaging (MRI), and the challenges in developing these nanocrystals for these applications have been discussed.

The synthesis of core-shell nanocrystals and the limited knowledge in the actual growth mechanism of the shell are also discussed.

Chapter 3 demonstrates the synthesis of colloidal upconverting nanocrystals (UCNCs) stabilized with hydrophobic surface oleate ligands and subsequent replacement of the surface oleates ligands with biocompatible amphiphilic polyvinylpyrrolidone (PVP). The exchange of the surface ligands with amphiphilic PVP makes them dispersible in a wide range of solvents such as chloroform, dichloromethane, ethanol, dimethyl sulfoxide, dimethylformamide, and water. The success of the ligand replacement was confirmed by growing a thin silica shell on the PVP-stabilized UCNCs utilizing the affinity of silica to PVP. Silica-coated UCNCs described here were also compared with the silica-coated UCNCs synthesized by reverse-microemulsion synthesis. The results demonstrate that the PVP-stabilized and subsequently silica-coated UCNCs had a longer colloidal stability (5 days) compared to the silica-coated UCNCs by reverse-microemulsion synthesis (1-2 days).

The limited shelf-life of the silica-coated UCNCs by both methods led to the investigation of end-group functionalized PVP described in Chapter 4, as a single-step protocol for phase-transfer of UCNCs to target specifically human prostate cancer cells (LNCaP). End-group functionalized PVP with a terminal carboxylic acid/amine group were synthesized by radical polymerization of 1-vinylpyrrolidone. The developed ligand-exchange strategy in Chapter 3 was utilized, and the UCNCs were phase-transferred to water using either PVP-COOH or PVP-NH_2. To confirm the reactivity of the surface bound PVP-COOH ligands, coupling reaction with bi-functional molecules were performed and confirmed by zeta-potential analysis. Having established the reactivity of

surface PVP-COOH ligands, the UCNCs were studied for specific labeling of LNCaP cells which over-express prostate specific membrane antigen (PSMA). The carboxylic acid group of the PVP-COOH coated UCNCs were coupled to an antibody (*i.e.* anti-PSMA) which recognises the over-expressed membrane antigen (PSMA) of LNCaP cells. The incubated LNCaP cells with the antibody-modified UCNCs and UCNCs without any antibody under fluorescence microscope clearly demonstrated the specific labeling of only the antibody-modified UCNCs. The specificity was further confirmed using PC3 cells (a prostate cancer cell line which does not over-express PSMA), and no specific labeling of the antibody-modified UCNCs was observed. This strategy of using end-group functionalized PVP combines the advantages of the biocompatible nature of PVP, while simultaneously allowing for specific bioconjugation reactions and targeting of cancer cells.

The limitations of previously synthesized gadolinium-based NCs for MRI applications have been addressed in Chapter 5 by developing a synthetic procedure to obtain ultrasmall size-tunable $NaGdF_4$ NCs. The precise control of NC size with the developed procedure allowed, for the first time, a systematic investigation on the effect of surface gadolinium ions towards T_1 relaxivity enhancement. The results show that the surface gadolinium ions are the major contributors for the T_1 relaxivity enhancement, and that previous reports on gadolinium-ions in the core and the surface co-operatively enhancing the T_1 relaxivity are not true. Further analysis also shows that the surface gadolinium ions on a larger NC affect the relaxivity more strongly than those on a smaller NC. This effect is due to the difference in tumbling time of the differently sized NCs.

The development of synthetic procedures to generate core-shell UCNCs have not explicitly addressed the challenges in precisely tunable shell growth, and a novel strategy was developed in this regard as demonstrated in Chapter 6. The systematic analysis of the well-known seed-mediated core shell synthesis revealed that the shell growth is actually not seed-mediated but a ripening-mediated process contrary to the general assumption. Based on this insight a simple but precisely controllable epitaxial growth technique was developed utilizing a common physical phenomenon of ripening in colloids. Deliberate injection of small(er) sacrificial nanocrystals (SNCs) into a solution of core NCs (*i.e.* defocusing) resulted in the rapid dissolution of the SNCs and deposition on the core NCs (*i.e.* focusing) generating core-shell NCs. Just by changing the amount of SNCs injected or by successive injection of SNCs it is demonstrated that the epitaxial layer growth can be tuned precisely without the need for controlling multiple parameters. The developed strategy was also extended to bi-modal/dual-mode emitting NCs, and to relatively smaller sized core NCs. The work demonstrated in this chapter is the first *experimental* evidence of utilizing ripening as a synthetic route for generating tunable epitaxial shell growth in colloidal NCs.

The effect of the sign of lattice mismatch affecting the isotropic core-shell growth was investigated in Chapter 7. The general rule of minimal lattice mismatch between the core and shell (epitaxial layer) does not take into account the sign of mismatch caused by a compressive or tensile epitaxial layer. Depending on the deviation in the lattice parameters of the shell relative to the core, the epitaxial layer either needs to compress/expand to adapt to the core lattice parameters. Utilizing the contraction of lanthanides along the series multiple core-shell NCs with compressive and tensile strain

were investigated. The results demonstrate unequivocally that given the same magnitude of mismatch a tensile strained shell grows isotropically while a compressive strained shell does not, even with minimal lattice mismatch. This effect is universal for any epitaxial shell growth in colloidal nanocrystals, as it is due to the anharmonic nature of the attractive and repulsive part of the pair potentials directly affecting the interfacial strain.

8.2. Possible Future Work

This dissertation has demonstrated the potential of lanthanide fluoride nanocrystals in diagnosis/targeting of cancer cells and MRI applications. Moreover, the ability to control the synthesis of core-shell NCs and the conditions for isotropic shell growth covering a broader outlook of colloidal NCs in general is also demonstrated. However, this progress needs additional work to understand further and develop these NCs for future applications. The possible future work to develop these demonstrated synthetic strategies is discussed below.

The ligand exchange protocol to label specifically UCNCs to cancer cells demonstrated in this dissertation addresses only the conditions exploited for *in vitro* studies. However, their use towards *in vivo* tumor targeting needs further exploration. When used *in vivo* the surface coating used should also avoid opsonization due to the adhering of plasma proteins, as this might potential lead to the NCs elimination from the blood stream and not reaching the target. PVP is known to avoid opsonization; however the functional group and the surface charge may still lead to (some) opsonization and this needs to be addressed. Strategies such as zwitterionic surface coating by derivatizing the PVP ligand could be explored, as zwitterionic surfaces are known to avoid non-specific binding of plasma proteins.

The enhancement of T_1 relaxivity with ultrasmall $NaGdF_4$ NCs demonstrated here was studied with PVP surface modification. However, as discussed the surface properties and the accessibility of water protons greatly influences the T_1 relaxivity. In this regard, different surface modification strategies need to be explored, which might potentially lead to further relaxivity enhancement than that demonstrated here. The effect of access of water to the surface gadolinium ions *vs.* the rate of tumbling of the NCs affecting the relaxivity can potentially be studied. One such exploration should focus on comparing the ligand-exchanged NCs and interdigitation/micellization of NCs, as the water access and the tumbling time should be different between the two. Therefore, there is ample room for exploration and investigation with these ultrasmall $NaGdF_4$ NCs.

In case of the tunable epitaxial layer growth demonstrated in Chapter 7, further work can be done with extending the ripening protocol to other colloidal nanocrystal systems. Especially, given that there is no need of precise control over the rate of injection of SNCs this protocol should ideally address some of the challenges in other colloidal core-shell synthesis. The tensile and compressive strain effects on the core-shell growth demonstrated here in this dissertation focussed only on undoped systems. The general effect of doping on the shell growth and the ability to grow graded shells could be investigated to understand further the influence of interfacial strain on the core-shell growth. Moreover, in doped systems there might be a driving force where the smaller lattice parameter dopant is explicitly pushed to the surface during growth to reduce the strain (especially when the dopant concentration is large). This can only be addressed with advancement in characterization techniques where atomic resolution of the individual dopants can clearly be mapped.

Literature Cited

(1) Auffan, M.; Rose, J.; Bottero, J. Y.; Lowry, G. V.; Jolivet, J. P.; Wiesner, M. R. *Nat. Nanotechnol.* **2009**, *4*, 634.

(2) Whitesides, G. M. *Small* **2005**, *1*, 172.

(3) Lieber, C. M. *Mater. Res. Soc. Bull.* **2003**, *28*, 486.

(4) LaVan, D. A.; McGuire, T.; Langer, R. *Nat. Biotechnol.* **2003**, *21*, 1184.

(5) Serrano, E.; Rus, G.; Garcia-Martinez, J. *Renew. Sust. Energ. Rev.* **2009**, *13*, 2373.

(6) Shimomura, M.; Sawadaishi, T. *Curr. Opin. Colloid Interface Sci.* **2001**, *6*, 11.

(7) LaMer, V. K.; Dinegar, R. H. *J. Am. Chem. Soc.* **1950**, *72*, 4847.

(8) Murray, C. B.; Kagan, C. R.; Bawendi, M. G. *Annu. Rev. Mater. Sci.* **2000**, *30*, 545.

(9) Reiss, P.; Protiere, M.; Li, L. *Small* **2009**, *5*, 154.

(10) Pimentel, G. C.; Sprately, R. D. *Understanding Chemistry* Holden-Day, 1971; 862.

(11) Selvin, P. R. *Annu. Rev. Biophys. Biomolec. Struct.* **2002**, *31*, 275.

(12) Fricker, S. P. *Chem. Soc. Rev.* **2006**, *35*, 524.

(13) Bunzli, J. C. G.; Comby, S.; Chauvin, A. S.; Vandevyver, C. D. B. *J Rare Earth* **2007**, *25*, 257.

(14) van der Ende, B. M.; Aarts, L.; Meijerink, A. *Phys. Chem. Chem. Phys.* **2009**, *11*, 11081.

(15) Andraud, C.; Maury, O. *Eur. J. Inorg. Chem.* **2009**, 4357.

(16) Bottrill, M.; Nicholas, L. K.; Long, N. J. *Chem. Soc. Rev.* **2006**, *35*, 557.

(17) Sun, Y. G.; Xia, Y. N. *Science* **2002**, *298*, 2176.

(18) Hu, J. T.; Odom, T. W.; Lieber, C. M. *Acc. Chem. Res.* **1999**, *32*, 435.

(19) Puntes, V. F.; Krishnan, K. M.; Alivisatos, A. P. *Science* **2001**, *291*, 2115.

(20) Yin, Y.; Alivisatos, A. P. *Nature* **2005**, *437*, 664.

(21) Manna, L.; Milliron, D. J.; Meisel, A.; Scher, E. C.; Alivisatos, A. P. *Nat. Mater.* **2003**, *2*, 382.

(22) Wang, F.; Tan, W. B.; Zhang, Y.; Fan, X. P.; Wang, M. Q. *Nanotechnology* **2006**, *17*, R1.

(23) Meltzer, R. S.; Feofilov, S. P.; Tissue, B.; Yuan, H. B. *Phys. Rev. B* **1999**, *60*, 14012.

(24) Riwotzki, K.; Meyssamy, H.; Kornowski, A.; Haase, M. *J. Phys. Chem. B* **2000**, *104*, 2824.

(25) Sivakumar, S.; Diamente, P. R.; van Veggel, F. C. J. M. *Chem. Eur. J.* **2006**, *12*, 5878.

(26) Bazzi, R.; Flores, M. A.; Louis, C.; Lebbou, K.; Zhang, W.; Dujardin, C.; Roux, S.; Mercier, B.; Ledoux, G.; Bernstein, E.; Perriat, P.; Tillement, O. *J. Colloid Interface Sci.* **2004**, *273*, 191.

(27) Yi, G. S.; Lu, H. C.; Zhao, S. Y.; Yue, G.; Yang, W. J.; Chen, D. P.; Guo, L. H. *Nano Lett.* **2004**, *4*, 2191.

(28) Wang, F.; Banerjee, D.; Liu, Y. S.; Chen, X. Y.; Liu, X. G. *Analyst* **2010**, *135*, 1839.

(29) Na, H. B.; Hyeon, T. *J. Mater. Chem.* **2009**, *19*, 6267.

(30) Yuan, J. L.; Wang, G. L. *Trac-Trends Anal. Chem.* **2006**, *25*, 490.

(31) Dosev, D.; Nichkova, M.; Kennedy, I. M. *J. Nanosci. Nanotechnol.* **2008**, *8*, 1052.

(32) Auzel, F. *Chem. Rev.* **2004**, *104*, 139.

(33) Menyuk, N.; Pierce, J. W.; Dwight, K. *Appl. Phys. Lett.* **1972**, *21*, 159.

(34) Murray, C. B.; Norris, D. J.; Bawendi, M. G. *J. Am. Chem. Soc.* **1993**, *115*, 8706.

(35) Kwon, S. G.; Hyeon, T. *Acc. Chem. Res.* **2008**, *41*, 1696.

(36) Hyeon, T.; Lee, S. S.; Park, J.; Chung, Y.; Na, H. B. *J. Am. Chem. Soc.* **2001**, *123*, 12798.

(37) Park, J.; An, K. J.; Hwang, Y. S.; Park, J. G.; Noh, H. J.; Kim, J. Y.; Park, J. H.; Hwang, N. M.; Hyeon, T. *Nat. Mater.* **2004**, *3*, 891.

(38) Boyer, J. C.; Cuccia, L. A.; Capobianco, J. A. *Nano Lett.* **2007**, *7*, 847.

(39) Mai, H. X.; Zhang, Y. W.; Si, R.; Yan, Z. G.; Sun, L. D.; You, L. P.; Yan, C. H. *J. Am. Chem. Soc.* **2006**, *128*, 6426.

(40) Yi, G. S.; Chow, G. M. *Adv. Funct. Mater.* **2006**, *16*, 2324.

(41) Wang, F.; Han, Y.; Lim, C. S.; Lu, Y. H.; Wang, J.; Xu, J.; Chen, H. Y.; Zhang, C.; Hong, M. H.; Liu, X. G. *Nature* **2010**, *463*, 1061.

(42) Li, Z. Q.; Zhang, Y. *Nanotechnology* **2008**, *19*, 345606.

(43) Li, Z. Q.; Zhang, Y.; Jiang, S. *Adv. Mater.* **2008**, *20*, 4765.

(44) Ye, X.; Collins, J. E.; Kang, Y.; Chen, J.; Chen, D. T. N.; Yodh, A. G.; Murray, C. B. *Proc. Natl. Acad. Sci. U.S.A.* **2010**, *107*, 22430.

(45) Mai, H. X.; Zhang, Y. W.; Sun, L. D.; Yan, C. R. *J. Phys. Chem. C* **2007**, *111*, 13730.

(46) Qian, H. S.; Zhang, Y. *Langmuir* **2008**, *24*, 12123.

(47) Abel, K. A.; Boyer, J.-C.; Andrei, C. M.; van Veggel, F. C. J. M. *J. Phys. Chem. Lett.* **2011**, 185.

(48) Zhou, J.; Liu, Z.; Li, F. Y. *Chem. Soc. Rev.* **2012**, *41*, 1323.

(49) Xiong, L. Q.; Yang, T. S.; Yang, Y.; Xu, C. J.; Li, F. Y. *Biomaterials* **2010**, *31*, 7078.

(50) Naccache, R.; Vetrone, F.; Mahalingam, V.; Cuccia, L. A.; Capobianco, J. A. *Chem. Mater.* **2009**, *21*, 717.

(51) Chen, G.; Ohulchanskyy, T. Y.; Law, W. C.; Agren, H.; Prasad, P. N. *Nanoscale* **2011**, *3*, 2003.

(52) Boyer, J. C.; Manseau, M. P.; Murray, J. I.; van Veggel, F. C. J. M. *Langmuir* **2010**, *26*, 1157.

(53) Nyk, M.; Kumar, R.; Ohulchanskyy, T. Y.; Bergey, E. J.; Prasad, P. N. *Nano Lett.* **2008**, *8*, 3834.

(54) Kumar, R.; Nyk, M.; Ohulchanskyy, T. Y.; Flask, C. A.; Prasad, P. N. *Adv. Funct. Mater.* **2009**, *19*, 853.

(55) Chen, Q.; Wang, X.; Chen, F.; Zhang, Q.; Dong, B.; Yang, H.; Liu, G.; Zhu, Y. *J. Mater. Chem.* **2011**, *21*, 7661.

(56) Zhou, J.; Yu, M. X.; Sun, Y.; Zhang, X. Z.; Zhu, X. J.; Wu, Z. H.; Wu, D. M.; Li, F. Y. *Biomaterials* **2011**, *32*, 1148.

(57) Cao, T.; Yang, T.; Gao, Y.; Yang, Y.; Hu, H.; Li, F. *Inorg. Chem. Commun.* **2010**, *13*, 392.

(58) Li, L. L.; Zhang, R. B.; Yin, L. L.; Zheng, K. Z.; Qin, W. P.; Selvin, P. R.; Lu, Y. *Angew. Chem., Int. Ed.* **2012**, *51*, 6121.

(59) Cheng, L.; Yang, K.; Zhang, S.; Shao, M.; Lee, S.; Liu, Z. *Nano Res.* **2010**, *3*, 722.

(60) Jiang, G.; Pichaandi, J.; Johnson, N. J. J.; Burke, R. D.; van Veggel, F. C. J. M. *Langmuir* **2012**, *28*, 3239.

(61) Chen, Z.; Chen, H.; Hu, H.; Yu, M.; Li, F.; Zhang, Q.; Zhou, Z.; Yi, T.; Huang, C. *J. Am. Chem. Soc.* **2008**, *130*, 3023.

(62) Zhou, H.-P.; Xu, C.-H.; Sun, W.; Yan, C.-H. *Adv. Funct. Mater.* **2009**, *19*, 3892.

(63) Jalil, R. A.; Zhang, Y. *Biomaterials* **2008**, *29*, 4122.

(64) Jayakumar, M. K. G.; Idris, N. M.; Zhang, Y. *Proc. Natl. Acad. Sci. U.S.A.* **2012**, *109*, 8483.

(65) Qian, H. S.; Guo, H. C.; Ho, P. C.-L.; Mahendran, R.; Zhang, Y. *Small* **2009**, *5*, 2285.

(66) Yu, M. K.; Park, J.; Jon, S. *Theranostics* **2012**, *2*, 3.

(67) Farokhzad, O. C.; Langer, R. *Acs Nano* **2009**, *3*, 16.

(68) Gao, X.; Cui, Y.; Levenson, R. M.; Chung, L. W. K.; Nie, S. *Nat. Biotech.* **2004**, *22*, 969.

(69) Nie, S. M. *Nanomedicine* **2010**, *5*, 523.

(70) Lundqvist, M.; Sethson, I.; Jonsson, B. H. *Langmuir* **2004**, *20*, 10639.

(71) Robinson, S.; Williams, P. A. *Langmuir* **2002**, *18*, 8743.

(72) Kinnane, C. R.; Such, G. K.; Antequera-Garcia, G.; Yan, Y.; Dodds, S. J.; Liz-Marzan, L. M.; Caruso, F. *Biomacromolecules* **2009**, *10*, 2839.

(73) Torchilin, V. P.; Trubetskoy, V. S. *Adv. Drug Deliver. Rev.* **1995**, *16*, 141.

(74) Na, H. B.; Song, I. C.; Hyeon, T. *Adv. Mater.* **2009**, *21*, 2133.

(75) Aime, S.; Fasano, M.; Terreno, E. *Chem. Soc. Rev.* **1998**, *27*, 19.

(76) Aime, S.; Botta, M.; Terreno, E. *Adv. Inorg. Chem.* **2005**, *57*, 173.

(77) Caravan, P. *Chem. Soc. Rev.* **2006**, *35*, 512.

(78) Werner, E. J.; Datta, A.; Jocher, C. J.; Raymond, K. N. *Angew. Chem., Int. Ed.* **2008**, *47*, 8568.

(79) Yang, J. J.; Yang, J. H.; Wei, L. X.; Zurkiya, O.; Yang, W.; Li, S. Y.; Zou, J.; Zhou, Y. B.; Maniccia, A. L. W.; Mao, H.; Zhao, F. Q.; Malchow, R.; Zhao, S. M.; Johnson, J.; Hu, X. P.; Krogstad, E.; Liu, Z. R. *J. Am. Chem. Soc.* **2008**, *130*, 9260.

(80) Zhu, W. L.; Mollie, B.; Bhujwalla, Z. M.; Artemov, D. *Magn. Reson. Med.* **2008**, *59*, 679.

(81) Louie, A. *Chem. Rev.* **2010**, *110*, 3146.

(82) Evanics, F.; Diamente, P. R.; van Veggel, F. C. J. M.; Stanisz, G. J.; Prosser, R. S. *Chem. Mater.* **2006**, *18*, 2499.

(83) Bridot, J. L.; Faure, A. C.; Laurent, S.; Riviere, C.; Billotey, C.; Hiba, B.; Janier, M.; Josserand, V.; Coll, J. L.; Vander Elst, L.; Muller, R.; Roux, S.; Perriat, P.; Tillement, O. *J. Am. Chem. Soc.* **2007**, *129*, 5076.

(84) Hifumi, H.; Yamaoka, S.; Tanimoto, A.; Akatsu, T.; Shindo, Y.; Honda, A.; Citterio, D.; Oka, K.; Kuribayashi, S.; Suzuki, K. *J. Mater. Chem.* **2009**, *19*, 6393.

(85) Hifumi, H.; Yamaoka, S.; Tanimoto, A.; Citterio, D.; Suzuki, K. *J. Am. Chem. Soc.* **2006**, *128*, 15090.

(86) Zhou, J.; Sun, Y.; Du, X.; Xiong, L.; Hu, H.; Li, F. *Biomaterials* **2010**, *31*, 3287.

(87) Ryu, J.; Park, H. Y.; Kim, K.; Kim, H.; Yoo, J. H.; Kang, M.; Im, K.; Grailhe, R.; Song, R. *J. Phys. Chem. C* **2010**, *114*, 21077.

(88) Park, Y. I.; Kim, J. H.; Lee, K. T.; Jeon, K. S.; Bin Na, H.; Yu, J. H.; Kim, H. M.; Lee, N.; Choi, S. H.; Baik, S. I.; Kim, H.; Park, S. P.; Park, B. J.; Kim, Y. W.; Lee, S. H.; Yoon, S. Y.; Song, I. C.; Moon, W. K.; Suh, Y. D.; Hyeon, T. *Adv. Mater.* **2009**, *21*, 4467.

(89) Johnson, N. J. J.; Sangeetha, N. M.; Boyer, J. C.; van Veggel, F. C. J. M. *Nanoscale* **2010**, *2*, 771.

(90) Liu, S. H.; Han, M. Y. *Adv. Funct. Mater.* **2005**, *15*, 961.

(91) Santra, S.; Yang, H. S.; Holloway, P. H.; Stanley, J. T.; Mericle, R. A. *J. Am. Chem. Soc.* **2005**, *127*, 1656.

(92) Schroedter, A.; Weller, H. *Angew. Chem., Int. Ed.* **2002**, *41*, 3218.

(93) Hoshino, A.; Fujioka, K.; Oku, T.; Suga, M.; Sasaki, Y. F.; Ohta, T.; Yasuhara, M.; Suzuki, K.; Yamamoto, K. *Nano Lett.* **2004**, *4*, 2163.

(94) Male, K. B.; Lachance, B.; Hrapovic, S.; Sunahara, G.; Luong, J. H. T. *Anal. Chem.* **2008**, *80*, 5487.

(95) Meiser, F.; Cortez, C.; Caruso, F. *Angew. Chem., Int. Ed.* **2004**, *43*, 5954.

(96) Stouwdam, J. W.; Hebbink, G. A.; Huskens, J.; van Veggel, F. C. J. M. *Chem. Mater.* **2003**, *15*, 4604.

(97) Traina, C. A.; Schwartz, J. *Langmuir* **2007**, *23*, 9158.

(98) Wang, F.; Xue, X. J.; Liu, X. G. *Angew. Chem., Int. Ed.* **2008**, *47*, 906.

(99) Yan, Z. G.; Yan, C. H. *J. Mater. Chem.* **2008**, *18*, 5046.

(100) Krämer, K. W.; Biner, D.; Frei, G.; Güdel, H. U.; Hehlen, M. P.; Lüthi, S. R. *Chem. Mater.* **2004**, *16*, 1244.

(101) Yi, G. S.; Chow, G. M. *Chem. Mater.* **2007**, *19*, 341.

(102) De Palma, R.; Peeters, S.; Van Bael, M. J.; Van den Rul, H.; Bonroy, K.; Laureyn, W.; Mullens, J.; Borghs, G.; Maes, G. *Chem. Mater.* **2007**, *19*, 1821.

(103) Lin, W.; Fritz, K.; Guerin, G.; Bardajee, G. R.; Hinds, S.; Sukhovatkin, V.; Sargent, E. H.; Scholes, G. D.; Winnik, M. A. *Langmuir* **2008**, *24*, 8215.

(104) Bin Na, H.; Lee, I. S.; Seo, H.; Il Park, Y.; Lee, J. H.; Kim, S. W.; Hyeon, T. *Chem. Commun.* **2007**, 5167.

(105) Kim, S. W.; Kim, S.; Tracy, J. B.; Jasanoff, A.; Bawendi, M. G. *J. Am. Chem. Soc.* **2005**, *127*, 4556.

(106) Le Garrec, D.; Gori, S.; Luo, L.; Lessard, D.; Smith, D. C.; Yessine, M. A.; Ranger, M.; Leroux, J. C. *J. Controlled Release* **2004**, *99*, 83.

(107) Rabin, O.; Perez, J. M.; Grimm, J.; Wojtkiewicz, G.; Weissleder, R. *Nat. Mater.* **2006**, *5*, 118.

(108) Pachon, L. D.; Rothenberg, G. *Appl. Organomet. Chem.* **2008**, *22*, 288.

(109) Sun, Y. G.; Yin, Y. D.; Mayers, B. T.; Herricks, T.; Xia, Y. N. *Chem. Mater.* **2002**, *14*, 4736.

(110) Lu, X. Y.; Niu, M.; Qiao, R. R.; Gao, M. Y. *J. Phys. Chem. B* **2008**, *112*, 14390.

(111) Li, Z. Q.; Zhang, Y. *Angew. Chem., Int. Ed.* **2006**, *45*, 7732.

(112) Wang, M.; Mi, C. C.; Liu, J. L.; Wu, X. L.; Zhang, Y. X.; Hou, W.; Li, F.; Xu, S. K. *J. Alloys Compd.* **2009**, *485*, L24.

(113) Li, C. X.; Yang, J.; Quan, Z. W.; Yang, P. P.; Kong, D. Y.; Lin, J. *Chem. Mater.* **2007**, *19*, 4933.

(114) Liang, X.; Wang, X.; Zhuang, J.; Peng, Q.; Li, Y. D. *Adv. Funct. Mater.* **2007**, *17*, 2757.

(115) Wang, L. Y.; Li, Y. D. *Chem. Mater.* **2007**, *19*, 727.

(116) Zeng, J. H.; Su, J.; Li, Z. H.; Yan, R. X.; Li, Y. D. *Adv. Mater.* **2005**, *17*, 2119.

(117) Kaneda, Y.; Tsutsumi, Y.; Yoshioka, Y.; Kamada, H.; Yamamoto, Y.; Kodaira, H.; Tsunoda, S.; Okamoto, T.; Mukai, Y.; Shibata, H.; Nakagawa, S.; Mayumi, T. *Biomaterials* **2004**, *25*, 3259.

(118) Graf, C.; Vossen, D. L. J.; Imhof, A.; van Blaaderen, A. *Langmuir* **2003**, *19*, 6693.

(119) Yi, D. K.; Lee, S. S.; Papaefthymiou, G. C.; Ying, J. Y. *Chem. Mater.* **2006**, *18*, 614.

(120) Jana, N. R.; Earhart, C.; Ying, J. Y. *Chem. Mater.* **2007**, *19*, 5074.

(121) Zhang, T. R.; Ge, J. P.; Hu, Y. P.; Yin, Y. D. *Nano Lett.* **2007**, *7*, 3203.

(122) Pastoriza-Santos, I.; Perez-Juste, J.; Liz-Marzan, L. M. *Chem. Mater.* **2006**, *18*, 2465.

(123) Wang, Y.; Tang, Z. Y.; Liang, X. R.; Liz-Marzan, L. M.; Kotov, N. A. *Nano Lett.* **2004**, *4*, 225.

(124) Liu, C.; Wang, H.; Li, X.; Chen, D. *J. Mater. Chem.* **2009**, *19*, 3546.

(125) Hebbink, G. A.; Stouwdam, J. W.; Reinhoudt, D. N.; van Veggel, F. C. J. M. *Adv. Mater.* **2002**, *14*, 1147.

(126) Schafer, H.; Ptacek, P.; Kompe, K.; Haase, M. *Chem. Mater.* **2007**, *19*, 1396.

(127) Zhao, J. W.; Sun, Y. J.; Kong, X. G.; Tian, L. J.; Wang, Y.; Tu, L. P.; Zhao, J. L.; Zhang, H. *J. Phys. Chem. B* **2008**, *112*, 15666.

(128) Chen, F.; Zhang, S.; Bu, W.; Liu, X.; Chen, Y.; He, Q.; Zhu, M.; Zhang, L.; Zhou, L.; Peng, W.; Shi, J. *Chem. Eur. J.* **2010**, *16*, 11254.

(129) Idris, N. M.; Li, Z.; Ye, L.; Wei Sim, E. K.; Mahendran, R.; Ho, P. C.-L.; Zhang, Y. *Biomaterials* **2009**, *30*, 5104.

(130) Jeong, S.; Won, N.; Lee, J.; Bang, J.; Yoo, J.; Kim, S. G.; Chang, J. A.; Kim, J.; Kim, S. *Chem. Commun.* **2011**, *47*, 8022.

(131) Wang, Z.-L.; Hao, J.; Chan, H. L. W.; Law, G.-L.; Wong, W.-T.; Wong, K.-L.; Murphy, M. B.; Su, T.; Zhang, Z. H.; Zeng, S. Q. *Nanoscale* **2011**, *3*, 2175.

(132) Chatterjee, D. K.; Rufaihah, A. J.; Zhang, Y. *Biomaterials* **2008**, *29*, 937.

(133) Liu, Q.; Sun, Y.; Li, C.; Zhou, J.; Li, C.; Yang, T.; Zhang, X.; Yi, T.; Wu, D.; Li, F. *ACS Nano* **2011**, *5*, 3146.

(134) Xiong, L.-Q.; Chen, Z.-G.; Yu, M.-X.; Li, F.-Y.; Liu, C.; Huang, C.-H. *Biomaterials* **2009**, *30*, 5592.

(135) Zhan, Q.; Qian, J.; Liang, H.; Somesfalean, G.; Wang, D.; He, S.; Zhang, Z.; Andersson-Engels, S. *ACS Nano* **2011**, *5*, 3744.

(136) Wang, M.; Mi, C.-C.; Wang, W.-X.; Liu, C.-H.; Wu, Y.-F.; Xu, Z.-R.; Mao, C.-B.; Xu, S.-K. *ACS Nano* **2009**, *3*, 1580.

(137) Robinson, S.; Williams, P. A. *Langmuir* **2002**, *18*, 8743.

(138) Baldoli, C.; Oldani, C.; Maiorana, S.; Ferruti, P.; Ranucci, E.; Bencini, M.; Contini, A. *J. Polym. Sci., Part A: Polym. Chem.* **2008**, *46*, 1683.

(139) Lee, H. Y.; Yu, S. A.; Jeong, K. H.; Kim, Y. J. *Macromol. Res.* **2007**, *15*, 547.

(140) Torchilin, V. P.; Levchenko, T. S.; Whiteman, K. R.; Yaroslavov, A. A.; Tsatsakis, A. M.; Rizos, A. K.; Michailova, E. V.; Shtilman, M. I. *Biomaterials* **2001**, *22*, 3035.

(141) Ranucci, E.; Tarabic, M.; Gilberti, M.; Albertsson, A. C. *Macromol. Chem. Phys.* **2000**, *201*, 1219.

(142) Johnson, N. J. J.; Oakden, W.; Stanisz, G. J.; Prosser, R. S.; van Veggel, F. C. J. M. *Chem. Mater.* **2011**, *23*, 3714.

(143) Burda, C.; Chen, X. B.; Narayanan, R.; El-Sayed, M. A. *Chem. Rev.* **2005**, *105*, 1025.

(144) De, M.; Ghosh, P. S.; Rotello, V. M. *Adv. Mater.* **2008**, *20*, 4225.

(145) Pellegrino, T.; Kudera, S.; Liedl, T.; Javier, A. M.; Manna, L.; Parak, W. J. *Small* **2005**, *1*, 48.

(146) Shipway, A. N.; Katz, E.; Willner, I. *ChemPhysChem* **2000**, *1*, 18.

(147) Wang, F.; Liu, X. G. *Chem. Soc. Rev.* **2009**, *38*, 976.

(148) Caravan, P.; Ellison, J. J.; McMurry, T. J.; Lauffer, R. B. *Chem. Rev.* **1999**, *99*, 2293.

(149) Aime, S.; Castelli, D. D.; Crich, S. G.; Gianolio, E.; Terreno, E. *Acc. Chem. Res.* **2009**, *42*, 822.

(150) Ahren, M.; Selegard, L.; Klasson, A.; Soderlind, F.; Abrikossova, N.; Skoglund, C.; Bengtsson, T.; Engstrom, M.; Kall, P. O.; Uvdal, K. *Langmuir* **2010**, *26*, 5753.

(151) Park, J. Y.; Baek, M. J.; Choi, E. S.; Woo, S.; Kim, J. H.; Kim, T. J.; Jung, J. C.; Chae, K. S.; Chang, Y.; Lee, G. H. *ACS Nano* **2009**, *3*, 3663.

(152) Petoral, R. M.; Soderlind, F.; Klasson, A.; Suska, A.; Fortin, M. A.; Abrikossova, N.; Selegard, L.; Kall, P. O.; Engstrom, M.; Uvdal, K. *J. Phys. Chem. C* **2009**, *113*, 6913.

(153) Abel, K. A.; Boyer, J. C.; van Veggel, F. C. J. M. *J. Am. Chem. Soc.* **2009**, *131*, 14644.

(154) Das, G. K.; Heng, B. C.; Ng, S. C.; White, T.; Loo, J. S. C.; D'Silva, L.; Padmanabhan, P.; Bhakoo, K. K.; Selvan, S. T.; Tan, T. T. Y. *Langmuir* **2010**, *26*, 8959.

(155) Guo, H.; Li, Z. Q.; Qian, H. S.; Hu, Y.; Muhammad, I. N. *Nanotechnology* **2010**, *21*, 125602.

(156) Parak, W. J.; Gerion, D.; Pellegrino, T.; Zanchet, D.; Micheel, C.; Williams, S. C.; Boudreau, R.; Le Gros, M. A.; Larabell, C. A.; Alivisatos, A. P. *Nanotechnology* **2003**, *14*, R15.

(157) Park, J.; Joo, J.; Kwon, S. G.; Jang, Y.; Hyeon, T. *Angew. Chem., Int. Ed.* **2007**, *46*, 4630.

(158) De Jong, W. H.; Hagens, W. I.; Krystek, P.; Burger, M. C.; Sips, A.; Geertsma, R. E. *Biomaterials* **2008**, *29*, 1912.

(159) Pan, Y.; Neuss, S.; Leifert, A.; Fischler, M.; Wen, F.; Simon, U.; Schmid, G.; Brandau, W.; Jahnen-Dechent, W. *Small* **2007**, *3*, 1941.

(160) Semmler-Behnke, M.; Kreyling, W. G.; Lipka, J.; Fertsch, S.; Wenk, A.; Takenaka, S.; Schmid, G.; Brandau, W. *Small* **2008**, *4*, 2108.

(161) Liu, Y. S.; Tu, D. T.; Zhu, H. M.; Li, R. F.; Luo, W. Q.; Chen, X. Y. *Adv. Mater.* **2010**, *22*, 3266.

(162) Wang, F.; Wang, J. A.; Liu, X. G. *Angew. Chem., Int. Ed.* **2010**, *49*, 7456.

(163) Bullen, C. R.; Mulvaney, P. *Nano Lett.* **2004**, *4*, 2303.

(164) van Embden, J.; Mulvaney, P. *Langmuir* **2005**, *21*, 10226.

(165) Caravan, P.; Farrar, C. T.; Frullano, L.; Uppal, R. *Contrast Media Mol. Imaging* **2009**, *4*, 89.

(166) Caravan, P. *Acc. Chem. Res.* **2009**, *42*, 851.

(167) Song, Y.; Xu, X. Y.; MacRenaris, K. W.; Zhang, X. Q.; Mirkin, C. A.; Meade, T. J. *Angew. Chem., Int. Ed.* **2009**, *48*, 9143.

(168) Ananta, J. S.; Godin, B.; Sethi, R.; Moriggi, L.; Liu, X.; Serda, R. E.; Krishnamurthy, R.; Muthupillai, R.; Bolskar, R. D.; Helm, L.; Ferrari, M.; Wilson, L. J.; Decuzzi, P. *Nat. Nanotechnol.* **2010**, *5*, 815.

(169) Longmire, M.; Choyke, P. L.; Kobayashi, H. *Nanomedicine* **2008**, *3*, 703.

(170) Boyer, J. C.; Gagnon, J.; Cuccia, L. A.; Capobianco, J. A. *Chem. Mater.* **2007**, *19*, 3358.

(171) Chen, G. Y.; Ohulchanskyy, T. Y.; Kumar, R.; Agren, H.; Prasad, P. N. *ACS Nano* **2010**, *4*, 3163.

(172) Zhang, J.; Shade, C. M.; Chengelis, D. A.; Petoud, S. *J. Am. Chem. Soc.* **2007**, *129*, 14834.

(173) Cheung, E. N. M.; Alvares, R. D. A.; Oakden, W.; Chaudhary, R.; Hill, M. L.; Pichaandi, J.; Mo, G. C. H.; Yip, C.; Macdonald, P. M.; Stanisz, G. J.; van Veggel, F. C. J. M.; Prosser, R. S. *Chem. Mater.* **2010**, *22*, 4728.

(174) Johnson, N. J. J.; Korinek, A.; Dong, C.; van Veggel, F. C. J. M. *J. Am. Chem. Soc.* **2012**, *134*, 11068.

(175) Boyer, J. C.; van Veggel, F. C. J. M. *Nanoscale* **2010**, *2*, 1417.

(176) Vetrone, F.; Naccache, R.; Mahalingam, V.; Morgan, C. G.; Capobianco, J. A. *Adv. Funct. Mater.* **2009**, *19*, 2924.

(177) Haase, M.; Schafer, H. *Angew. Chem., Int. Ed.* **2011**, *50*, 5808.

(178) Wang, G. F.; Peng, Q.; Li, Y. D. *Acc. Chem. Res.* **2011**, *44*, 322.

(179) Carling, C. J.; Nourmohammadian, F.; Boyer, J. C.; Branda, N. R. *Angew. Chem., Int. Ed.* **2010**, *49*, 3782.

(180) Schietinger, S.; Aichele, T.; Wang, H. Q.; Nann, T.; Benson, O. *Nano Lett.* **2010**, *10*, 134.

(181) Wang, F.; Deng, R.; Wang, J.; Wang, Q.; Han, Y.; Zhu, H.; Chen, X.; Liu, X. *Nat Mater* **2011**, *10*, 968.

(182) Wang, M.; Hou, W.; Mi, C. C.; Wang, W. X.; Xu, Z. R.; Teng, H. H.; Mao, C. B.; Xu, S. K. *Anal. Chem.* **2009**, *81*, 8783.

(183) Wu, W.; Yao, L. M.; Yang, T. S.; Yin, R. Y.; Li, F. Y.; Yu, Y. L. *J. Am. Chem. Soc.* **2011**, *133*, 15810.

(184) Talapin, D. V.; Rogach, A. L.; Haase, M.; Weller, H. *J. Phys. Chem. B* **2001**, *105*, 12278.

(185) Chen, Y.; Johnson, E.; Peng, X. *J. Am. Chem. Soc.* **2007**, *129*, 10937.

(186) Kwon, S. G.; Piao, Y.; Park, J.; Angappane, S.; Jo, Y.; Hwang, N.-M.; Park, J.-G.; Hyeon, T. *J. Am. Chem. Soc.* **2007**, *129*, 12571.

(187) Talapin, D. V.; Lee, J.-S.; Kovalenko, M. V.; Shevchenko, E. V. *Chem. Rev.* **2010**, *110*, 389.

(188) Thessing, J.; Qian, J.; Chen, H.; Pradhan, N.; Peng, X. *J. Am. Chem. Soc.* **2007**, *129*, 2736.

(189) Peng, X. G.; Wickham, J.; Alivisatos, A. P. *J. Am. Chem. Soc.* **1998**, *120*, 5343.

(190) Finsy, R. *Langmuir* **2004**, *20*, 2975.

(191) Chen, F.; Bu, W. B.; Zhang, S. J.; Liu, X. H.; Liu, J. N.; Xing, H. Y.; Xiao, Q. F.; Zhou, L. P.; Peng, W. J.; Wang, L. Z.; Shi, J. L. *Adv. Funct. Mater.* **2011**, *21*, 4285.

(192) Carbone, L.; Cozzoli, P. D. *Nano Today* **2010**, *5*, 449.

(193) Milliron, D. J.; Hughes, S. M.; Cui, Y.; Manna, L.; Li, J.; Wang, L.-W.; Paul Alivisatos, A. *Nature* **2004**, *430*, 190.

(194) Buck, M. R.; Bondi, J. F.; Schaak, R. E. *Nat. Chem.* **2012**, *4*, 37.

(195) Habas, S. E.; Lee, H.; Radmilovic, V.; Somorjai, G. A.; Yang, P. *Nat. Mater.* **2007**, *6*, 692.

(196) Fitzgerald, E. A.; Samavedam, S. B.; Xie, Y. H.; Giovane, L. M. *J. Vac. Sci. Technol. A-Vac. Surf. Films* **1997**, *15*, 1048.

(197) Lu, Y. F.; Przybylski, M.; Trushin, O.; Wang, W. H.; Barthel, J.; Granato, E.; Ying, S. C.; Ala-Nissila, T. *Phys. Rev. Lett.* **2005**, *94*, 146105.

(198) Jalkanen, J.; Rossi, G.; Trushin, O.; Granato, E.; Ala-Nissila, T.; Ying, S. C. *Phys. Rev. B* **2010**, *81*, 041412.

(199) Hsiao, P. Y.; Tsai, Z. H.; Huang, J. H.; Yu, G. P. *Phys. Rev. B* **2009**, *79*, 155414.

(200) Shannon, R. D. *Acta Crystallogr. A* **1976**, *32*, 751.

(201) Dunstan, D. J.; Young, S.; Dixon, R. H. *J. Appl. Phys.* **1991**, *70*, 3038.

(202) Bauer, E.; van der Merwe, J. H. *Phys. Rev. B* **1986**, *33*, 3657.

(203) Zhang, F.; Che, R. C.; Li, X. M.; Yao, C.; Yang, J. P.; Shen, D. K.; Hu, P.; Li, W.; Zhao, D. Y. *Nano Lett.* **2012**, *12*, 2852.

(204) Huang, R.; Wen, Y. H.; Zhu, Z. Z.; Sun, S. G. *J. Phys. Chem. C* **2012**, *116*, 8664.

(205) Sanchez, S. I.; Small, M. W.; Zuo, J. M.; Nuzzo, R. G. *J. Am. Chem. Soc.* **2009**, *131*, 8683.

(206) Yang, C. W.; Chanda, K.; Lin, P. H.; Wang, Y. N.; Liao, C. W.; Huang, M. H. *J. Am. Chem. Soc.* **2011**, *133*, 19993.

(207) Fan, F. R.; Liu, D. Y.; Wu, Y. F.; Duan, S.; Xie, Z. X.; Jiang, Z. Y.; Tian, Z. Q. *J. Am. Chem. Soc.* **2008**, *130*, 6949.

(208) Jin, M. S.; Zhang, H.; Wang, J. G.; Zhong, X. L.; Lu, N.; Li, Z. Y.; Xie, Z. X.; Kim, M. J.; Xia, Y. N. *ACS Nano* **2012**, *6*, 2566.

(209) Tsuji, M.; Yamaguchi, D.; Matsunaga, M.; Ikedo, K. *Cryst. Growth Des.* **2011**, *11*, 1995.

Appendix A. Supplementary Information to Chapter 3

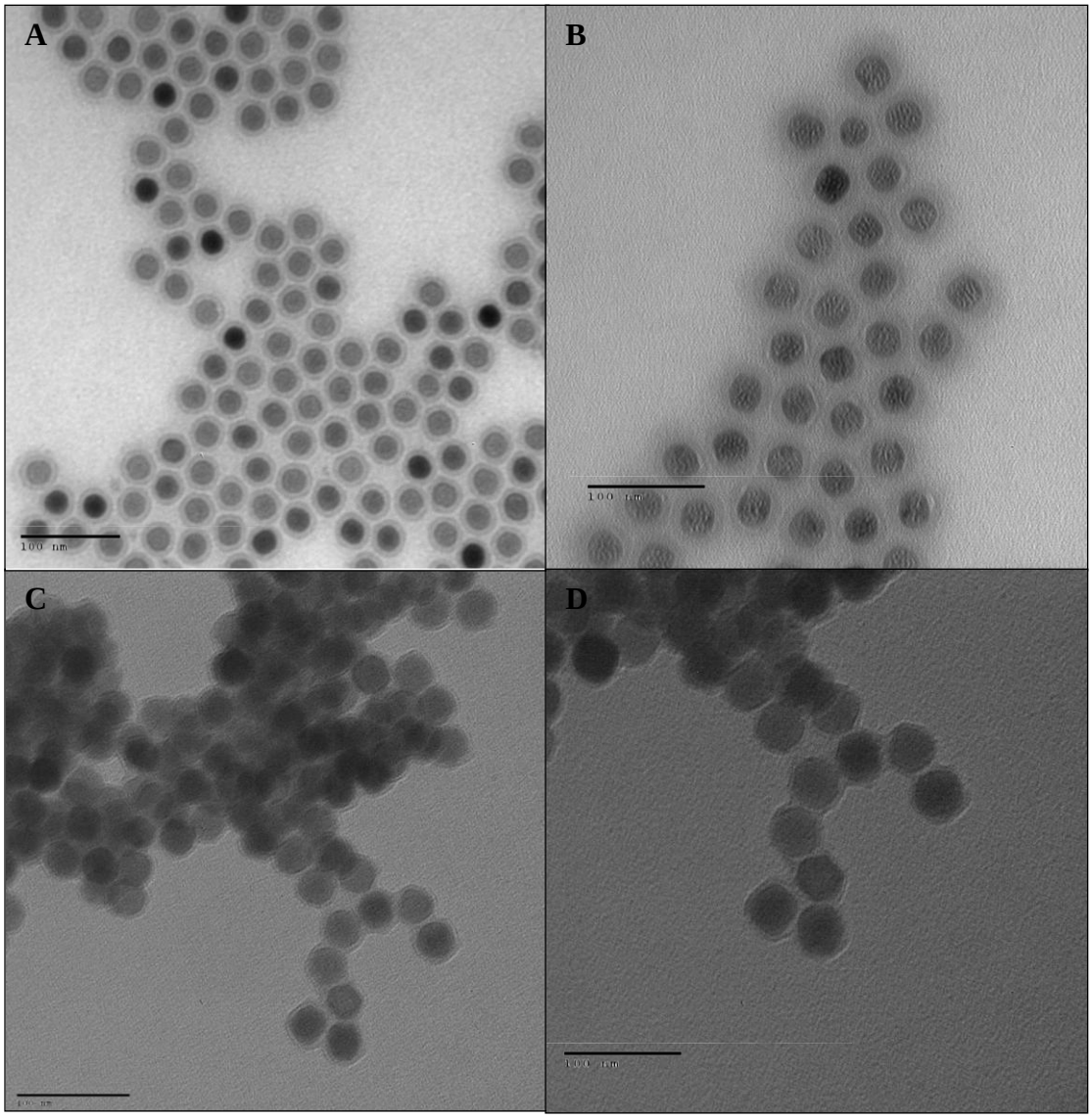

Figure A1. TEM images of β-$NaYF_4$:Yb^{3+}/Er^{3+} coated with silica in reverse emulsion, immediately after coating **(A and B)**, and after washing vigorously **(C and D)**. Scale bar = 100 nm.

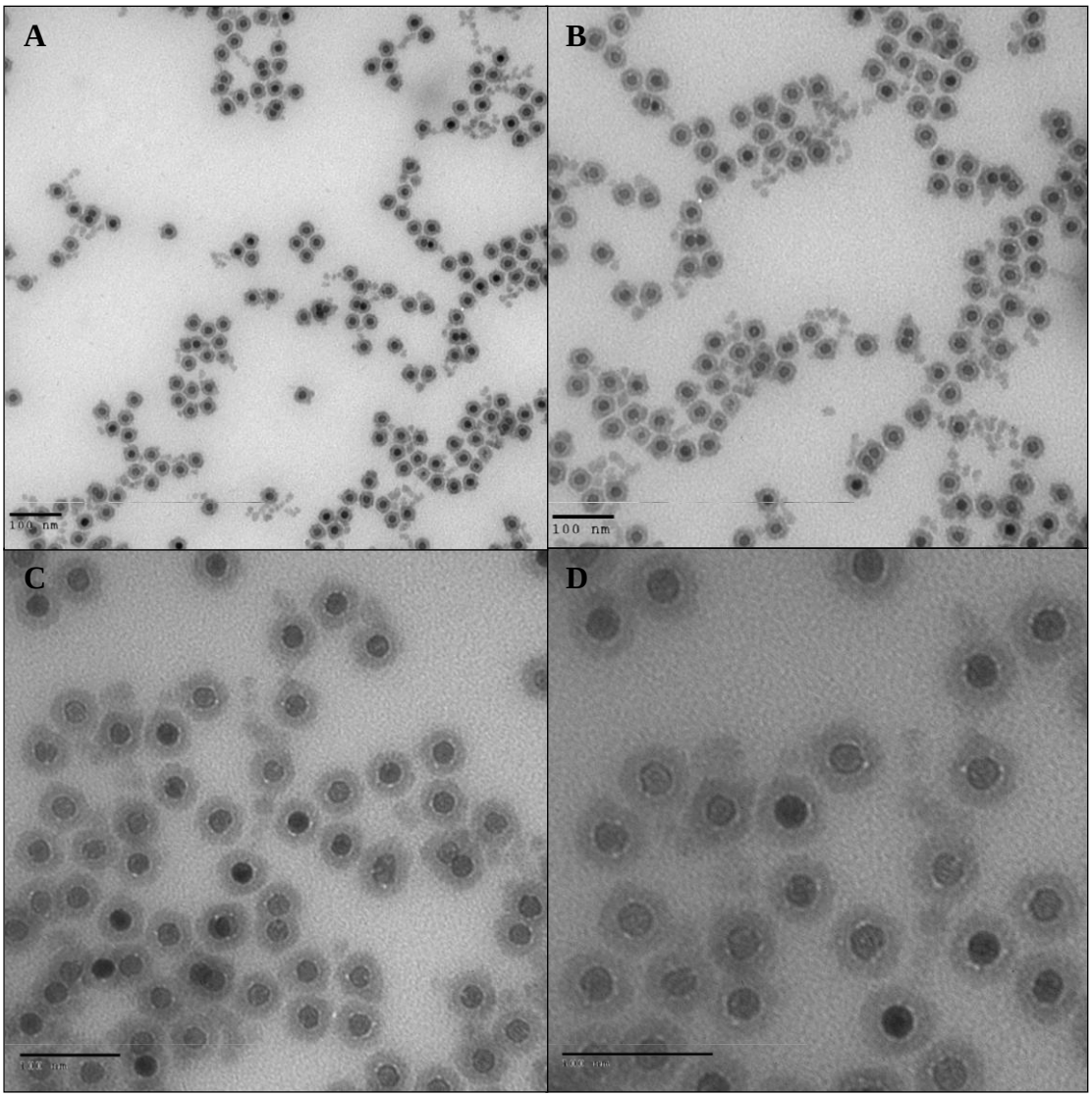

Figure A2. TEM images of PVP-stabilized β-$NaYF_4$:Yb^{3+}/Er^{3+} coated with silica after washing and stored in water for 2 days. Scale bar = 100 nm.

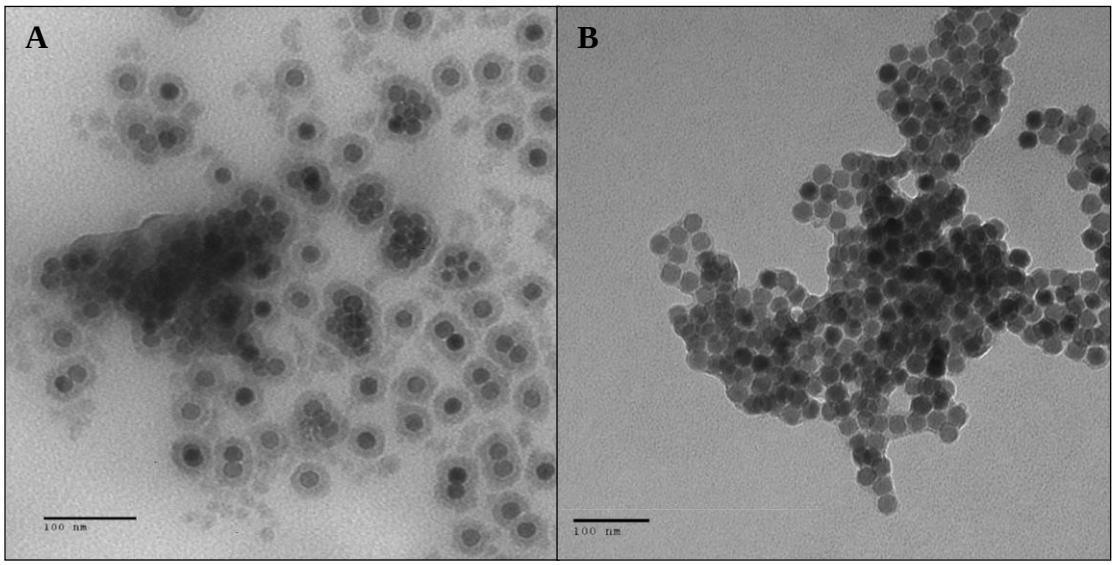

Figure A3. TEM images of PVP-stabilized β-$NaYF_4$:Yb^{3+}/Er^{3+} coated with silica after washing and stored in water for 5 days **(A)**, and more than a week **(B)**. Scale bar = 100 nm.

Table A1. Appearance of the silica coated nanocrystals as observed from TEM showing their stability over 7 days in dispersion.

	Silica coated after PVP exchange	**Silica coated by Reverse microemulsion**
Immediately after coating	*individual core-shell*	*individual core-shell*
After vigorous washing and centrifuge cycles (~5 times with ethanol)	*individual*	*necking between the silica shells*
2 days after silica coating	*individual*	*aggregated*
5 days after silica coating	*some aggregation*	*aggregated*
> 7 days after silica coating	*aggregated*	*aggregated*

Appendix B. Supplementary Information to Chapter 4

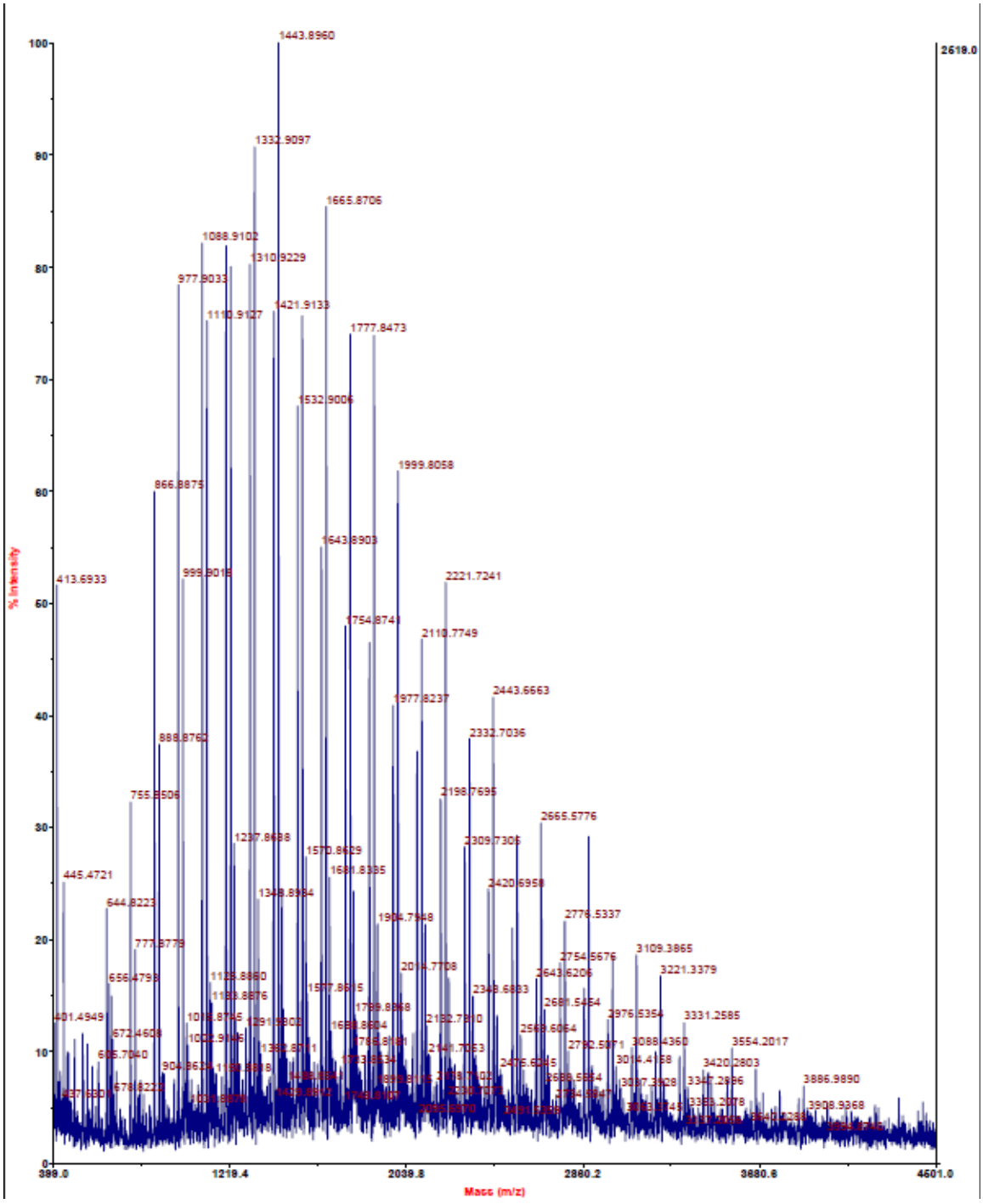

Figure B1. MALDI-mass spectra of carboxylic acid terminated polyvinylpyrrolidone (PVP-COOH).

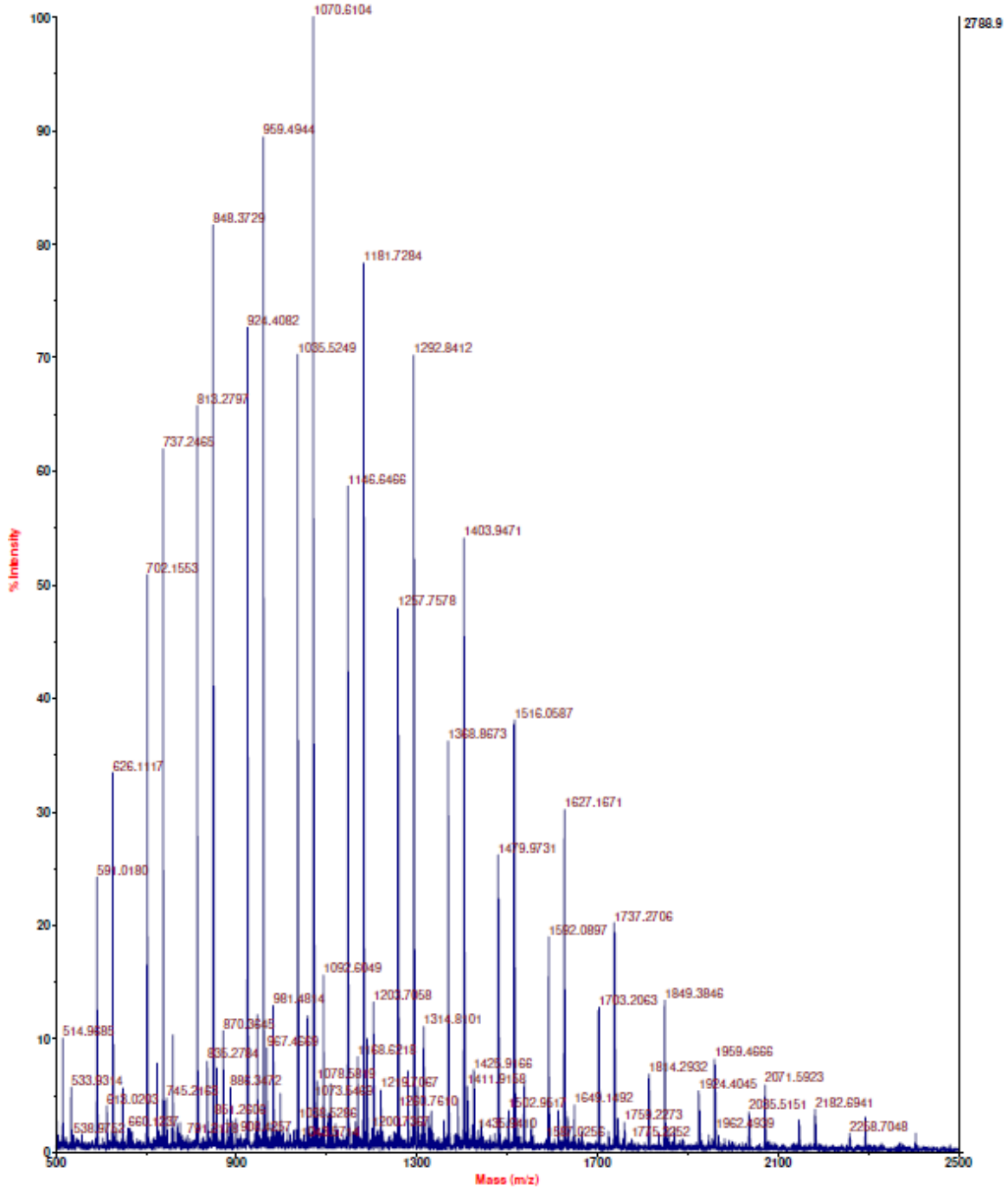

Figure B2. MALDI-mass spectra of amine terminated polyvinylpyrrolidone (PVP-NH_2).

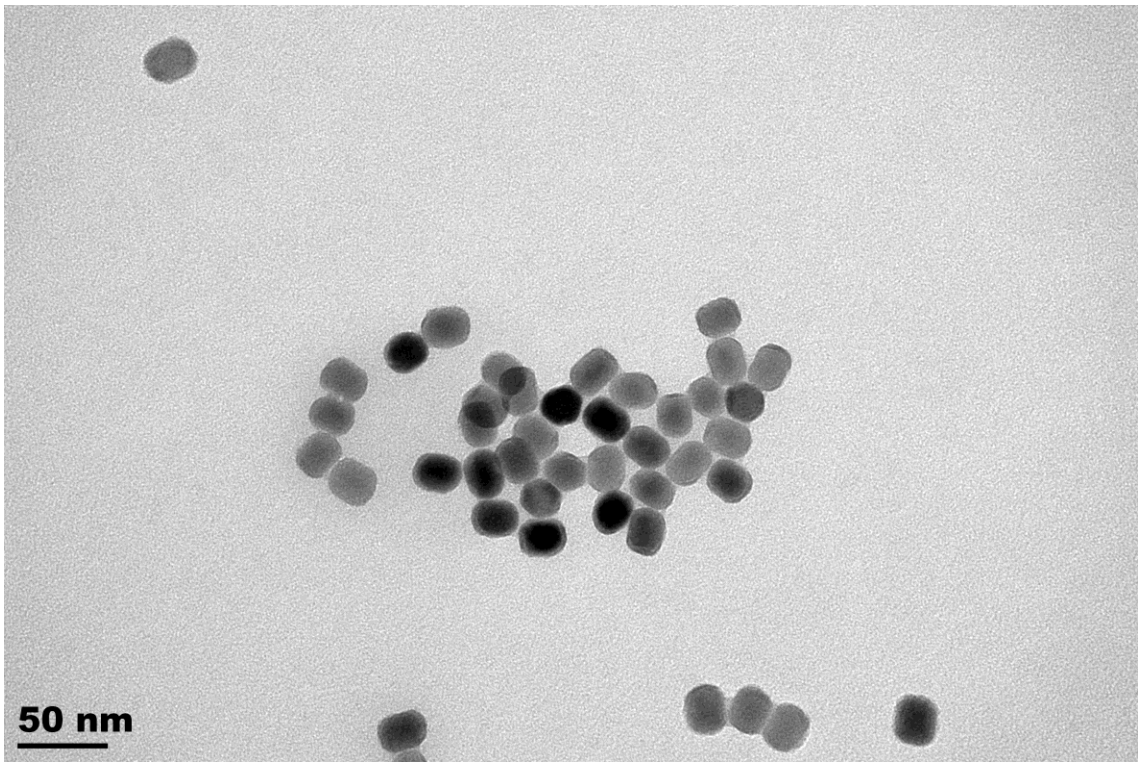

Figure B3. TEM image of core-shell PVP-COOH coated UCNCs phase-transferred to water.

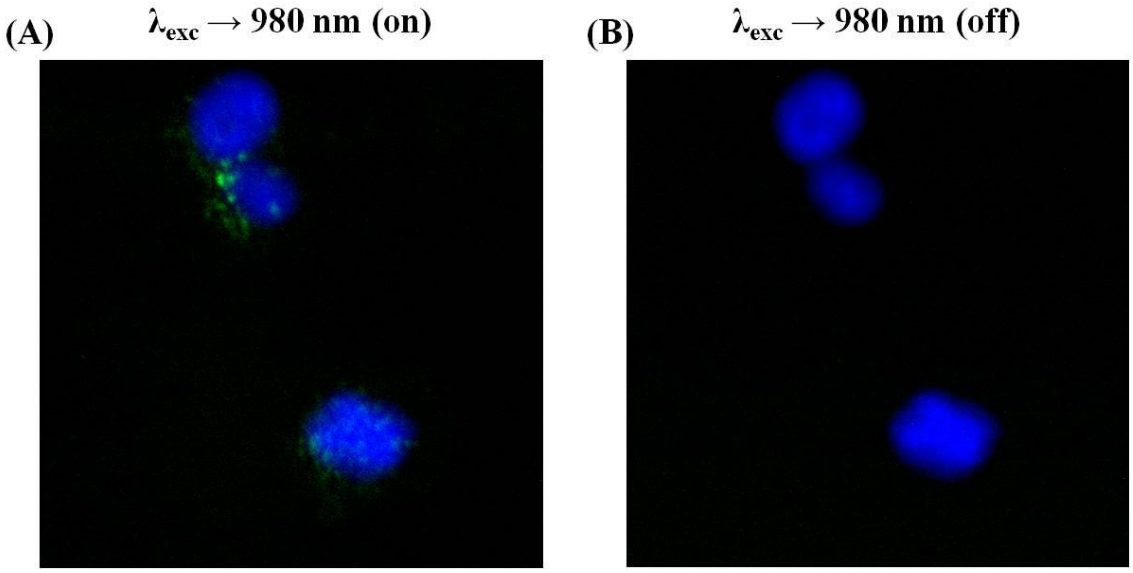

Figure B4. Overlay of upconverted emission from UCNCs and DAPI emission (nuclei stain) of LNCaP cells **(A)** under 980 nm excitation turned on, and **(B)** under 980 nm excitation turned off.

Appendix C. Supplementary Information to Chapter 5

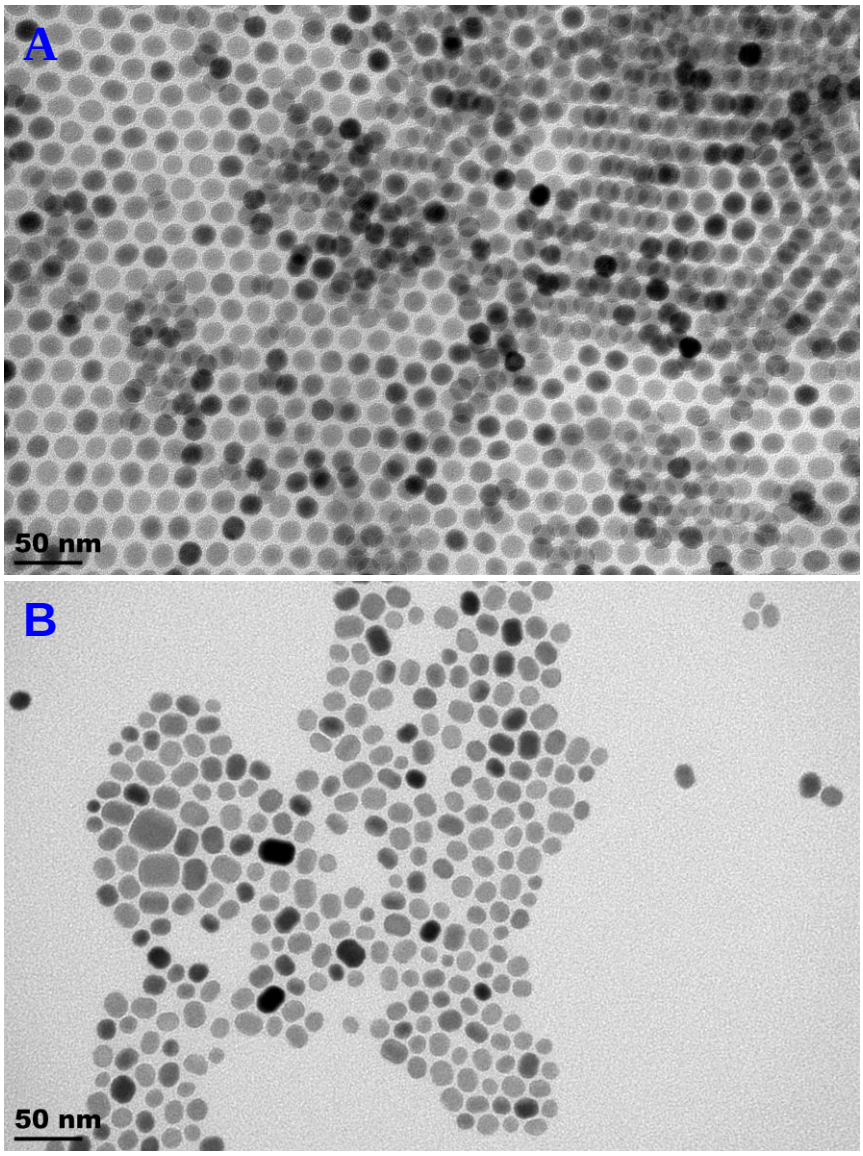

Figure C1. Low resolution TEM images of **(A)** monodisperse $NaYF_4$ NCs, and **(B)** polydisperse $NaGdF_4$ NCs grown at the same conditions.

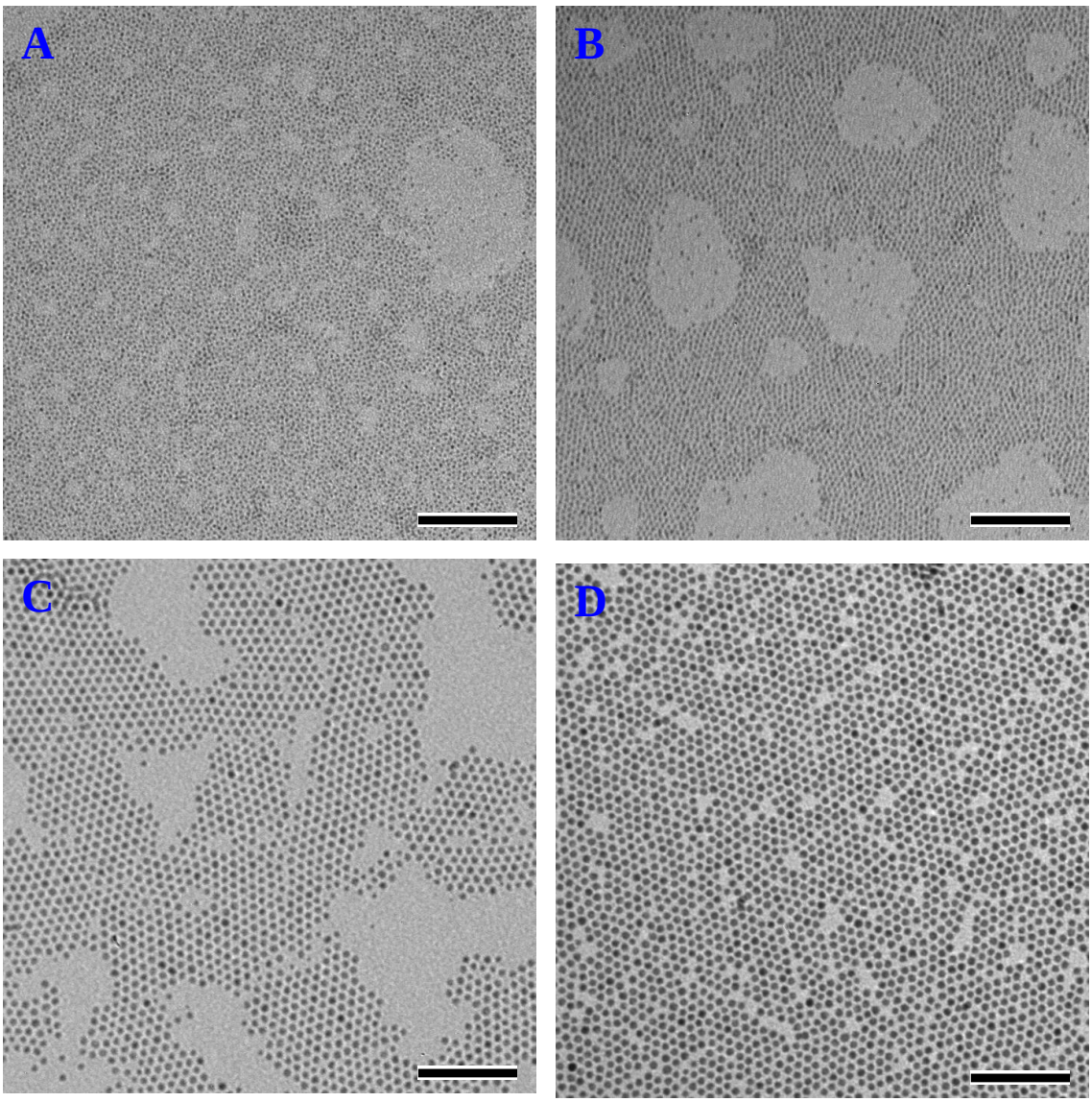

Figure C2. Low resolution TEM images of as synthesized oleate-coated $NaGdF_4$ NCs **(A)** 2.5 nm, (B) 4.0 nm, **(C)** 6.5 nm, and **(D)** 8.0 nm, *Scale bar =100 nm*.

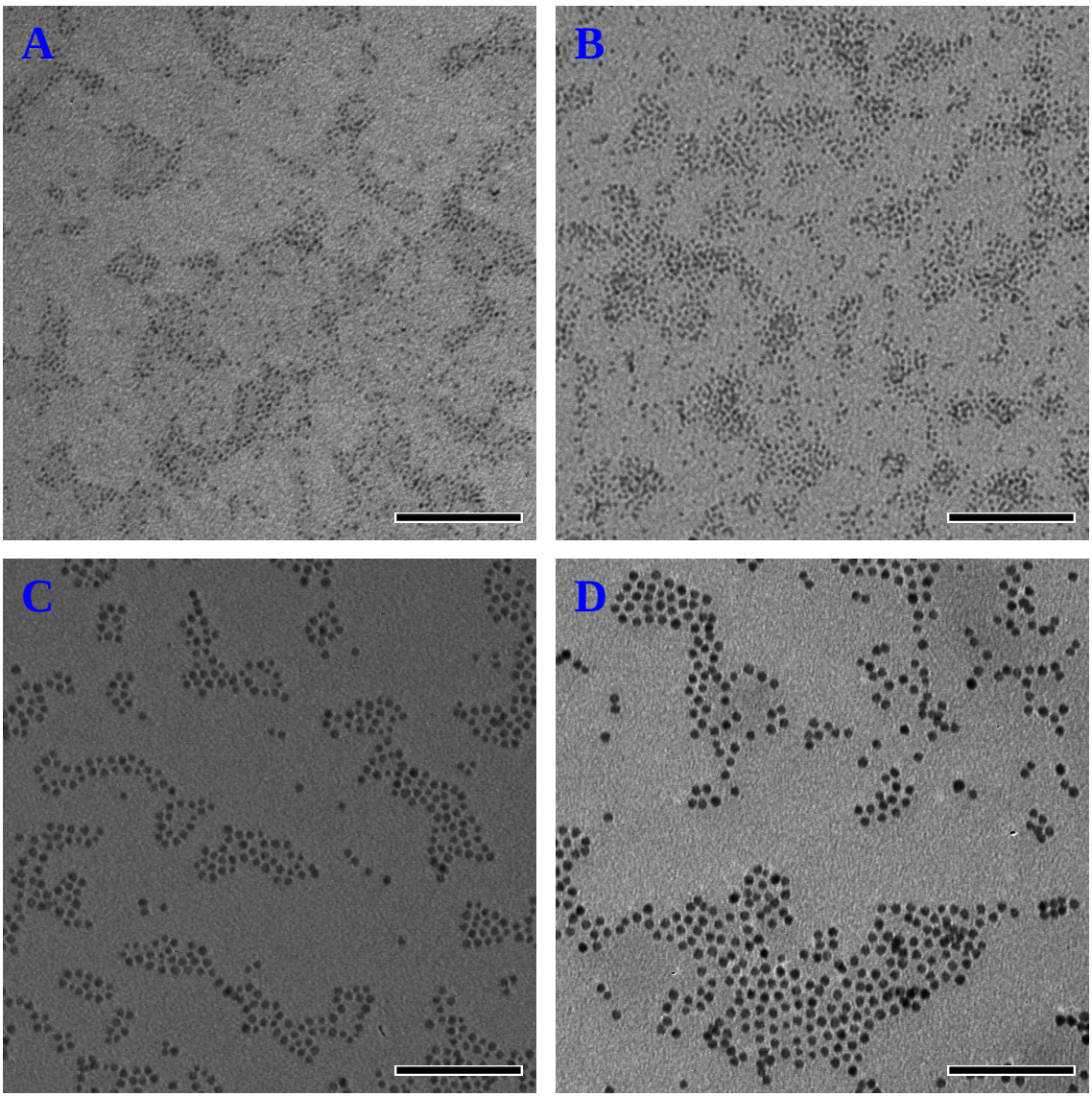

Figure C3. Low resolution TEM images of ligand exchanged hydrophilic PVP-coated $NaGdF_4$ NCs, **(A)** 2.5 nm, **(B)** 4.0 nm, **(C)** 6.5 nm, and **(D)** 8.0 nm, *Scale bar =100 nm*.

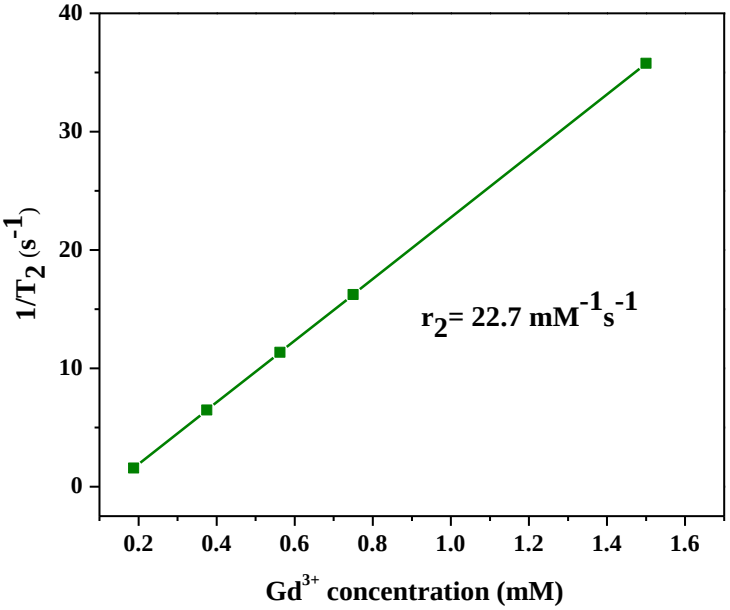

Figure C4. T_2 relaxivity plot of 2.5 nm PVP-coated $NaGdF_4$ NCs measured at 1.5 T.

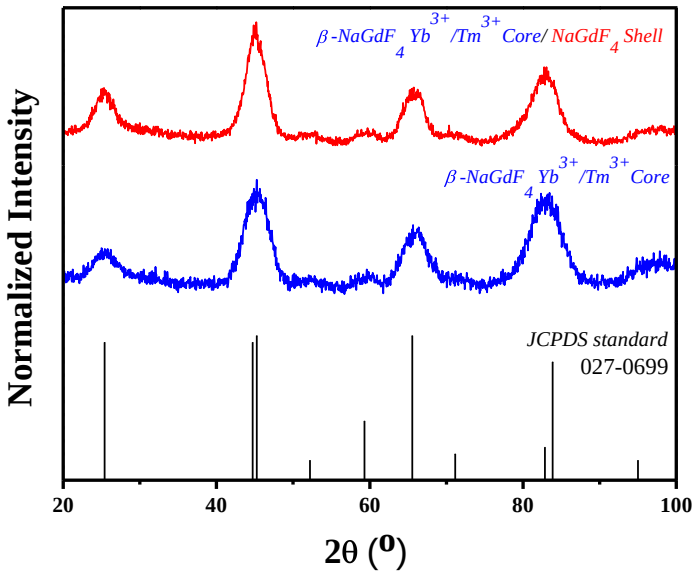

Figure C5. Powder X-Ray Diffraction spectra of $NaGdF_4/Yb^{3+}/Tm^{3+}$ core, and $NaGdF_4/Yb^{3+}/Tm^{3+}$ /$NaGdF_4$ core/ shell NCs matched with β-$NaGdF_4$ reference pattern.

Relaxivity Calculations*

The concentration of Gd^{3+} ions determined by ICP-MS in the stock solution was used to calculate the molecular mass of $NaGdF_4$ in the specimen using the ratio

$m(Gd) / m(NaGdF_4) = 0.6137$

This was used to calculate the **r_1/M (Mass relaxivity)** values.

The $NaGdF_4$ NCs synthesized have Hexagonal closed pack (HCP)- crystal structure and the density of HCP $NaGdF_4$ 5.65 g/cc was used to determine the mass of a NC, considering that the NCs are perfect spheres and their volume determined using

$V = 4/3\ \pi R^3$ (where R is the radius of the NC)

Comparing the mass of the single NC and the total mass determined from ICP-MS the total number of NCs (N) in the stock solution was determined and used to calculate the **r_1/NC (Nanocrystal or per probe relaxivity)** values.

The surface area (SA) of the NC was then calculated using

$SA = 4\pi R^2$ (where R is the radius of the NC)

Using that the total surface area of the NC in the stock solution was calculated

Total surface area (TSA) = N * SA

TSA value was used to determine the **r_1 /SA (relaxivity per m^2 of nanocrystal surface)** values.

* Average ionic relaxivity values were used to calculate the r_1/M, r_1/NC, r_1 /SA.

Tumbling time of the NCs (τ_R)

$\tau_R = 4\pi\eta a^3/3k_BT$

where, η dynamic viscosity = 10^{-3} pa.s, $k_BT = 4 \times 10^{-21}$ J, a = hydrodynamic radius of the NC, T = 298 K.

Ligand Exchange conditions for different-sized $NaGdF_4$ NCs

The ligand exchange of the oleate-stabilized NCs to get PVP-stabilized NCs was done following the procedure described in Chapter 3. No major modifications were done to this procedure, except for the amount of polyvinylpyrrolidone-10 (PVP-10) used. In a typical exchange procedure, 0.2 ml of 1 wt% oleate-stabilized NCs in toluene (this amount was kept constant for all NC sizes) was slowly added to 5 ml of 1:1 dichloromethane (DCM)/ dimethylformamide (DMF) under continuous stirring to obtain a clear solution. Subsequently, 5 ml solution of PVP-10 in 1:1 DCM/DMF (see Table C1 for the amount of PVP-10 used for different NC sizes) was added. The resulting mixture was refluxed at 100 ºC for 6 h, and then cooled to room temperature. The polymer-coated NCs were then precipitated by pouring the reaction mixture into excess ethyl ether (250 ml) and the precipitate was collected by centrifugation (1800 x g), washed with ethyl ether and dried overnight at 70 ºC to obtain a thin oily product. This material was dispersed in 30 ml of deionized water and purified by dialysis as explained in the experimental section. After purification, the water from the colloidal dispersion of NCs was removed by rotary evaporation and fresh deionized water was added (3-4 ml) for relaxivity measurements. For higher concentrations two different batches were added and concentrated to 3-4 ml. The final concentrations of gadolinium ions in these NC dispersions were determined using ICP-MS.

Table C1. Reagent concentrations used for ligand exchange of different sized $NaGdF_4$ nanocrystals.

NC size (nm)	NC concentration (μM) (5 ml DCM/DMF)	PVP-10 concentration (mM) (5 ml DCM/DMF)*
2.5	14	17
4.0	3.5	11
6.5	0.81	6.6
8.0	0.42	5.3

*Note that the PVP-10 used was calculated such that there were ~60 PVP-10 molecules per nm^2 of NC surface. The PVP-10 concentration increases with decrease in NC size as surface area increases with decreasing size for the given mass of NCs.

Appendix D. Supplementary Information to Chapter 6

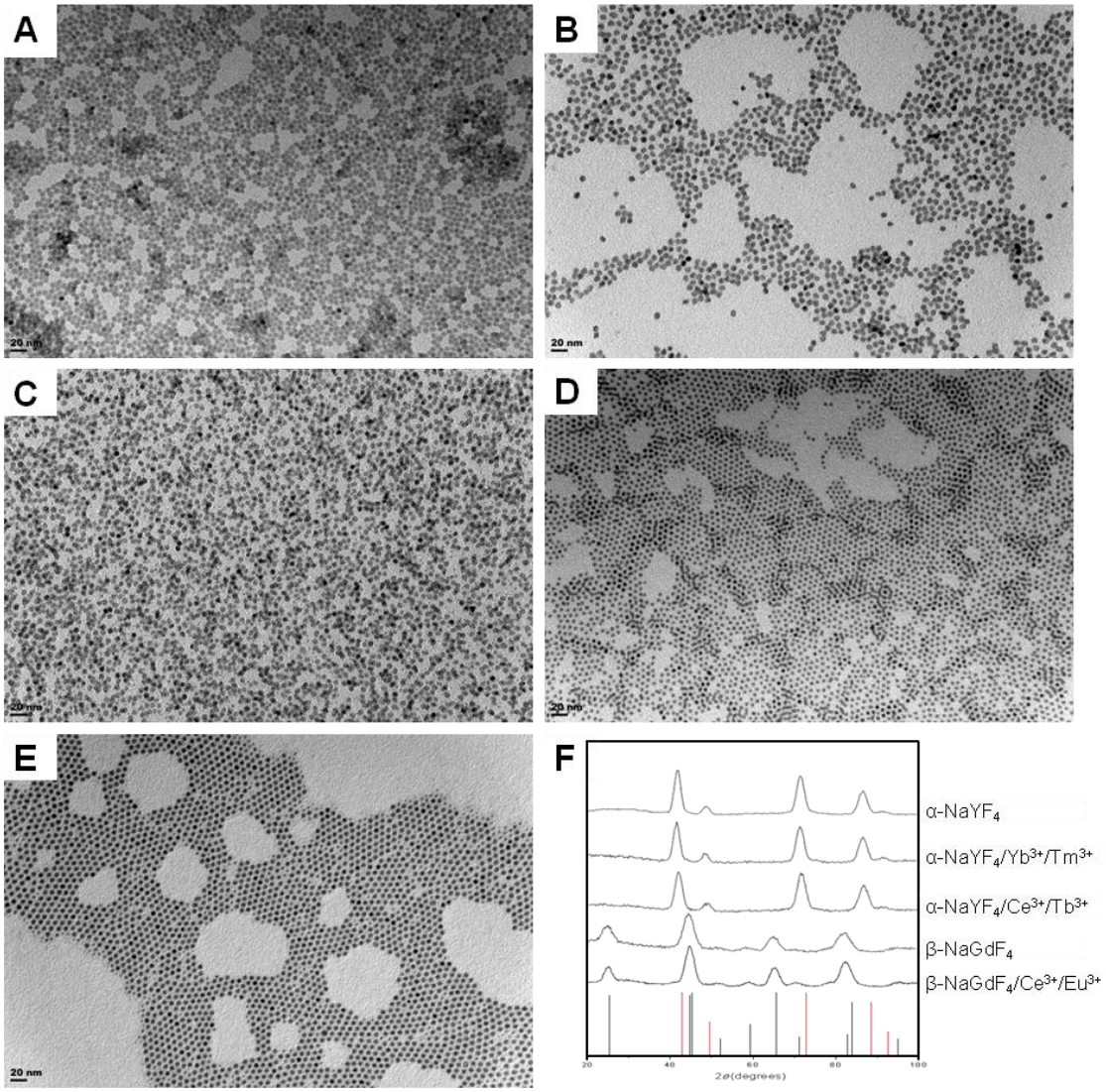

Figure D1. TEM images of SNCs **(A)** α-$NaYF_4$, **(B)** α-$NaYF_4$ (1 mol% Tm^{3+}, 15 mol% Yb^{3+}), **(C)** α-$NaYF_4$ (15 mol% Ce^{3+}, 5 mol% Tb^{3+}), **(D)** β-$NaGdF_4$, **(E)** β-$NaGdF_4$ (2 mol% Ce^{3+}, 5 mol% Eu^{3+}), and **(F)** XRD pattern of the SNCs and the standard reference pattern of α-$NaYF_4$ (red), and β-$NaGdF_4$ (black) (JCPDS- 06-0342 -α-$NaYF_4$, 027-0699 - β-$NaGdF_4$), the average crystallite size of the SNCs were determined from the XRD peak broadening using Scherrer equation to be 6.8, 7.4, 6.4, 5.1, and 5.5 nm for A-E respectively.

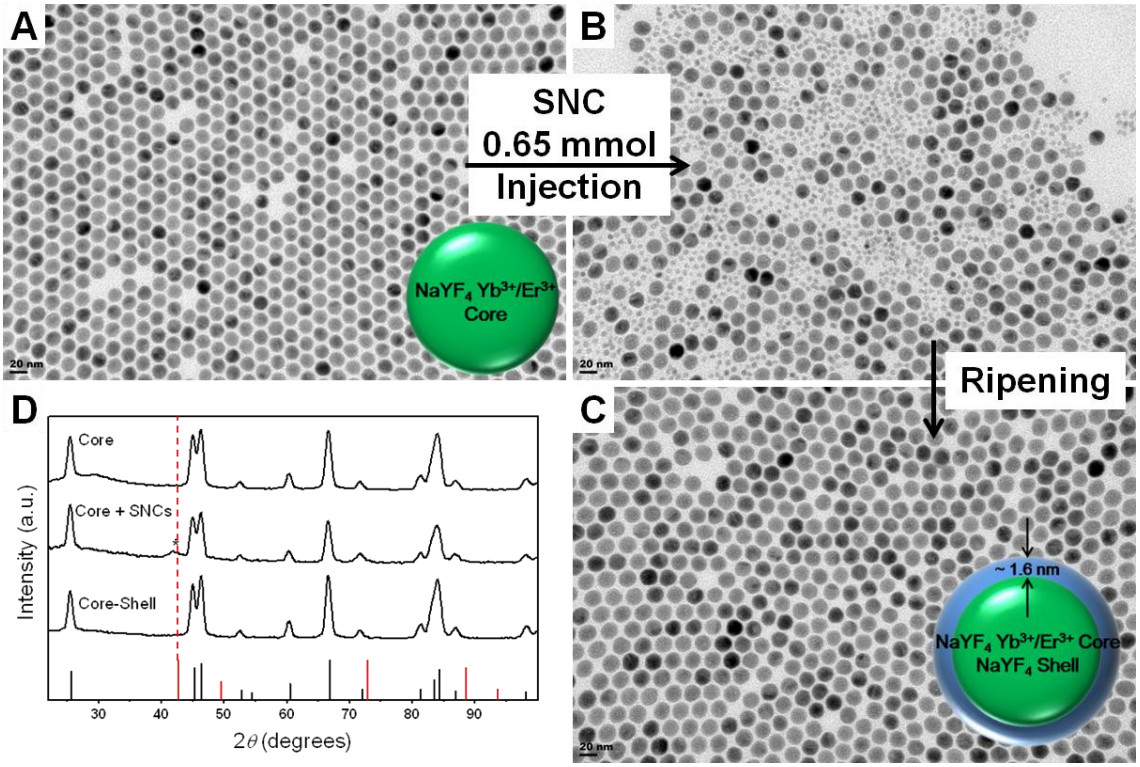

Figure D2. Uncropped TEM images (of NCs shown in Figure 6.2A-C in main text) **(A)** $NaYF_4$: Yb^{3+}/Er^{3+} (15/2%) core NCs (@t=0), **(B)** after injection of α-$NaYF_4$ SNCs (@t=5 sec), **(C)** after self-focusing $NaYF_4$: Yb^{3+}/Er^{3+} (15/2%) core/$NaYF_4$ shell NCs (@t=10 min), and **(D)** XRD pattern of the NCs and the standard reference pattern of α-$NaYF_4$ (red), and β-$NaYF_4$ (black) (JCPDS- 06-0342 -α-$NaYF_4$, 016-0334 -β-$NaYF_4$). (NCs size histograms are provided in Figure 6.2D in main text).

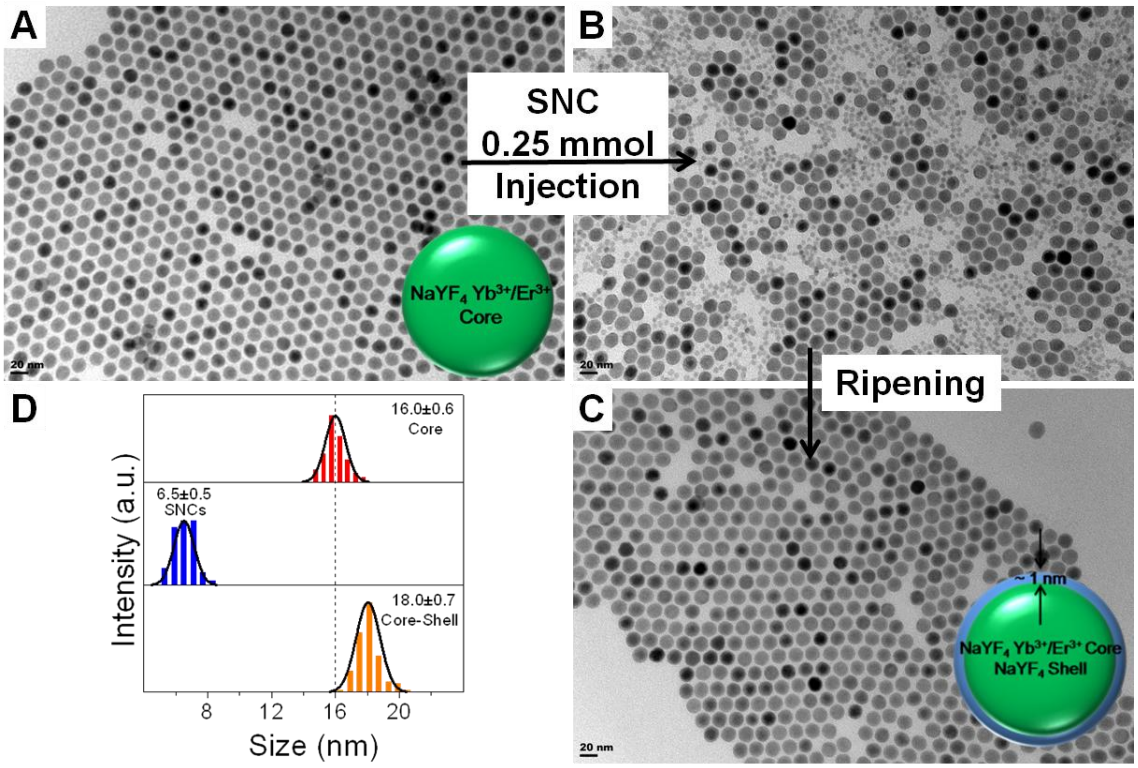

Figure D3. TEM images of **(A)** $NaYF_4$: Yb^{3+}/Er^{3+} (15/2%) core NCs (@t=0), **(B)** after injection of α-$NaYF_4$ SNCs (@t=5 sec), **(C)** after self-focusing $NaYF_4$: Yb^{3+}/Er^{3+} (15/2%) core/$NaYF_4$ shell NCs (@t=5 min), and **(D)** size distribution of the core and core-shell NCs.

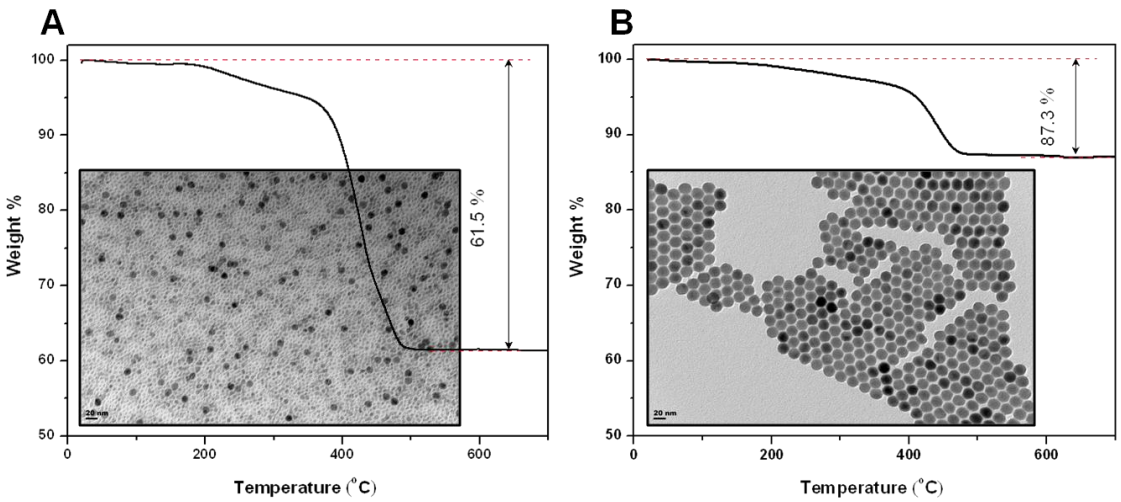

Figure D4. TGA analysis of core NCs with a reaction time of **(A)** 30 min, and **(B)** 60 min, *inset* corresponds to the TEM images of the NCs obtained from the reaction.

To confirm the monomer depleted ripening-mediated growth of hexagonal (β) NCs at the expense of cubic (α) NCs, the core reaction was performed for two different reaction times 30 and 60 min, and the inorganic crystal yield was determined for both the reactions. The reaction yield of only the inorganic NC content was determined after taking into account the percentage of organic ligand determined from TGA. The presence of small NCs at 30 min resulted in high percentage of organic ligands relative to the ripened larger NCs at 60 min. The average inorganic NC yield determined was 81% and 83% for 30 min and 60 min, respectively. The inorganic NC yield was almost the same at $t_{1/2}$ (30 min) relative to the core NCs grown for 60 min; this unequivocally confirms the ripening-mediated growth of hexagonal (β) NCs at the expense of cubic (α) NCs. The fact that the yield was determined after precipitating the NCs from the reaction mixture followed by multiple washing and centrifugation confirms the high yield of NCs and the monomer depleted process in the growth of hexagonal (β) NCs.

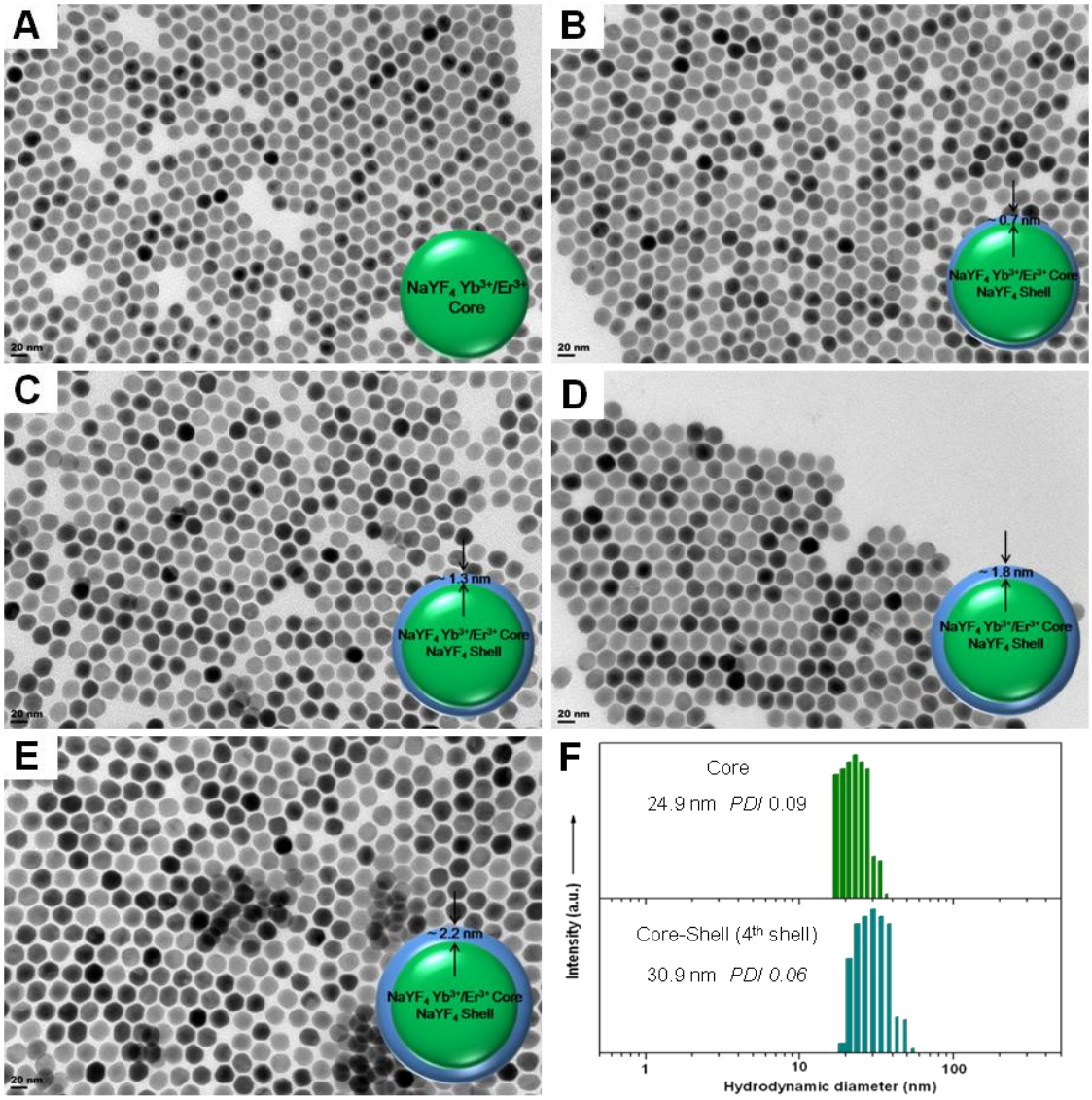

Figure D5. Uncropped TEM images (of NCs shown in Figure 6.4A-E in main text) **(A)** $NaYF_4$: Yb^{3+}/Er^{3+} (15/2%) core NCs, **(B-E)** $NaYF_4$: Yb^{3+}/Er^{3+} (15/2%) core/$NaYF_4$ shell NCs after successive defocusing and self-focusing cycle using 0.2 mmol SNCs in each step, and **(F)** Hydrodynamic size of the core and the final core-shell NCs after four ripening cycles determined by Dynamic Light Scattering (DLS). The size analysis from TEM images of the NCs is shown in Figure 6.4A-E in main text, and the hydrodynamic size determined by DLS shown here also confirms the unimodal distribution for both the core and core/shell NCs ensemble after four successive defocusing and self-focusing cycle with narrow polydispersity index (PDI).

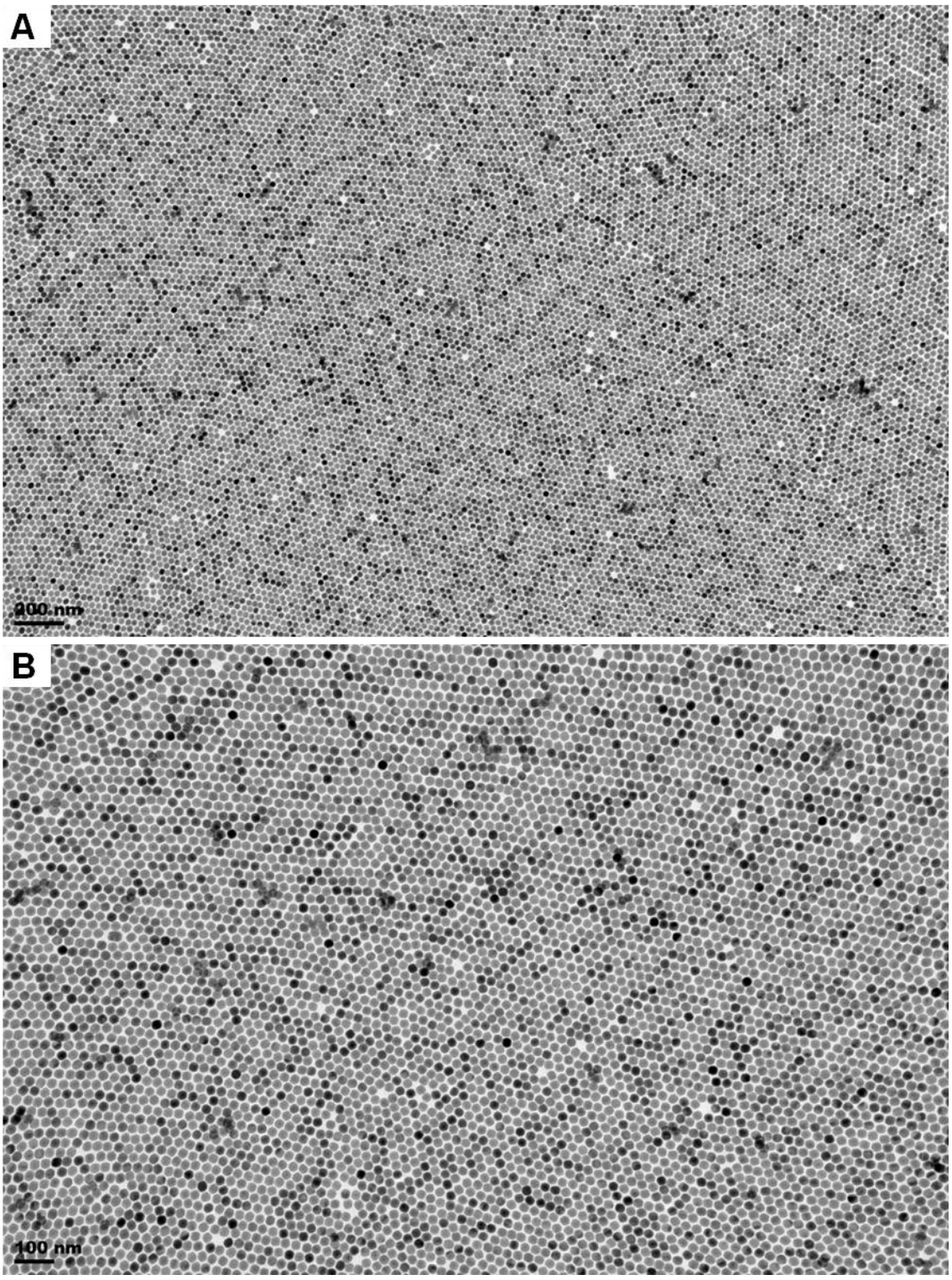

Figure D6. Low magnification TEM images for the NCs shown in Figure D5E/Figure 6.4E demonstrating 2D assembly of core-shell NCs obtained after four ripening cycles. The large array of NCs confirms the high monodispersity and uniformity of the obtained core-shell NCs.

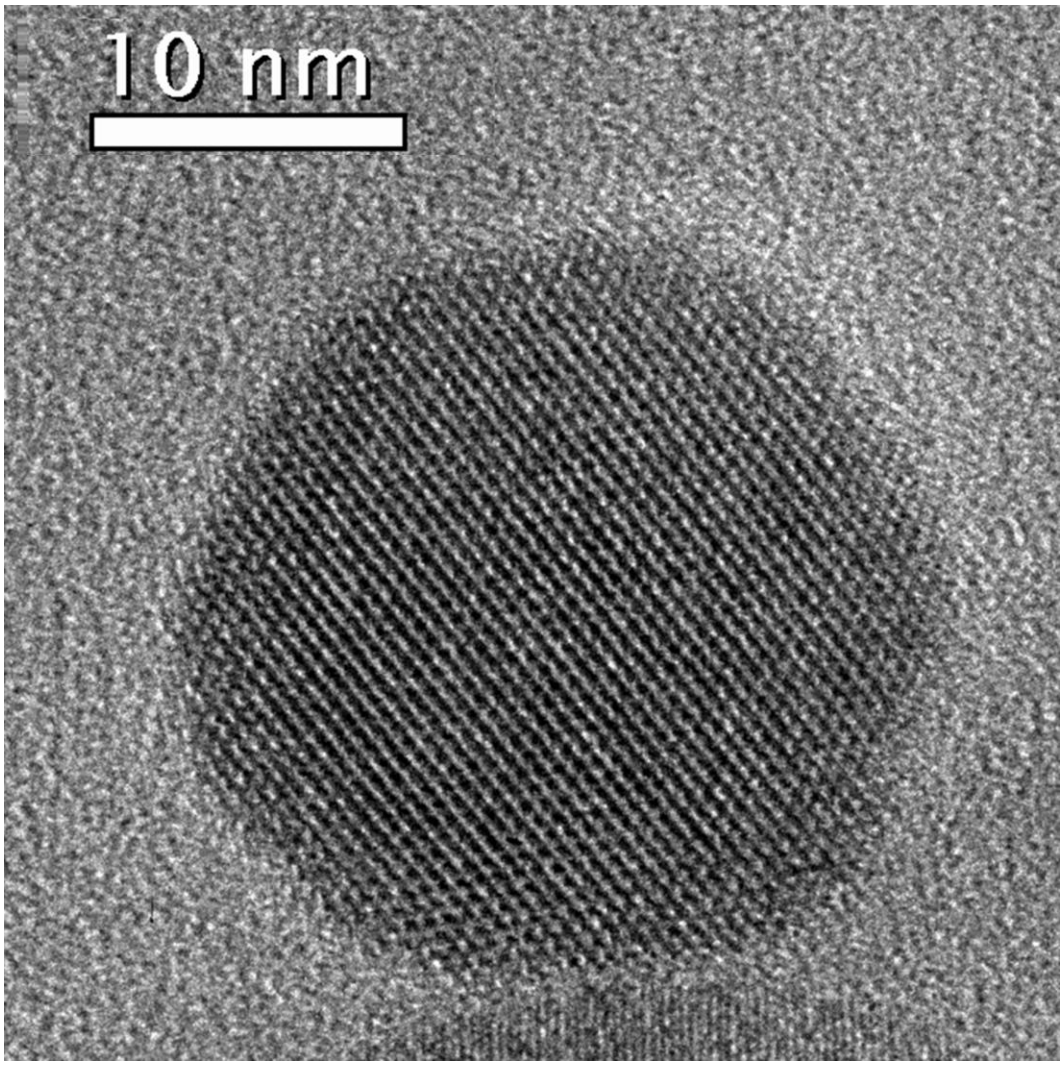

Figure D7. High-resolution TEM image of a single core-shell NC obtained after four successive defocusing and ripening cycles shown in Figure D5E/Figure D6/Figure 6.4E demonstrating high-crystallinity.

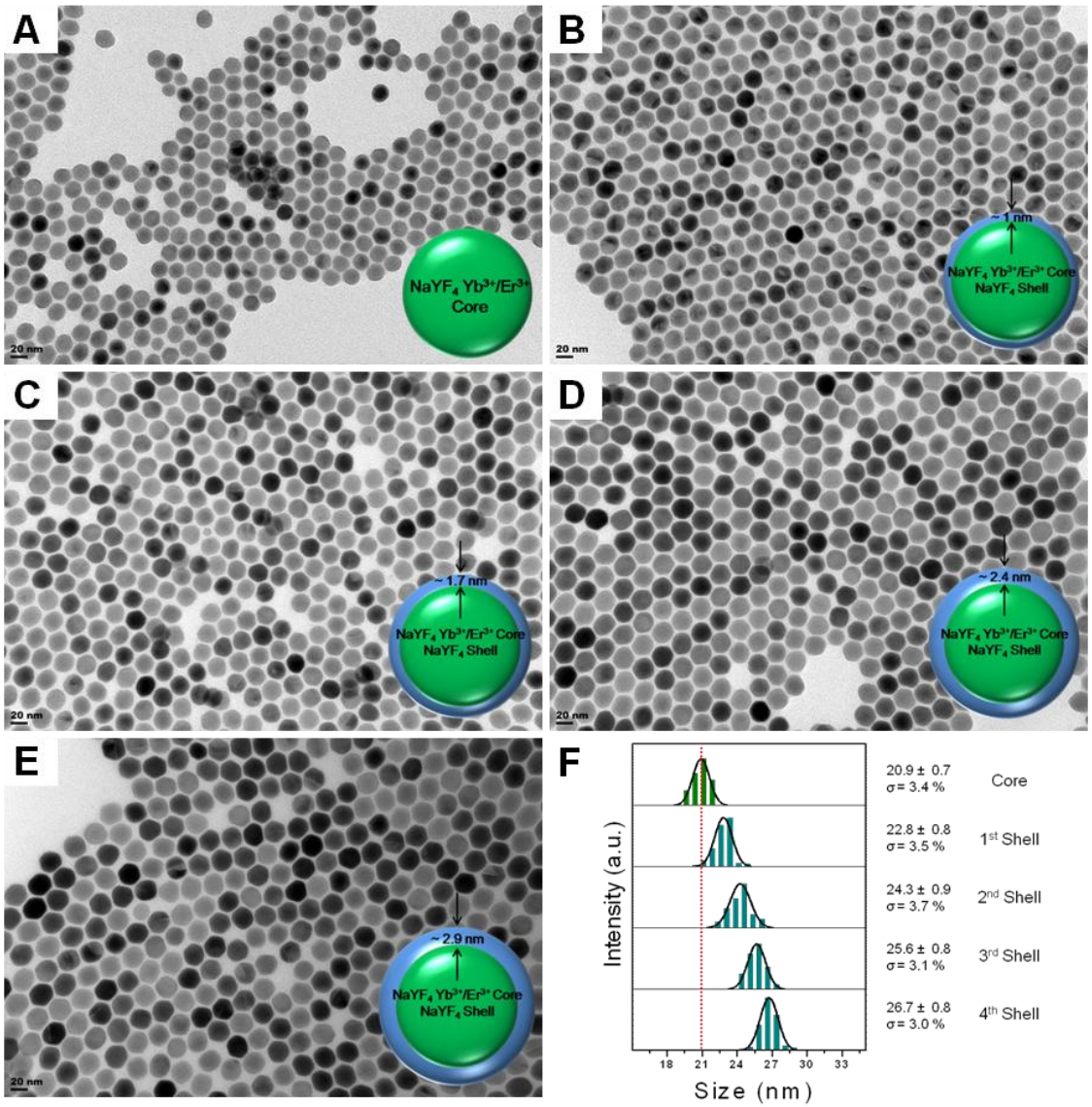

Figure D8. TEM images of **(A)** $NaYF_4$: Yb^{3+}/Er^{3+} (15/2%) core NCs, **(B-E)** $NaYF_4$: Yb^{3+}/Er^{3+} (15/2%) core/$NaYF_4$ shell NCs after successive defocusing and self-focusing cycle using 0.25 mmol SNCs in each step, and **(F)** size distribution of the core and core-shell NCs.

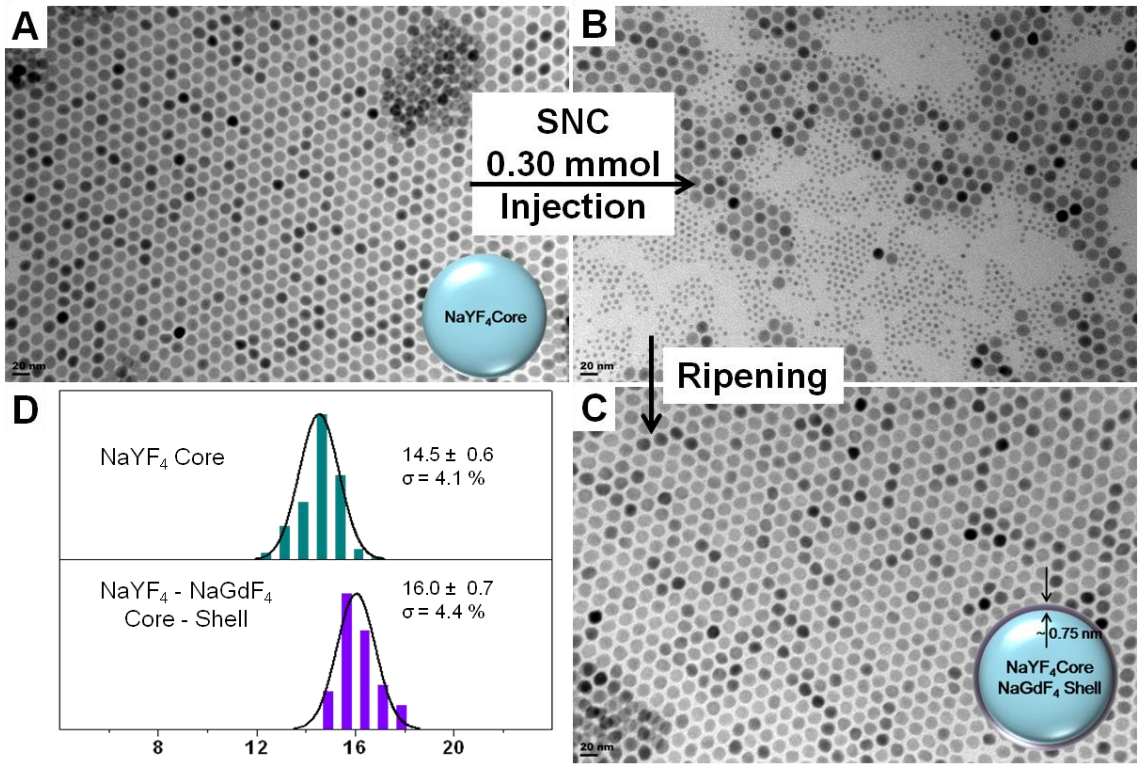

Figure D9. Uncropped TEM images (of NCs shown in Figure 6.6A-B in main text) **(A)** $NaYF_4$ core NCs (@t=0), **(B)** after injection of β-$NaGdF_4$ SNCs (@t=5 sec), **(C)** after self-focusing $NaYF_4$ core/$NaGdF_4$ shell NCs (@t=10 min), and **(D)** size distribution of the core and core-shell NCs.

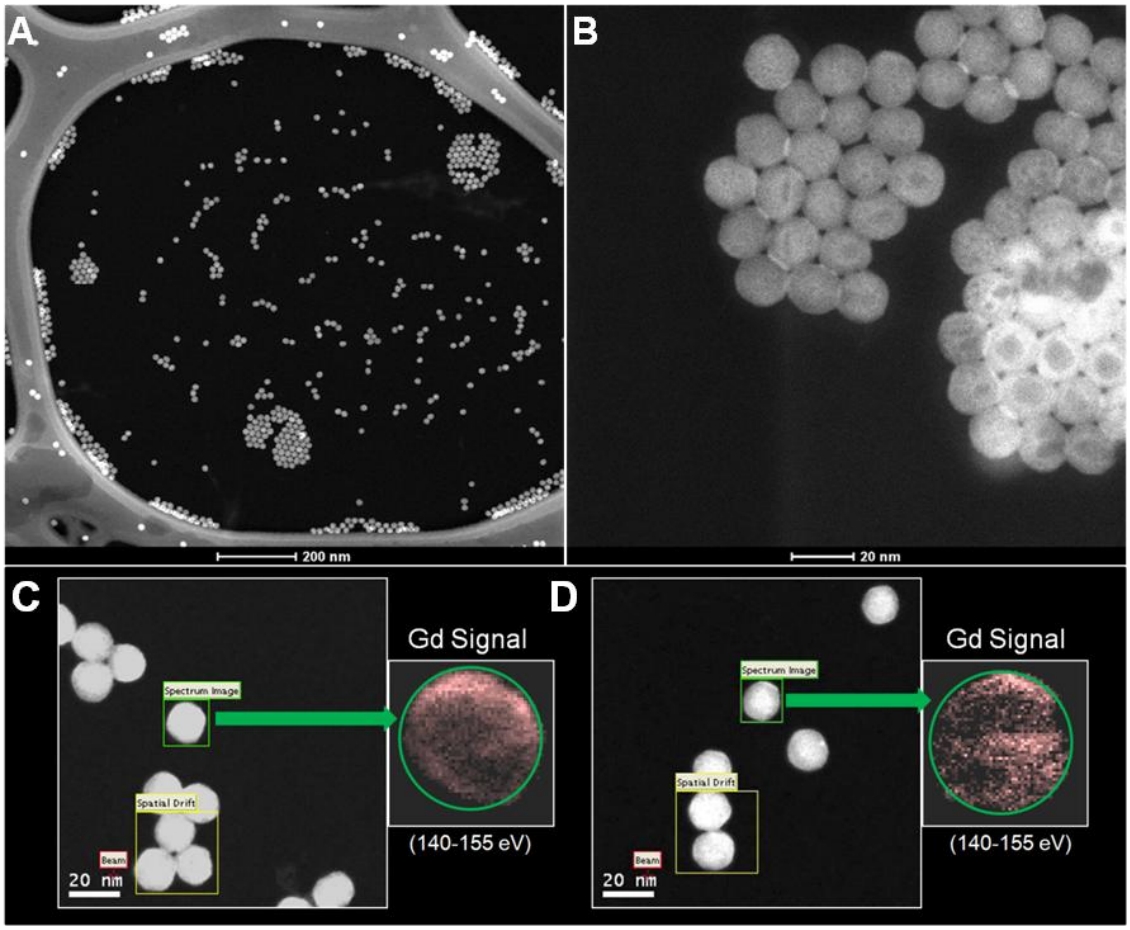

Figure D10. (A) HAADF TEM images of $NaYF_4$ core/$NaGdF_4$ shell NCs low magnification, **(B)** HAADF TEM images of $NaYF_4$ core/$NaGdF_4$ shell NCs high magnification confirming the uniform size distribution, and **(C-D)** EELS mapping of gadolinium demonstrating the deposition of $NaGdF_4$ shell in two different randomly selected $NaYF_4$ core/$NaGdF_4$ shell NCs.

The control sample of core $NaYF_4$ NCs (NCs shown in Figure D9A @t=0 before SNC injection) by EELS mapping did not show any localized gadolinium signal as observed for the core/shell NCs confirming the ability to deposit epitaxial layer of choice by ripening.

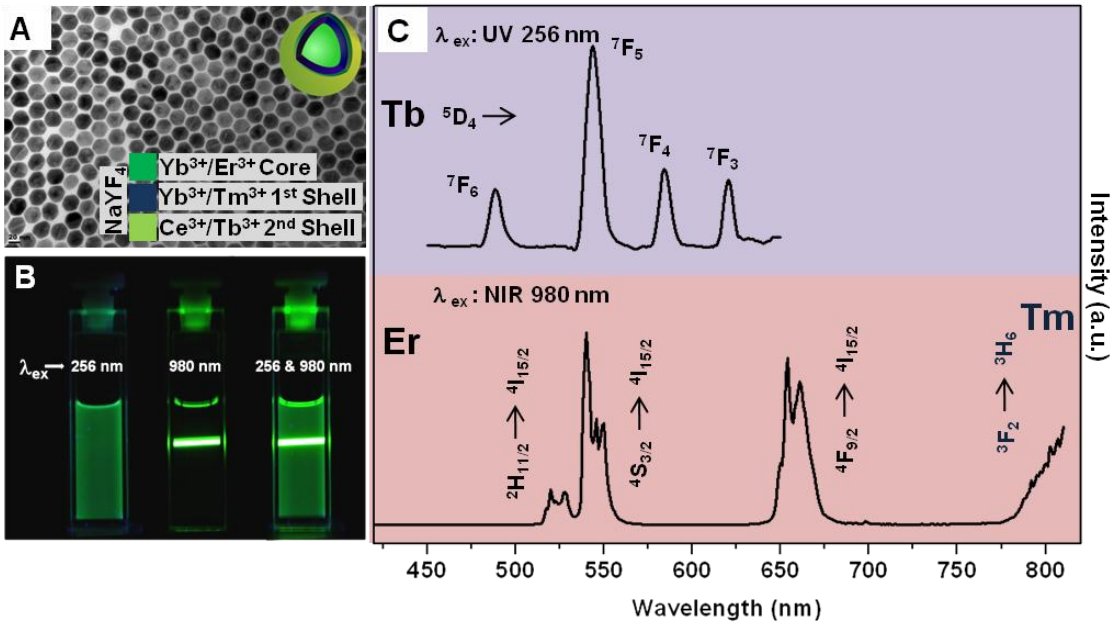

Figure D11. (A) TEM image of $NaYF_4$ (2 mol% Er^{3+}, 15 mol% Yb^{3+} doped) core / $NaYF_4$ (1 mol% Tm^{3+}, 15 mol% Yb^{3+} doped) shell/ $NaYF_4$ (5 mol% Tb^{3+}, 15 mol% Ce^{3+} doped) shell NCs, **(B)** Colloidal dispersions of core-shell NCs in hexane **(left to right)** under 256 nm UV excitation, 980 nm NIR excitation, and combined UV and NIR excitation,* and **(C)** Emission profiles of the core-shell NCs showing Tb^{3+} emission under 256 nm UV excitation **(top)**, and up-converted Er^{3+}/Tm^{3+} emission under 980 nm NIR excitation **(bottom)**. For the up-converted Tm^{3+} emission only the predominant 800 nm emission is observed, and the less intense blue emission was very low compared to the other emission bands due to the dopant and sensitizer concentrations.

* The Tb^{3+} green emission upon 256 nm excitation was obtained with a table top UV light and thus illuminates the whole dispersion. The upconverted Er^{3+} green emission upon 980 nm excitation was obtained with a laser diode excitation and the emission in observed only along the laser path. The combined excitation (256 and 980 nm) photograph shows both the green emission from Tb^{3+} and Er^{3+}, respectively.

To confirm the spatial orientation of dopant ions in the core-shell NCs shown in Figure D11, NCs with the same dopant ratio were synthesized by co-doping the ions in a single NC matrix. $NaYF_4$ doped with Yb^{3+} (13%), Er^{3+} (1%), Ce^{3+} (2%), Tb^{3+} (0.8%), Tm^{3+} (0.3%) was synthesized following the core (β-$NaYF_4$) NC synthesis protocol outlined in the experimental section. The hexane dispersion of the synthesized co-doped NCs was taken in the same ionic concentration of the core-shell NCs for optical measurements shown in Figure D12.

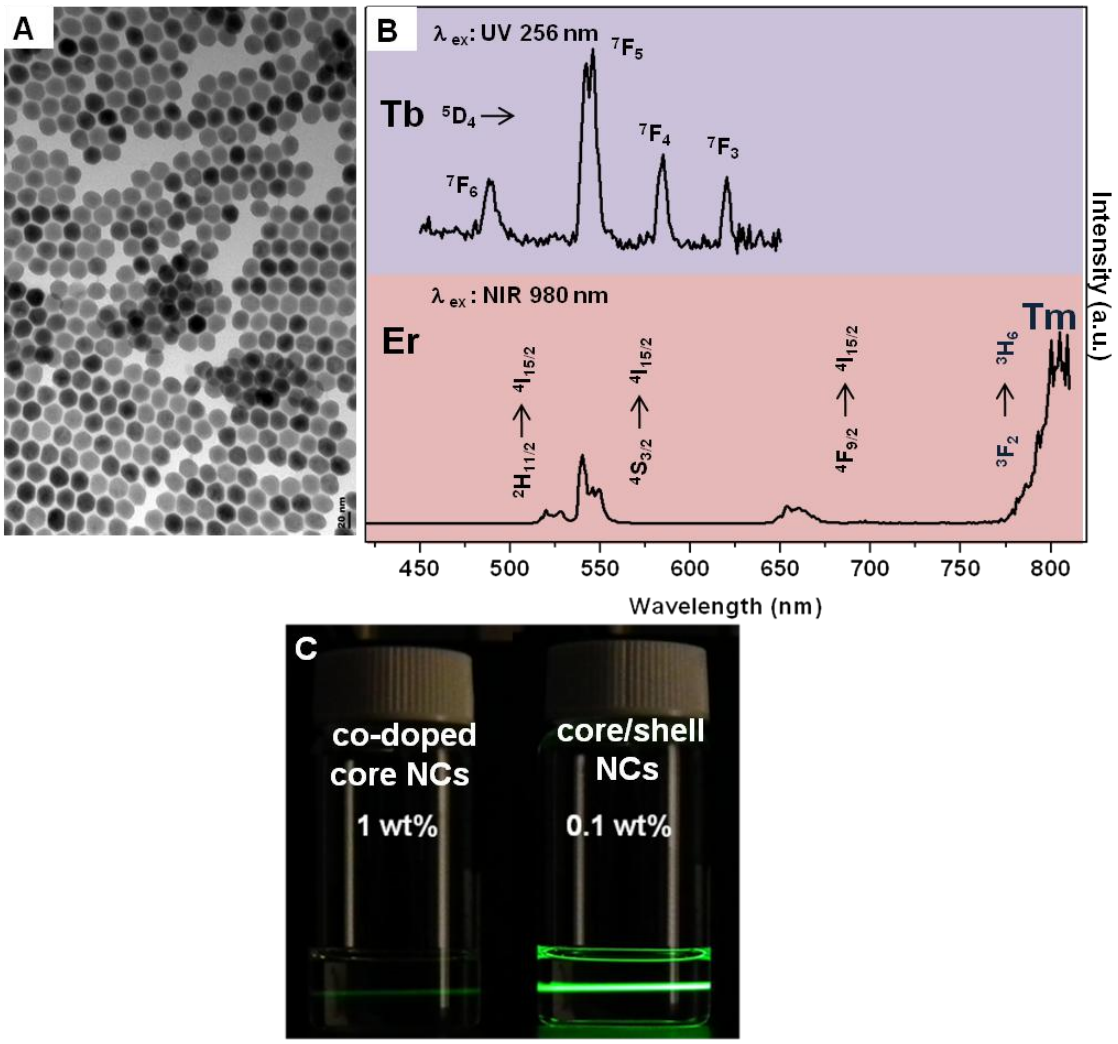

Figure D12. (A) TEM image of $NaYF_4$ (Yb^{3+} (13%), Er^{3+} (1%), Ce^{3+} (2%), Tb^{3+} (0.8%), Tm^{3+} (0.3%) co-doped) NCs, **(B)** Emission profiles of the NCs showing Tb^{3+} emission under 256 nm UV excitation **(top)**, and up-converted Er^{3+}/Tm^{3+} emission under 980 nm NIR excitation **(bottom)**, and **(C)** Colloidal dispersions of co-doped NCs (1 wt %) and core-shell NCs (0.1 wt %) in hexane **(left to right)** under 980 nm NIR excitation.

For the co-doped NCs shown in Figure D12, both the emission from Er^{3+} and Tb^{3+} respectively was heavily quenched. The overlapping green emission bands of the ions results in detrimental cross-relaxation, which was not observed in the core-shell NCs. Moreover as the upconverted red emission from Er^{3+} is predominantly fed from green emitting level ($^4S_{3/2} \rightarrow {}^4F_{9/2}$) (see Figure D17), resulted in very low red emission band. The non-overlapping NIR (800 nm) emission from Tm^{3+} was predominant compared to the other emission bands. The dispersion photograph in Figure D12C shows the emission from 1 wt % dispersion of co-doped NCs which is comparatively very low than a 0.1 wt% dispersion of core-shell NCs.

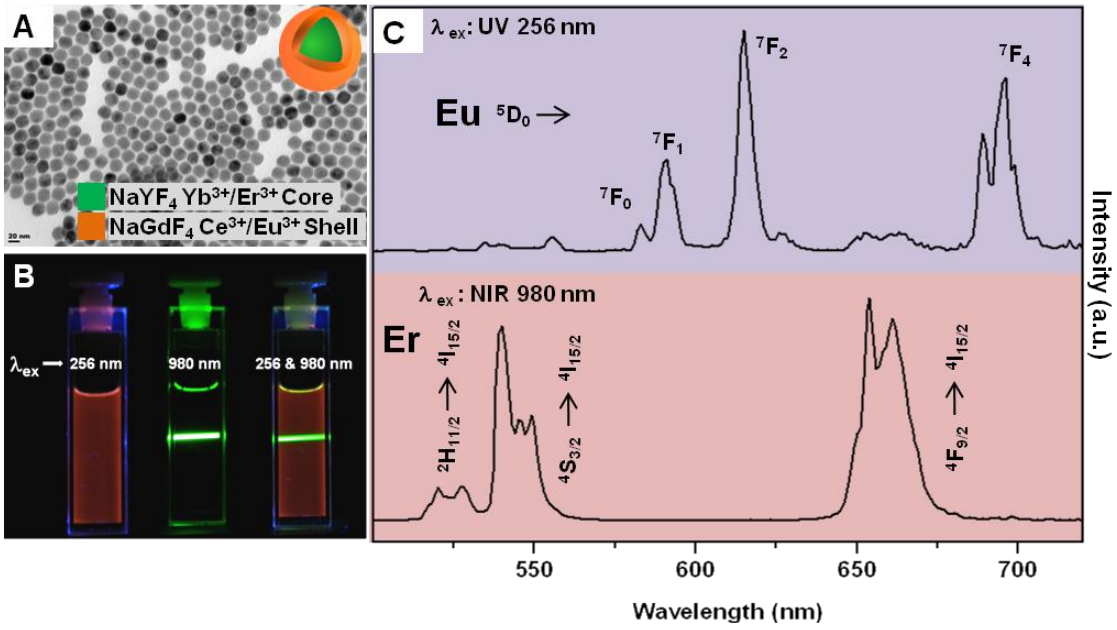

Figure D13. (A) TEM image of $NaYF_4$ (2 mol% Er^{3+}, 15 mol% Yb^{3+} doped) core / $NaGdF_4$ (5 mol% Eu^{3+}, 2 mol% Ce^{3+} doped) shell NCs, **(B)** Colloidal dispersions of core-shell NCs in hexane (left to right) under 256 nm UV excitation, 980 nm NIR excitation, and combined UV and NIR excitation, and **(C)** Emission profiles of the core-shell NCs showing Eu^{3+} emission under 256 nm UV excitation **(top)**, and up-converted Er^{3+} emission under 980 nm NIR excitation **(bottom)**.

To confirm the spatial orientation of dopant ions in the core-shell NCs shown in Figure D13, NCs with the same dopant ratio were synthesized by co-doping the ions in a single NC matrix. $NaYF_4$ doped with Yb^{3+} (12%), Er^{3+} (1.6%), Gd^{3+} (22%), Eu^{3+} (1%), Ce^{3+} (0.4%) was synthesized following the core (β-$NaYF_4$) NC synthesis protocol outlined in the experimental section. The hexane dispersion of the synthesized co-doped NCs was taken in the same ionic concentration of the core-shell NCs for optical measurements shown in Figure D14.

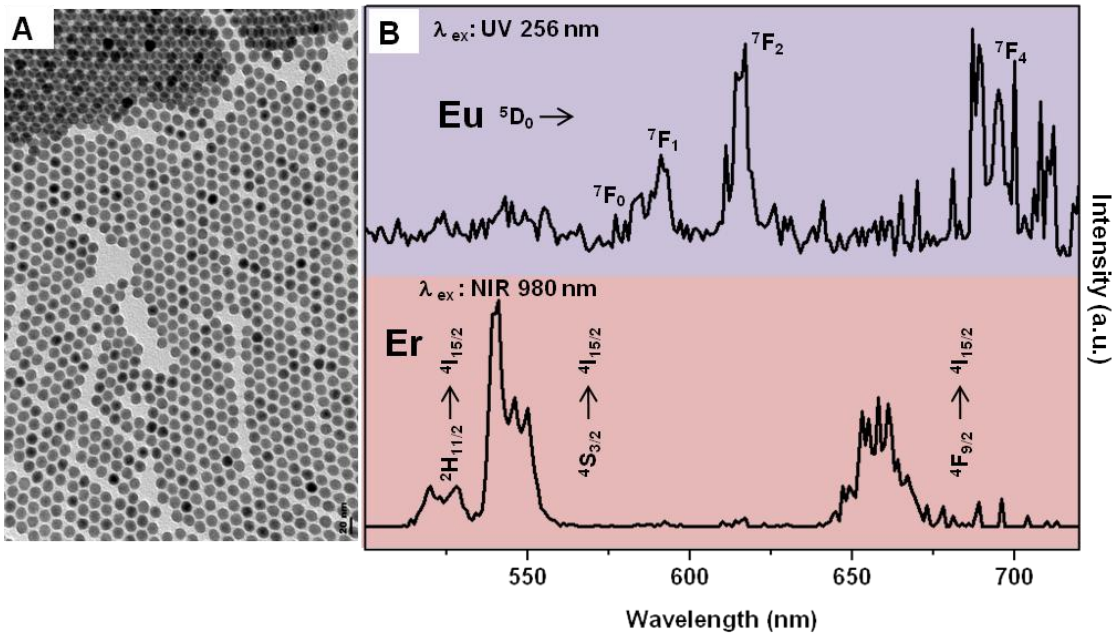

Figure D14. (A) TEM image of $NaYF_4$ (Yb^{3+} (12%), Er^{3+} (1.6%), Gd^{3+} (22%), Eu^{3+} (1%), Ce^{3+} (0.4%) co-doped) NCs, and **(B)** Emission profiles of the NCs showing Eu^{3+} emission under 256 nm UV excitation **(top)**, and up-converted Er^{3+} emission under 980 nm NIR excitation **(bottom)**.

For the co-doped NCs shown in Figure D14, the emission from Eu^{3+} was heavily quenched. The energy transfer from excited Ce^{3+} to the Eu^{3+} is mainly through the higher energy levels of Gd^{3+} (see Figure D17), and thus in the co-doped NCs the spatial separation of ions are more than that of the core-shell NCs shown in Figure D13. For the upconverted Er^{3+} emission the red emission was heavily quenched owing to the overlap of the emission bands of Eu^{3+} and Er^{3+}, and such detrimental cross-relaxation was not observed in core-shell NCs.

To demonstrate that this protocol can be extended to relatively smaller sized upconverting core NCs with a different host matrix, using 7.5±0.3 nm upconverting $NaGdF_4$ NCs and 6.4 nm α-$NaYF_4$(5 mol% Tb^{3+}, 15 mol% Ce^{3+} doped) SNCs, 9.5±0.3 nm dual-mode emitting core-shell NCs were obtained as shown in Figure D15 and D16.

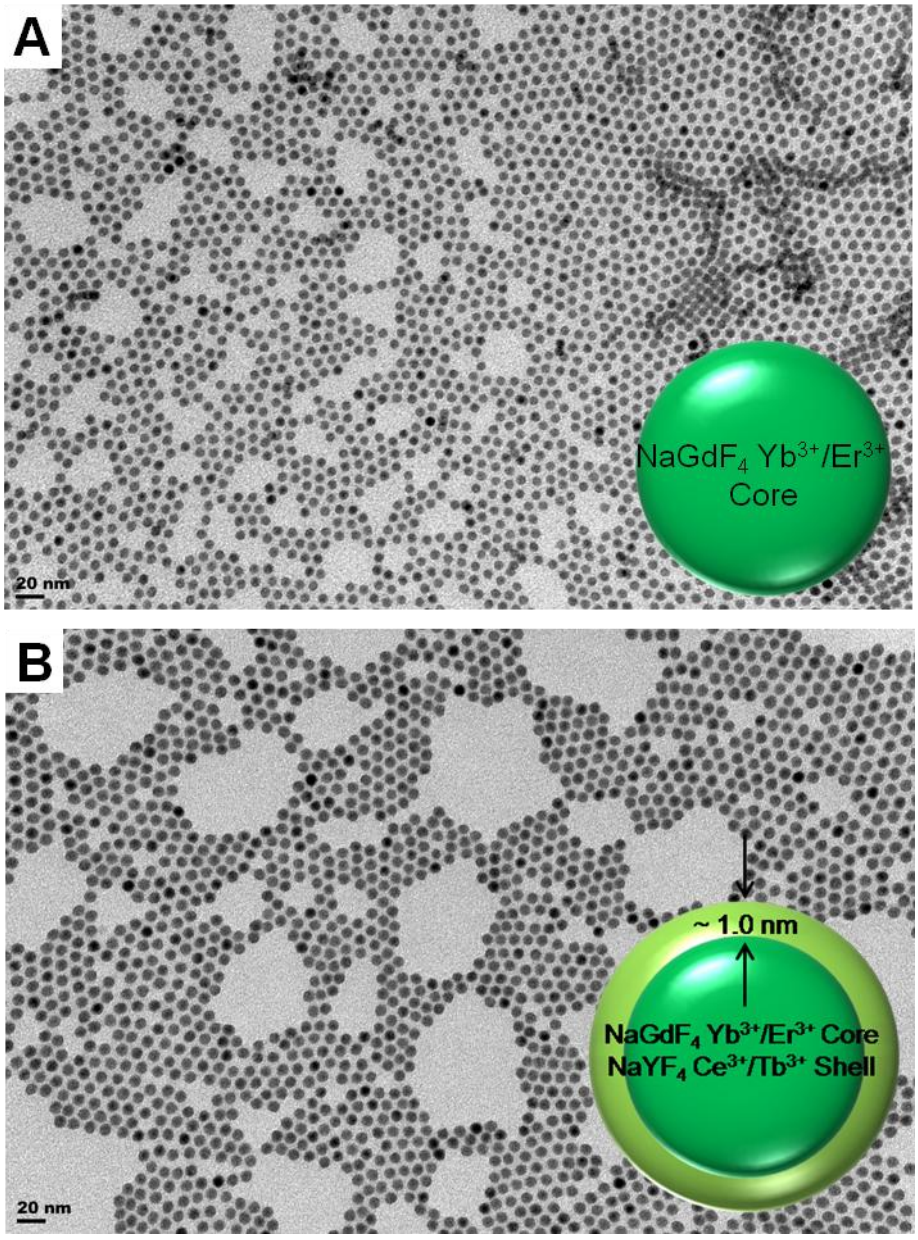

Figure D15. TEM images of **(A)** $NaGdF_4$ (2 mol% Er^{3+}, 25 mol% Yb^{3+}, 10 mol% Y^{3+} doped) core NCs, and **(B)** $NaGdF_4$ (2 mol% Er^{3+}, 25 mol% Yb^{3+}, 10 mol% Y^{3+} doped) core / $NaYF_4$ (5 mol% Tb^{3+}, 15 mol% Ce^{3+} doped) shell NCs.

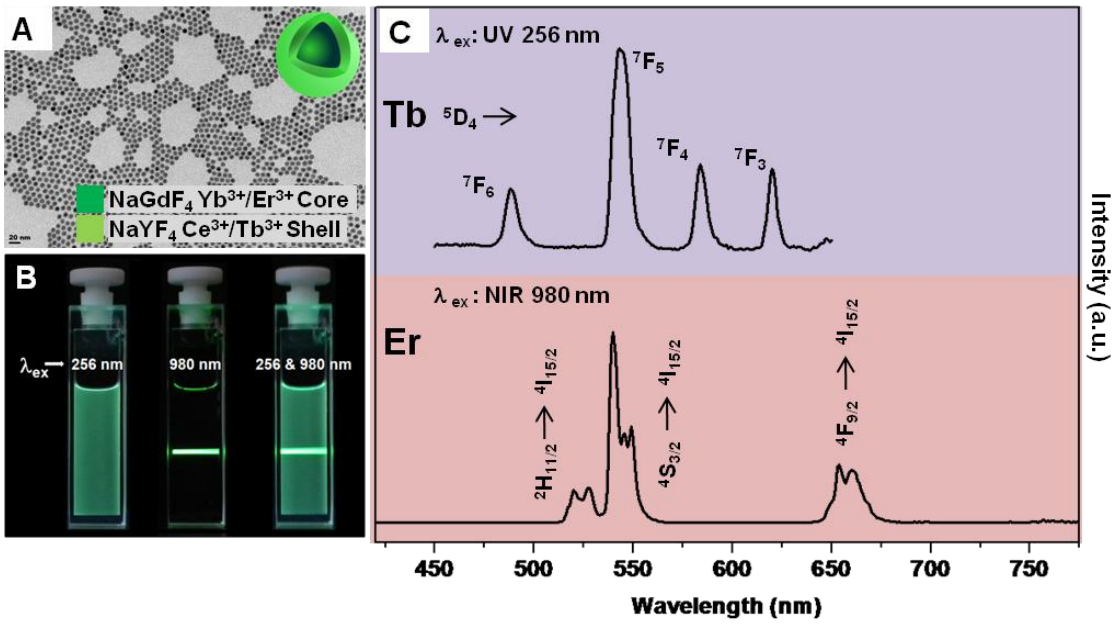

Figure D16. (A) $NaGdF_4$ (2 mol% Er^{3+}, 25 mol% Yb^{3+}, 10 mol% Y^{3+} doped) core / $NaYF_4$ (5 mol% Tb^{3+}, 15 mol% Ce^{3+} doped) shell NCs, **(B)** Colloidal dispersions of core-shell NCs in hexane (left to right) under 256 nm UV excitation, 980 nm NIR excitation, and combined UV and NIR excitation, and **(C)** Emission profiles of the core-shell NCs showing Tb^{3+} emission under 256 nm UV excitation **(top)**, and up-converted Er^{3+} emission under NIR 980 nm excitation **(bottom)**.

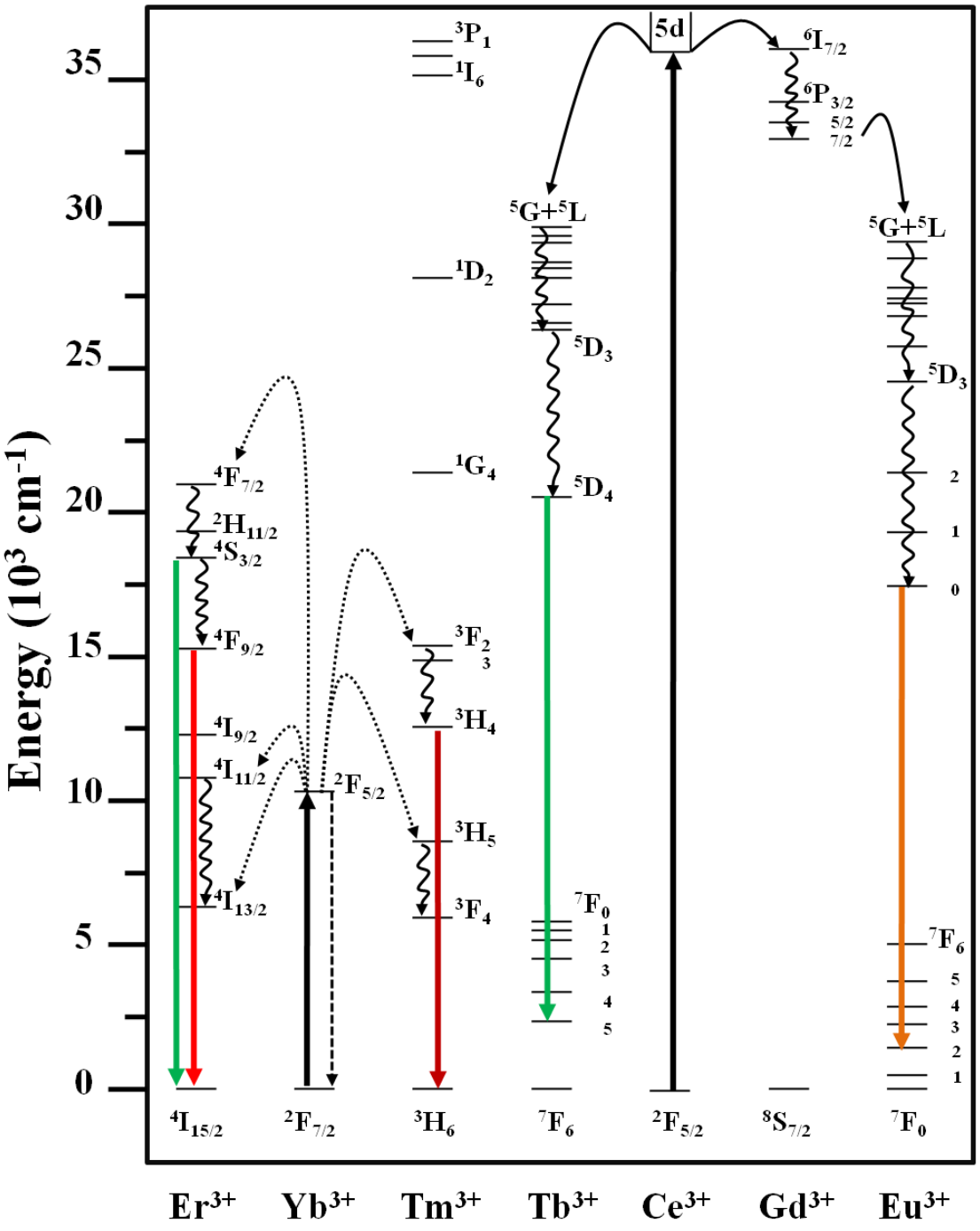

Figure D17. Energy level diagram and the excitation/emission pathways of the lanthanide ions investigated. Only the predominantly observed emission pathways are highlighted.

Core and core-shell NCs with same number concentration of NCs

To determine the number of NCs in each retrieved aliquot obtained from layer-by-layer successive epitaxial shell growth, we first assumed that there are x NCs/ml in the reaction mixture of core NCs (21 ml). In each step 1 ml of the reaction mixture was retrieved followed by injection of 1 ml of SNCs in octadecene resulting in constant reaction mixture volume (21 ml) throughout the growth process. Taking into account that the SNCs injected dissolve and deposit on the core NCs, the number concentration of NCs retrieved decreases with each successively retrieved aliquot. Based on this, the number of NCs in each aliquot was mathematically determined to be x, $(20/21)x$, $(20/21)^2x$, $(20/21)^3x$, $(20/21)^4x$, for the core and core-shell NCs with each layer growth respectively. Calculated volume of the above dispersions were taken and diluted with hexanes such that there were same number concentration of NCs for ICP-MS analysis (Table D1) and the same dispersions were used for optical measurements.

Table D1. Elemental concentration of lanthanide ions in core and core-shell NCs determined by ICP-MS.

	Y^{3+} (mM)	Yb^{3+} (mM)	Er^{3+} (μM)
Core	1.656 ± 0.1	0.269 ± 0.01	32.9 ± 0.8
Core/1st Shell	1.801 ± 0.1	0.259 ± 0.01	30.9 ± 0.7
Core/2nd Shell	2.117 ± 0.1	0.261 ± 0.01	30.9 ± 0.7
Core/3rd Shell	2.429 ± 0.1	0.257 ± 0.01	30.3 ± 0.9
Core/4th Shell	2.965 ± 0.3	0.275 ± 0.02	32.2 ± 2.8

The determined ionic concentrations of the lanthanide ions in the core and successive core-shell NCs clearly demonstrate the increase in Y^{3+} concentration with the addition of each shell while the Yb^{3+} and Er^{3+} concentration almost remains the same. The final core/4th shell NCs should have ~91% Y^{3+} based on the reaction concentration. The Y^{3+} calculated from the above table for the core/4th shell is indeed ~91% relative to the Yb^{3+} and Er^{3+} concentration, confirming the mass balance throughout the ripening cycle.

Determination of crystal yield of SNCs and amount injected for core-shell growth

The SNCs synthesized and dispersed in hexane were taken, and measured volume of the dispersion was transferred to a pre-weighed vial and the hexane then removed by bubbling with argon. The SNCs in the vial were dried over-night at 70 ºC under vacuum, and the vial was then weighed to determine the total organic and inorganic content (ligand+SNCs). The percentage of organic ligands were then determined by Thermogravimetric Analysis (TGA) and subtracted to obtain the total inorganic content in a given volume and the crystal yield. Three such measurements were done, averaged and utilized for calculating the amount of SNCs injected (Table D2). The average inorganic crystal yield for the cubic (α) SNCs was between 70-80 %, and 80-90 % for the hexagonal (β) SNCs.

Table D2. Amount of SNCs injected and ripening steps.

Core/Shell NCs	Amount of SNCs injected*	Steps
β-$NaYF_4$ (2 mol% Er^{3+}, 15 mol% Yb^{3+}) core / $NaYF_4$ shell	0.65 mmol (α-$NaYF_4$)	Single step
β-$NaYF_4$ (2 mol% Er^{3+}, 15 mol% Yb^{3+}) core / $NaYF_4$ shell	0.25 mmol (α-$NaYF_4$)	Single step
β-$NaYF_4$ (2 mol% Er^{3+}, 15 mol% Yb^{3+}) core / $NaYF_4$ shell	0.20 mmol x 4 times (α-$NaYF_4$)	Layer-by-layer
β-$NaYF_4$ (2 mol% Er^{3+}, 15 mol% Yb^{3+}) core / $NaYF_4$ shell	0.25 mmol x 4 times (α-$NaYF_4$)	Layer-by-layer
β-$NaYF_4$ core / $NaGdF_4$ shell	0.3 mmol (β-$NaGdF_4$)	Single step
β-$NaYF_4$ (2 mol% Er^{3+}, 15 mol% Yb^{3+}) core / $NaYF_4$ (1 mol% Tm^{3+}, 15 mol% Yb^{3+}) shell / $NaYF_4$ (5 mol% Tb^{3+}, 15 mol% Ce^{3+}) shell	0.6 mmol α-$NaYF_4$ (1 mol% Tm^{3+}, 15 mol% Yb^{3+}) followed by 0.3 mmol α- $NaYF_4$ (5 mol% Tb^{3+}, 15 mol% Ce^{3+})	Layer-by-layer
β-$NaYF_4$ core (2 mol% Er^{3+}, 15 mol% Yb^{3+}) / $NaGdF_4$ (5 mol% Eu^{3+}, 2 mol% Ce^{3+}) shell	0.3 mmol β-$NaGdF_4$ (5 mol% Eu^{3+}, 2 mol% Ce^{3+})	Single step
β-$NaGdF_4$ (2 mol% Er^{3+}, 25 mol% Yb^{3+}, 10 mol% Y^{3+}) core / $NaYF_4$ (5 mol% Tb^{3+}, 15 mol% Ce^{3+}) shell	0.2 mmol α- $NaYF_4$ (5 mol% Tb^{3+}, 15 mol% Ce^{3+}) followed by 0.2 mmol α- $NaYF_4$ (5 mol% Tb^{3+}, 15 mol% Ce^{3+})	Layer-by-layer

Appendix E. Supplementary Information to Chapter 7

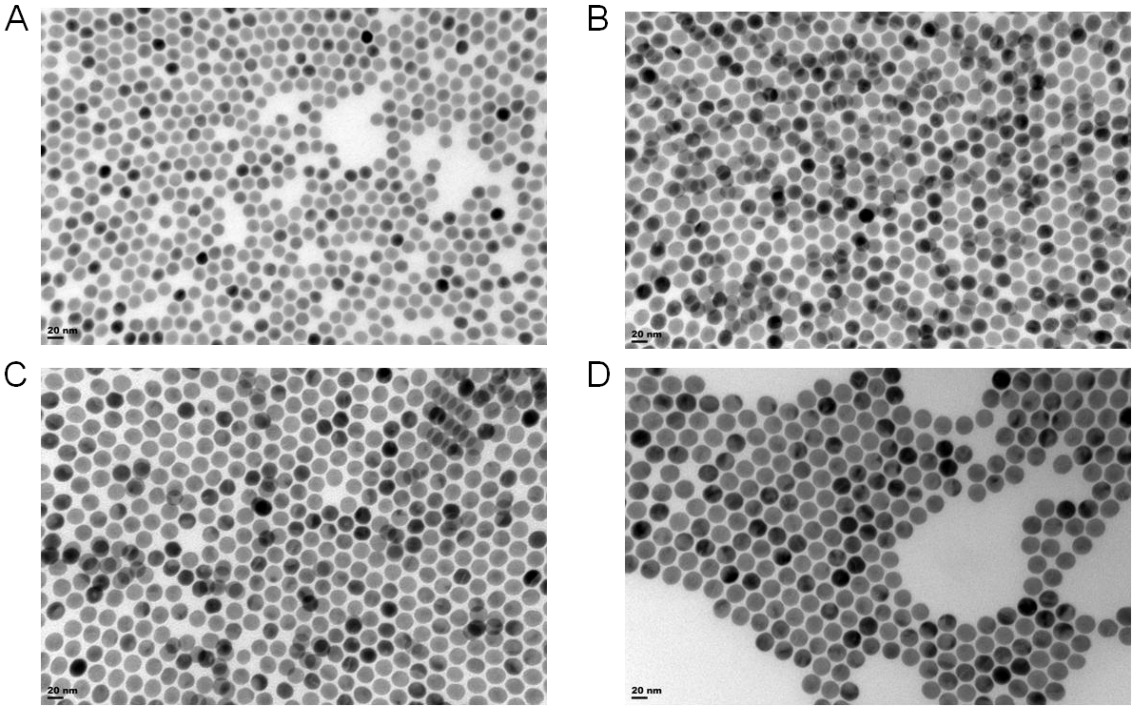

Figure E1. TEM images of **(A)** $NaYF_4$ core NCs, and **(B-D)** $NaYF_4/NaTmF_4$ core/shell NCs after each successive defocusing and self-focusing cycle to deposit 0.5 mmol of $NaTmF_4$ in each cycle, respectively.

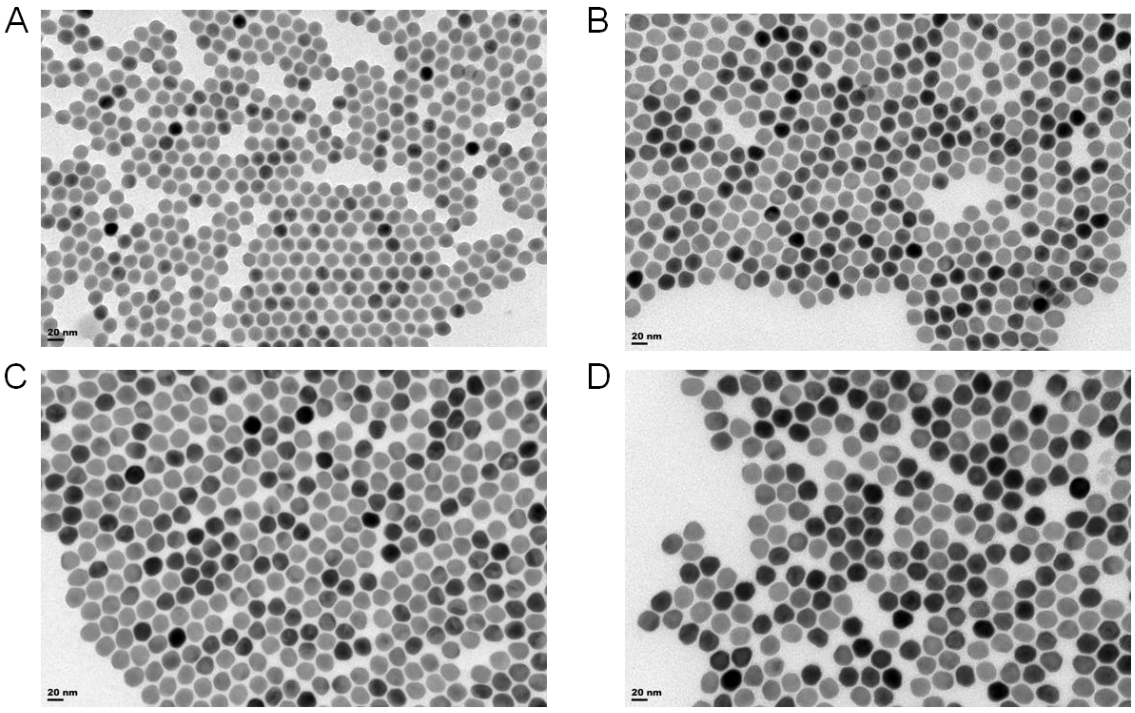

Figure E2. TEM images of **(A)** $NaYF_4$ core NCs, and **(B-D)** $NaYF_4/NaDyF_4$ core/shell NCs after each successive defocusing and self-focusing cycle to deposit 0.5 mmol of $NaDyF_4$ in each cycle, respectively.

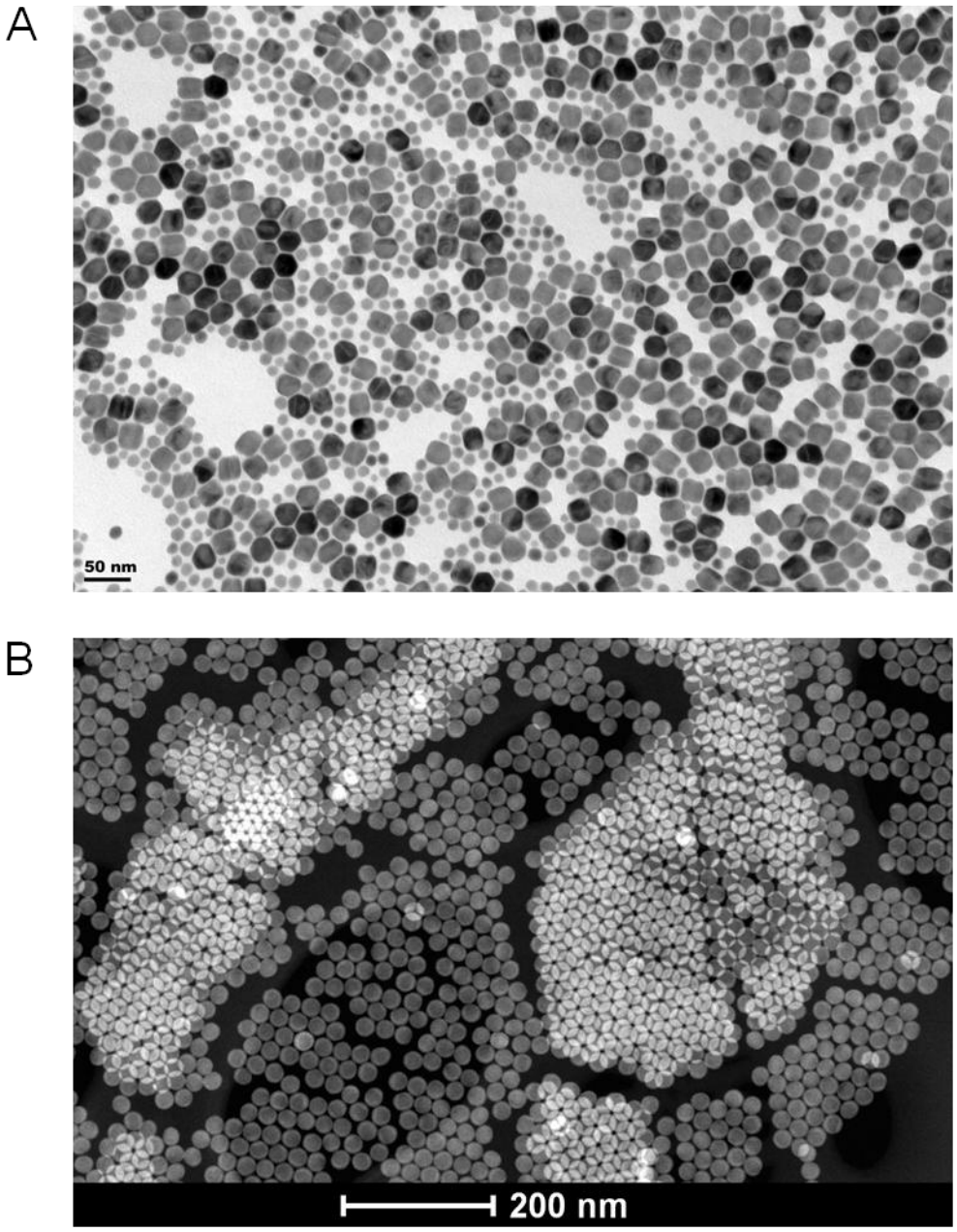

Figure E3. (A) Low-magnification TEM image of $NaYF_4/NaGdF_4$ core/shell NCs, and **(B)** Low-magnification HAADF image of $NaYF_4/NaLuF_4$ core/shell NCs.

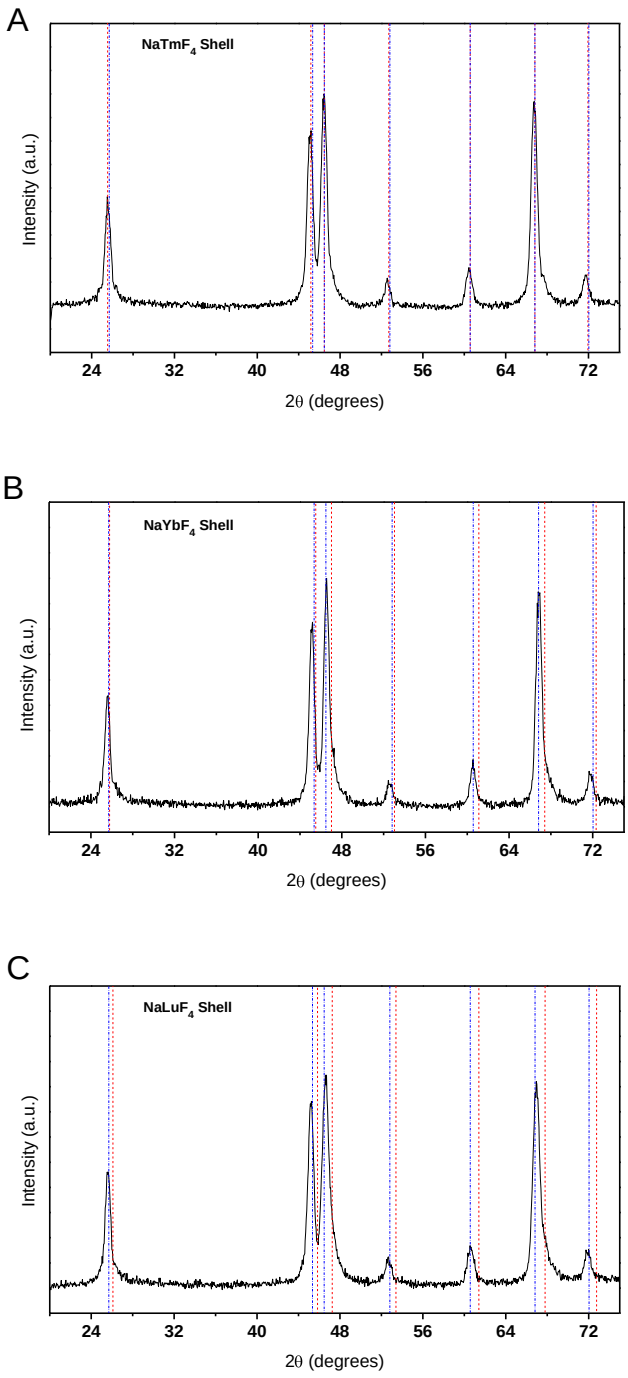

Figure E4. XRD patterns of tensile strained shell growth on $NaYF_4$ NCs **(A)** $NaTmF_4$ shell, **(B)** $NaYbF_4$ shell, and **(C)** $NaLuF_4$ shell. The blue dotted lines in **(A-C)** are the standard reference lines (JCPDS #) of β-$NaYF_4$ (016-0334) and the red dotted lines are the standard reference lines of **(A)** β-$NaTmF_4$ (027-0814), **(B)**, β-$NaYbF_4$ (027-1427), and **(C)** β-$NaLuF_4$ (027-0726).

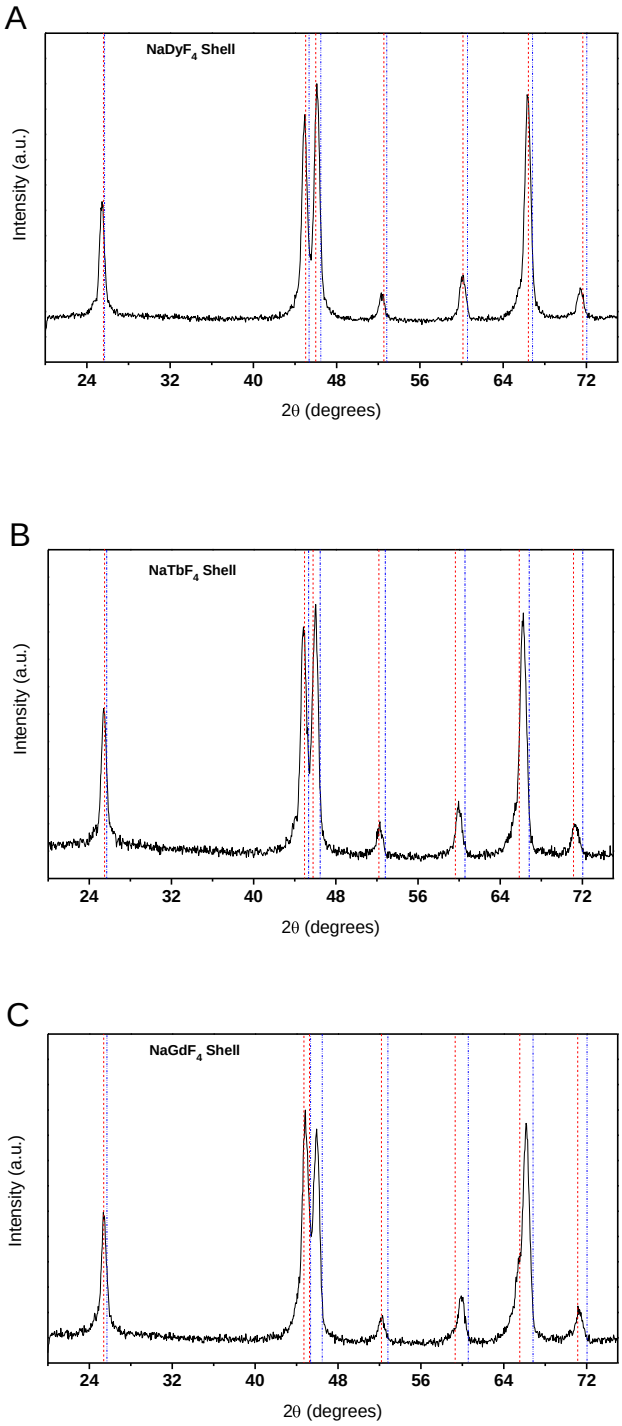

Figure E5. XRD patterns of compressive strained shell growth on $NaYF_4$ NCs **(A)** $NaDyF_4$ shell, **(B)** $NaTbF_4$ shell, and **(C)** $NaGdF_4$ shell. The blue dotted lines in **(A-C)** are the standard reference lines (JCPDS #) of β-$NaYF_4$ (016-0334) and the red dotted lines are the standard reference lines of **(A)** β-$NaDyF_4$ (027-0687), **(B)**, β-$NaTbF_4$ (027-0809), and **(C)** β-$NaGdF_4$ (027-0699).

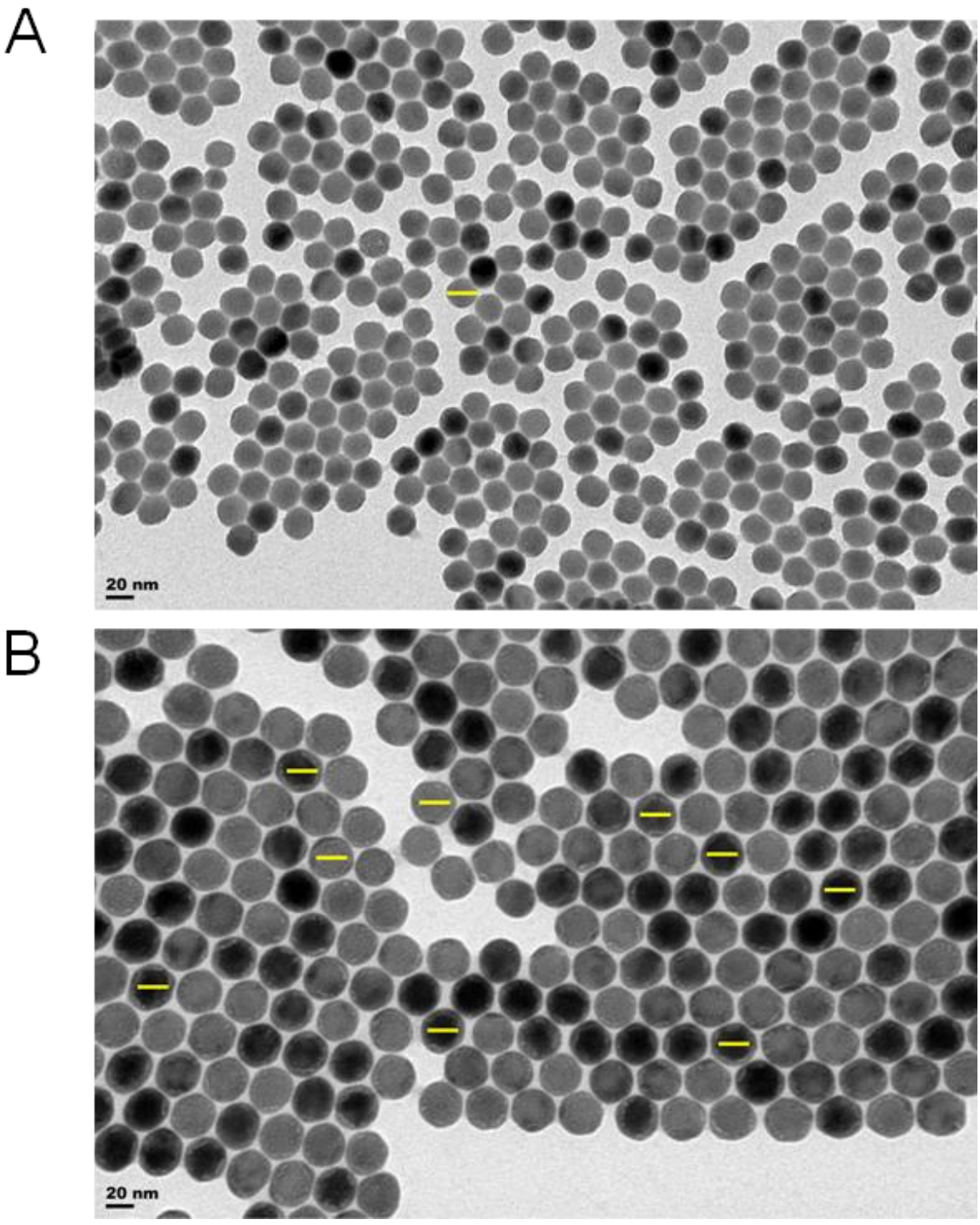

Figure E6. TEM images of **(A)** $NaYF_4$ core NCs, and **(B)** $NaYF_4/NaLuF_4$ core/shell NCs. The yellow lines refer to the size of the core NCs, and in the core-shell images the beam damage caused by the electron beam along the core-shell interface can be seen as white spots.

List of Publications

Portions of this dissertation are from some of these following publications:

10. **Hetero-Epitaxy in Colloidal Nanocrystals: Compressive *vs.* Tensile Strain Asymmetry**
Noah J. J. Johnson *et al.*
To be submitted.

9. **End-group Functionalized Polyvinylpyrrolidone Coated Upconverting Nanocrystals for Immunolabeling of Human Prostate Cancer Cells (LNCaP)**
Noah J. J. Johnson *et al.*
To be submitted.

8. **Long-Term Colloidal Stability and Photoluminescence Retention of Lead-Based Quantum Dots in Saline Buffers and Biological media through Surface Modification**
Jothir Pichaandi, Keith A. Abel, Noah J. J. Johnson, and Frank C. J. M. van Veggel
To be submitted.

7. **Conversion of LaF_3 to Nanocrystalline Lanthanum Silicate and Lanthanum Zirconate: Highly Efficient Near-Infrared Emissions from the Doped Lanthanides**
Neralagatta M. Sangeetha, Noah J. J. Johnson, Frank C. J. M. van Veggel, Bryan E. G. Lucier, and Robert W. Schurko
S*ubmitted.*

6. **Self-focusing by Ostwald Ripening: A Strategy for Layer-by-Layer Epitaxial Growth on Upconverting Nanocrystals**
Noah J. J. Johnson, Andreas Korinek, Cunhai Dong, and Frank C. J. M. van Veggel
Journal of the American Chemical Society **2012**, *134*, 11068.

5. **$NaDyF_4$ Nanoparticles as T_2 Contrast Agents for Ultrahigh Field Magnetic Resonance Imaging**
Gautom Kumar Das, Noah J. J. Johnson, Jordan Cramen, Barbara Blasiak, Peter Latta, Boguslaw Tomanek, and Frank C. J. M. van Veggel
Journal of Physical Chemistry Letters **2012**, *3*, 524.

4. **An Effective Polymer Cross-Linking Strategy to Obtain Stable Dispersions of Upconverting $NaYF_4$ Nanoparticles in Buffers and Biological Growth Media for Biolabeling Applications**
Guicheng Jiang, Jothirmayanantham Pichaandi, Noah J. J. Johnson, and Frank C. J. M. van Veggel
Langmuir **2012**, *28*, 3239.

3. **Size-Tunable, Ultrasmall $NaGdF_4$ Nanoparticles: Insights into their T_1 MRI Contrast Enhancement**
Noah J. J. Johnson, Wendy Oakden, Greg J. Stanisz, R. Scott Prosser, and Frank C. J. M. van Veggel
Chemistry of Materials **2011**, *23*, 2011.

2. **Facile Ligand-Exchange with Polyvinylpyrrolidone and Subsequent Silica Coating of Hydrophobic Upconverting -$NaYF_4$:Yb^{3+}/Er^{3+} Nanoparticles**
Noah J. J. Johnson, Neralagatta M. Sangeetha, John-Christopher Boyer, and Frank C. J. M. van Veggel
Nanoscale **2010**, *2*, 771.

1. **Upconverting Lanthanide-Doped $NaYF_4$-PMMA Polymer Composites Prepared by in Situ Polymerization**
J. C. Boyer, N. J. J. Johnson, and F. C. J. M. van Veggel
Chemistry of Materials **2009**, *21*, 2010.